EPFL

Thèse n° 8207

Syntheses and Applications of Boronate Ester-Capped Clathrochelate Complexes

Présentée le 2 juillet 2021

Faculté des sciences de base
Laboratoire de chimie supramoléculaire
Programme doctoral en chimie et génie chimique

pour l'obtention du grade de Docteur ès Sciences

par

Ophélie Marie PLANES

Acceptée sur proposition du jury

Prof. M. Mazzanti, présidente du jury
Prof. K. Severin, directeur de thèse
Dr E. Kataev, rapporteur
Dr F. Beuerle, rapporteur
Prof. A.-S. Chavin, rapporteuse

École polytechnique fédérale de Lausanne

2021

Table of Contents

Acknowledgements

« Faire une thèse, c'est comme faire un marathon. » C'est finalement, après coup, bien plus que cela. Il aurait été simplement impossible de courir mon marathon de thèse sans une aide extérieure. C'est pourquoi je tiens à exprimer ma reconnaissance et ma gratitude envers ces personnes extérieures venant de tous horizons.

Pour commencer, Prof. Kay Severin qui m'a accepté dans son laboratoire. Merci d'avoir pris le temps de me former, de discuter et d'avoir su rendre la route du marathon enrichissante. Tous les commentaires, conseils et remarques ont sans nul doute, contribué à mon épanouissement au laboratoire.

Je souhaite pareillement remercier les membres du Jury, Dr Anne-Sophie Chauvin, Dr Evgeny Kataev, and Dr Florian Beuerle pour leur temps à lire, corriger, et évaluer ma thèse, ainsi que Prof. Marinella Mazzanti pour avoir tenu le rôle de Présidente du Jury.

Je remercie l'équipe administrative qui a toujours su répondre à mes nombreuses interrogations: Christina et Anne Lene.

De plus, à l'EPFL j'ai eu la chance d'être entourée d'un personnel technique dévoué et toujours prêt à aider. Je remercie donc chaleureusement le personnel de la RMN, de la spectrométrie de masse et du magasin BCH: Anton, Aurélien, Emilie, Daniel, Laure, Fransisco, Gladys, Annelise, Benjamin, Maurizio.

Je remercie également toutes les personnes impliquées dans le IT support qui ont contribué à développer une relation plus saine et coopérative entre mon ordinateur, les logiciels et moi-même.

Il va sans dire que faire une thèse en Chimie Supramoléculaire implique des cristaux difficiles à monter, fragiles et hautement désordonnés. Je remercie donc l'aide indispensable de l'équipe cristallographie: Farzaneh, Rosario, Pascal et Euro. Une mention spéciale pour Euro et sa bienveillance à toute épreuve pour les cristaux et pour tout autre sujet, qui a, sans aucun doute, rendu le chemin de ce marathon bien moins escarpé.

Mieux que des ravitaillements lors d'un marathon, il y a eu les pauses cafés-thés, les escapes-games, les voyages à Paris et Amsterdam, les bowlings, le canoé, les sorties ski et l'hydrospeed avec mes collègues du LCS et nos apprenties. Je vous exprime ma reconnaissante pour tout ce temps ensemble qui m'a aidé à relativiser les échecs des réactions chimiques et qui m'a

donné la force, la motivation de toujours continuer: Yizhu, Léonard, Nicolas, Florian, Giacomo, Aliq, Suzanne, Tim, Mark, Loïc, Mathieu, Aude, Margarida, Sarah, Cristian, Carl, Iris, Cesare, Sylvain, Wolfram, Paul, Anastasia, Dong, Rujin, José et Erica.

Mention spéciale pour Erica (et Mathieu) et José (et Hale), qui ont illuminé mes journées au laboratoire et en dehors. Votre amitié m'est précieuse et je vous remercie de votre soutien sans faille durant plus de 5 ans. De plus, je ne pouvais pas rêver meilleure partenaire de laboratoire, et amie, pour courir ce marathon ensemble. Merci Erica pour tout.

Je remercie ensuite toutes les personnes qui même à distance ont joué un rôle important dans cette course marathonienne: Angela, Joanna, Gwénaël, La team Ability (Dominique et Lucille), La Team TEDx (Faten, Tristan, Alix), La team Chalet (François et Isabelle), ma belle-famille (Marie Lyse, Georges, Alexandra, Jeremy), Elise, Elina, Mathilde, Victoria et Bastien.

Je remercie ensuite, celle qui chaque jour de ma thèse (ou presque) a toujours su trouver les mots pour me motiver à poursuivre ma thèse, mon marathon, mon rêve qu'importe les obstacles : Stéphanie. Merci mille fois d'être mon amie au quotidien !

Ce marathon est finalement loin d'être un sport individuel mais bien au contraire un sport d'équipe. Et dans mon équipe rapprochée, j'ai la chance inouïe de compter les meilleurs membres que l'on puisse imaginer.

Maman, Papa, je vous remercie du fond de mon cœur pour chaque mot, phrase, moment où vous avez patiemment écouter mes « problèmes de chimie » sans jamais comprendre mais toujours à l'écoute. Je vous remercie d'avoir toujours cru en moi et de m'avoir toujours soutenue. Merci encore de m'avoir donné cette rage de me battre pour n'importe quel rêve et notamment pour celui-là. Votre amour qui me berce depuis le premier jour m'a permis d'arriver aujourd'hui à la fin du plus beau marathon qui m'a été donné de courir, ma thèse. Je vous dédie donc les premiers 50% de celle-ci.

Dernier mais pas des moindres, je tiens à exprimer une gratitude immense à celui avec qui je passe, enfin, cette ligne d'arrivée : Sébastien. Tu as accepté de te délocaliser loin de ta famille et de tes amis pour mon rêve de thèse, je t'en serai éternellement reconnaissante. Je te remercie d'être si merveilleux chaque jour et d'avoir accepté les clathrochélates dans notre vie. Il n'existe pas suffisamment de mots pour que je puisse te témoigner à quel point je t'aime, je te dédie alors les 50% restants de ma thèse, et tu sais à quel point c'est précieux et cher à mon cœur.

(N.B: A part ce marathon, je n'en ai couru aucun autre.)

Abstract

This thesis describes the syntheses of novel boronate ester-capped clathrochelate complexes and their application in supramolecular chemistry, materials science, and chemical biology.

Chapter 2 shows the synthesis of long Fe(II) dinuclear clathrochelates, up to 3 nm, with low synthetic effort. Their ability to be used as building blocks in supramolecular chemistry is evidenced by the formation of a Cu_4L_4-type coordination cage, and by the formation of a 2-dimensional metal-organic framework (MOF).

The incorporation of clathrochelate complexes with terminal pyridyl groups into pillared MOFs by using solvent-assisted ligand exchange is described in Chapter 3. The strong basicity of clathrochelates with pyridyl groups makes them particularly suited for this approach.

In Chapter 4, the structural characterization of novel cobalt clathrochelates is described. A first example of a Co(II) clathrochelate with potentially redox non-innocent phenanthrenequinone dioximato groups is reported. Chemical reductions of cobalt clathrochelates were carried out, and ligand effects are investigated by crystallography.

Moreover, in the Chapter 5, clathrochelates with elongated π–dioximate groups are described, along with preliminary attempts of using them as three-way junction (TWJ) stabilizers.

The synthesis of clathrochelate complexes with a chiral dioximato ligand and terminal pyridyl, bromo or carboxylic acid groups are described in Chapter 6. Potential applications of this new metalloligand in supramolecular chemistry are investigated.

Keywords

Clathrochelates complexes • supramolecular chemistry • metal-organic frameworks • coordination cages • redox-active complexes

Résumé

Cette thèse décrit les synthèses de nouveaux complexes de clathrochélate encapsulés par des esters boronates et leurs applications en chimie supramoléculaire, en science des matériaux, et en biologie chimique.

Le chapitre 2 montre la synthèse de longs clathrochélates dinucléaires de fer(II), jusqu'à 3 nm, avec peu d'efforts de synthèse. Leur capacité à être utilisé comme briques moléculaires en chimie supramoléculaire est mise en évidence par la formation d'une cage de coordination de type Cu_4L_4 ainsi que par la formation d'un réseau métallo-organique en deux dimensions.

L'incorporation dans un empilage de réseaux métallo-organiques de complexes de clathrochélate avec des groupes terminaux tels que pyridyls, est décrite dans le Chapitre 3. La forte basicité des clathrochélates avec des groupes pyridyls fait d'eux des candidats adaptés à cette approche incorporatrice.

Dans le Chapitre 4, des nouveaux clathrochélates de cobalt sont décrits et caractérisés structuralement. Un premier exemple de clathrochélate de cobalt (II) avec des groupes phenanthrenequinone dioximato potentiellement redox-actifs est décrit. Les réductions chimiques de clathrochélates de cobalt sont présentées et les effets des ligands sont examinés par cristallographie.

De plus, dans le Chapitre 5, des clathrochélates avec des groupes π–dioximate étendus sont rapportés, ainsi que des résultats préliminaires d'utilisation dans le cadre de stabilisateurs de jonctions à trois voies.

La synthèse de complexes de clathrochélate avec un groupe dioximato qui est chiral et des groupes terminaux tels que pyridyl, brome, ou acide carboxylique, sont dépeints dans le Chapitre 6. Des potentielles applications de ce nouveau métalloligand en chimie supramoléculaire sont également analysées.

Mots clés

Complexes de clathrochélate • chimie supramoléculaire • réseaux métallo-organiques • cages de coordination • complexes redox-actifs

Abbreviation and Symbols

°	degree
2D	two-dimensional
Å	Ångström
Ar	aryl
av.	Average
BET	Brunauer-Emmet-Teller
˚C	degree Celsius
calcd	calculated
CH_3CN	acetonitrile
d	doublet
dd	double doublet
td	double triplet
DMSO	dimethylsulfoxide
DMA	N,N'-dimethylacetamide
DMF	N,N'-dimethylformamide
DNA	deoxyribonucleic acid
DOSY	diffusion-ordered NMR spectroscopy
δ	chemical shift
ESI-MS	electrospray ionisation mass spectrometry
Et	ethyl
Et_2O	diethyl ether
EtOAc	ethyl acetate
EtOH	ethanol
et al.	*et alia*
g	gram
h	hour
HR-MS	high-resolution mass spectrometry
Hz	Hertz
J	coupling constant
K	Kelvin

m	multiplet
m	meta
M	molar (mol.L-1)
m/z	mass:charge ratio
Me	methyl
MeOH	methanol
mg	milligram
MHz	megahertz
mL	millilitre
mmol	millimole
MOP	metal-organic polyhedra
MOF	metal-organic framework
mol	mole
µmol	micromole
n	number
n-Bu	normal-butyl
nm	nanometre
NMR	nuclear magnetic resonance
o	ortho
p	para
Ph	phenyl
ppm	parts per million
PXRD	powder X-ray diffraction
q	quartet
ref	reference
RNA	ribonucleic acid
RT	room temperature
s	singlet
t	triplet or time
T	temperature
TGA	thermogravimetric analysis
UV	ultraviolet
UV/Vis	ultraviolet-visible

Note: additional abbreviation for specific compounds are defined within the manuscript.

Chapter 1

Introduction

1.1 Clathrochelate Complexes

In 1964, Curry and Busch introduced the concept of “clathrochelates” by defining them as coordination compounds with a metal ion trapped by coordinating ligands.[1] This new class of compounds can also be denominated as “cage complexes”.[2] The definition has been refined over time to describe clathrochelates as complexes with a metal ion encapsulated and saturated by macrobicyclic ligands with donor atoms. Subsequently, the resulting metal ion is isolated from the external environment. In 1968, Boston and Rose reported the synthesis of a clathrochelate that perfectly illustrates this definition in **Scheme 1.1**.[3]

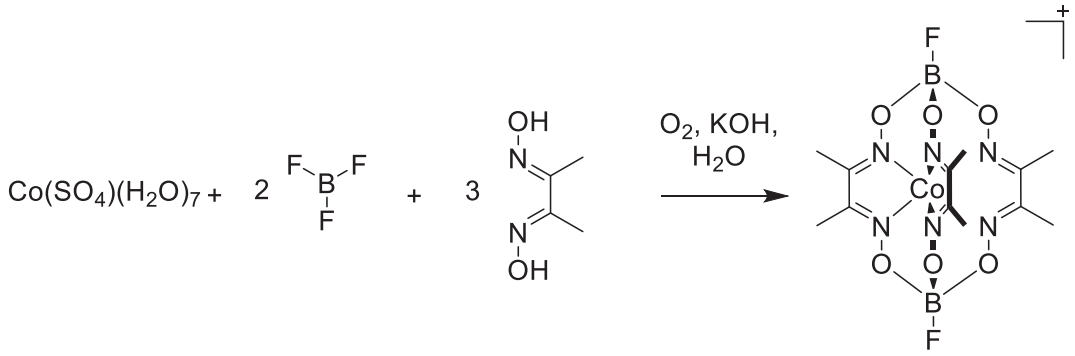

1.1

Scheme 1.1 Synthesis of tris(dimethylglyoximato)-based Co(III) clathrochelate **1.1**. The counterion is omitted for clarity.

The resulting complex **1.1** is composed of a central cobalt (III) metal ion surrounded by three dimethylglyoximato ligands and with two BF capping groups forming boronate esters. The one-pot synthesis of clathrochelates is straightforward. It has been reported that the rate-limiting step is the formation of the complex with the central metal ion coordinated to the three dioximate-based ligands.[4] This metal complex can be capped by reaction with a Lewis-acid.

The reported capping groups include germanium,[5-7] tin[7-8] or antimony[9] and some d- and f- block metals.[10-14] Boronate ester-capped clathrochelates are the most represented examples in literature. They are very popular because a large library of starting boronic acids is commercially available.[15] Selected examples of clathrochelates with different capping groups are shown in **Figure 1.1**; all examples have iron(II) as the central metal ion.

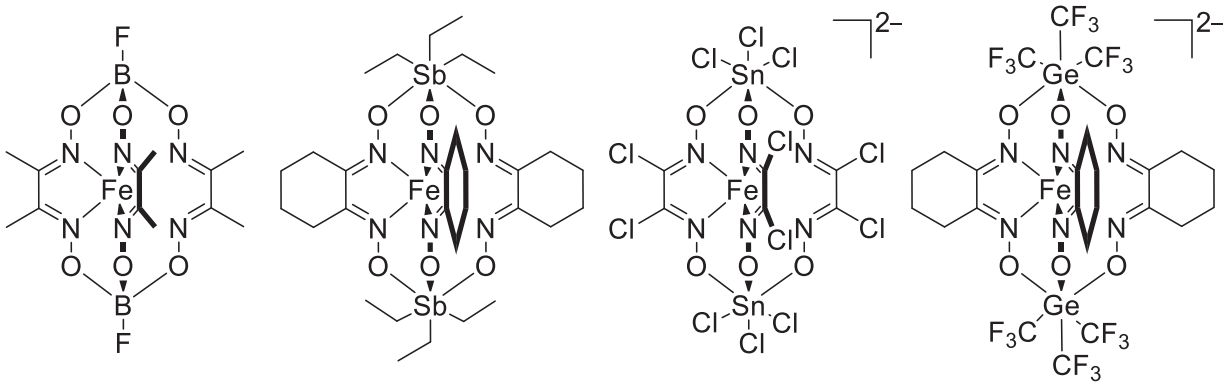

1.2 **1.3** **1.4** **1.5**

Figure 1.1 Selected examples of Fe(II) clathrochelates **1.2**-**1.5** with different capping groups: **1.2** (boronate ester), **1.3** (antimony), **1.4** (tin) and **1.5** (germanium). Counterions are omitted for clarity.

In this chapter, we will only discuss boronate ester-capped clathrochelates and selected applications relevant to this thesis.

1.1.1 Boronate Ester-Capped Clathrochelates

Boronate ester-capped clathrochelate complexes can be synthesized from a metal salt, an *α*-dioxime ligand and a boronic acid as shown in **Scheme 1.2**.

Typical metal ions incorporated in such clathrochelates are cobalt (Co(I), Co(II), Co(III)), iron (Fe(I), Fe(II) and ruthenium (Ru(II)).[16]

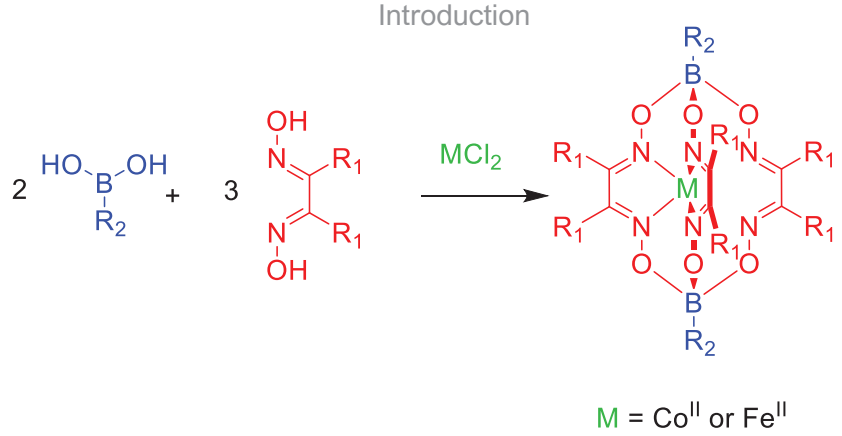

Scheme 1.2 General synthesis of boronate ester-capped clathrochelate complexes.

An alternative approach for obtaining the clathrochelate complexes is based on post-modification of halogenated clathrochelates. This method has the advantage to overcome difficult synthesis of corresponding dioximes. Voloshin *et al.* have developed a strategy to obtain alicyclic S_2-, N_2- and O_2- clathrochelates by nucleophilic substitutions of polyhalogenated clathrochelate. Selected examples of such post-modification reactions are shown in **Scheme 1.3**.[17]

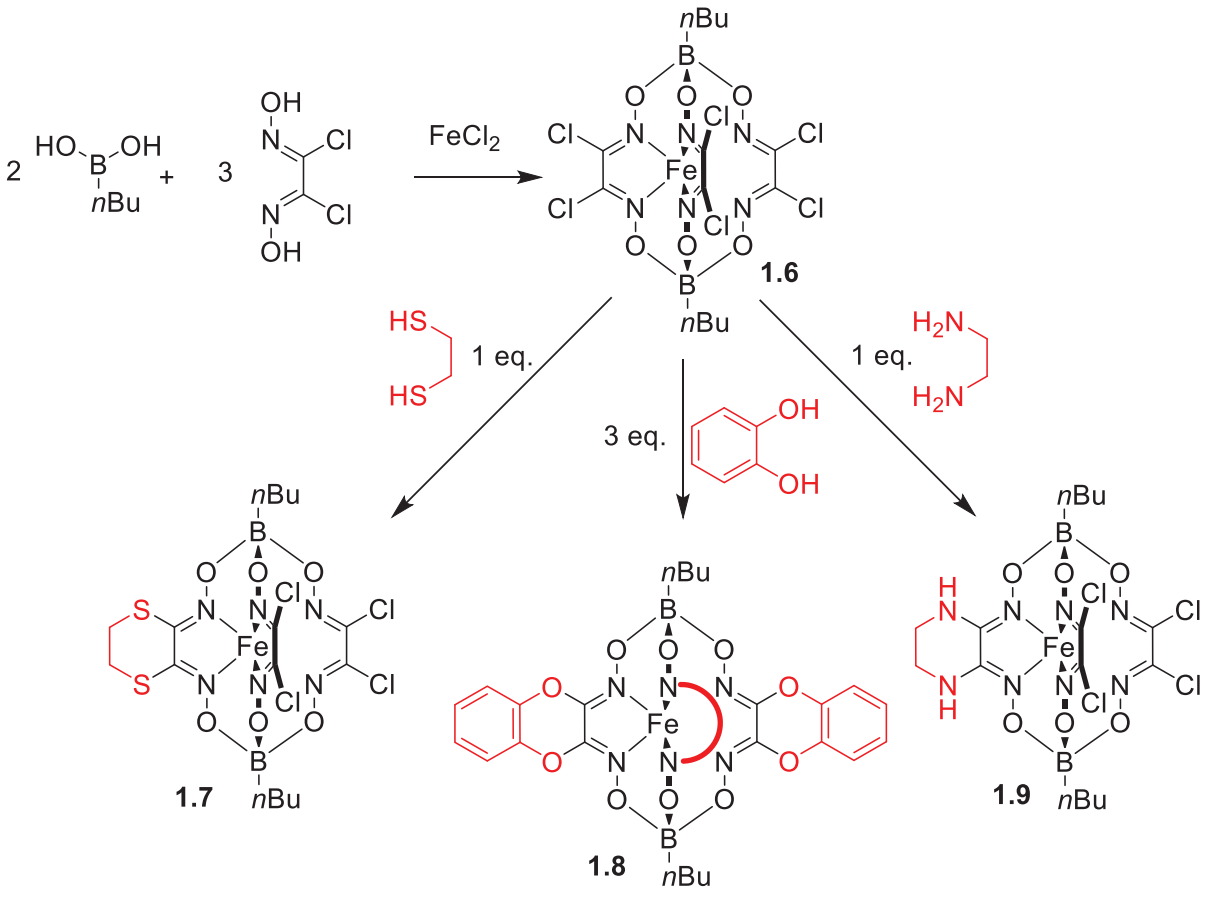

Scheme 1.3 Selected examples of nucleophilic substitution on a Fe(II) boronate ester-capped clathrochelate to give alicyclic S_2-, N_2- and O_2- clathrochelates.

Moreover, polyhalogenated clathrochelates are suitable precursors in metal-catalyzed cross coupling reactions. Recently, the group of Voloshin has reported multi-step syntheses of clathrochelates by palladium- and copper-promoted reactions such as perfluoroarylation (compound **1.11**), cyanination (compound **1.12**), halogen exchange (compound **1.13**), perfluoroalkylation (compound **1.14**), homocoupling and hydrodehalogenation.[18] Selected examples of resulting clathrochelates are shown in **Scheme 1.4** to illustrate the variety of complexes reached successfully.

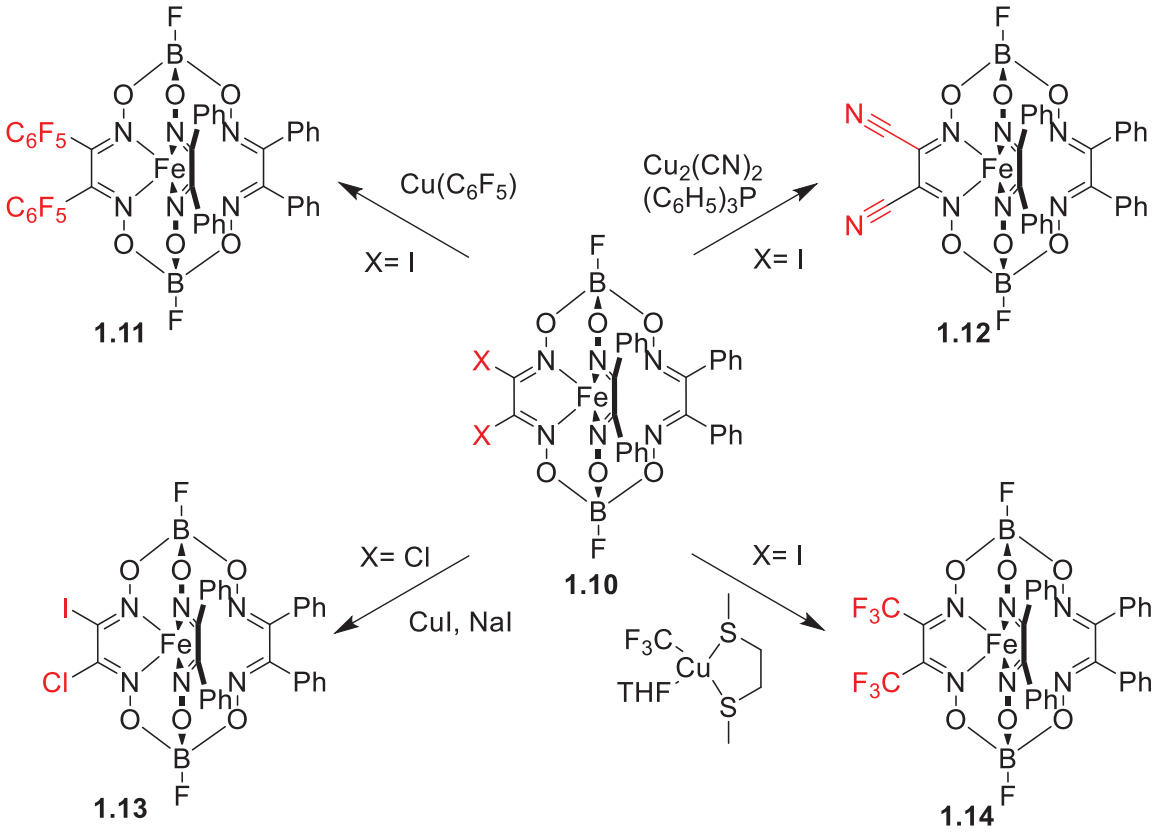

Scheme 1.4 Selected examples of post-modification on a Fe(II) boronate ester-capped clathrochelate.

The synthetic versatility of clathrochelates arises from either the capping groups (boronate esters) or by the dioximato ligands. The solubility[12], reactivity[19] and redox behavior[20-21] can be tuned easily via modification of surrounding functional groups. A comprehensive overview of the dioxime and boronic acid libraries is described in two books by Voloshin *et al*.[2]

1.1.2 Selected Applications of Clathrochelate Complexes

This section does not claim to cover all applications of boronate ester-caped clathrochelates. For clarity, “boronate ester-capped clathrochelates” will be shortened and referred as “clathrochelates” in the following chapter. Only applications relevant to the scope of this thesis are presented. The purpose of this section is to illustrate a wide variety of applications employing clathrochelates. We will review the use of clathrochelates as building blocks in supramolecular chemistry either for the synthesis of discrete coordination cages or for infinite networks such as MOFs or polymers. Furthermore, we will discuss the use of clathrochelates as catalyst in hydrogen evolution reaction (HER) or as TWJ stabilizers.

1.1.2.1 Clathrochelate Complexes as Building Blocks for Discrete Nanostructures

Supramolecular discrete nanostructures can be obtained by self-assembly of ligands and metal salts to give the most thermodynamically favored product.[22] Recently, clathrochelates were explored as building blocks in supramolecular chemistry.[15] Due to their encapsulated metal ion, they classify as metalloligands. Furthermore, the lateral size, the length and the angles of the coordinative vectors are easily tunable. Therefore a large variety of discrete nanostructures based on clathrochelates was obtained. Two main types of structures can be found in literature depending on the terminal group on the boronic acid: either as pyridyl-based or carboxylic acid-based clathrochelates.

The first example of a clathrochelate complex, which was used as a metalloligand, was reported in 2000 by Grzybowski *et al.*[19] They have synthesized a tris(oximehydrazone) Fe(II) clathrochelate with one pyridyl boronate ester capping group. The latter was coordinated to a Co(III) cobaloxime, yielding to a complex **1.15**, elucidated by X-ray crystallography (**Figure 1.2**).

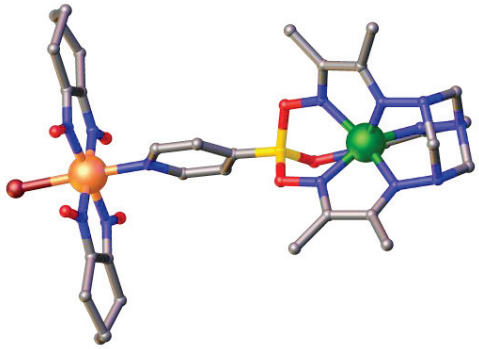

1.15

Figure 1.2 X-ray crystal structure of complex **1.15**. Color coding: Fe: green, C: grey, B: yellow, N: blue, O: red, Co: orange and Br: brown. Hydrogen atoms and solvent molecules are omitted for clarity.

In 2013, Severin and coworkers have started to investigate a more general use of clathrochelates as building blocks to build nanostructures.[23] They have reported the synthesis of 4,4'-bipyridyl Fe(II) clathrochelates (**1.16**) and the first example of a clathrochelate-based metallacycle (**1.17**). The metallacycle **1.17** was obtained from four 4,4-bipyridyl Fe(II) clathrochelates (**1.16**) upon the reaction with *fac*-$ReCl(CO)_3(CH_3CN)_2$ (**Scheme 1.5**).

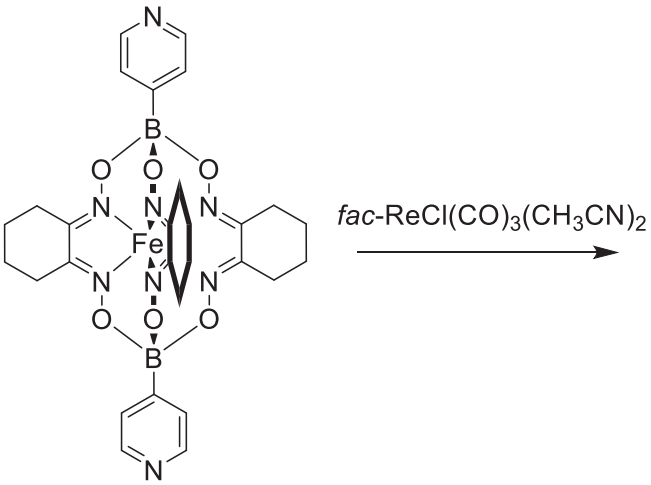

1.16

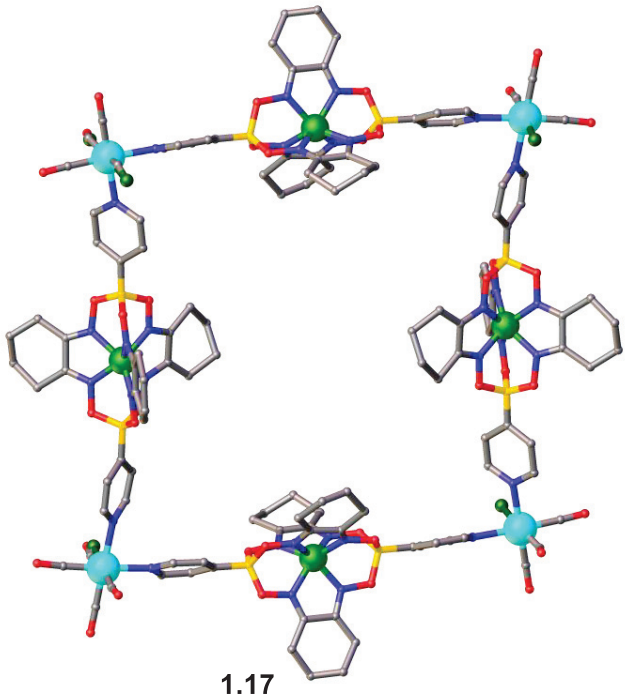

1.17

Scheme 1.5 Synthesis of metallacycle **1.17** from clathrochelate **1.16** with the X-ray crystal structure of complex **1.17**. Color coding: Fe: green, C: grey, B: yellow, N: blue, O: red and Re: turquoise. Hydrogen atoms and solvent molecules are omitted for clarity.

In 2014, Jin *et al.* followed a similar strategy. They isolated two metallacycles (**1.18** and **1.19**) using $[Cp^*IrCl_2]_2$ and two clathrochelates **1.16**. X-ray structures have been obtained and they are shown in **Figure 1.3**.[24] Furthermore, they have reported nano-sized cavities in each iridium(III)-iron(II) hybrid metallacycle. Small molecules such as dichloromethane or triflate anions were found inside the cavities, opening the potential of clathrochelates in host guest chemistry.

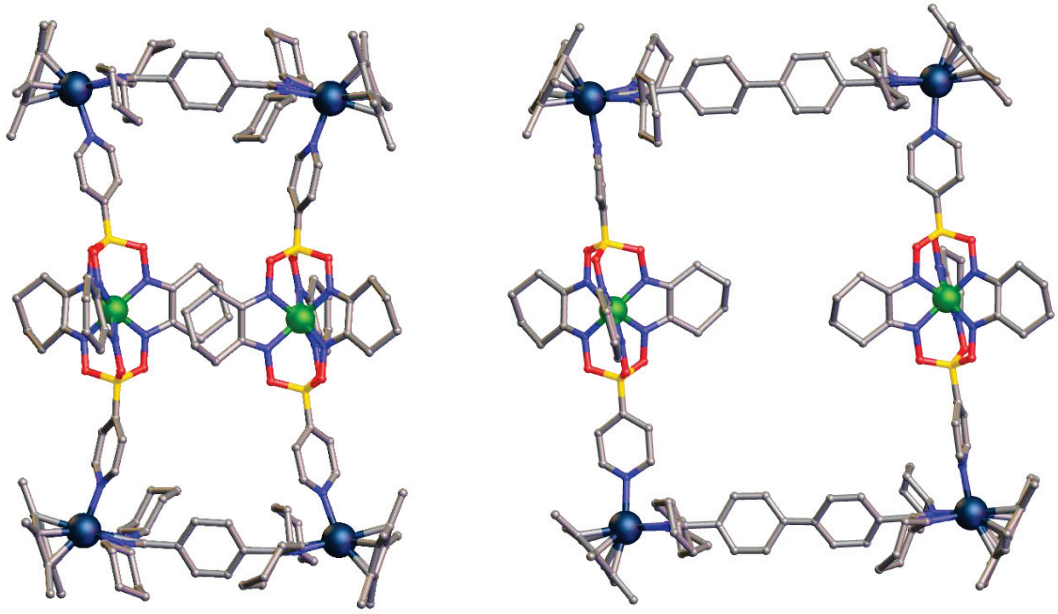

1.18 **1.19**

Figure 1.3 X-ray crystal structure of metallacycles **1.18** and **1.19**. Color coding: Fe: green, C: grey, B: yellow, N: blue, O: red and Ir: dark blue. Hydrogen atoms and solvent molecules are omitted for clarity.

As described in Section 1.1, a large variety of lateral sizes of clathrochelates can be achieved by changing the dioxime moiety. Changing the lateral size of the clathrochelate play a role in the final solubility and it could influence the selective formation of supramolecular nanostructures. Severin *et al*. have synthesized a library of 3-pyridyl clathrochelates **1.20-1.23** which have been used as building blocks to form discrete nanostructures as shown in **Figure 1.4**.[25-26]

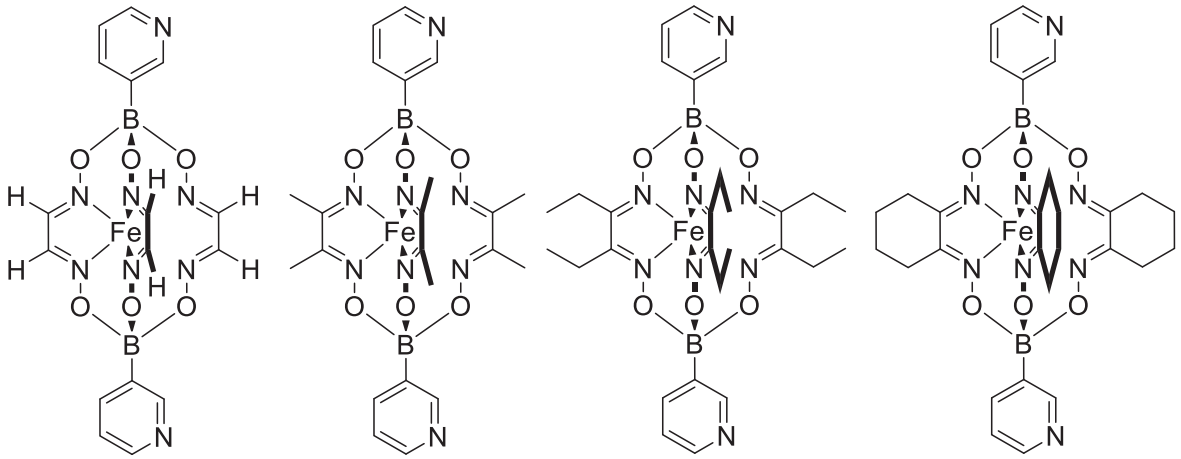

1.20 **1.21** **1.22** **1.23**

Figure 1.4 Fe(II) clathrochelates **1.20** to **1.23** with 3-pyridyl moiety as capping group.

The reaction of **1.20** with $[Pd(CH_3CN)_4(BF_4)_2]$ lead to the formation of a tetrahedral cage **1.24,** whereas the reaction of **1.22** with the same metal salt gave an octahedral structure **1.25** (**Figure 1.5**).

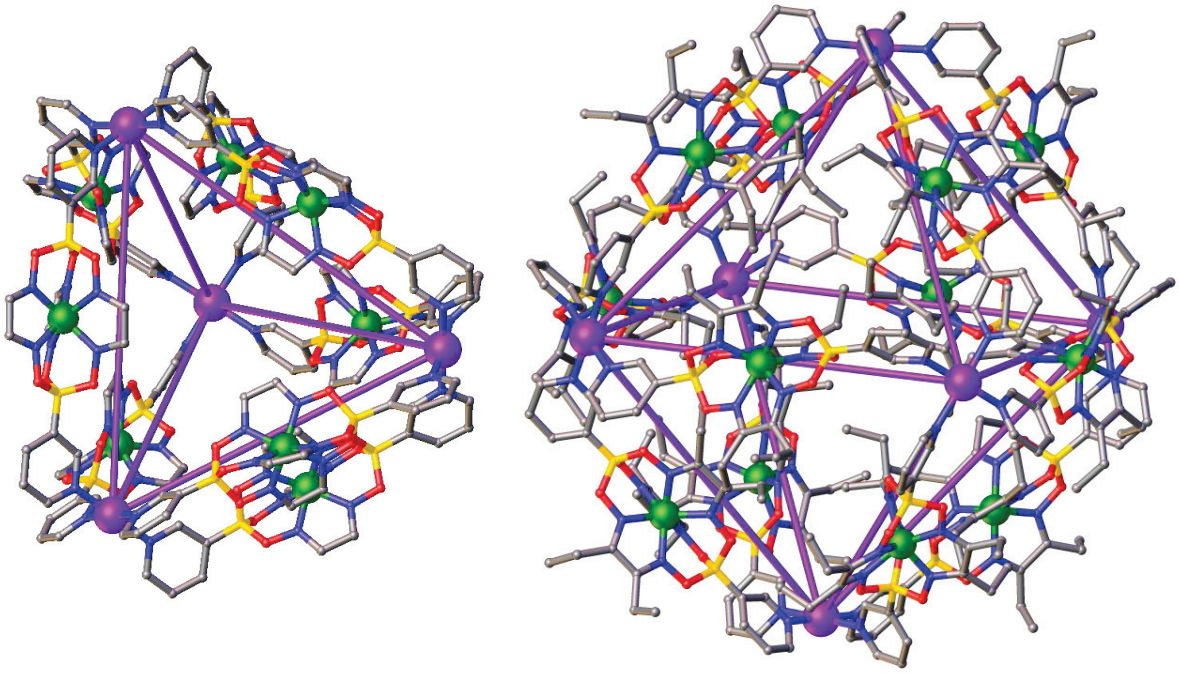

1.24 **1.25**

Figure 1.5 X-ray crystal structure of coordination cages **1.24** and **1.25**. Color coding: Fe: green, C: grey, B: yellow, N: blue, O: red and Pd: purple. Hydrogen atoms, counterions and solvent molecules are omitted for clarity.

The authors highlighted that the only difference depicted between the two clathrochelates, used as metalloligands, is the lateral size. A strong effect on the final nanostructure was observed. Indeed, with L= clathrochelate **1.21** or **1.22** or **1.23**, an octahedral Pd_6L_{12} structure was exclusively obtained. The authors rationalize that the minimum lateral size of these clathrochelates, limited by the minimum distance between dioximes, prevent the formation of structures smaller than a tetrahedron. On the other hand, having a less bulky dioxime with only hydrogen atoms showed only the formation of a tetrahedral cage with two doubly bridged edges.[26] The same concept of varying the ligand aspect-ratio was extended to other clathrochelates with formylpyridine as terminal groups. Upon reaction of clathrochelates **1.26** or **1.27** with *para*-toluidine and Fe(II) salts, two different structures were selectively observed (**Scheme 1.6**).

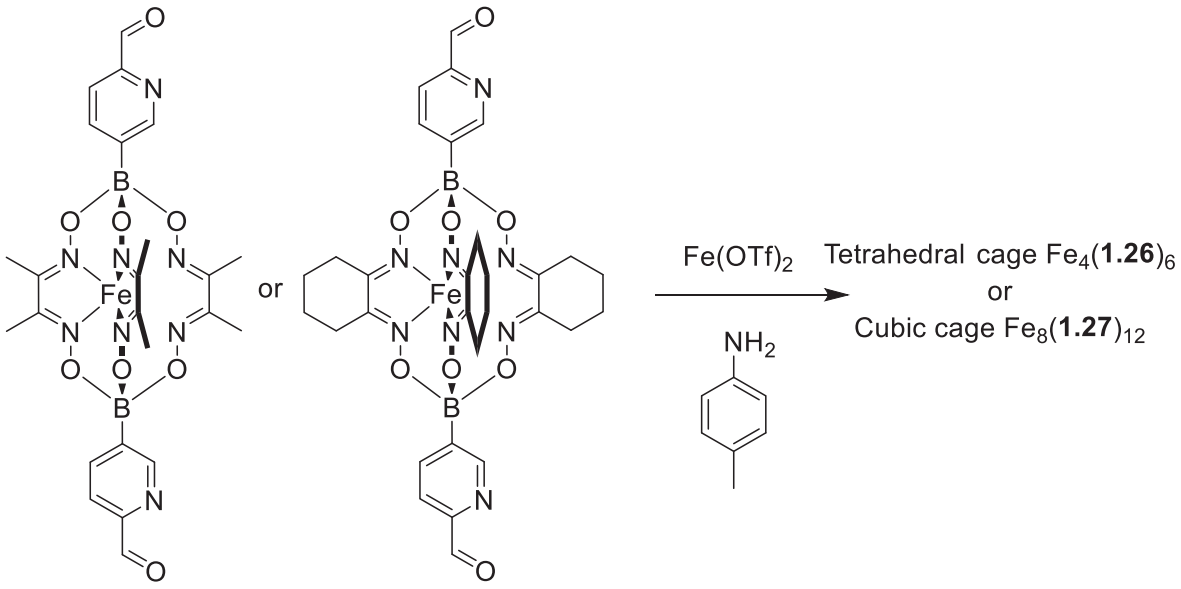

Scheme 1.6 Synthesis of Fe(II)-based coordination cages from clathrochelates **1.26** and **1.27**.

For the reaction of L = clathrochelate **1.26** with $Fe(OTf)_2$, a triangle Fe_4L_6 was observed whereas with L = clathrochelate **1.27** with the same Fe(II) source, a cubic Fe_8L_{12} nanostructure was observed. The authors have explained this structural difference by the change in the lateral size of each clathrochelate involved.[26] Indeed, the lateral size of clathrochelates gives selectively cubic nanostructures in presence of bulky dioximate groups or tetrahedral nanostructures with less bulky ones.

Moreover, the importance of the length of clathrochelate ligands in the formation of discrete nanostructures was evidenced by the combination of clathrochelates **1.28** and **1.29** with terminal amino groups in para positions with formylpyridine and $Fe(OTf)_2$ (**Scheme 1.7**). With this reversed strategy, longer ligands were created and they have formed exclusively tetrahedral cages in both cases, independently of the lateral size of the clathrochelate involved.

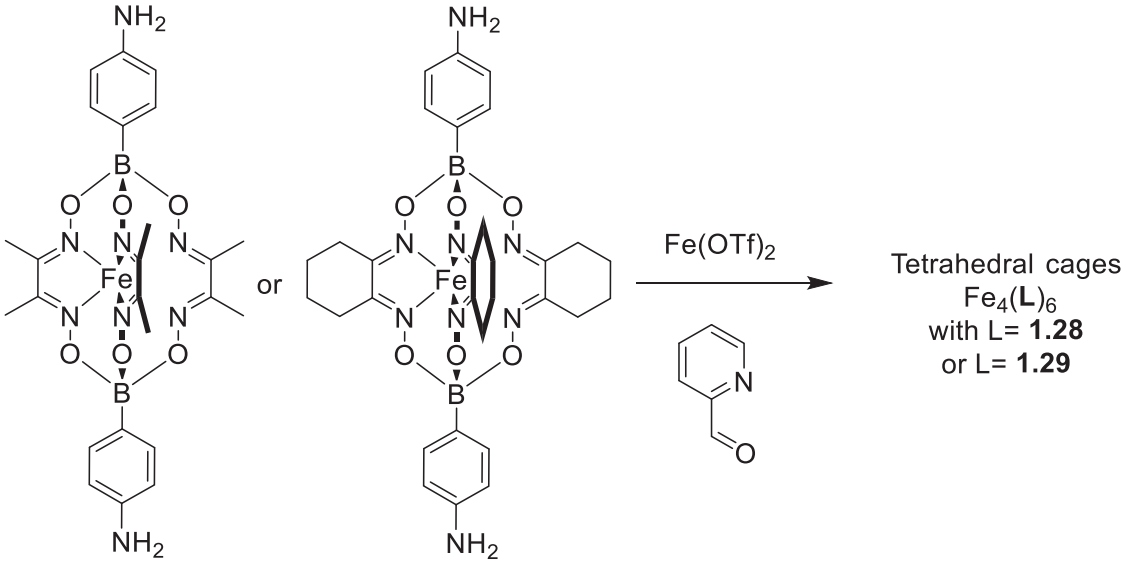

1.28 **1.29**

Scheme 1.7 Synthesis of Fe(II)-based tetrahedral coordination cages from clathrochelates **1.28** and **1.29**.

One example of the resulting Fe_4L_6 cage (**1.30**) with L = clathrochelate **1.29** has been highlighted by its X-ray structure in **Figure 1.6**.

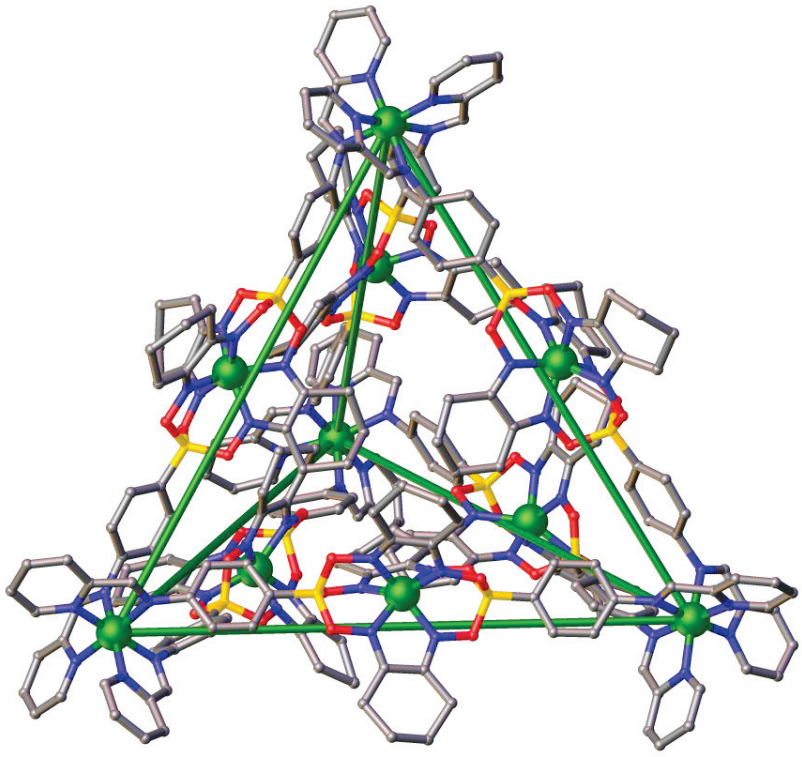

1.30

Figure 1.6 X-ray crystal structure of tetrahedral cage **1.30**. Color coding: Fe: green, C: grey, B: yellow, N: blue and O: red. Hydrogen atoms, counterions and solvent molecules are omitted for clarity.

Increasing the complexity in supramolecular nanostructures remains challenging. Our group has used clathrochelates to illustrate the importance of the lateral size and ligand-ligand interactions by achieving palladium and platinum-based nanostructures with high complexity. They have performed reactions with *cis*-blocked Pt (II) salts and tetrapyridyl clathrochelates. Those tetrapyridyl clathrochelates were synthesized in two steps: after the synthesis of tetrabrominated clathrochelates, a cross-coupling reaction with 4-pyridyl boronic acid afforded clathrochelates **1.31**-**1.36** (**Figure 1.7**).[27-29] The factors controlling the outcome geometry of an assembly with tetratopic N-donor ligands with cis-blocked Pd(II) or Pt(II) salts are not fully understood. Most of the examples reported are $M_{2n}L_n$ prismatic structures as illustrated in **Figure 1.8** by the X-ray structure of the barrel Pt_8L_4 (**1.37**) with L = **1.36**.[29]

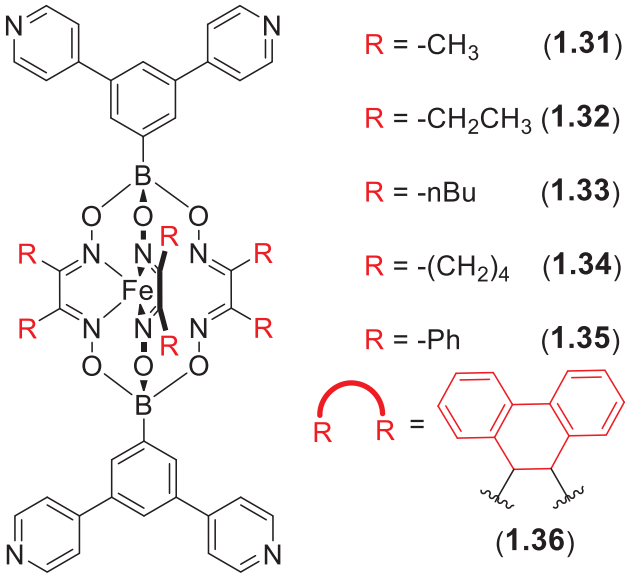

Figure 1.7 Tetrapyridyl clathrochelates **1.31**-**1.36**.

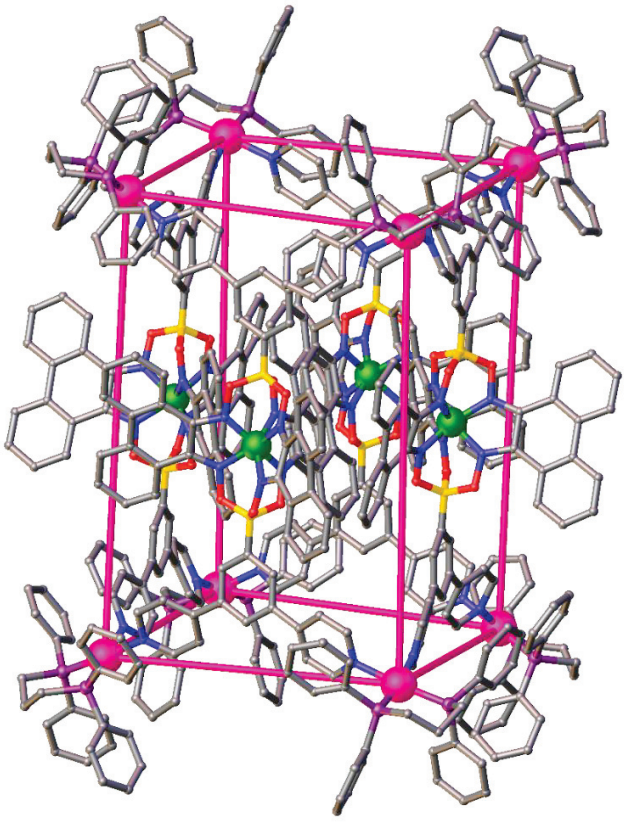

1.37

Figure 1.8 X-ray crystal structure of complex **1.37**. Color coding: Fe: green, C: grey, B: yellow, N: blue, O: red, P: violet and Pt: pink. Hydrogen atoms, counterions and solvent molecules are omitted for clarity.

The authors reported that phenanthrene moieties as lateral groups on each clathrochelate was a decisive element to induce a barrel-like geometry. Indeed, phenanthrene intermolecular π-π interactions were crucial to favor tight packing into a barrel-like geometry. Other surprising structures were found using less bulky clathrochelates ligands. For example, a Pt_8L_4 nanostructure **1.36** with L = **1.31**, was reported with a gyrobifastigium-like geometry. Each rectangular face of the structure was paneled by a clathrochelate as shown in **Figure 1.9**.[27]

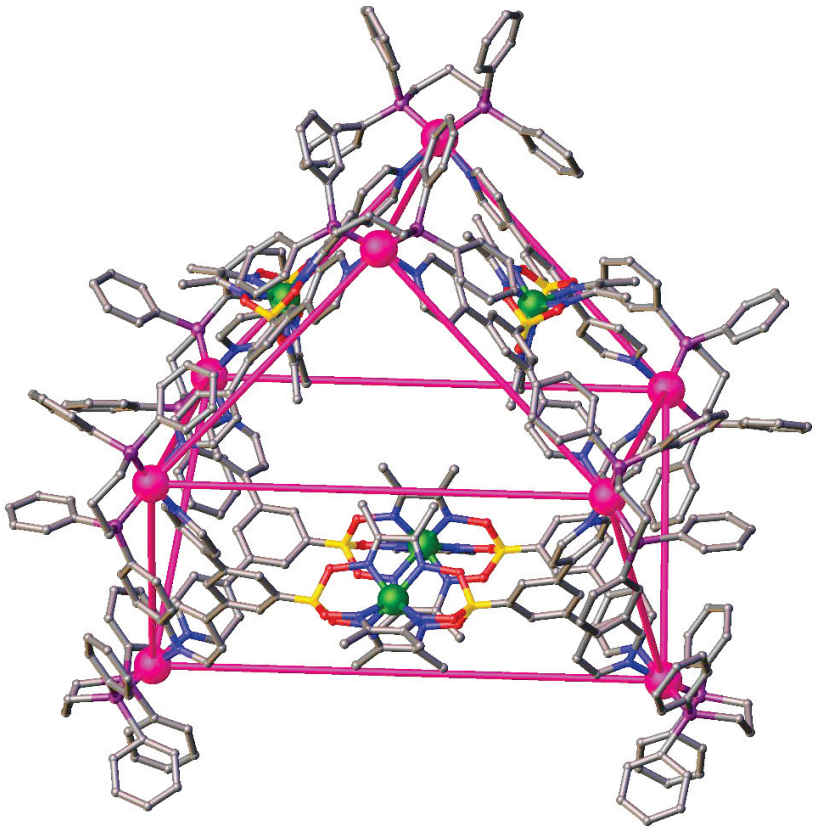

1.38

Figure 1.9 X-ray crystal structure of complex **1.38**. Color coding: Fe: green, C: grey, B: yellow, N: blue, O: red, P: violet and Pt: pink Hydrogen atoms, counterions and solvent molecules are omitted for clarity.

The authors have explained the formation of this highly complex nanostructure by taking into account steric considerations. The driving force for the formation of **1.38** appeared to be linked to the steric demand of the clathrochelate complexes **1.31**, which is less favorable for the formation of barrel-like structure. Indeed, in that case intermolecular considerations between clathrochelates does not play a role in the formation of a constraint structure. Consequently, an open structure with less constraint was obtained.

In the same study, with *n*-butyl alkyl chains as lateral groups on each tetratopic N-donor clathrochelate (**1.33**), an interesting $Pt_{16}L_8$ structure was obtained and characterized by single crystal X-ray diffraction. The Pt atoms were arranged in a distorted square orthobicupola structure **1.39** (**Figure 1.10**).

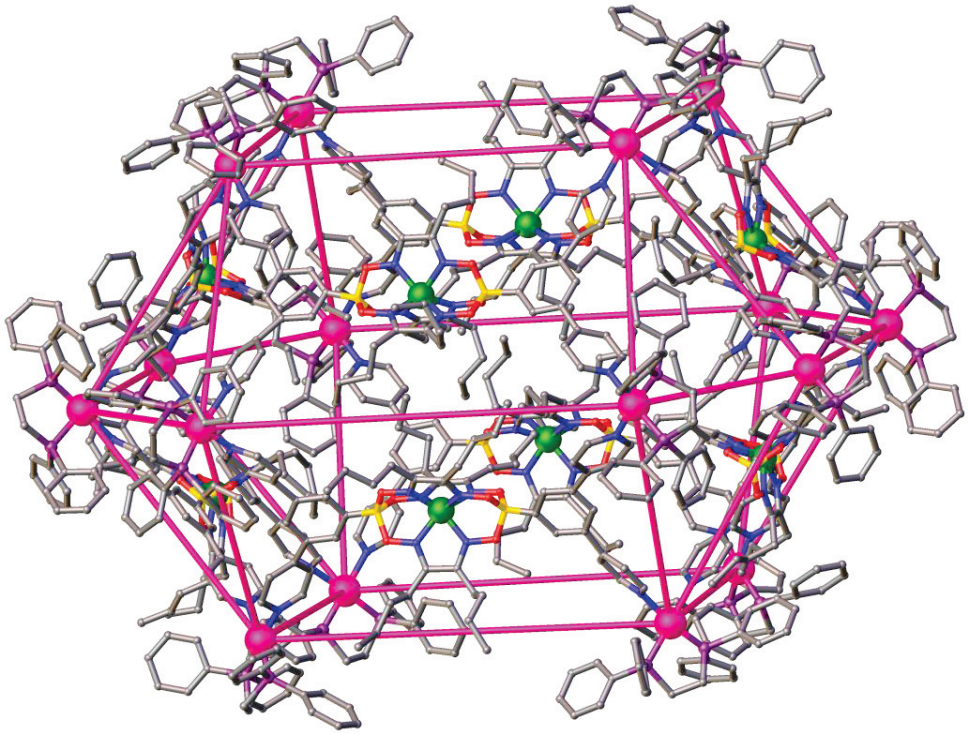

1.39

Figure 1.10 X-ray crystal structure of complex **1.39**. Color coding: Fe: green, C: grey, B: yellow, N: blue, O: red, P: violet and Pt: pink Hydrogen atoms, counterions and solvent molecules are omitted for clarity.

The square orthobicupola geometry is part of the Johnson polyhedra's family and is composed of ten rectangular faces with eight equilateral triangles, wherein tetratopic clathrochelates occupy eight of the rectangular faces. With a diameter of 4.5 nm, this complex **1.39** is one of the largest Pt(II)-based assembly, which could be structurally characterized so far (comparison done with CCDC database).

Moreover, in the field of large and complex nanostructures, clathrochelates have been employed to form Pd_6L_n-type cages. For that purpose, tritopic clathrochelates **1.40** were combined with $[Pd(CH_3CN)_4(BF_4)_2]$ to generate octahedral Pd_6L_8 (**1.41**) as illustrated in **Scheme 1.8**.[30]

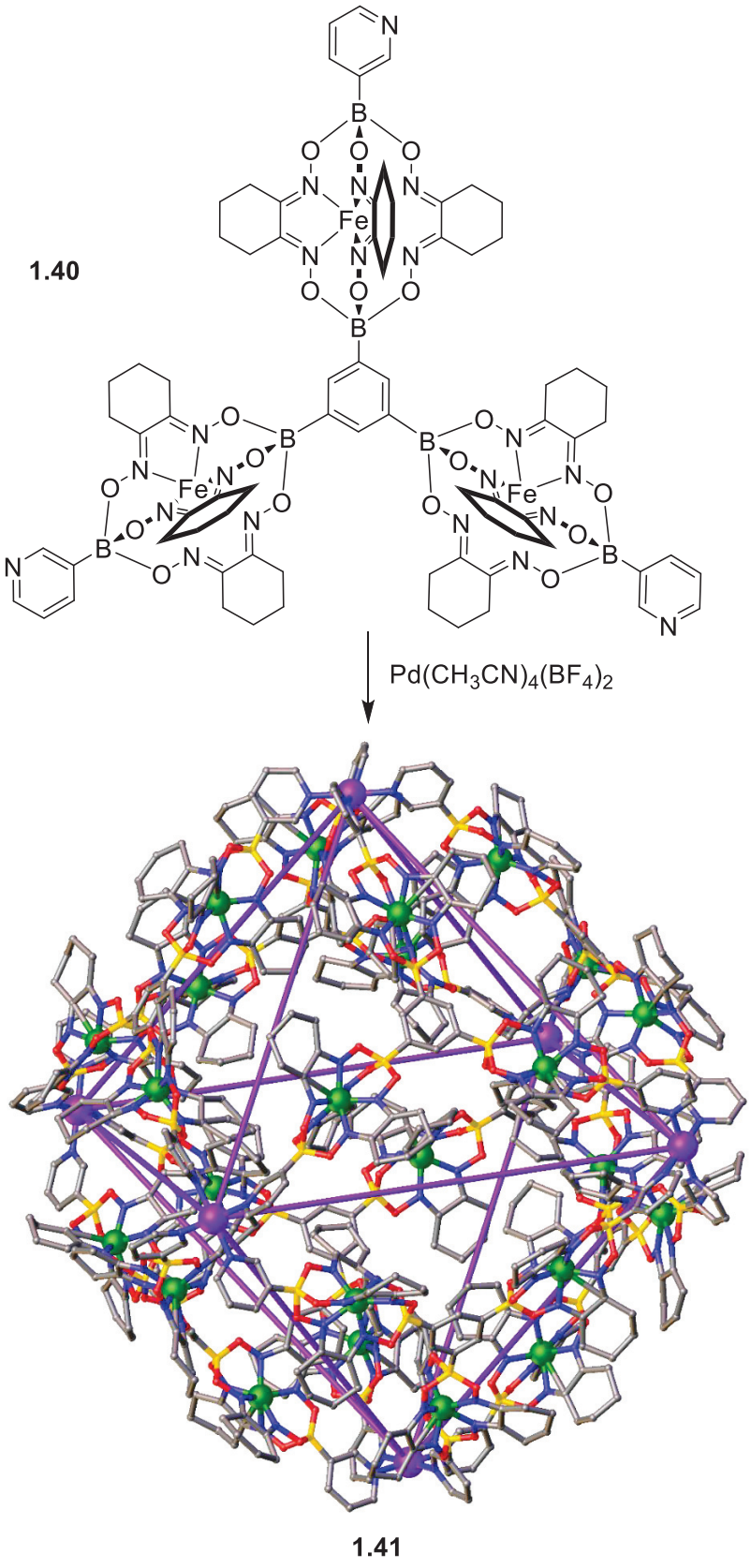

Scheme 1.8 Synthesis of octahedral cage **1.41** from clathrochelates **1.40** with the X-ray crystal structure of complex **1.41**. Color coding: Fe: green, C: grey, B: yellow, N: blue, O: red and Pd: purple. Hydrogen atoms, counterions and solvent molecules are omitted for clarity.

1.1.2.2 Materials Chemistry with Clathrochelate Complexes

In the previous section, we have shown that clathrochelates can be employed as building blocks for the construction of discrete nanostructures. Clathrochelates have also been utilized successfully as monomers in polymeric materials. A first example of a clathrochelate-based metal-organic framework (MOF) has been reported using metalloligand **1.16**, presented in the previous section, combined with Zn(II) salts. The 2D-MOF **1.42** obtained is a crystalline material with pillared layers interconnected by clathrochelates. It has been structurally characterized by X-ray crystallography (**Figure 1.11**).[24]

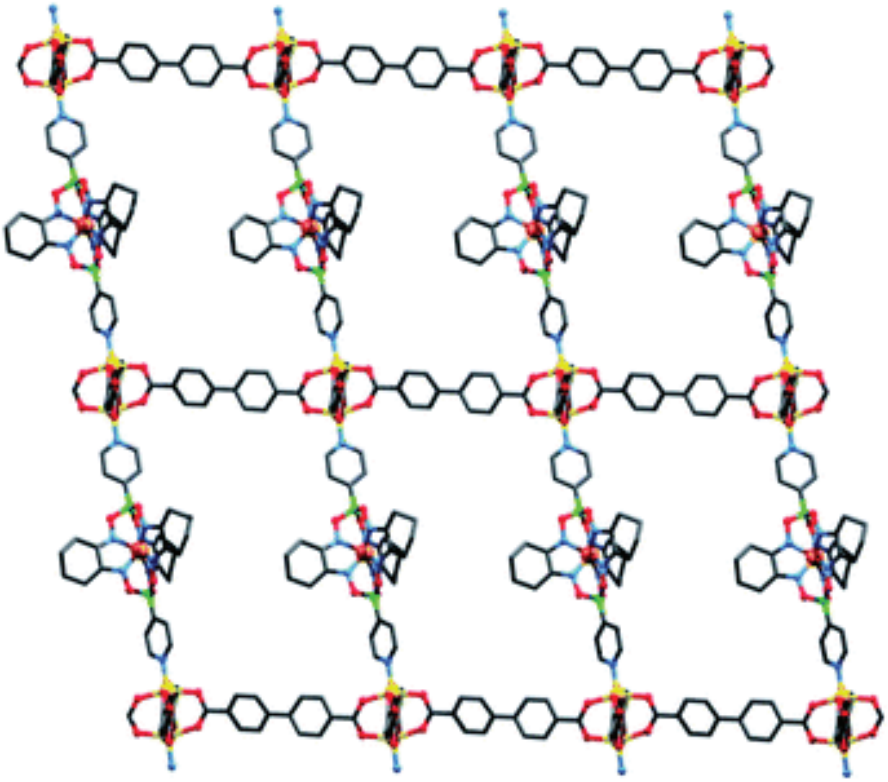

1.42

Figure 1.11 X-ray crystal structure of MOF **1.42**. Color coding: Fe: orange, C: black, B: green, N: light blue, O: red and Zn: yellow. Hydrogen atoms and solvent molecules are omitted for clarity. Reproduced with permission from reference [24].

Following this direction, Severin *et al*. have reported another example of a MOF employing clathrochelates with carboxylic acids as capping groups. Carboxylic-acid-based clathrochelate **1.43** was synthesized from anhydrous $FeCl_2$, commercially available nioxime and 4-

carboxyphenylboronic acid as capping group. The corresponding MOF was synthesized by a solvothermal reaction mixing clathrochelate **1.43** and $Zn(NO_3)_2$ as Zn(II) source in DMA. A 2D-MOF **1.44** was obtained as a crystalline material (**Scheme 1.9**).[31]

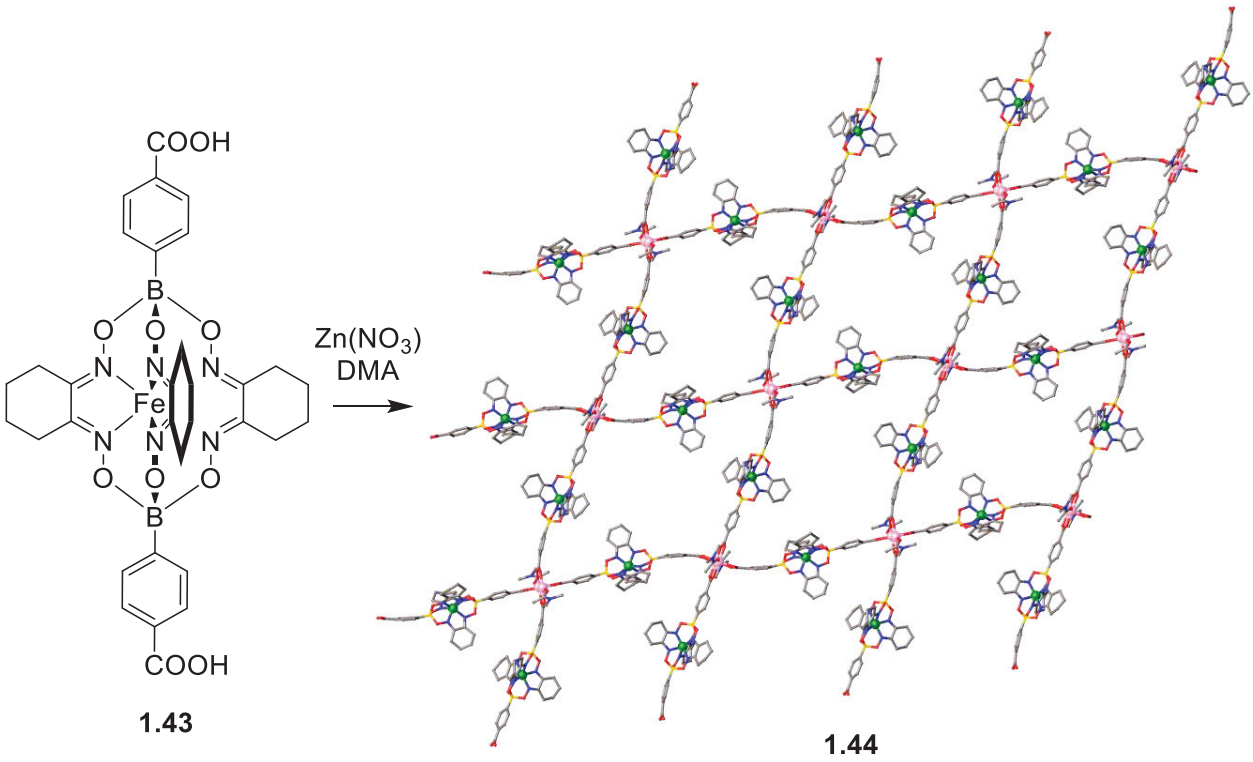

Scheme 1.9 Synthesis of MOF **1.44** from clathrochelates **1.43** with the X-ray crystal structure of MOF **1.44.** Color coding: Fe: green, C: grey, B: yellow, N: blue, O: red and Zn: light pink. Hydrogen atoms and solvent molecules are omitted for clarity.

During the last decade, clathrochelate-based covalent polymers have emerged as an interesting class of functional materials. Lee and coworkers have reported a clathrochelate-based conducting polymer synthesis done by an efficient electropolymerization, favored by using clathrochelates.[32] Depending on the metal inside the clathrochelate, conductivity and redox activity were tuned. The clathrochelate-based conducting polymers have been successfully involved in interlayer charge transport.

Recently, another study by Severin and coworkers illustrated the potential use as an enantiodifferentiating clathrochelate-based polymer. The synthesis of polymer **1.46** was done by mixing clathrochelate **1.45** with $Pd(PPh_3)_4$, K_2CO_3 and 4,4'-benzenediboronic acid for polycross-coupling reactions as shown in **Scheme 1.10**.[33] It is worth to notice that clathrochelate **1.45** is enantiomerically pure and therefore, it makes polymer **1.46** homochiral.

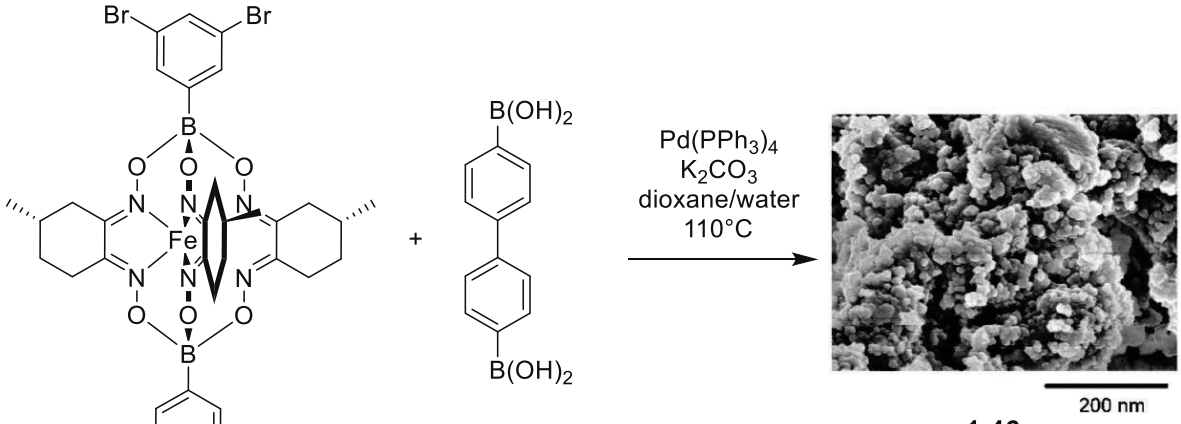

1.45 **1.46**

Scheme 1.10 Synthesis of polymer **1.46** from clathrochelate **1.45**. SEM image of **1.46** as polymer's illustration, Reproduced with permission from reference [33].

The authors have used activated polymer **1.46** to measure the difference in adsorption of L- or D-tryptophan. They have found that the homochiral polymer **1.46** has a preference to adsorb D-tryptophan over L-tryptophan after 100 minutes, which is illustrating the potential use of clathrochelate-based polymer for enantioselective recognition.

Overall, it has been shown that clathrochelates can be used as building blocks to easily form functional porous polymers with interesting properties.

1.1.2.3 Biological Applications of Clathrochelate Complexes

The potential of clathrochelates is not limited to their use in supramolecular chemistry. Recently, a review article has been discussing biological applications of clathrochelate complexes.[34] With their specific geometry and the inherent versatility of either dioximate or capping groups, clathrochelates are also of interest for biological applications. For the purpose of this thesis, we will focus only on interactions of boronate ester-capped clathrochelates with DNA/RNA and proteins.

In 2013, Voloshin and co-workers have studied for the first time the interaction of clathrochelates with DNA and RNA.[35] Clathrochelates **1.47**-**1.49** (**Figure 1.12**) bind to with RNA mainly through electrostatic interactions.

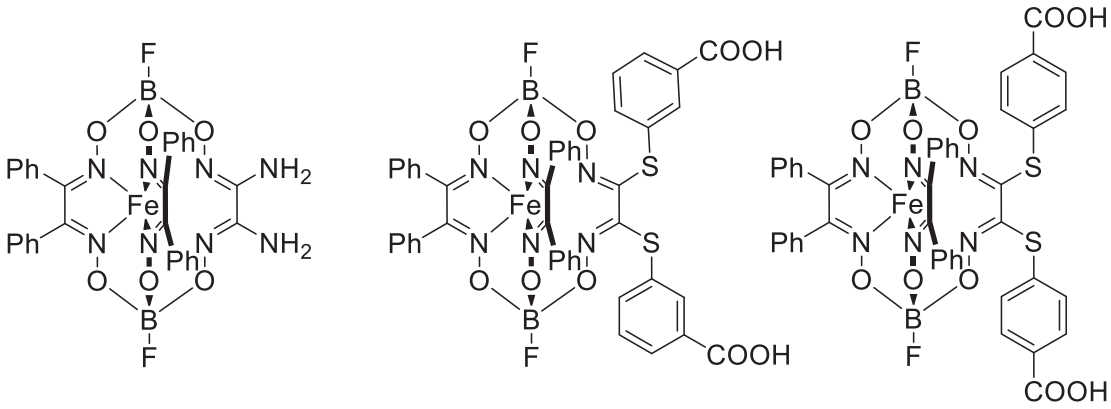

1.47 **1.48** **1.49**

Figure 1.12 Fe(II) clathrochelates **1.47** to **1.49**.

Furthermore, electrostatic interactions between clathrochelates and DNA lead to their localization in the transcription bubble (**Figure 1.13**), causing the clathrochelate to inhibit the transcription process. Clathrochelates are some of the most efficient metal-based transcription inhibitors reported to date.

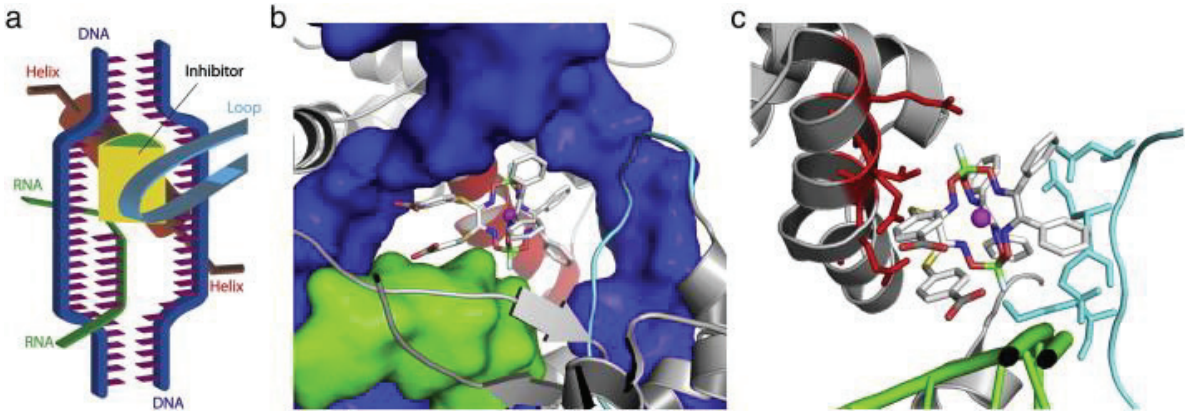

Figure 1.13 Representation of the inhibition mode by clathrochelate **1.49**: a) schematic representation, b) best calculated binding solution (DNA in blue, RNA in green), c) side view of best calculated binding solution (DNA not shown, helix in red, loop in cyan). Reproduced with permission from reference [35].

Transcription inhibition has also been reported with clathrochelates functionalized with morpholine groups **1.50**-**1.52** (**Figure 1.14**).[36]

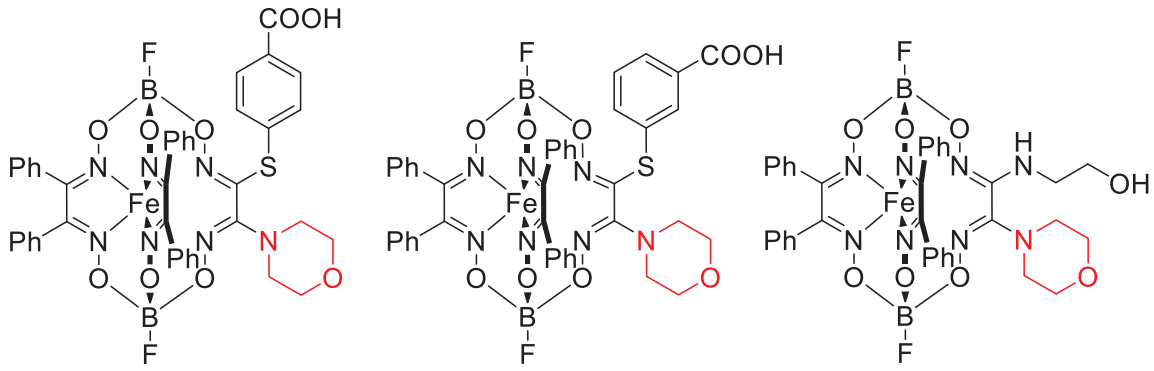

1.50 **1.51** **1.52**

Figure 1.14 Fe(II) clathrochelates **1.50** to **1.52** with morpholine groups highlighted in red.

The importance of such groups has been crucial to link efficiently DNA and RNA with clathrochelates through intermolecular contacts as illustrated in **Figure 1.15**. Hydrogen bonds and Van der Waals interactions are among the most observed contacts between DNA/RNA and clathrochelates. Moreover, the authors claimed that the hydrophobic mercaptobenzoic acid group is a key structural fragment to help clathrochelates to interact with DNA and RNA.

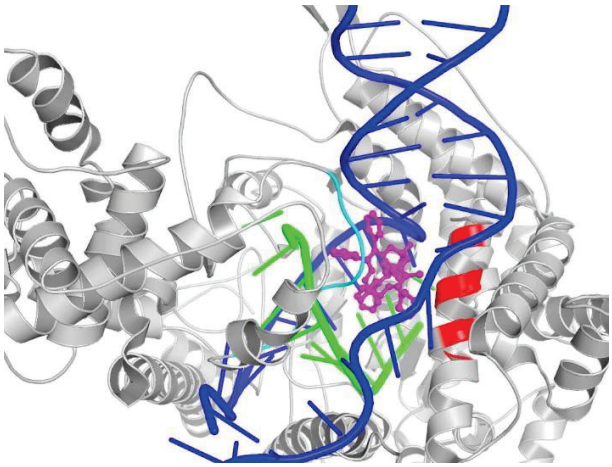

Figure 1.15 Most favorable calculated solution of inhibition mode (DNA in blue, RNA in green, helix in red, loop in cyan, clathrochelate-based inhibitor in magenta). Reproduced with permission from reference [35].

In 2014, the group of Voloshin reported the synthesis of C-C conjugated *bis*-clathrochelate **1.53** (**Figure 1.16**), which involves the copper promoted homocoupling of two clathrochelates.[37] The resulting *bis*-clathrochelate **1.53** has an even higher transcription inhibition activity. Joining two clathrochelates together by a copper-promoted homocoupling increases the inhibition effect by multiplying intermolecular contacts with DNA and RNA.

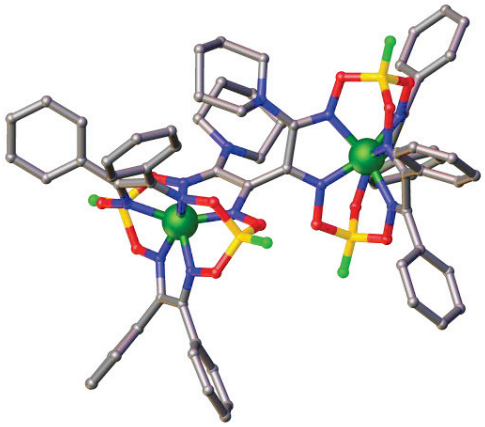

1.53

Figure 1.16 X-ray crystal structure of complex **1.53**. Color coding: Fe: green, C: grey, B: yellow, N: blue, O: red and F: light green. Hydrogen atoms and solvent molecules are omitted for clarity.

In summary, clathrochelates were recently described as efficient inhibitors in RNA transcription. The binding of clathrochelates to DNA, RNA and proteins is of interest for

biological applications. The clathrochelate's versatility given by functional groups is of advantage in this area.

1.1.2.4 Clathrochelates as Catalyst-Precursors for the Hydrogen Evolution Reaction

Growing interest in inexpensive alternatives of electrocatalytic systems for hydrogen production focuses on cheap and earth abundant 3d-transition metal complexes. Since first being reported by Connolly and Espenson, *bis*(dimethylgyloximate) cobalt complexes have attracted attention in sustainable energy development for hydrogen evolution.[38] Afterwards, cobalt clathrochelates, which have similar dioximate environment, were investigated as potential catalyst precursors for hydrogen production systems. In 2008, Aukauloo and coworkers have shown that cobalt(II) clathrochelates **1.54**-**1.56** can give active catalysts for hydrogen production with a remarkable Faradaic efficiency (**Figure 1.17**).[39] Indeed, upon addition of acid ($HClO_4$ in acetonitrile) formation of a catalytic wave was observed by cyclic voltammetry.

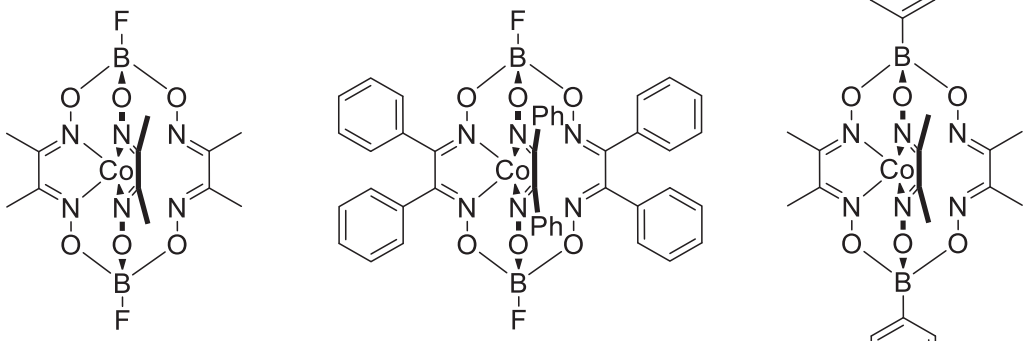

1.54 **1.55** **1.56**

Figure 1.17 Co(II) clathrochelates **1.54** to **1.56** have been employed as catalyst precursors for hydrogen production.

Two main categories of clathrochelate-based systems have emerged for hydrogen evolution reactions (HER): either clathrochelates were used directly in solution[39-42] or immobilized on a

surface.[43-51] Recently, the latter category has attracted attention of researchers. In this context, Muryumin and coworkers have immobilized clathrochelates with mercapto groups on the surface of a gold working electrode. They demonstrated a high electrocatalytic activity for a long time without any yield loss in the range of pH from 1 to 7.[49]

In 2013, another study reported that cobalt trisglyoximato-clathrochelates were implied in the formation of cobalt nanoparticles at the surface of the carbon electrode. These particles were then active catalysts for H_2 production in water at pH 7.[51]

In 2017, immobilization of clathrochelates was demonstrated on membrane-electrode assemblies. The current-voltage performances were significantly higher than a classical Pt system for HER.[46] Five chloro-clathrochelates were used in this study and they have all showed high current-voltage performances. Over the 0.5 $A.cm^{-2}$ density, the observed voltage was two times higher than the Pt control (Pt/Vulcan XC-72).

In 2020, a detailed study explored the effect of dioximate groups on clathrochelates—cobalt, ruthenium, or iron—on the in efficiency of HER. Clathrochelates functionalized with phenanthrene appended to their dioximate groups were observed to play a role in efficient physisorption of these complexes onto carbon materials, facilitating an increase in the HER efficiency. As an example, the following cobalt clathrochelate **1.57** has shown the best current-voltage efficiency reported to date (**Figure 1.18**).[44]

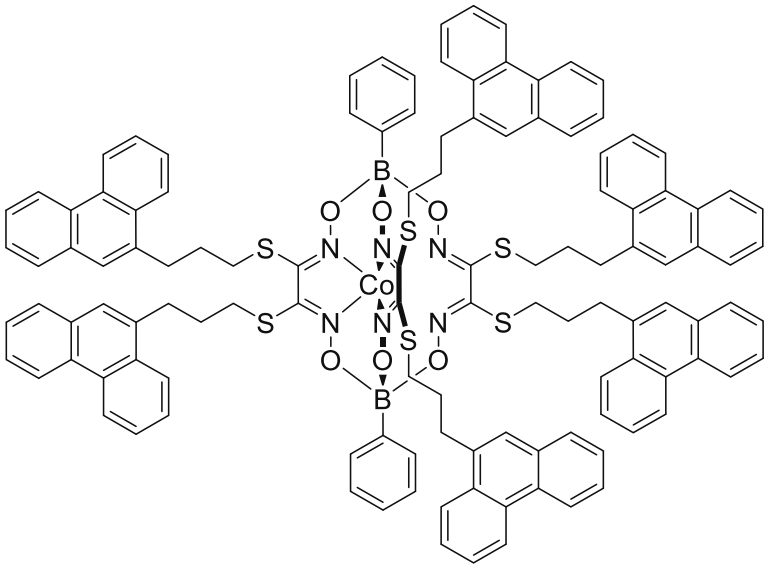

1.57

Figure 1.18 Co(II) clathrochelate **1.57** with phenanthrene groups.

1.2 Aims of the Project

Boronate ester-capped clathrochelate complexes are among the most studied clathrochelates over the last decades. Pyridyl-decorated clathrochelates have been widely described in literature as building blocks in supramolecular chemistry, particularly for the synthesis of coordination cages. We are interested in the investigation of coordination cages with carboxylate-decorated clathrochelates.

Recently, first examples of metal-organic frameworks containing clathrochelate metalloligands have been described. In order to enlarge the library of clathrochelate-based MOFs, we have investigated a technique called solvent-assisted ligand exchange to synthesize pillared MOFs with clathrochelates.

Low-valent cobalt clathrochelates are very reactive, and as a consequence they are hard to characterize. This high reactivity encouraged us to investigate the synthesis and structural characterization of analogs, which would potentially display fundamental knowledge about ligand effects on the overall stabilization.

Finally, we were intrigued by clathrochelate-based chemical biology applications. We concentrated our synthetic efforts first, in preparing π-elongated clathrochelates as potential stabilizers for three way junctions (TWJ) in DNA/RNA systems and then, chiral clathrochelates. Explorations along those lines are described in the last chapters.

Chapter 2

Linear and Bent Dicarboxylic Acid Clathrochelates with Lengths up to Three Nanometers

The work described in this Chapter has been published in *Inorganic Chemistry*: **O. M. Planes**, S. M. Jansze, R. Scopelliti, F. Fadaei-Tirani, K. Severin, *Inorg. Chem*. **2020**, 59, 19, 14544-14548.

O.M.P. synthesized and characterized the compounds, S.M contributed in designing the experiments, F.F.-T. and R.S. carried out the single crystal XRD analyses, and K.S. initiated and coordinated the study.

2.1 Introduction

Ligands with two or more carboxylate groups are widely used for the synthesis of metal-organic frameworks (MOFs),[52] but they have also been employed to prepare molecularly defined macrocycles[53] and cages (metal-organic polyhedra, MOPs).[54] An advantage of polycarboxylates over polypyridyl ligands is the fact that carboxylate ligands can provide a charge compensation for the metal ions. Accordingly, it is possible to form charge-neutral assemblies and networks. From a structural point of view, the key features of a polycarboxylate ligand are denticity (number of donor groups), geometry (orientation of the donor groups), flexibility, and size (distance between the donor groups). ‘Size’ matters, because ‘size’ defines the spacing of the metal centers, and, accordingly, the void size of MOFs, cages, and macrocycles. The synthesis of nanometer-sized polycarboxylates with sufficient solubility for solution-based reactions is still a challenging task because of substantial synthetic efforts

required. In this context, we have extended the utilization of clathrochelates as scaffolds for the construction of polycarboxylate metalloligands.[55,15] We describe the synthesis of dicarboxylic acid ligands containing two Fe(II) clathrochelate complexes. The new ligands have a length of up to three nanometers, and they are suited for applications in metallasupramolecular chemistry, as evidenced by the synthesis of an M_4L_4-type MOP and a Zn(II) coordination polymer.

2.2 Synthesis and Characterization

It is possible to obtain in a single step an extended dinuclear clathrochelate complex when the reaction is performed with a mixture of a diboronic acid and a monoboronic acid, Fe(II) salts and dioxime ligands (**Scheme 2.1**). We have previously used this approach to make long dipyridyl ligands.[56,30] As expected, this multicomponent reaction is not selective, and mononuclear complexes are obtained along with higher oligomers. The formation of oligomers can be suppressed by using an excess of the monoboronic acid, but a chromatographic separation is in most cases needed to isolate the double cage complex in pure form. Size exclusion chromatography with dichloromethane was found to be particularly useful for this purpose.[56a]

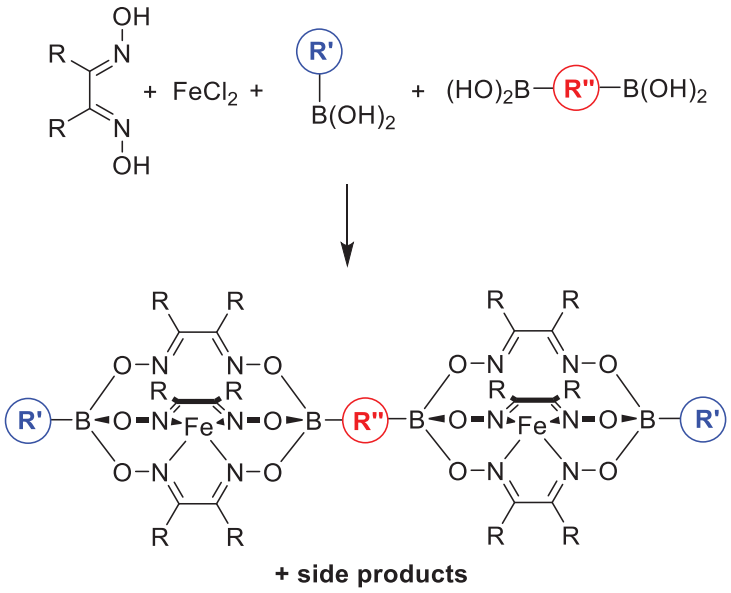

Scheme 2.1 Synthesis of dinuclear iron cage complexes.

We wanted to use the procedure outlined in **Scheme 2.1** to make double cage complexes with terminal carboxylic acid groups. However, test reactions quickly revealed a problem: the products were only soluble in polar organic solvents, and a chromatographic separation of the product mixture was not accomplished. Therefore, we decided to use arylboronic acids featuring ester groups. Heating a mixture of nioxime (6 equiv), $FeCl_2$ (2 equiv), 3- or 4-ethoxycarbonylphenyl boronic acid (4 equiv), and 1,3- or 1,4-phenylenediboronioc acid (1 equiv) in methanol under reflux for 12 h gave a mixture of complexes. An excess of ester boronic acid was used to favor double cage complexes formation instead of oligomers formation, which could be separated by size exclusion chromatography. The desired double cage complexes **2.1**–**2.3** were isolated in yields between 14 and 27% (**Scheme 2.2**).

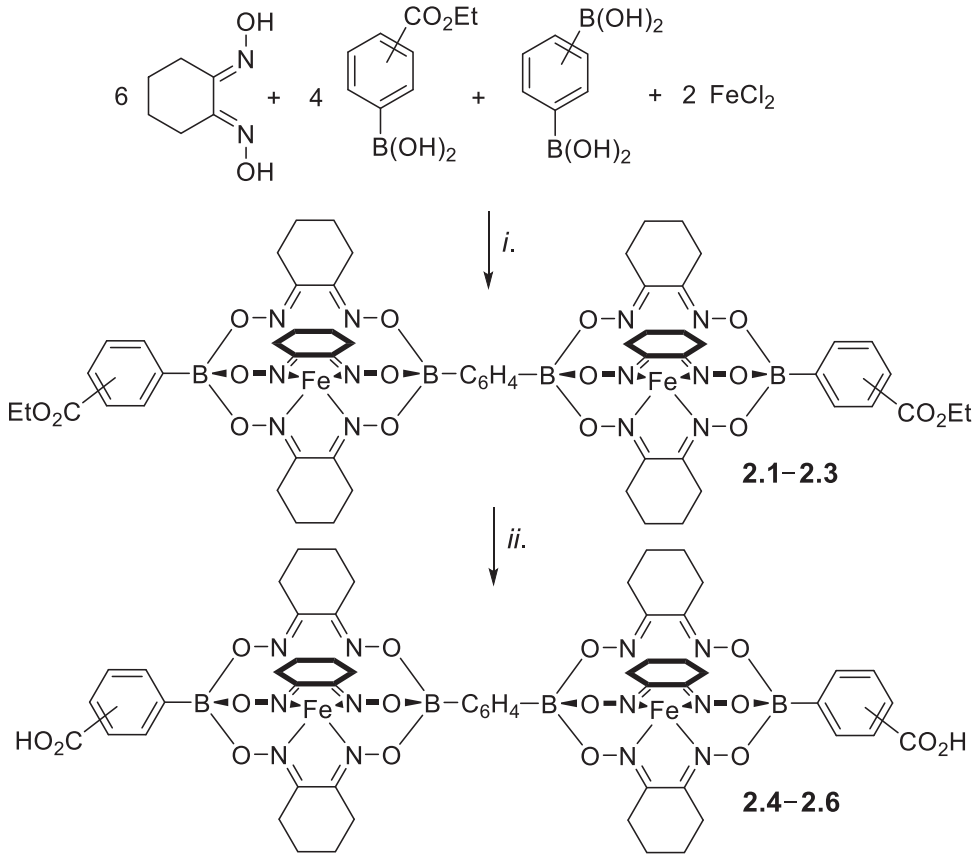

	B-C_6H_4-B	B-C_6H_4-CO_2R
2.1 and **2.4**	*para*	*para*
2.2 and **2.5**	*meta*	*para*
2.3 and **2.6**	*meta*	*meta*

Scheme 2.2 Synthesis of the Double Cage Complexes **2.1**–**2.6**. Conditions: (*i*) MeOH, Reflux, 12 h, 14–27% Yield; (*ii*) H_2O/THF/CH_2Cl_2/MeOH, NaOH (100 Equiv), 60°C, 2–12 h, 62–85% Yield.

The esters were characterized by ^{1}H and ^{13}C NMR spectroscopy, and by high-resolution mass spectrometry. In addition, the solid-state structures of **2.1**–**2.3** were determined by single crystal X-ray diffraction (**Figure 2.1**). For the linear complex **2.1**, the terminal ester groups are 3 nm apart from each other ($O_2C\cdots C'O_2$ distance). Due to the presence of a *meta*-connected phenylene spacer, the complexes **2.2** and **2.3** display an overall bent geometry, with the ester groups being 2.5 nm (**2.2**) and 2.1 nm (**2.3**) apart from each other. In line with what is observed for other Fe clathrochelate complexes,[2] the geometry around the Fe centers can be described as distorted trigonal prismatic.

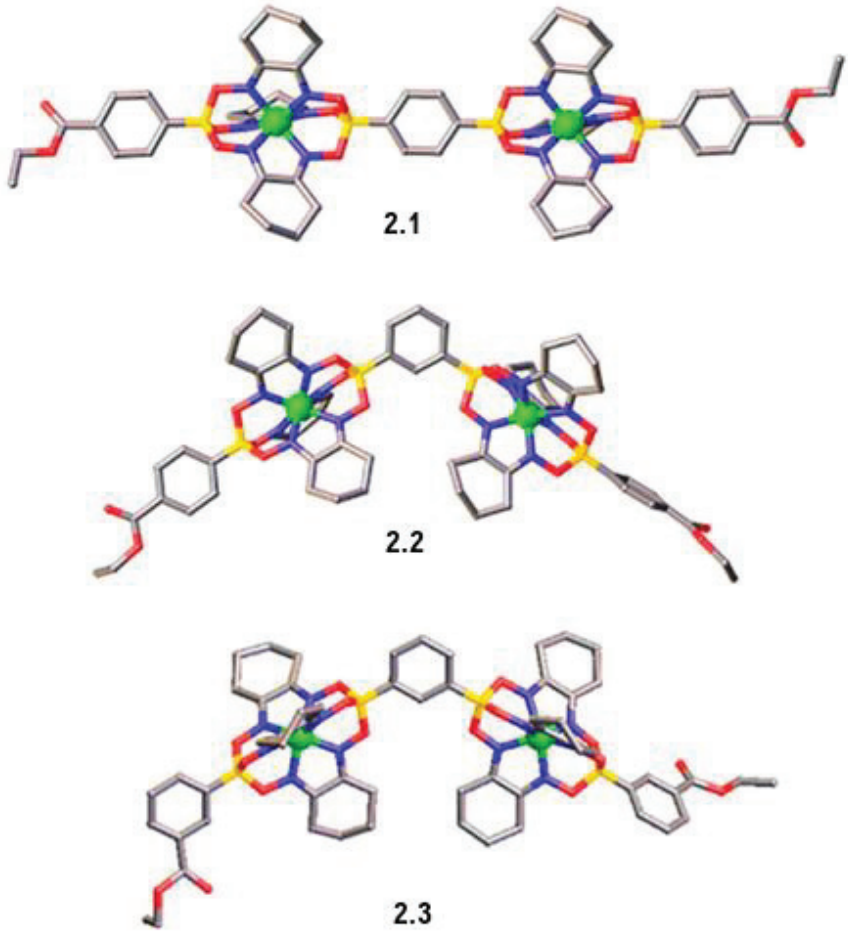

Figure 2.1 The molecular structures of **2.1** (a), **2.2** (b) and **2.3** (c) in the crystal. Hydrogen atoms and solvent molecules (CH_2Cl_2) are not shown for clarity. Color coding: C: grey, B: yellow, O: red, N: blue, Fe: green.

Saponification of **2.1**–**2.3** was achieved with NaOH at 60 °c using a solvent mixture of H_2O/THF/CH_2Cl_2/MeOH (the exact ratio depends on the compound, see Chapter 8). Under these conditions, only minimal decomposition of the iron cage complexes was observed. The carboxylic acid ligands **2.4**–**2.6** can be dissolved in polar organic solvents such as DMF, DMAc and DMSO, but they are poorly soluble in MeOH or CH_2Cl_2.

2.3 Dicarboxylic Acid Clathrochelates as Building Blocks in Supramolecular Chemistry

Considering all structural types of MOPs reported to date, coordination cages having paddlewheel (PW) complexes as metal nodes are among the most reported in literature.[54g] In the PW metal node [M_2(μ-O_2C-R)$_4$], each metal has an octahedral coordination sphere with four bidentate ligands localized on the equatorial plane, and one or two ligand(s) on the vertical axis, often occupied by the solvent. A PW node has a C_4 symmetry with an angle of ≈90° between each coordinated ligand (**Figure 2.2**).

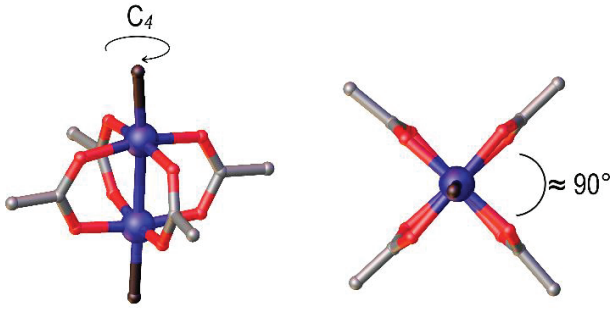

Figure 2.2 Model of a paddlewheel complex (side view and top view). Hydrogen atoms are not shown for clarity. Color coding: C: grey, O: red, N: blue and brown: solvent.

In order to demonstrate that the new polycarboxylate metalloligands are useful building blocks for the synthesis of more complex nanostructures, we have investigated the formation of an M_4L_4-type MOP. Assemblies of this general formula can be obtained by combination of bent dicarboxylate ligands with Cu(II), Mo(II), Cr(II) or Rh(II) metal precursors.[57] In the resulting cages, the four ligands are connected by $M_2(O_2CR)_4$ paddlewheel complexes. Only few examples are reported to date, summarized in **Figure 2.3**. We have prepared a Cu-based MOP, which represents the largest M_4L_4 cage described so far.

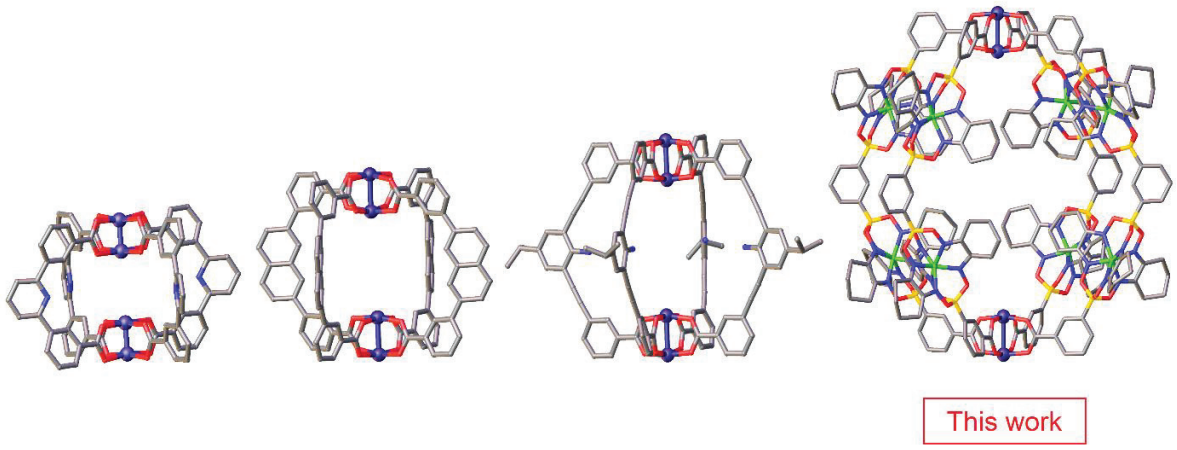

Figure 2.3 Selected reported examples of Cu_4L_4 MOPs.[57]

2.3.1 Synthesis of a Cu_4L_4 Coordination Cage

The reaction of metalloligand **2.6** with $Cu(NO_3)(H_2O)_3$ in DMF at room temperature resulted in the formation of a crystalline material (**2.7**). The very low solubility of the product hampered a solution-based characterization.[57] However, we were able to obtain crystals of sufficient quality for a crystallographic analysis by X-ray diffraction (XRD). The results showed that a Cu_4L_4-type cage had indeed formed (**Scheme 2.3** and **Figure 2.4**).

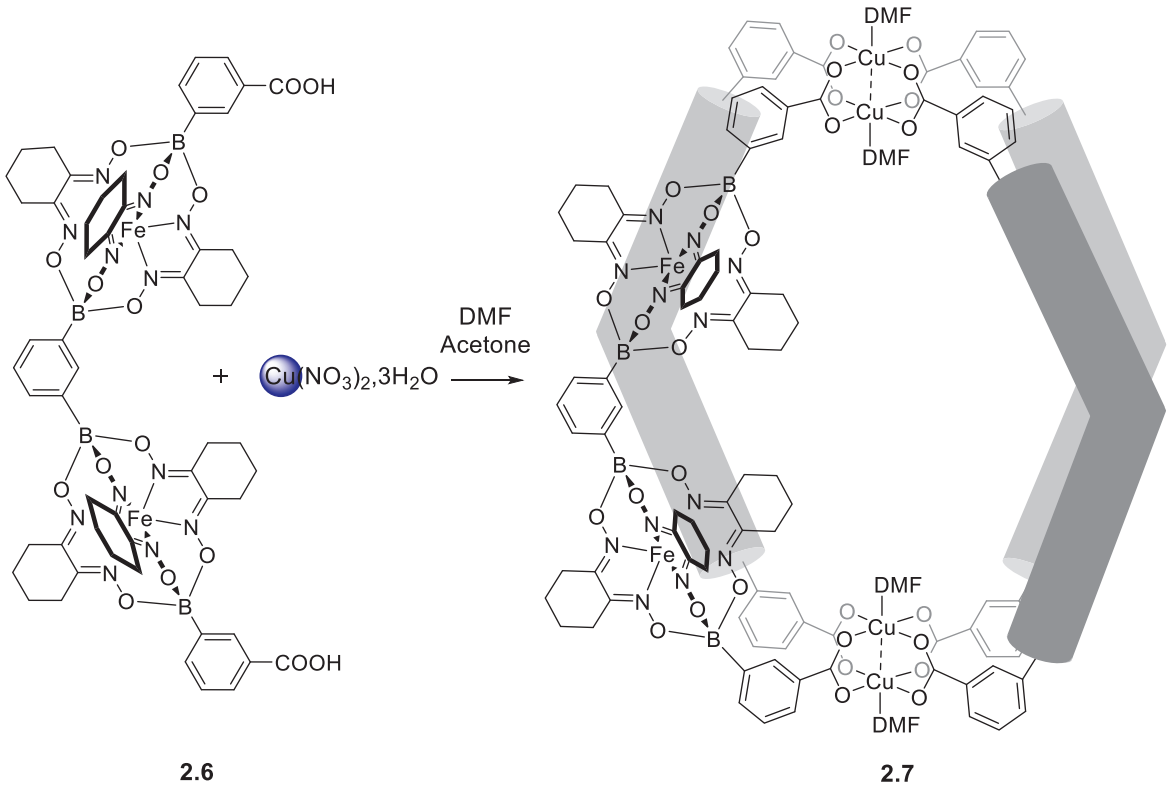

Scheme 2.3 Synthesis of coordination cage **2.7**.

As observed for other M_4L_4 cages, the ligands are connected via $Cu_2(O_2C)_4$ paddle wheel complexes. Each Cu is coordinated to one DMF molecule. The Cu···Cu distances within the two $Cu_2(O_2C)_4$ units of 2.618(1) Å are within the range found for other Cu(II) carboxylate complexes.[58] In simple dinuclear Cu complexes such as $Cu_2(OAc)_4(OH_2)$,[59] the planes defined by the carboxylate groups cross at an angle of approximately 90°. For cage **2.7**, one can observe a strong deviation of from the ideal square arrangement of the carboxylate ligands. This distortion is evident when the structure of **2.7** is viewed along the Cu···Cu axis (**Figure 2.4c**). As a consequence of the symmetry reduction at Cu, the eight Fe centers in **2.7** describe a rectangular-prismatic and not a square-prismatic structure. One can observe pairs of clathrochelate complexes with closely interdigitated cyclohexyl side chains. The contacts between the aliphatic groups can contribute to the stability of the structure via dispersion interactions and solvophobic effects.[56a] The overall 'height' of the cage, as defined by the maximum Cu···Cu distances, is 2.35 nm. This value is significantly larger than what is found other crystallographically characterized M_4L_4 cages, which show maximal M···M distances between 0.9 and 1.44 nm (**Figure 2.3**).[57]

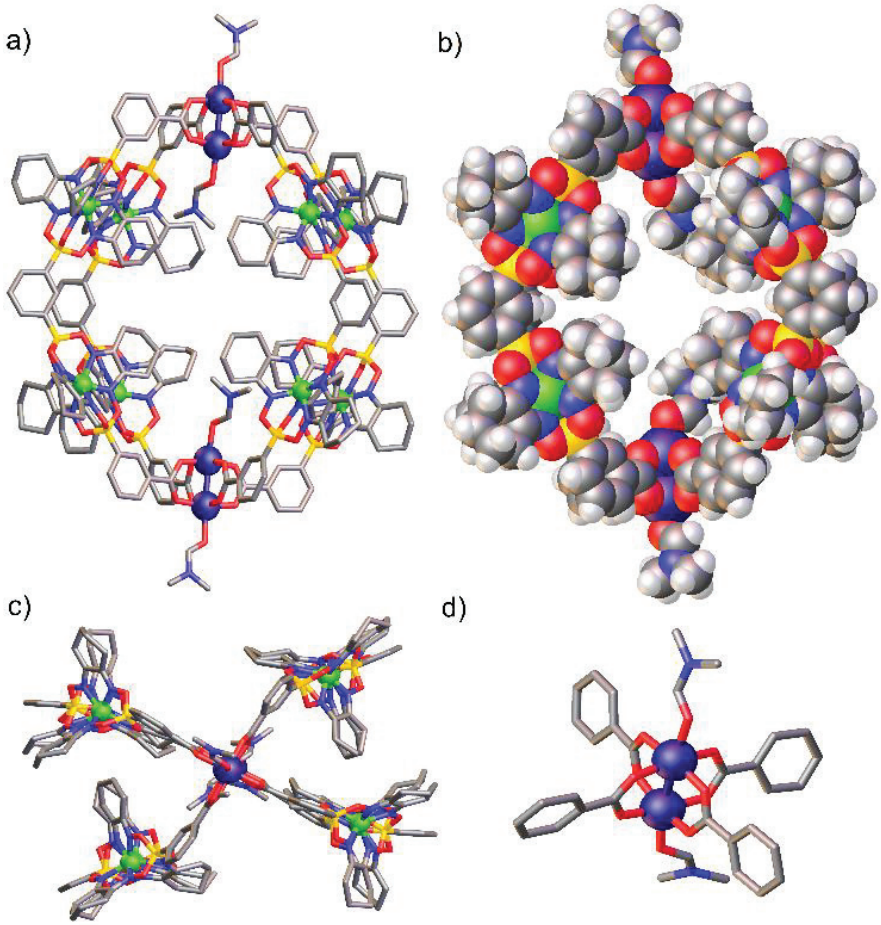

Figure 2.4 Different views of the molecular structure of **2.7** in the crystal (a–c), and close-up on one of the bridging $Cu_2(O_2C)_4(DMF)_2$ units (d). Hydrogen atoms are not shown for the stick representations a, c, and d. Color coding: C: grey, B: yellow, O: red , N: blue, Fe: green.

Charge-neutral MOPs can display permanent porosity in the solid state.[54] Analysis of the void volume in crystalline **2.7** revealed a solvent accessible volume of >6000 $Å^3$, which represents more than 50% of the unit cell. Most of the potential void volume is found in-between the cages, and not in the cage interior. In crystalline **2.7**, the accessible voids are filled with disordered solvent molecules, which have been removed by the solvent-masking program in Olex2 (for details, see Chapter 8). The large voids in crystalline **2.7** suggested that it might be possible to obtain a material with high porosity. However, the crystals were found to be very fragile, and rapid loss of crystallinity was observed when they were removed from the mother liquor. N_2, H_2 and CO_2 sorption experiments were performed after drying the solid and results are shown in Chapter 8. A low porosity with an apparent BET surface area of 176 m^2/g was deduced from the binding isotherm. Attempts to increase this value by solvent-exchange procedures were not successful. Furthermore, thermogravimetric analyses were performed with ligand **2.6** and

cage **2.7**. Cage **2.7** was found to be stable until 286 °C, followed by a rapid mass loss. Ligand **2.6** was found to be stable up to temperatures of around 350°C (**Figure 2.5**).

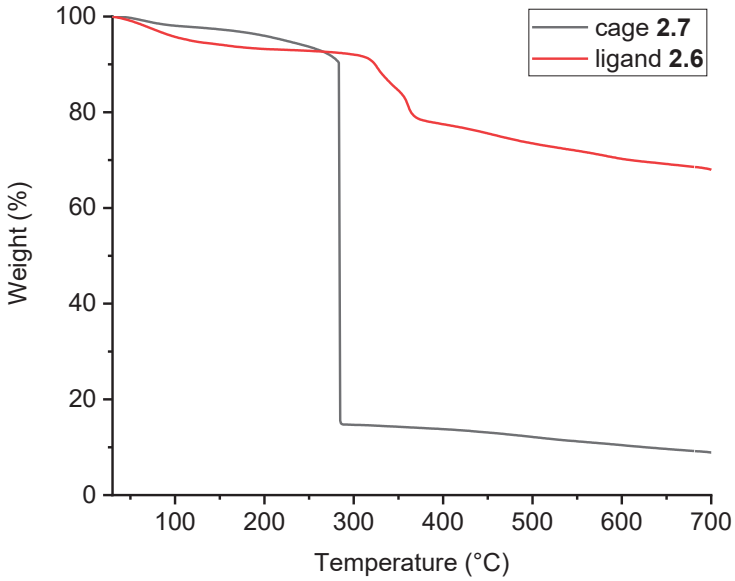

Figure 2.5 TGA profile of ligand **2.6** and cage **2.7**.

2.3.2 Synthesis of a Zn(II) Coordination Polymer

The reaction of metalloligand **2.6** with an equimolar amount of $Zn(NO_3)$, 6 H_2O in DMA at room temperature resulted in the formation of a crystalline material (**2.8**) (**Scheme 2.4**).

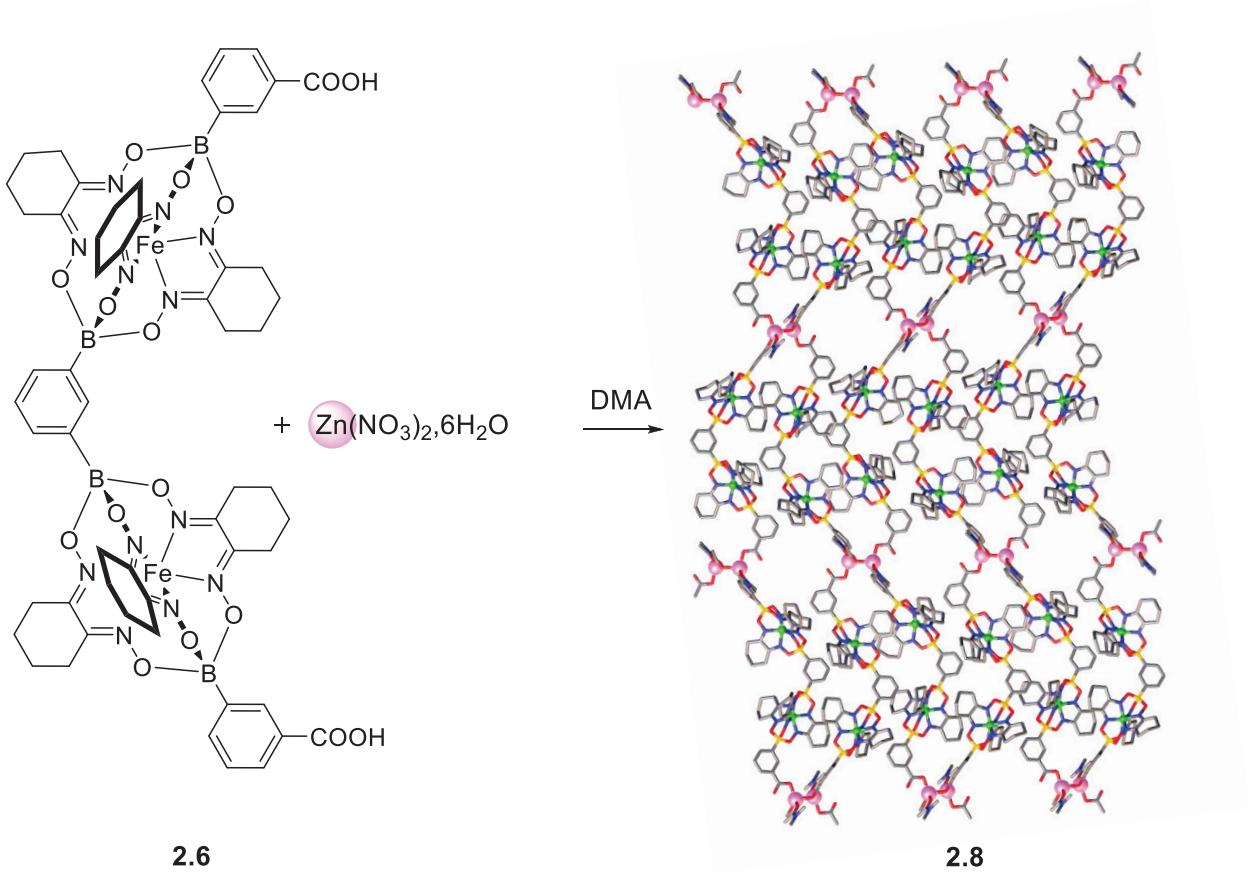

Scheme 2.4 Synthesis of 2D-MOF **2.8** from dinuclear clathrochelates **2.6**. Color coding: Fe: green, C: grey, B: yellow, N: blue, O: red and Zn: pink.

The crystals were found to display sufficient quality for a crystallographic analysis by X-ray diffraction (XRD). The results showed that a 2D Zn_n(**2.6**)$_n$-type polymer had formed: each Zn^{II} ion has a tetrahedral coordination sphere, with coordination of two bridging carboxylates, and terminal carboxylate group, and one solvent molecule (DMA) (**Figure 2.6**).

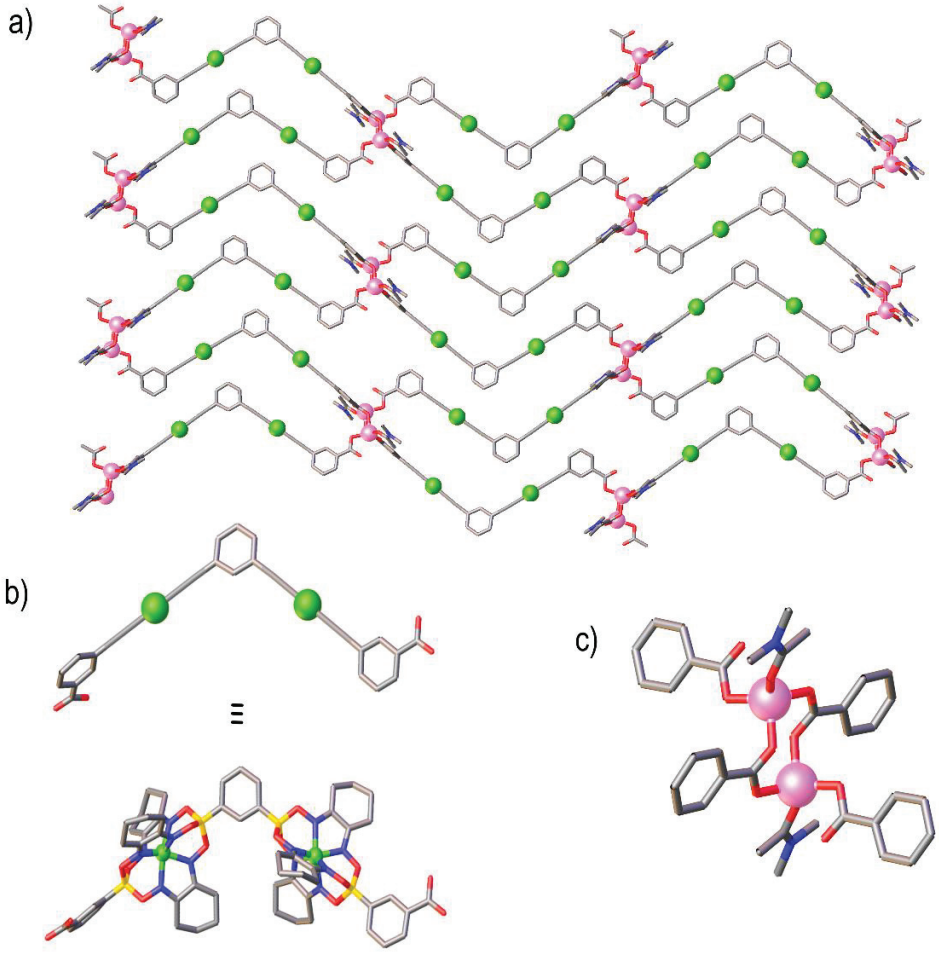

Figure 2.6 Part of the molecular structure of Zn_n(**2.6**)$_n$ in the crystal. a) view along the crystallographic y axis. b) simplified representation of ligand **2.6** c) zoom around Zn^{II} nodes. Color coding: C: grey, Fe: green, Zn: pink, O: red, B: yellow, N: blue. Free solvent molecules and hydrogen atoms are omitted for clarity.

The solvent accessible volume is around 4954 $Å^3$ based on calculations done by Olex (for details see Chapter 8).

2.4 Conclusion

We have developed a protocol, which allows synthesizing nanometer-sized dicarboxylate ligands in two steps from commercial starting materials. The first step of the procedure is an iron-templated condensation reaction between nioxime, a functionalized monoboronic acid, and a diboronic acid. This reaction is inherently unselective, and it gives a mixture of products. The utilization of ester-substituted monoboronic acids allowed separation of the product mixture by size exclusion chromatography. The desired carboxylate ligands are then obtained by saponification, and we were able to find conditions, which result in minor decomposition of the iron cage complexes. In the present work, we describe three different metalloligands, a linear one and two bent ones, but we expect that the procedure is suited for accessing structurally related compounds when different boronic acids are employed. In order to demonstrate that these metalloligands are useful building blocks for metallasupramolecular assemblies, we have prepared a Cu_4L_4-type cage structure. This MOP represents the largest M_4L_4 cage described to date. We have also reported the structure of a 2D Zn(II) polymer.

Chapter 3

Incorporation of Clathrochelates in Metal-Organic Frameworks by Solvent-Assisted Ligand Exchange

The work described in this Chapter has been published in *Crystal Growth & Design*: **O. M. Planes**, P. A. Schouwink, J. L. Bila, F. Fadaei-Tirani, R. Scopelliti, K. Severin, *Cryst. Growth Des*. **2020**, 20, 3, 1394-1399.

O.M.P. synthesized and characterized the compounds, P.S. performed the powder XRD analyses, J.B. contributed to the synthesis of metalloligand **2d**, F.F.-T. and R.S. carried out the single crystal XRD analyses, and K.S. initiated and coordinated the study.

3.1 Introduction

The synthesis of novel metal-organic frameworks (MOFs) can be accomplished by post-synthetic modification of existing framework structures.[60-64] This approach provides MOFs with identical topologies, but with new properties, which can be advantageous for applications. Work in this area has primarily focused on the alteration of organic linkers by chemical means. Successful heterogeneous reactions of MOF linkers include condensation-, addition-, and deprotection reactions, as well as oxidation and reduction reactions, among others.[60-64]

An interesting alternative to the chemical modification of organic linkers is the complete replacement of one type of linker within a MOF by a new one.[60,61,65-69] This process is referred to as “solvent-assisted linker exchange” (SALE)[66] or “postsynthetic exchange” (PSE) (**Scheme 3.1**).[68]

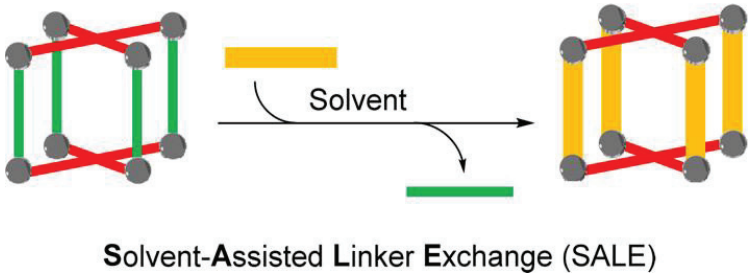

Scheme 3.1 Schematic illustration of the SALE technique for a representative MOF structure.

The first demonstration that SALE can be used to replace bridging ligands in 2- and 3-dimensional MOFs was reported in 2011 by the group of Choe (**Scheme 3.2**).[70] As starting materials, they have used pillared paddle-wheel MOFs constructed from tetrakis(4-carboxyphenyl)porphyrin (**TCPP**), N,N'-di-4-pyridylnaphtalenetetracarboxydiimide (**DPNI**) linkers, and $Zn_2(O_2C)_4$ metal nodes. When the MOFs were suspended in solutions containing 4,4'-bipyridine, a complete replacement of the **DPNI** pillars with the smaller bipyridine was observed. Despite a strong reduction of the layer-to-layer distance, the MOFs retained their crystallinity, and the products could be characterized by single crystal X-ray diffraction.

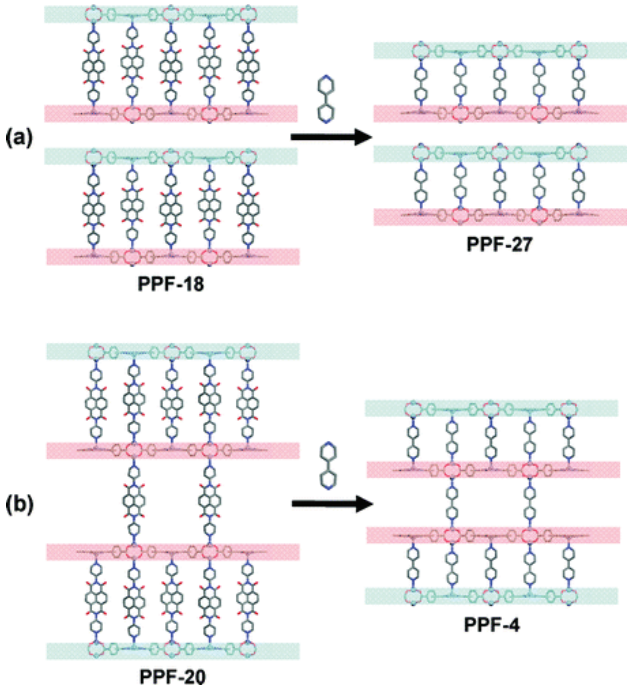

Scheme 3.2 First example of SALE methodology employed in MOFs synthesis. Introduction of the bridging linker BPY to crystals of (a) PPF-18 and (b) PPF-20, transforming them to PPF-27 and PPF-4, respectively. Blue and pink bands represent "A" and "B" layers, respectively. The AB and ABBA topologies in PPF-18 and PPF-20 are retained in PPF-27 and PPF-4, respectively, showing a templating effect. Reproduced with permission from reference [70].

Following this seminal report by Choe and co-workers, the SALE technique has been used for the synthesis of numerous other MOF structures, many of which are not accessible by standard solvothermal reactions.[60,61,65-68] In addition to exchange reactions of bipyridyl ligands,[70-86] linker exchange was demonstrated for carboxylate,[87-95] imidazolate,[95-100] and triazolate ligands.[101,102] These studies also revealed potential problems of the SALE methodology. Incomplete ligand exchange was encountered, even after prolonged reaction times. Moreover, the quality of the crystals tends to degrade during SALE, often preventing single crystal X-ray diffraction analysis of the daughter materials.[70-102]

Pyridyl-capped clathrochelate complexes turned out to be valuable components for the construction of molecularly defined nanostructures,[15] but we had only limited success in using them for MOF synthesis.[23,32,33] In a recent study, we noticed that iron cages complexes with terminal pyridylboronate ester groups are more basic than standard pyridyl ligands.[103] The high proton affinity of these metalloligands is likely related to the presence of the boronate ester group, which has a formal negative charge. Highly basic pyridyl ligands are expected to be well suited for SALE experiments.[81] Therefore, we have explored the possibility to incorporate iron cage complexes in MOFs using ligand exchange reactions instead of solvothermal reactions. The SALE technique indeed allowed synthesizing MOFs containing clathrochelate complexes. Notably, the quality of the daughter crystals was sufficient for single crystal XRD analyses. The results of our investigations are summarized below.

3.2 Incorporation of Clathrochelates in Pillared MOFs

3.2.1 Reactions with MOFs Containing Organic Tetracarboxylic Acid Ligands

First, we examined ligand exchange reactions using a paddle-wheel MOF containing a tetracarboxylic acid ligand and **DPNI** pillars (**Scheme 3.3**). The synthesis of MOF **3.1** was described by Hupp and co-workers.[104] The bromo substituents on the carboxylate ligand prevent interpenetration. Consequently, **3.1** features large pores, which were expected to facilitate ligand exchange with sterically demanding clathrochelate complexes.

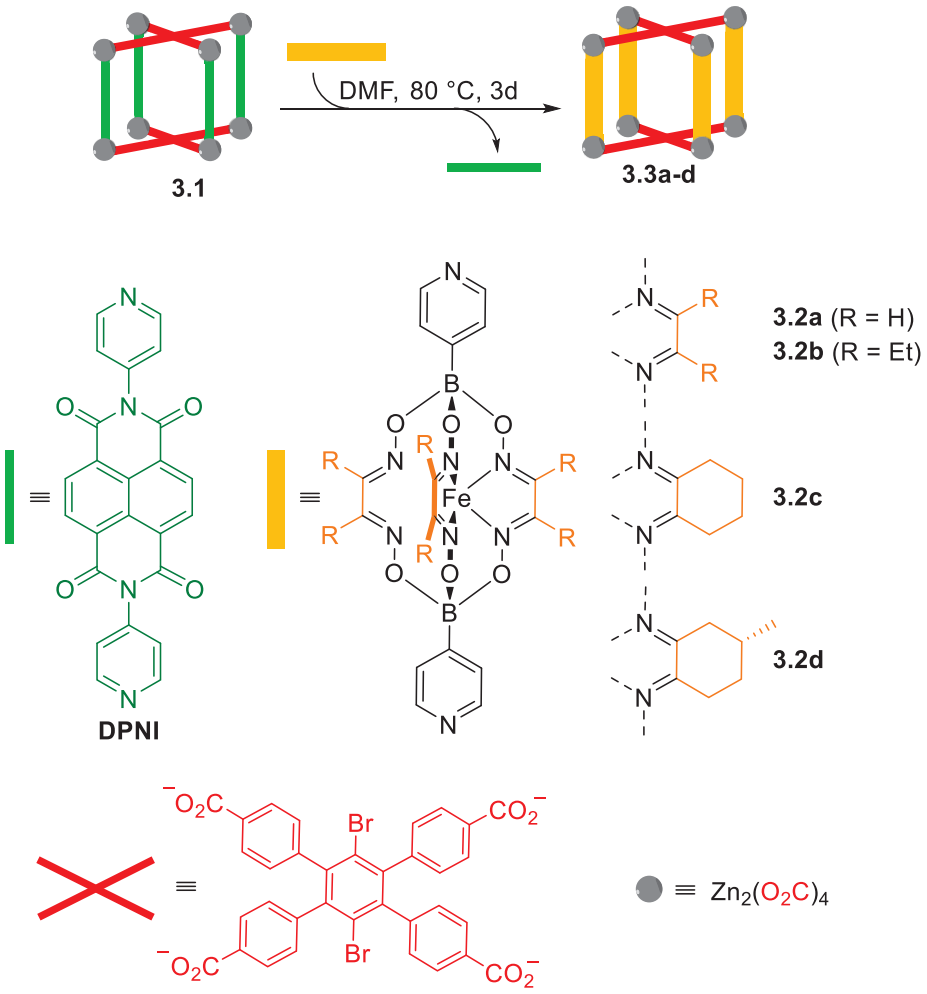

Scheme 3.3 Synthesis of the MOFs **3.3a–d**.

For SALE experiments with **3.1**, we have used the pyridyl-capped cage complexes **3.2a–d** (**Scheme 3.3**). The complexes were prepared from 4-pyridylboronic acid, $FeCl_2$ and the corresponding dioxime in analogy to reported procedures.[15] It is worth noting that **3.2d** features a chiral side chain, because the dioxime is derived from (*R*)-Pulgeone.

The phase purity of crystalline **3.1** was verified by powder XRD (details in Chapter 8). Ligand exchange was then initiated by suspending crystals of **3.1** in a DMF solution of **3.2**. The mixture was heated to 80 °C, and progress of the reaction was monitored by UV-Vis and ^{1}H NMR.

First, to monitor the reaction progress, UV/Vis spectra were taken of the reaction solution after 5 min (orange) and after 3 days (green) (**Figure 3.1**). The two peaks at 360 and 380 nm are related to transitions of the naphthalene diimide (**DPNI**) ligand, which are coming out from the framework into solution after 3 days. In the same time, the concentration of the clathrochelate (**3.2a**, **3.2b**, **3.2c** or **3.2d**) is decreasing because they are incorporated into the framework.

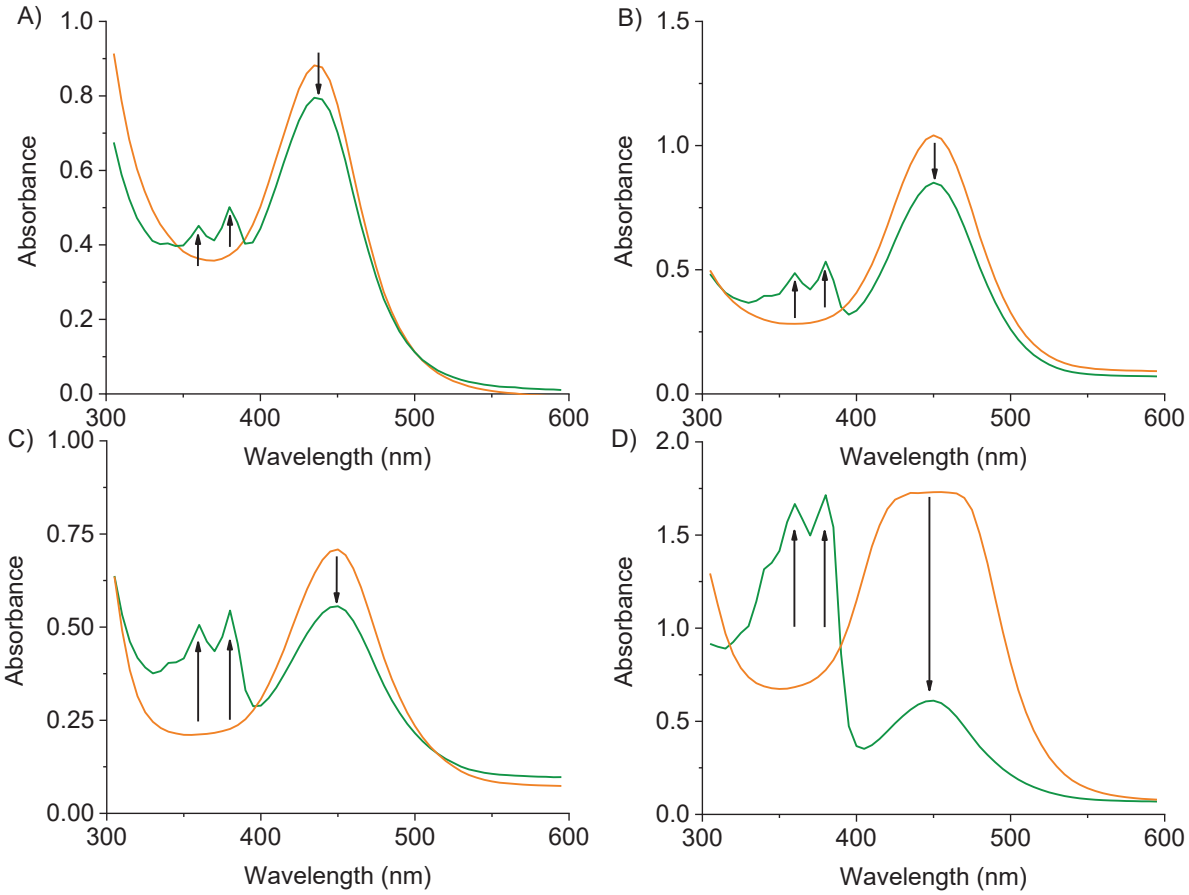

Figure 3.1 Stacking of UV-Vis spectra obtained from solutions of SALE with MOFs **3.3a** (A), **3.3b** (B), **3.3c** (C) and **3.3d** (D) in DMF, after 5 min (orange) and after 3 days (green).

Secondly, to monitor the ligand exchange evolution, we have used ^{1}H NMR (**Figures 3.2**). Approximately 1-5 mg of MOF crystals were removed from the reaction mixture, and washed with DMF several times. The crystals were then placed in a 2 mL vial containing deuterated dimethyl sulfoxide (DMSO-d_6, 0.6 mL). 2 drops of H_2SO_4 were added and the mixture was sonicated for 5 min to achieve complete dissolution. The sample was then transferred to an NMR tube. The progress of the conversion for **3.3b**, **3.3c** and **3.3d** followed by ^{1}H NMR is shown in Chapter 8.

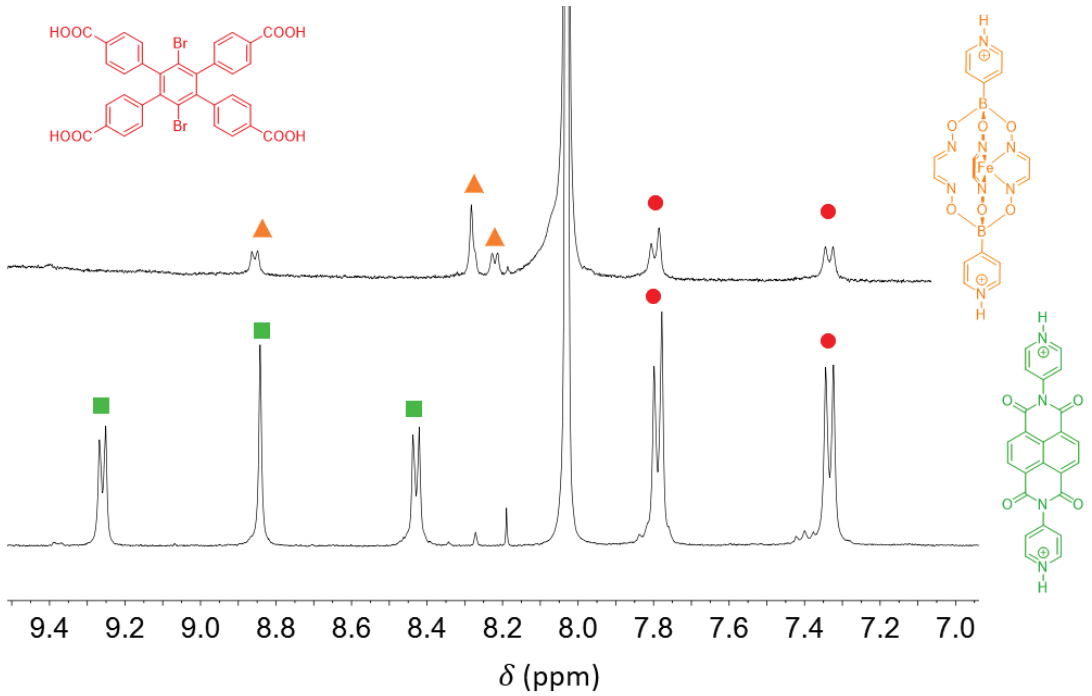

Figure 3.2 Progress of the conversion of **1** into **3.3a** as monitored by ^{1}H NMR spectroscopy (DMSO-d_6 + H_2SO_4, zoom on the aromatic region). Sample composition after 5 min (bottom), and after 3 days (top). Signals depicted in green correspond to the protonated **DPNI** linker, orange for the protonated clathrochelate **3.2a**, and red for the carboxylic acid ligand.

Clean pillar exchange was observed for all four cage complexes. Even for the sterically demanding complex **3.2d**, we observed nearly quantitative ligand exchange after 3 days. We have also attempted to prepare MOFs of type **3.3** using standard solvothermal reaction conditions, but we were unable to obtain crystalline products. The phase-purity of **3.3a** was established by powder XRD (**Figure 3.3**). In the same phase-purity for **3.3b**, **3.3c** and **3.3d** can be found in Chapter 8.

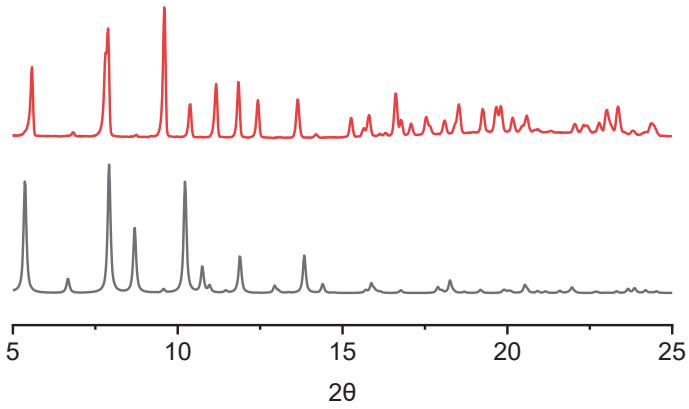

Figure 3.3 Comparison between **3.1** (black) as published and **3.3a** (red).

Interestingly, the crystal quality was largely preserved during ligand exchange (**Figure 3.4**). We were therefore able to perform single crystal X-ray analyses of the products **3.3a** and **3.3d** (**Figure 3.5**). The quality of **3.3b** and **3.3c** crystals obtained were not good enough to perform X-ray analyses.

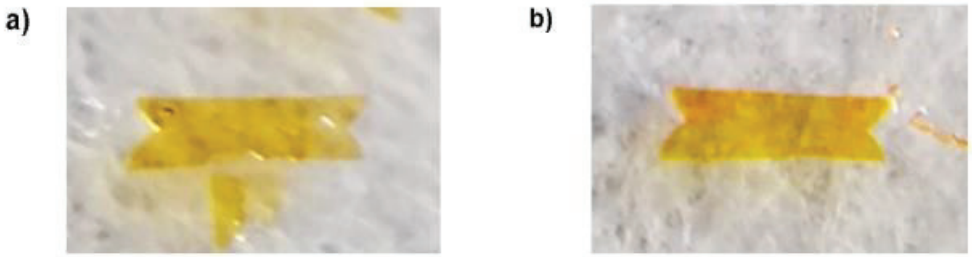

Figure 3.4 Photographs of a crystal of **3.1** before (a) and after (b) immersion into a DMF solution of **3.2a** for 5 days at RT.

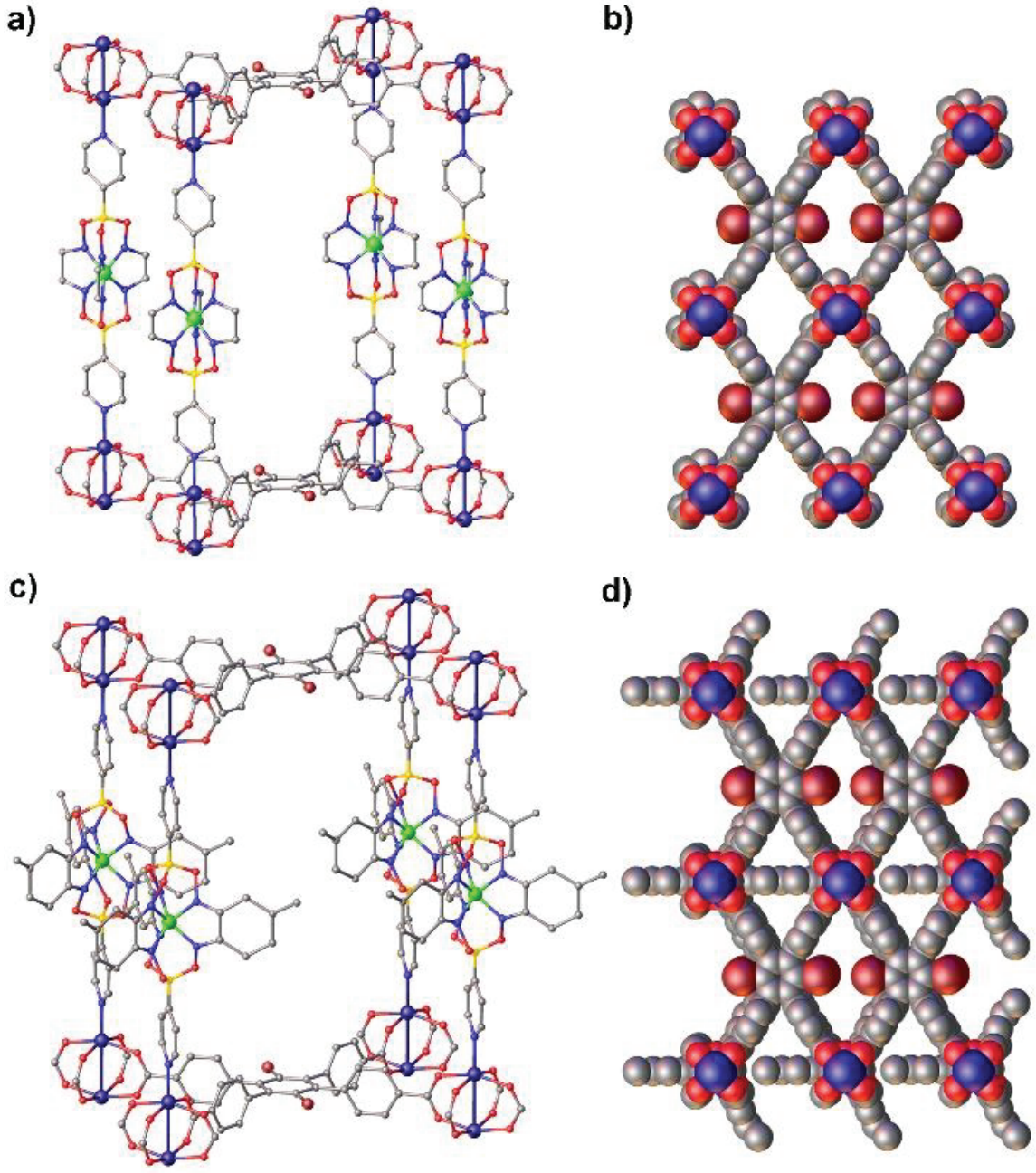

Figure 3.5 Part of the molecular structure of **3.3a** (a and b) and **3.3d** (c and d) in the crystal. H atoms and solvent are omitted for clarity. Color coding: C: grey, Fe: green, Zn: dark blue, O: red, B: yellow, N: blue, Br: brown.

Retention of the parent MOF topology (*Pmmm* space group) was found for both cases. However, slightly reduced interlayer distances were observed as a consequence of the shorter lengths of **3.2a** and **3.2d** when compared to **DPNI.** The length of the dipyridyl pillars is linked to unit cell parameter *c,* which is decreasing from 22.313(3) Å (**3.1**) to 21.8880(11) Å (**3.3a**)

and 21.8056(17) Å (**3.3d**), respectively. The increased steric demand of **3.2d** leads to a reduced solvent-accessible volume for **3.3d** (2333 $Å^3$) when compared to **3.3a** (2975 $Å^3$). The clathrochelate pillars in **3.3a** and **3.3d** are highly disordered, indicating conformational flexibility around the pillar axis. Based on the size of the central iron complex, one would assume a largely unhindered rotation for pillar **3.2a** in MOF **3.3a**. For **3.3d**, however, the clathrochelate side chains are interdigitated (**Figure 3.5d**), and correlated ligand movements are expected.

In addition, TGA measurements indicate high stabilities, as all MOFs **3.3a**, **3.3b**, **3.3c** and **3.3d** showed no sign of framework pyrolysis until at least 330°C. Large 3D noncatenated channels in the crystal structures were confirmed by the first mass loss (20-70%) which correspond to entrapped DMF molecules (**Figure 3.6**).

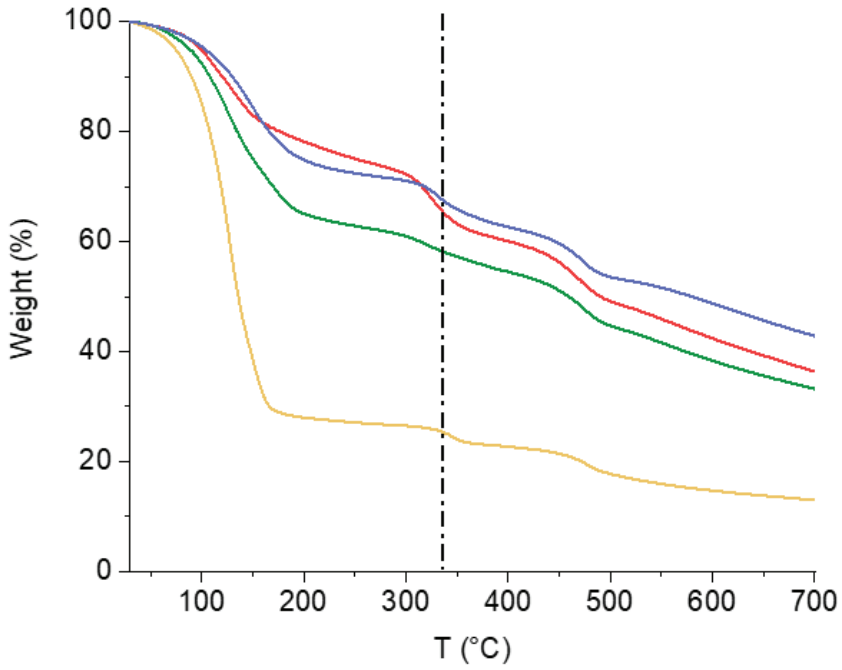

Figure 3.6 TGA profiles of as-synthesized MOFs **3.3a** (red), **3.3b** (yellow), **3.3c** (green) and **3.3d** (blue).

3.2.2 Reactions with MOFs Containing Metalloporphyrin Ligands

Next, we investigated if pyridyl-capped clathrochelate complexes can be incorporated into pillared MOFs with porphyrin-based carboxylate ligands. SALE experiments were performed with a 2-dimensional MOF termed 'PPF-18' (**Scheme 3.4**), which was reported by the group of Choe.[105] It features layers composed of $Zn_2(O_2C)$ nodes and metallated tetrakis(4-carboxyphenyl)porphyrin (**TCPP-Zn**) ligands. The layers are connected in a pair-wise fashion via **DPNI** pillars to give a double-layer structure. Each pillar coordinates to one $Zn_2(O_2C)$ node and to one Zn-porphyrin, resulting in an AB stacking pattern of the layers. When crystals of **3.4** (PPF-18) were immersed in a concentrated DMF solution of metalloligand **3.2a**, we were able to observe complete pillar exchange after heating to 80 °C for 3 days.

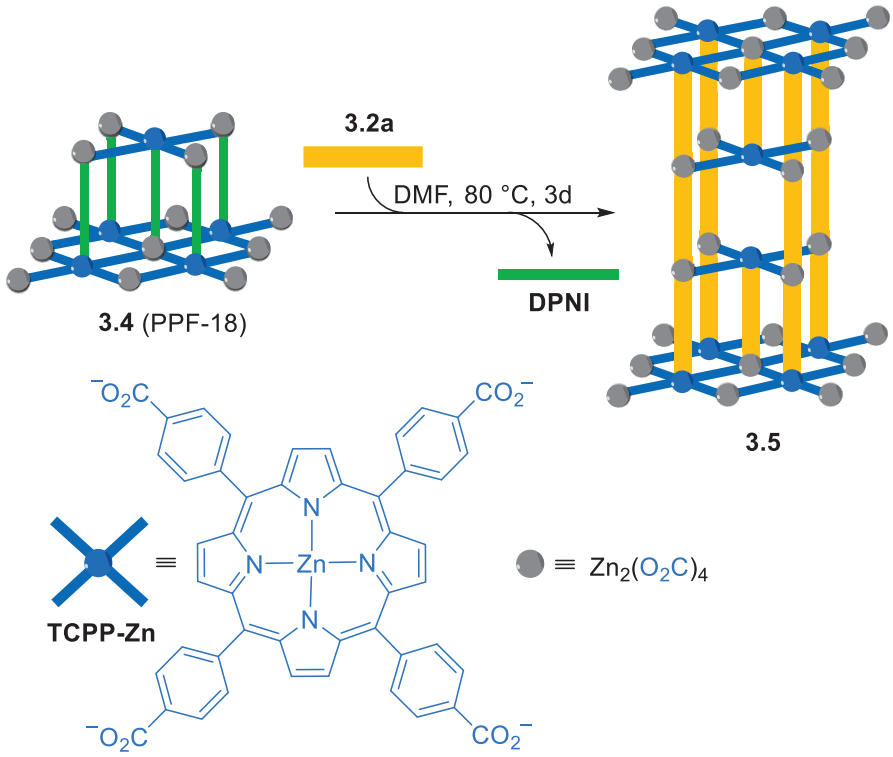

Scheme 3.4 Synthesis of MOF **3.5**.

Crystalline **3.4** was prepared as described and the phase purity was verified by powder XRD (experimental details in Chapter 8). Ligand exchange was then initiated by suspending crystals

of **3.4** in a DMF solution of **3.2a**. The mixture was heated to 80 °C, and progress of the reaction was monitored by UV-Vis and ^{1}H NMR.

An NMR analysis of the digested product showed that the new MOF structure **3.5** displayed an increased pillar content of **3.2a**:**TCPP-Zn** = 3:2 (**Figure 3.7**). For comparison, the corresponding ratio for **3.4** is **DPNI**:**TCPP-Zn**: = 1:1. The presence of additional pillars in **3.5** suggested cross-linking of the double layers.

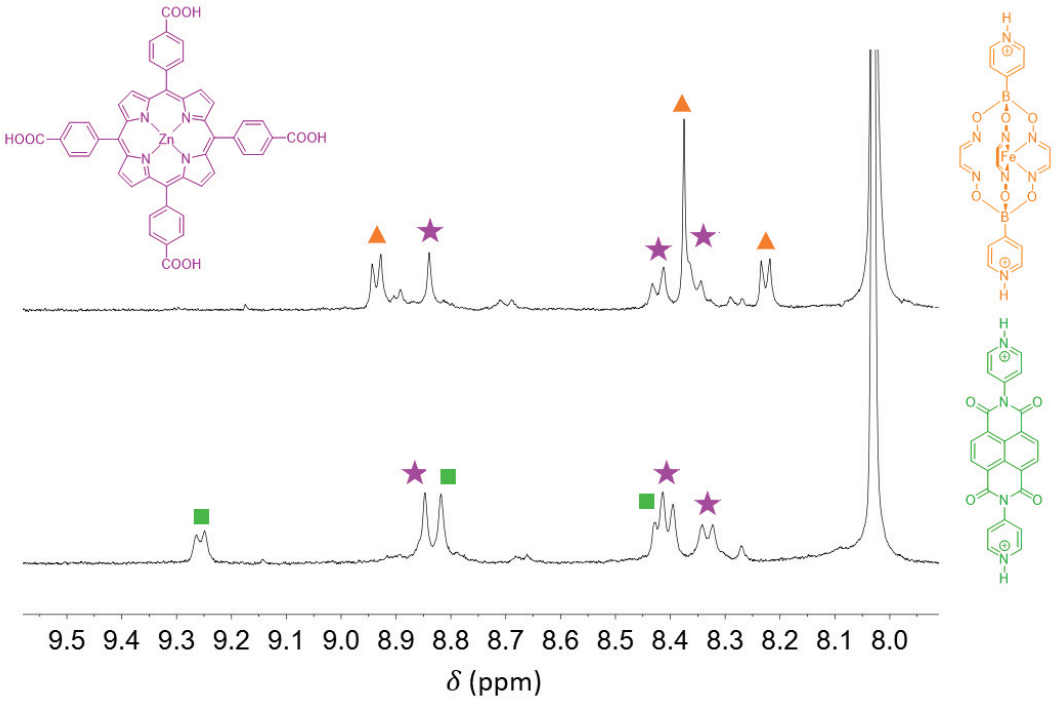

Figure 3.7 Progress of the conversion of **3.4** into **3.5** as monitored by ^{1}H NMR spectroscopy (DMSO-d_6 + H_2SO_4, zoom on the aromatic region). Sample composition after 5 min (bottom), and after 3 days (top). Signals depicted in green correspond to the protonated **DPNI** linker, orange for the protonated clathrochelate **3.2a**, and purple for the carboxylic acid ligand.

The phase-purity of **3.5** was established by powder XRD (experimental details in Chapter 8). Analysis of **3.5** by single crystal XRD confirmed that a 3-dimensional MOF had formed (**Figure 3.8**). Unfortunately, we were only able to obtain diffraction data of poor quality, and we therefore refrain from discussing structural details. Nevertheless, the topology of **3.5** could clearly be established and a schematic representation of the structure is depicted in **Scheme 3.5**.

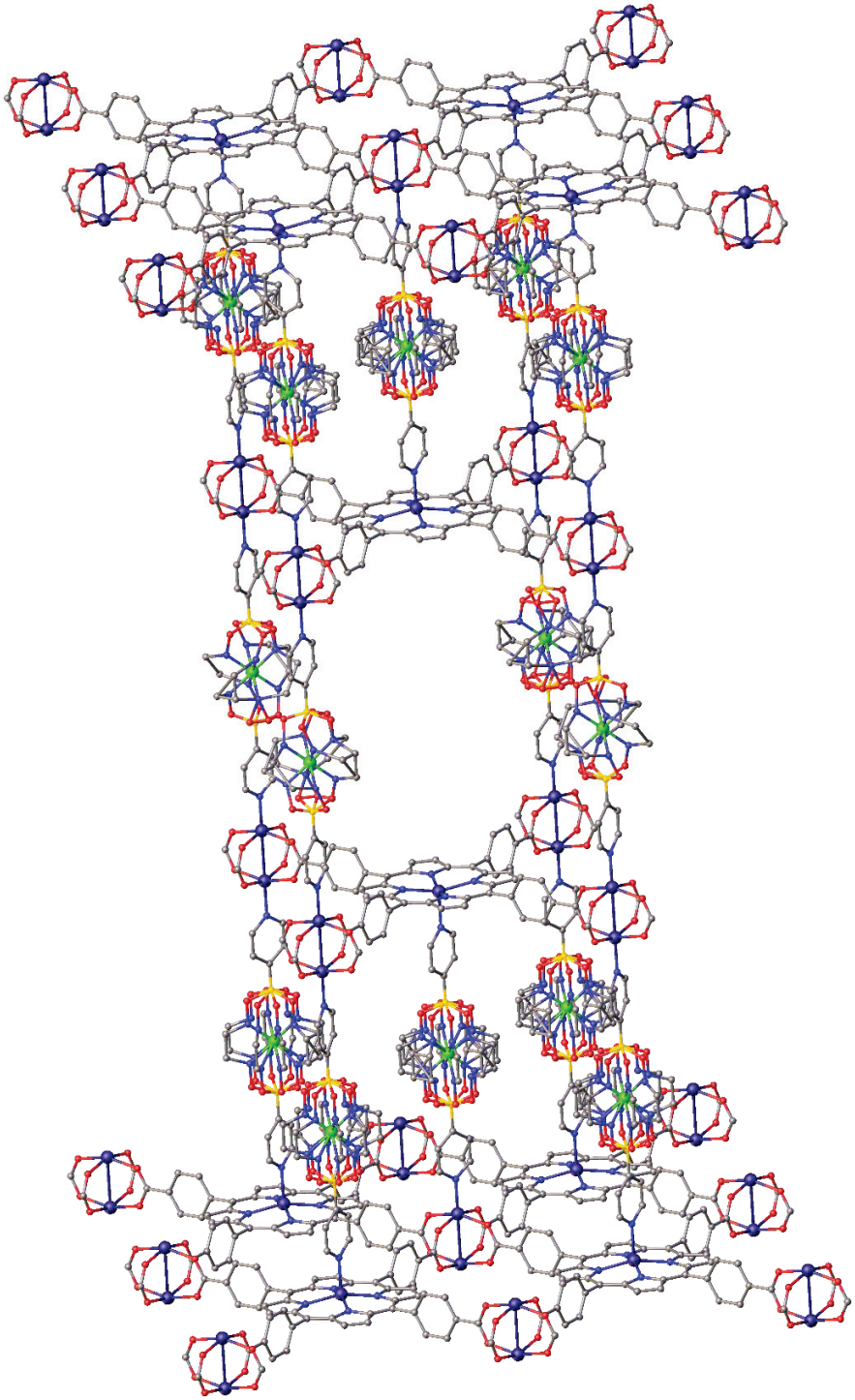

Figure 3.8 Part of the molecular structure of MOF **3.5** in the crystal. Color coding: C: grey, Fe: green, Zn: dark blue, O: red, B: yellow, N: blue. H atoms and solvent are omitted for clarity. Disorder around Fe is due to orientational or dynamical disorder.

In contrast to what was found for **3.4**, the $Zn_2(O_2C)$ nodes in **3.5** are linked to two pillars, resulting in an overall ABBA stacking pattern. It is worth noting that a similar topology change from 2D to 3D was observed when SALE experiments were performed with PPF-19 and an excess of 4,4'-bipyridine.[70] However, a cross-linking of layers was not successful with larger **DPNI** pillars.[106]

Furthermore, UV/Vis spectroscopy was used to follow the progress of the reaction. UV/Vis spectra and experimental data is shown in Chapter 8.

Finally, we have investigated pillar exchange using a **TCPP-Zn**-based MOF termed 'PPF-19'. PPF-19 is doubly interpenetrated and we anticipated that the SALE process would be impeded by the reduced pore size. However, this prediction turned out to be wrong, and clean pillar exchange was observed when crystalline **3.6** was heated in a solution of **3.2a** in DMF (**Scheme 3.5**).

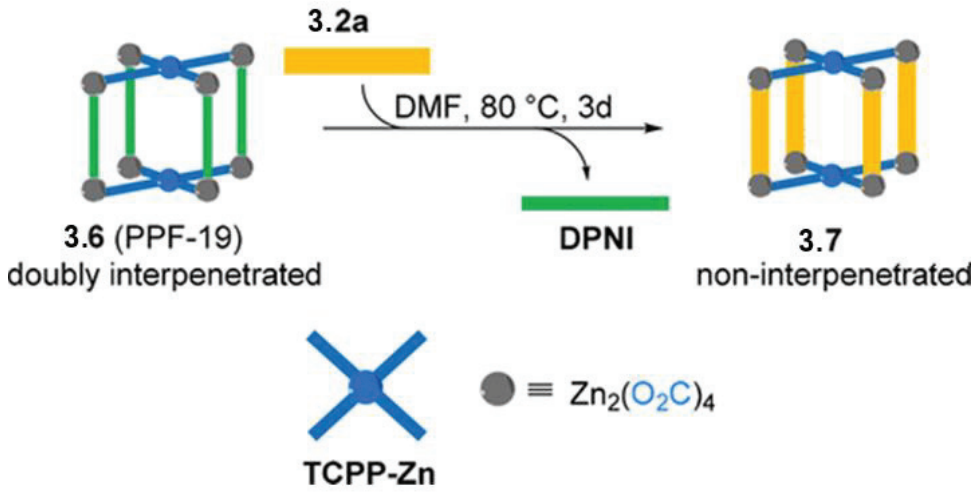

Scheme 3.5 Synthesis of MOF **3.7**.

Crystalline **3.6** was prepared as described by Hupp and co-workers.[105] The phase purity was verified by powder XRD (Experimental details in Chapter 8). Ligand exchange was then initiated by suspending crystals of **3.6** in a DMF solution of **3.2a**. The mixture was heated to 80 °C, and progress of the reaction was monitored by UV-Vis and ^{1}H NMR.

An NMR analysis of the digested product showed that the new MOF structure **3.7** displayed an increased pillar content of **3.2a**:**TCPP-Zn** = 3:2 (**Figure 3.9**).

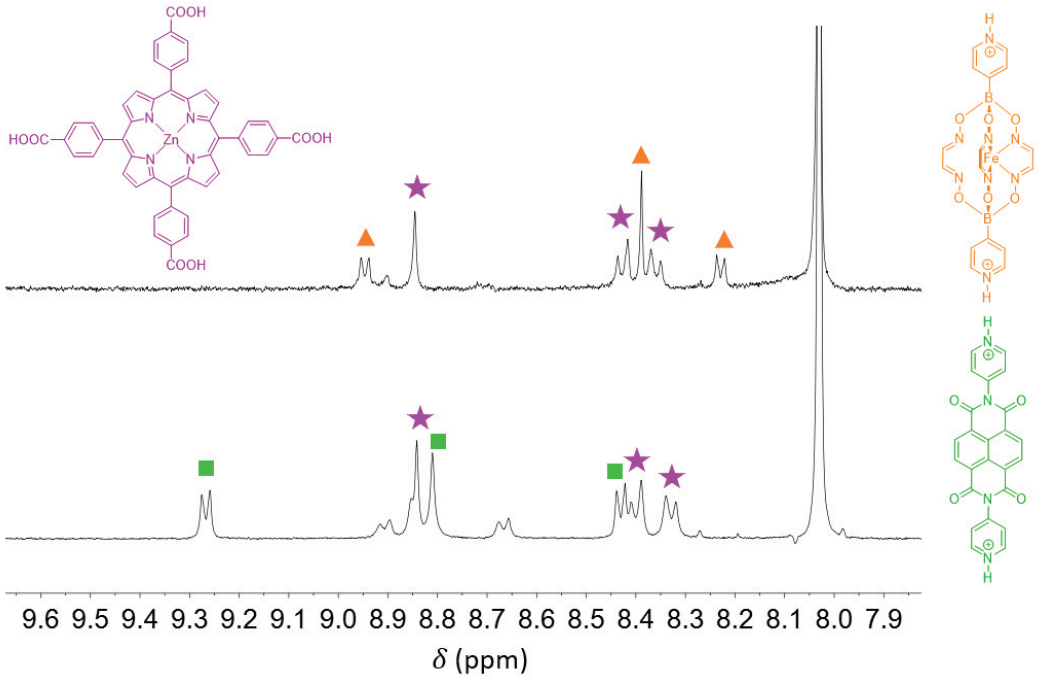

Figure 3.9 Progress of the conversion of **3.6** into **3.7** as monitored by ^{1}H NMR spectroscopy (DMSO-d_6 + H_2SO_4, zoom on the aromatic region). Sample composition after 5 min (bottom), and after 3 days (top). Signals depicted in green correspond to the protonated **DPNI** linker, orange for the protonated clathrochelate **3.2a**, and purple for the carboxylic acid ligand.

Additionally, UV/Vis spectra taken to follow the progress of the reaction and the PXRD spectra of phase-pure **3.7** are shown in Chapter 8.

As observed for the other reactions, the SALE process led only to a partial degradation of crystal quality. We were therefore able to perform a single crystal XRD analysis of MOF **3.7**. As in the case of **3.5**, we did not manage to obtain high quality diffraction data. The problem is in part related to the fact that the metalloligand in **3.7** is highly disordered. In view of these difficulties, we do not discuss any structural details. However, the topology of **3.7** could clearly be established. The connectivity of **3.7** is identical to that of **3.6**: Each $Zn_2(O_2C)$ node is coordinated to four **TCPP-Zn** ligands and to two dipyridyl pillars **3.2a** (**Figure 3.10**). The Zn porphyrin complexes are not involved in binding to the N-donor ligands. In contrast to what was found for **3.6**, there is no interpenetration in the network structure of **3.7**. As a result, we

observe large voids, with a solvent-accessible volume of approximately 4794 Å^3. Unfortunately, attempts to obtain a material with permanent porosity failed. Network collapse was observed upon removal of the solvent.

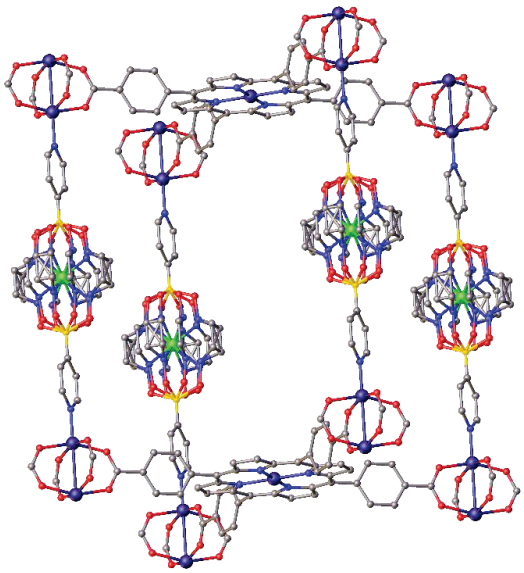

Figure 3.10 Part of the molecular structure of MOF **3.7** in the crystal. Color coding: C: grey, Fe: green, Zn: dark blue, O: red, B: yellow, N: blue. H atoms and solvent are omitted for clarity. Disorder around Fe is due to orientational or dynamical disorder.

The change in topology from **3.6** to **3.7** is likely related to the increased steric demand of the metalloligand **3.2a** when compared to **DPNI**. From a mechanistic point of view, the conversion of an interpenetrated structure into a non-interpenetrated daughter structure is intriguing, in particular since we were able to obtain single crystals of the product. A dissolution-recrystallization process appears to be the most likely scenario, but further investigations would be needed to clarify this point.

In addition, TGA measurements indicate high stabilities, as all MOFs **3.5** and **3.7** showed no sign of framework pyrolysis until at least 380°C. Large 3D noncatenated channels in the crystal structures were confirmed by the first mass loss (25-40%) which correspond to entrapped DMF molecules (**Figure 3.11**).

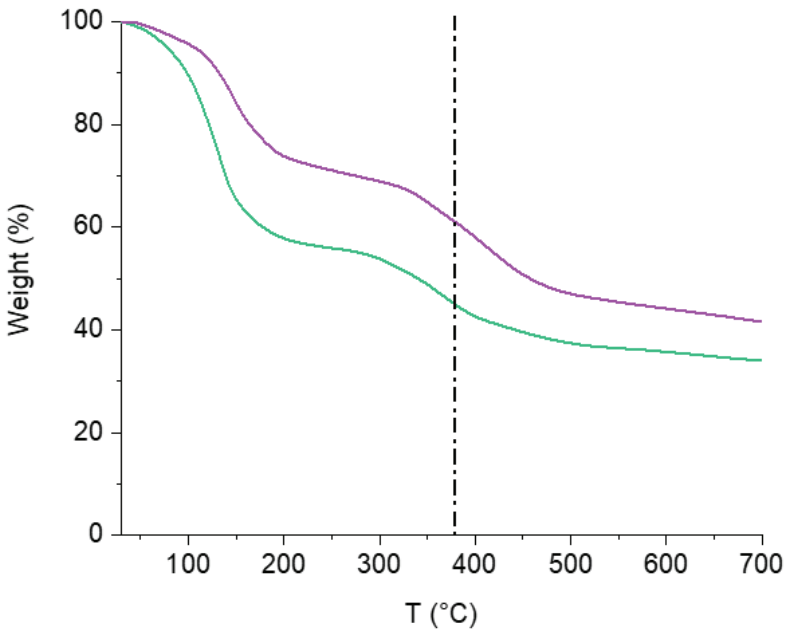

Figure 3.11 TGA profiles of as-synthesized MOFs **3.5** (green) and **3.7** (purple).

3.3 Conclusion

To conclude, we have shown that clathrochelate-based metalloligands with terminal 4-pyridyl groups can be incorporated in pillared paddle-wheel MOFs by using the SALE technique. Pillar exchange was found to be nearly quantitative, despite the fact that the metalloligands are long (~ 15 Å) and sterically demanding. We assume that the exchange process is facilitated by the high basicity of the metalloligands, which should lead to more stable metal-ligand interactions.[81,103] Indirect evidence for this assumption is the successful synthesis of the 3D MOF **3.5**, for which the analogous **DPNI** structure could not be prepared.[106] A noteworthy feature of the reactions is the good crystal quality of the products. Consequently, we were able to characterize some of the products by single crystal XRD.

The possibility to use the SALE technique for synthesizing MOFs containing clathrochelate complexes offers an interesting perspective for future developments. The method might be used as a simple way to prepare heterometallic[107] and redox-active MOFs.[108] Furthermore, the lateral groups on the clathrochelate can be varied substantially.[2] For the present study, we have used four different clathrochelates, including chiral **3.2d**, but more variations can be envisioned. It might also be possible to incorporate clathrochelates with dichloroglyoximate ligands, which could be used for post-synthetic modifications via nucleophilic substitution reactions.[2,18]

Chapter 4

Ligand Effects in Low-Valent Co(I) Clathrochelates

The work described in this Chapter is unpublished: **O. M. Planes**, R. Scopelliti, F. Fadaei-Tirani, K. Severin, **2021.**

O.M.P. synthesized and characterized the compounds, F.F.-T. and R.S. carried out the single crystal XRD analyses, and K.S. initiated and coordinated the study.

4.1 Introduction

Clathrochelate complexes of cobalt are known in the oxidation states I, II, and III. Low-valent Co(I) complexes are highly reactive compounds, and there is only limited knowledge about their structures in the solid state. Herein, we describe the crystallographic analyses of three low-valent clathrochelate complexes, along with analyses of the corresponding Co(II) precursors. Two different ligand environments were studied: a) ligands with alkyl substituents, which render the complexes highly reducing, and b) potentially redox non-innocent ligands. Our analyses show that the ligands have a large effect on the redox potentials, but only a small effect on the geometry and the electronic state of the central Co ion.

4.2 Low-Valent Co Clathrochelates

Cobalt clathrochelate complexes are known in the oxidation states I, II, and III, with most studies focusing on Co(II).[2,15,109-110] These complexes have either a low-spin or a high-spin d^7 electronic

configuration, and they display a distorted trigonal prismatic coordination environment. Low-valent Co(I) clathrochelates are of special interest, because they could be involved in the formation of the catalytically active species for HER.[38-51] A first crystallographic analysis of a Co(I) clathrochelate was reported by Voloshin and co-workers in 2005.[111] In order to stabilize the highly reactive reduced form, they have used a complex with six chloro substituents R in lateral position. Due to the electron-withdrawing nature of the chloride substituents, it is possible to achieve the reduction of the Co(II) precursor at rather high potential ($E_{1/2}$ = –0.46 V for R = Cl and R' = Bu; ref. = Fc/Fc^+ Figure 1a).[111] In the meantime, the solid state structures of two other Co(I) clathrochelates have been reported: one complex with R = Cl and R' = Ph ($E_{1/2}$ = –0.50 V),[112] and another complex with R = Ph and R' = dithiophenyl ($E_{1/2}$ = –1.03 V).[113] Complexes with alkyl groups in lateral position display a more negative reduction potential ($E_{1/2}$ ~ –1.4 V), impeding isolation and structural characterization (**Figure 4.1**).

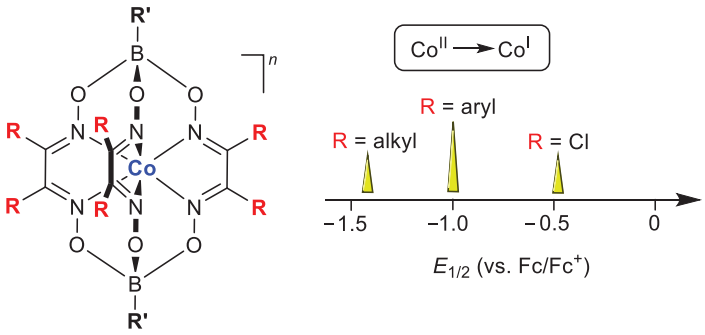

Figure 4.1 Structure and redox properties of Co clathrochelate complexes.

A theoretical analysis of a Co(I) clathrochelate with R = Me has shown that the complex should feature a high spin Co(I) center (S = 1) in a highly symmetric ligand environment.[114] However, the possibility that Co(I) clathrochelate complexes could adopt a singlet spin state (S = 0) was also considered in theoretical studies.[114-115] The calculations indicate that a diamagnetic Co(I) complex would show a very distorted ligand environment, with two long Co-N bonds.

Below, we report the first structural characterization of Co(I) clathrochelate complexes with alkyl groups in lateral position. Furthermore, we have prepared a Co(II) clathrochelate with a potentially redox non-innocent phenanthrenequinone imine ligand (**Figure 4.2**),[116] and we have examined the influence of this ligand on the structure of the corresponding low-valent Co(I) complex.

4.2.1 Nioxime-Based Cobalt Clathrochelates

We have prepared the complex **4.1** from $CoCl_2$, nioxime, and phenylboronic acid using the standard clathrochelate synthesis described in Section 1.1. Complex **4.2** with terminal B-C_6F_5 groups was prepared analogously in 53% yield. Both complexes were characterized by high resolution mass spectrometry, elemental analysis, UV-Vis spectroscopy, cyclic voltammetry, and single crystal X-ray analysis (See Chapter 8). The presence of electron-withdrawing pentafluorophenyl groups in **4.2** was found to have a negligible influence on the reduction potential: the reversible Co(II)/Co(I) transition of **4.1** occurs at $E_{1/2}$ = –1.40 V, and the corresponding wave for **4.2** is found at $E_{1/2}$ = –1.42 V (CH_2Cl_2, 0.1 M $TBAPF_6$, ref. = Fc/Fc^+).

The molecular structures of **4.1** and **4.2** in the crystal show an approximate trigonal prismatic coordination geometry around the Co ions (**Figure 4.2**). Due to Jahn-Teller distortion, one can observe four short Co–N bond distances of ~ 1.89 Å, and two long Co–N bond distances of ~ 2.11 Å (**Table 4.1**). The presence of short and long Co–N bonds is a characteristic feature of low-spin Co(II) clathrochelates.[2,15,117] For an ideal trigonal prismatic coordination environment, the Bailar twist angle φ is 0 °, whereas an octahedral complex has a twist angle of φ = 60° (**Figure 4.3**). For **4.1** and **4.2**, we observe small twist angles of 4.9 ° and 1.7 °, respectively (**Table 4.1**).

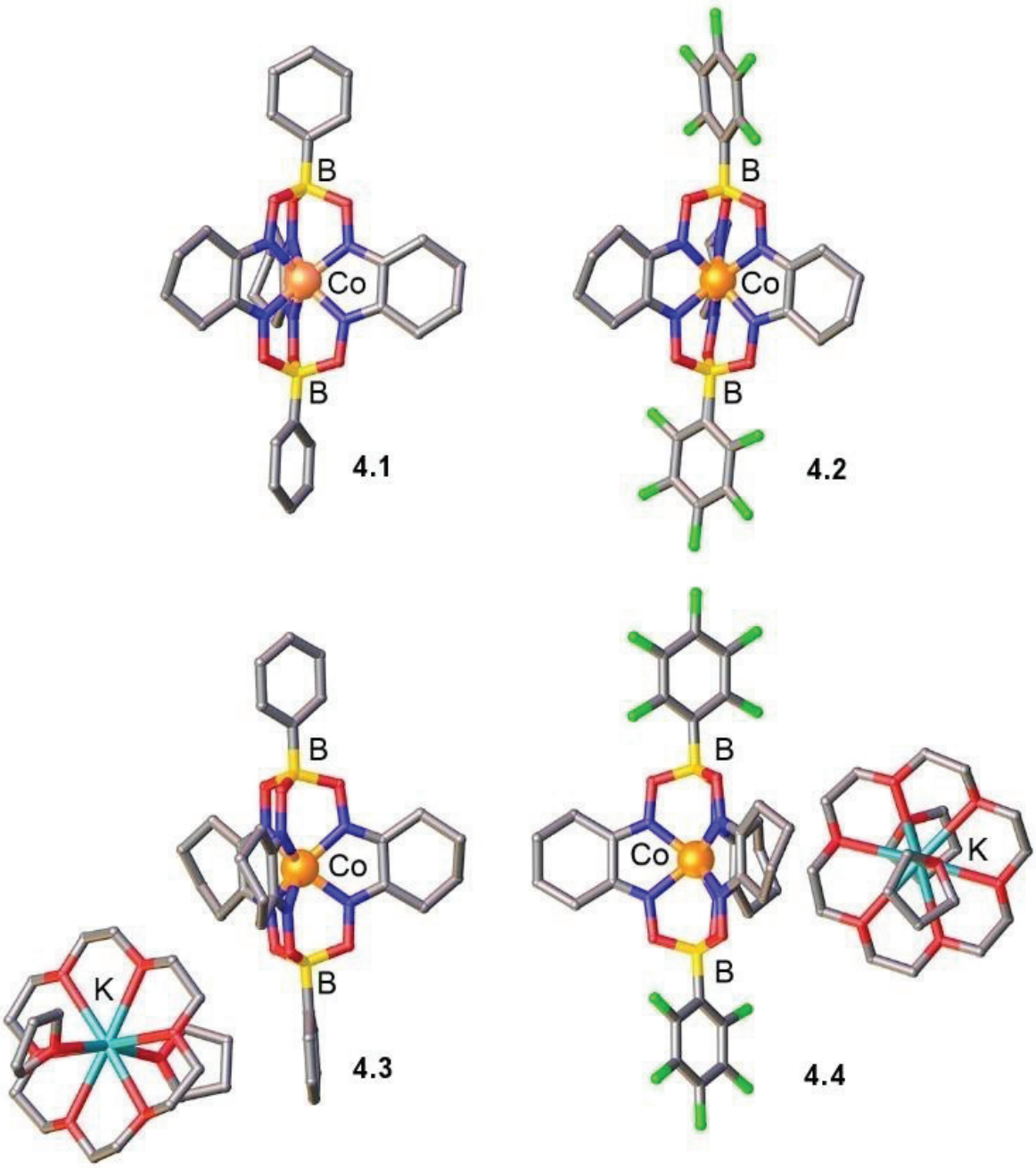

Figure 4.2 Molecular structures of the complexes **4.1**–**4.4** in the crystal. Color coding: C: grey, Co: orange, O: red, B: yellow, N: blue, F: green, K: turquoise. H atoms and solvent are omitted for clarity.

The reduction of the Co(II) complexes **4.1** and **4.2** was examined with different reducing agents (e.g. silver powder in the presence of tetraalkylammonium of tetra(dimethylamido)phosphonium halides) and reactions conditions. After several failed

attempts, we were finally successful with using C_8K and 18-crown-6 in THF at room temperature.

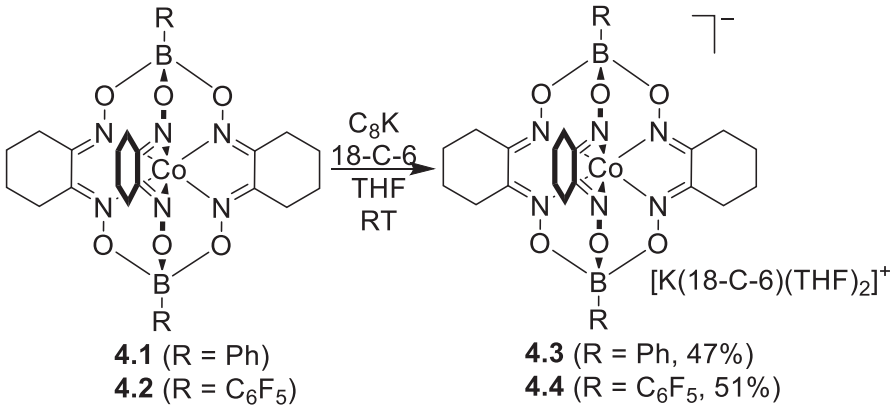

Scheme 4.1. Synthesis of the low-valent complexes **4.3** and **4.4** by reduction of the Co(II) clathrochelates **4.1** and **4.2** with C_8K (1.2 equiv) in the presence of 18-crown-6 (18-C-6, 1.2 equivalents).

Within 30 min, dark blue solutions were obtained, from which we were able to obtain the low-valent complexes **4.3** and **4.4** in 47% and 51% yield, respectively. Single crystals were obtained by slow diffusion of pentane into solutions of **4.3** and **4.4** in THF.

The average Co–N bond distances of **4.3** (1.992 Å) and **4.4** (1.991 Å) are very similar to what was found for **4.1** (1.970 Å) and **4.2** (1.968 Å). However, we do not observe a pronounced bond lengths alternation. Instead, all six Co-N bond are nearly equidistant (**Table 4.1**). The highly symmetric ligand environment points to the presence of high spin Co(I) centers.[111-115,117] The geometry around the Co ions is nearly trigonal prismatic, with small twist angles φ and B···Co···B' angles of close to 180 °. Overall, the structural data of **4.3** and **4.4** are very similar to what has been observed for the three other Co(I) clathrochelate complexes reported in the literature. It can be concluded that the electronic character of the dioximato ligand does have a pronounced effect on the redox potential of the Co(II)/Co(I) transition (**Figure 4.1**), but not on the electronic situation of the reduced Co center.

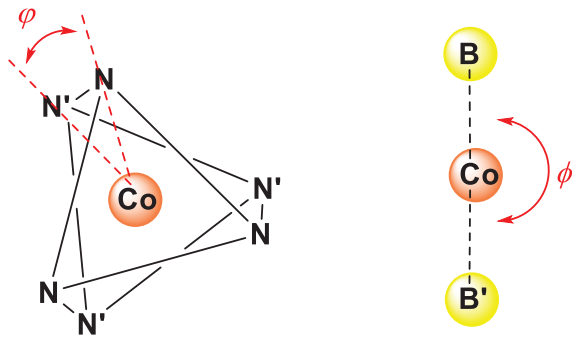

Figure 4.3 Representation of Bailar twist angle φ and B···Co···B' ϕ angle in a clathrochelate.

complex	**4.1**	**4.2**	**4.3**	**4.4**	**4.5**	**4.6**
Co1–N1	1.9058(14)	1.8986(8)	2.0004(19)	1.991(7)	2.160(5)	2.011(3)
Co1–N2	2.1023(13)	2.1183(9)	1.9840(20)	1.981(7)	1.902(5)	2.000(3)
Co1–N3	1.8928(13)	1.8865(8)	1.9978(17)	2.009(7)	1.896(5)	2.021(2)
Co1–N4	1.8886(13)	1.8913(9)	1.9807(17)	1.994(7)	2.127(5)	2.018(2)
Co1–N5	2.1254(15)	2.1135(9)	2.0072(19)	1.972(7)	1.907(5)	2.012(2)
Co1–N6	1.9022(14)	1.9001(8)	1.9817(19)	1.998(7)	1.915(5)	1.994(3)
Co–$N_{av.}$	1.970	1.968	1.992	1.991	1.985	2.009
C=$N_{av.}$	1.294	1.301	1.303	1.306	1.318	1.323
NC–$CN_{av.}$	1.455	1.454	1.457	1.447	1.466	1.467
φ (NBB'N')	4.9	1.7	1.5	0.88	0.44	0.88
ϕ (BCoB')	173	172	180	179	172	179

Table 4.1 Selected bond lengths [Å] and angles [°] for the complexes **4.1**–**4.6**.

4.2.2 Phenanthrene-Based Cobalt Clathrochelates

Next, we have investigated Co clathrochelate complexes with phenanthrenequinone dioximato ligands, which are potentially redox non-innocent (**Figure 4.4**).[116]

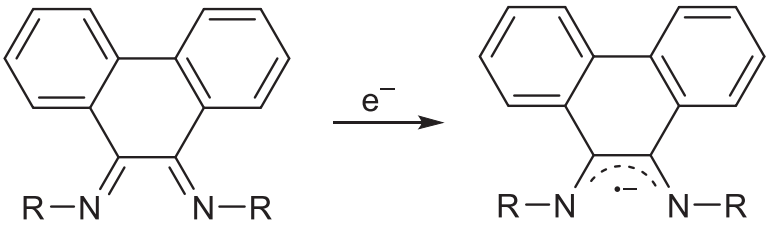

Figure 4.4 Phenanthrenequinone imines can act as redox non-innocent ligands.

The Co(II) complex **4.5** was prepared in 37% yield from $CoCl_2$, phenanthrenequinone dioxime,[116] and phenylboronic acid (**Scheme 4.2**). Complex **4.5** shows good solubility in CH_2Cl_2 and THF without any decomposition. Its stability lead us to store it under air as a purple powder without any precautions.

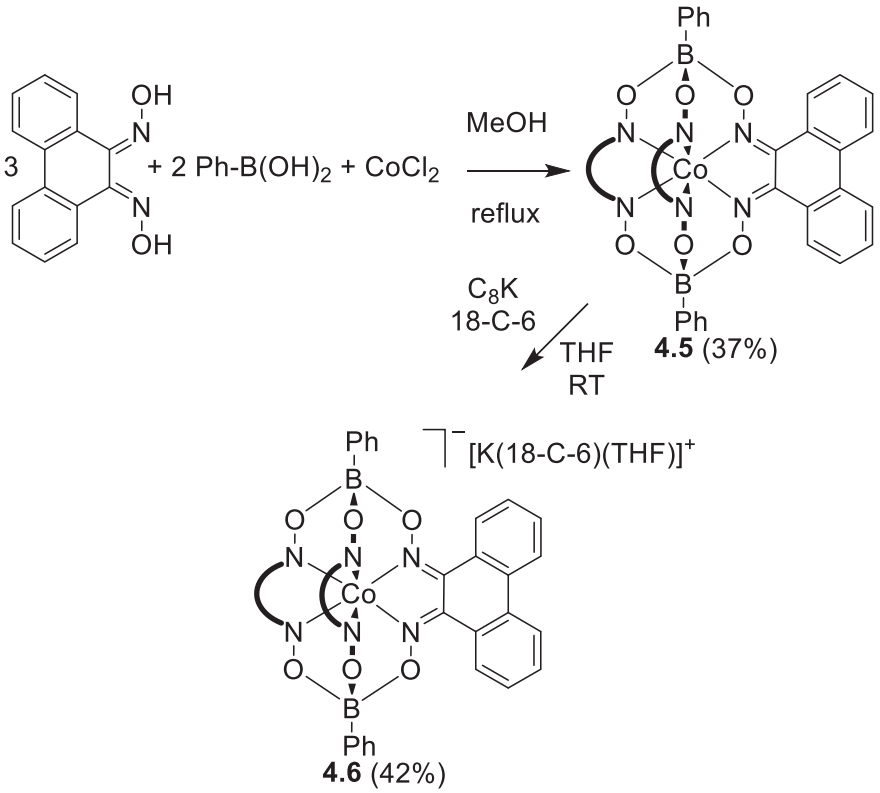

Scheme 4.2 Synthesis of the clathrochelate complexes **4.5** and **4.6**.

The solid-state structure of **4.5** was determined by single crystal X-ray diffraction, and a graphic representation of the structure is depicted in **Figure 4.5**. As observed for **4.1** and **4.2**, the encapsulated Co ion shows a distorted trigonal prismatic ligand environment, with two longer and four shorter Co–N bonds (Table 1). With 1.985 Å, the average Co–N bond distance is slightly larger than what was found for **1** and **2** (1.970 Å and 1.968 Å).

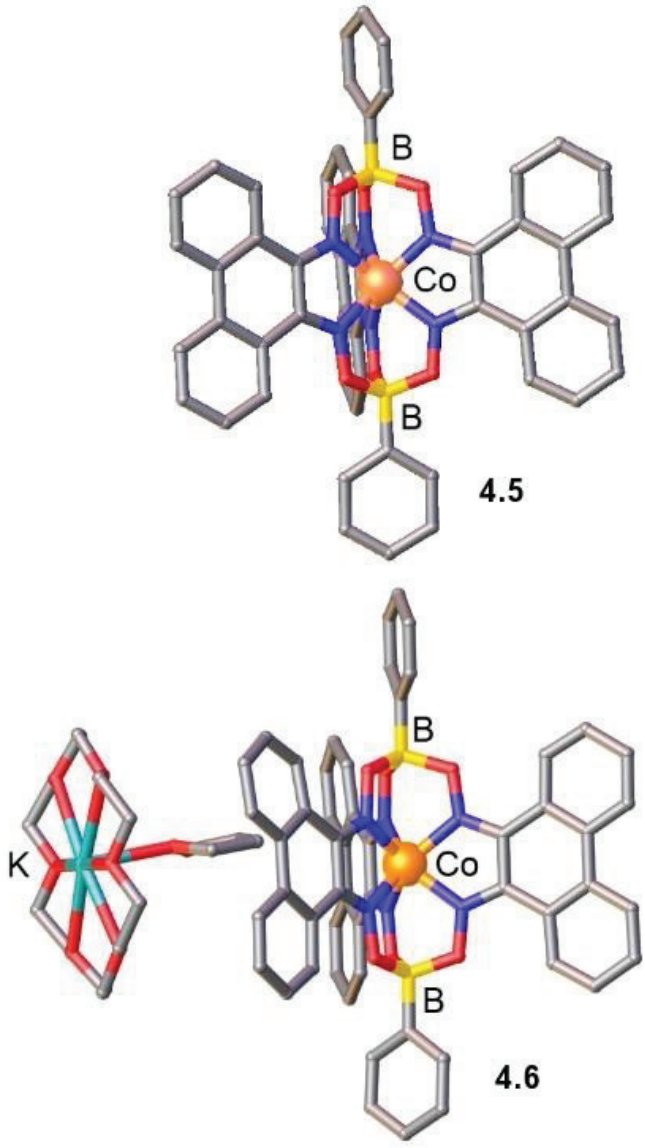

Figure 4.5 Molecular structures of the complexes **4.5** and **4.6** in the crystal. Color coding: C: grey, Co: orange, O: red, B: yellow, N: blue, K: turquoise. H atoms and solvent are omitted for clarity. Disorder around Fe is due to orientational or dynamical disorder.

The redox behavior of **4.5** was examined by cyclic voltammetry (CH_2Cl_2, 0.1 M $TBAPF_6$, ref. = Fc/Fc^+). Two reversible transitions were observed at $E_{1/2}$ = –0.10 V and $E_{1/2}$ = –0.85 V. The former transition is assigned to the Co(II)/Co(III) redox couple. The transition at –0.85 V could be related to either a ligand- or a metal-based reduction of the neutral Co(II) complex **4.5** (**Figure 4.6**).

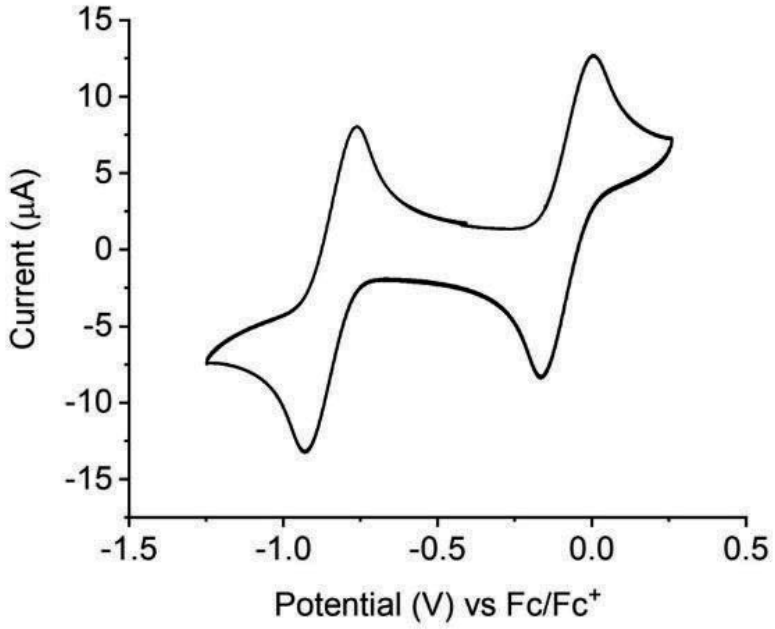

Figure 4.6 Cyclic voltammogram of complex **4.5** in DCM with $TBAPF_6$ (0.1 M) as electrolyte. (CE and WE: Pt, RE: 3M NaCl). Scan rate= 100 $mV.s^{-1}$.

To elucidate the nature of the reduced state, we have carried out a reaction of complex **4.5** with C_8K in THF in the presence of 18-crown-6 (**Scheme 4.2**). Stirring for 2 h at room temperature resulted in the formation of a green solution. Complex **4.6** could then be isolated in 42% yield by precipitation with diethyl ether. Single crystals of **4.6** were obtained by slow evaporation of a THF solution of **4.6** in a glovebox, and a crystallographic analysis was performed (**Figure 4.5**).

The coordination environment of the Co ion in complex **4.6** is very similar to what was found for **4.3** and **4.4**: one can observe six nearly equidistant Co–N bonds, and only a small distortion form an ideal trigonal prismatic coordination environment (**Table 4.1**). If complexes with phenanthrenequinone imine ligands undergo a ligand-based reduction, one can typically observe a shortening of the NC–CN bonds.[117] For complex **4.6**, however, the corresponding

value is very similar to that of **4.5**. Taken together, the structural data are good evidence that clathrochelate **4.6** should be described as a Co(I) complex.

4.3 Conclusion

We have performed crystallographic analyses of three Co(I) clathrochelate complexes (**4.3**, **4.4**, and **4.6**), along with analyses of the corresponding Co(II) precursors. The nioxime-derived complexes **4.3** and **4.4** have alkyl substituents in lateral position, and they are significantly more reducing than the Co(I) complexes with phenyl and chloro substituents described in the literature.[2,15,117] Complex **4.6**, on the other hand, features phenanthrenequinone dioximato ligands, which are potentially redox non-innocent. Our analyses show that the ligands have a large effect on the redox potentials, but only a small effect on the geometry and the electronic state of the central Co ion. The three low-valent complexes described herein are all Co(I) complexes with a nearly ideal trigonal prismatic coordination environment.

Chapter 5

Clathrochelates as Stabilizers of DNA/RNA Three-Way Junctions

In collaboration with Dr José Luis Bila (former member of the Severin group) and Dr Joanna Zell and Dr David Monchaud (Université de Bourgogne, Dijon).

O.M.P. synthesized and characterized the compounds **5.1**, **5.5**, **5.6**. J.L.B synthesized and characterized the compounds **5.2**, **5.3**, **5.4**. J.Z. carried out the analyses with DNA.

5.1 Introduction

The most abundant branched structure in DNA is the three-way junction (TWJ).[118] A TWJ is a meeting point of three DNA strands, which creates a central triangular prism-shaped hydrophobic cavity (**Figure 5.1**).[119]

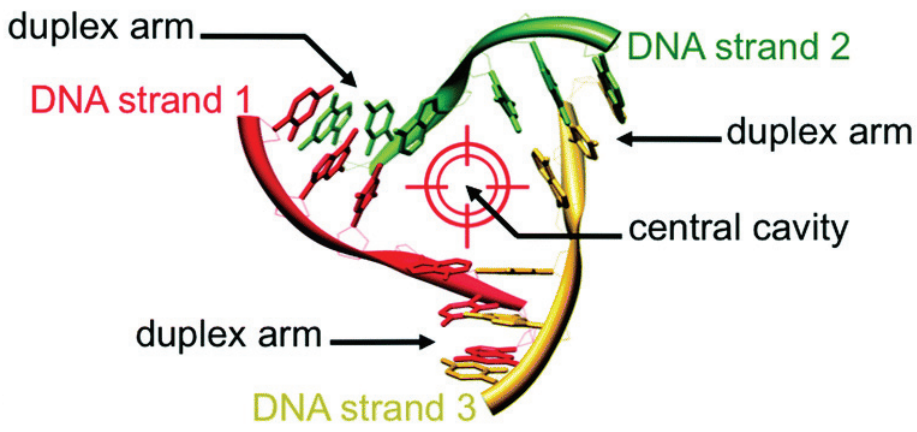

Figure 5.1 Schematic representation of the formation of DNA TWJ. Reproduced with permission from reference [120].

TWJs are involved in crucial biological processes such as DNA or RNA replication. Recently, specific TWJ-DNA recognition has attracted attention as a potential therapeutic solution to genetic disease.[121] Certain external molecules called synthetic agents can bind to DNA, and thus inhibit DNA interacting proteins or nucleic acids such as DNA repair enzymes, polymerases and topoisomerases.[122] Inducing DNA damage is the basis of most chemotherapy and radiotherapy treatments.[123] Consequently, it is crucial to improve specificity of DNA-binding agents, and targeting TWJ specifically in preference to duplexes[124] holds therapeutic potential. The development of synthetic agents that bind the central cavity of TWJ through non-covalent interactions thus requires study. Indeed, synthetic agents with a complementary size can interact with the TWJ's cavity. In 2006, Hannon and coworkers reported a highly specific molecular TWJ-DNA recognition by a metallosupramolecular $[Fe_2L_3]^{4+}$ helicate which is formed from three bis-pyridylimine organic strands (**Figure 5.2**).[125]

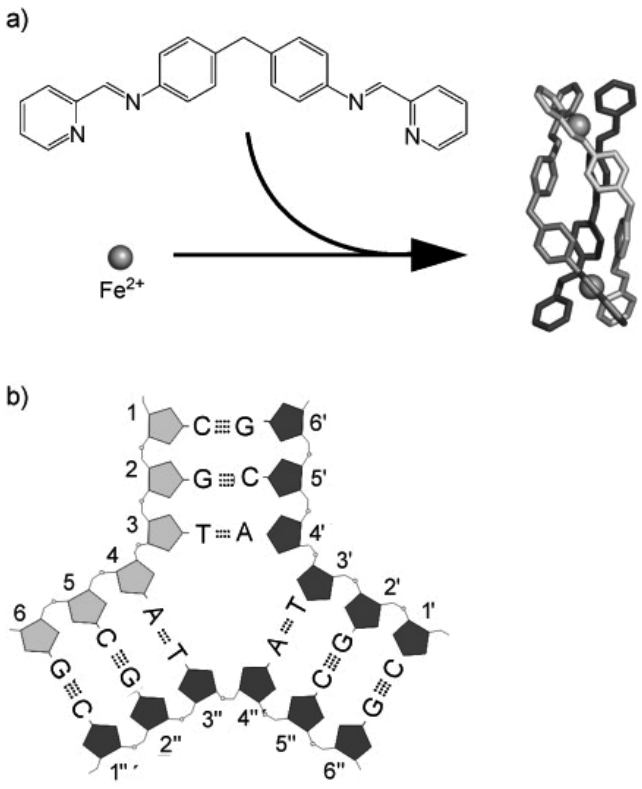

Figure 5.2 a) the $[Fe_2L_3]^{4+}$ helicate with ($L=C_{25}H_{20}N_4$) and Fe^{2+} ions represented as spheres b) TWJ of this study showing the DNA sequence used and the base-pair arrangement. Reproduced with permission from reference [125].

The authors reported that two major driving forces were acting in the DNA recognition. First, the threefold symmetry of the helicate matches with the threefold symmetry of the TWJ. Second, the presence of the phenyl rings at the center of the helicate has increased specific TWJ-DNA recognition by extensive π–stacking interactions.

The group of Chenoweth reported another example where they were able to achieve TWJ DNA recognition based on triptycenes as synthetic agents (**Figure 5.3a**).[126] They reported that triptycene-based scaffolds significantly stabilize RNA TWJ in a selective fashion over other junctions. The driving force to maximize the efficiency of specific recognition was the presence of an elongated three-fold non-planar π-system.[127] A clear stabilization over temperature of their triptycene-based TWJ system is illustrated in **Figure 5.3c**.

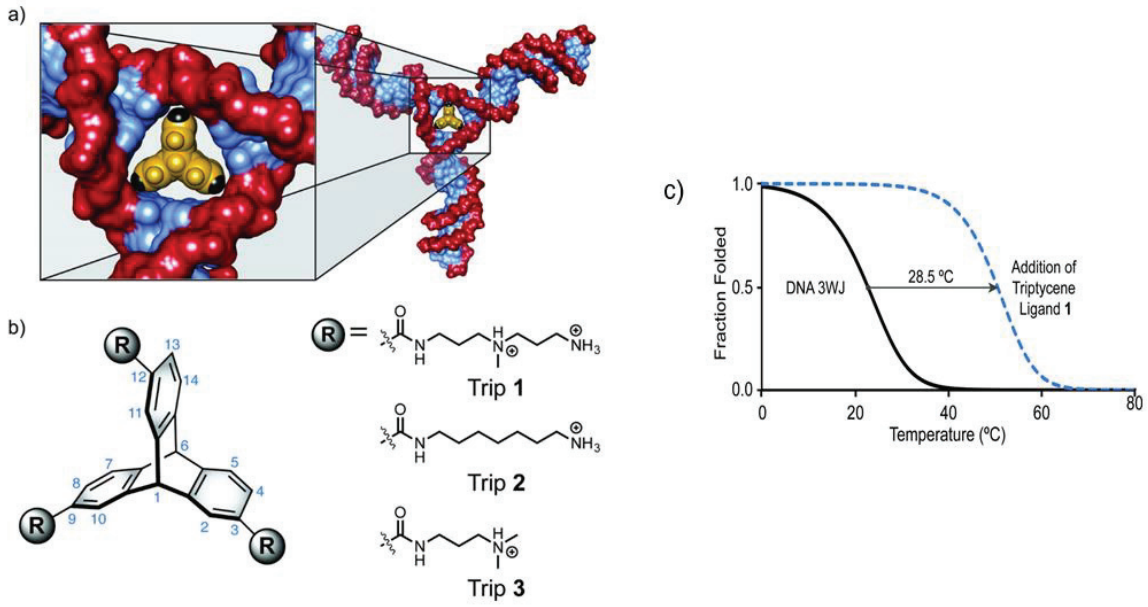

Figure 5.3 Triptycene scaffold for targeting nucleic acid TWJ a) Triptycene in the binding site of DNA TWJ. b) Structure of triptycene derivatives utilized for targeting nucleic acid junctions. c) FRET-melting assay with TWJ alone and triptycene-based TWJ. Reproduced with permission from reference [127].

Herein, we have tested the TWJ-binding capabilities of clathrochelates via their in vitro TWJ-stabilizing properties. For that purpose, we have designed clathrochelates with aromatic side chains to maximize π–stacking interactions with DNA. Moreover, it is worth noting that clathrochelates possess C_3 symmetry similar to triptycene molecules, which makes them suitable candidates as synthetic agents for TWJ recognition and stabilization.

5.2 Synthesis of Clathrochelate Complexes with Elongated π-Systems and Characterization

First, we focused our synthetic efforts on clathrochelates with phenanthrenequinone groups, which can be easily obtained from the corresponding phenanthrenequinone dioxime.

5.2.1 Phenanthrene-Based Iron Clathrochelates

Following the synthetic strategy described in Section 1.1, we have prepared clathrochelate complex **5.1** (**Scheme 5.1**) from phenanthrenequinone dioxime described in **Chapter 4**. For the one pot synthesis of **5.1**, we used commercially available 4-(bromomethyl)phenyl boronic acid. The bromo group was substituted with triethylamine afterwards. We hypothesized that the positively charged ammonium cation would improve the interaction of the clathrochelate with negatively charged DNA.

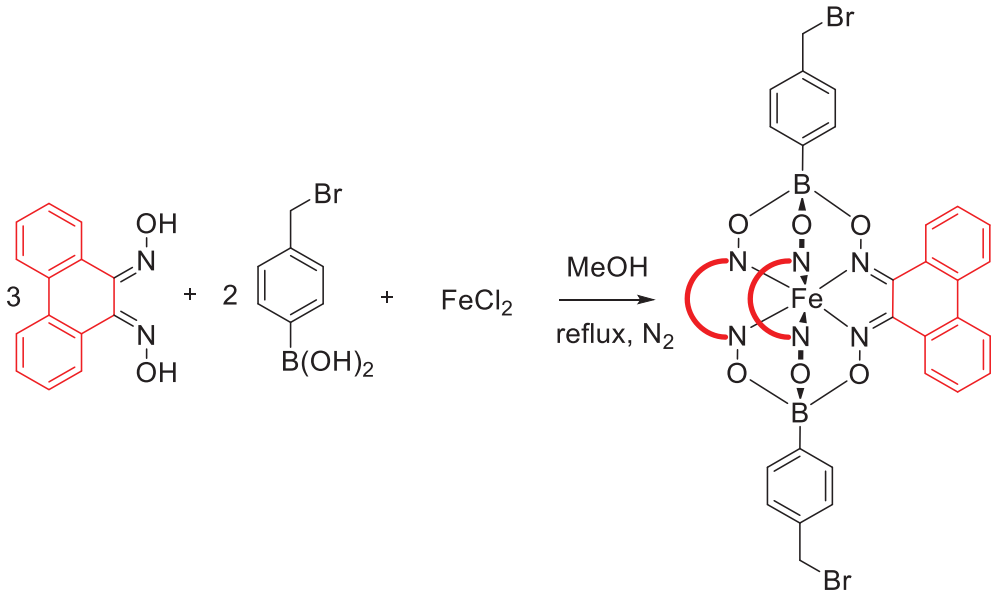

5.1 (48 %)

Scheme 5.1 Synthesis of clathrochelate complex **5.1**.

Purification by column chromatography was performed to obtain clathrochelate **5.1** as a pure purple powder in moderate yield. Synthetic details are given in **Chapter 8**.

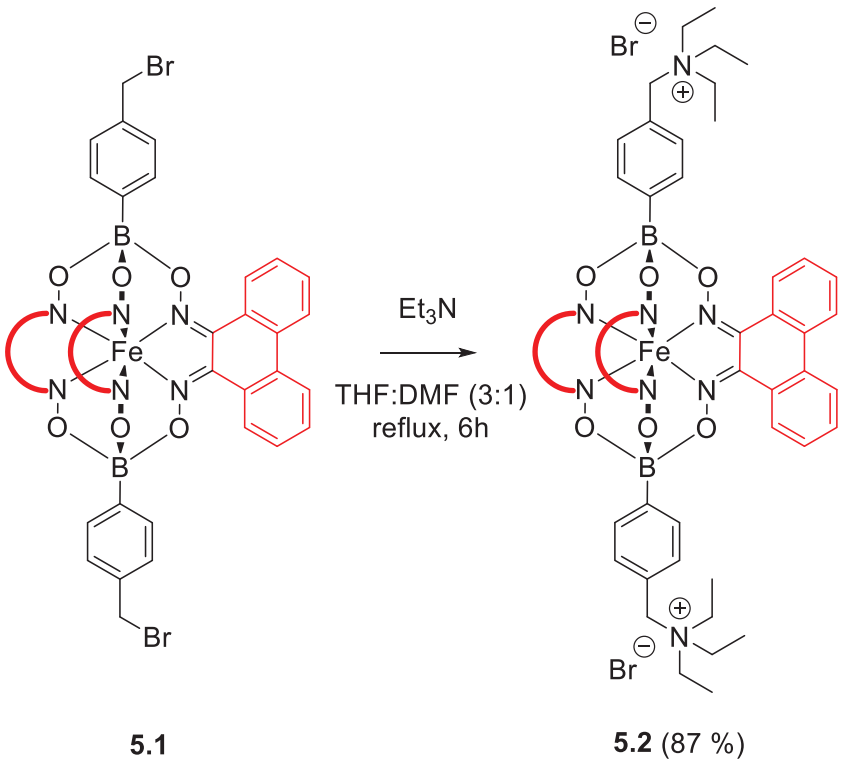

5.1 **5.2** (87 %)

Scheme 5.2 Synthesis of clathrochelate complex **5.2**.

This synthesis (**Scheme 5.2**) was performed by Dr José Bila. The compounds **5.1** and **5.2** were characterized by HRMS and NMR (Chapter 8). Despite several crystallization attempts , we were unable to isolate single-crystals of **5.1** and **5.2**.

5.2.1.1 Preliminary Attempts to Use Clathrochelates as Three-Way Junction Stabilizers

We first employed clathrochelate **5.1** to evaluate the potential of those complexes as stabilizers for TWJs. The in vitro analyses were performed by Dr Joanna Zell and Dr David Monchaud, from the University of Bourgogne, Dijon, France. In order to quantify the effect of the phenanthrenequinone π-systems, we used clathrochelates with non-aromatic side chains (**5.3** and **5.4, Figure 5.4**) for control experiments. The latter were synthesized by Dr José Bila following the same synthetic strategy used for **5.2**.

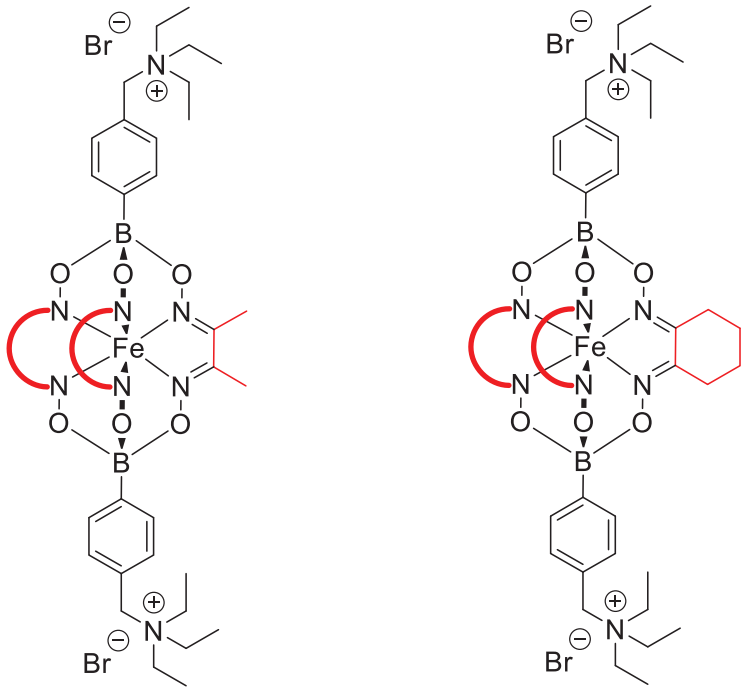

5.3 (96 %) **5.4** (83 %)

Figure 5.4 Clathrochelate complexes **5.3** and **5.4**.

In order to evaluate if the clathrochelates **5.2**-**5.4** are able to stabilize TWJs, a FRET-melting analysis was performed (**Figure 5.5**). A single-stranded TWJ-DNA oligonucleotide, labeled with two FRET partner fluorophores, was structured via heating cycles into a TWJ 3D structure. The FRET partners quench the fluorescent signal when the TWJ structure is formed (low temp.), and emit a fluorescent signal when the TWJ structure is melted and the FRET partners separate (high temp.).[128] The fluorescence of each system was measured and normalized: either TWJ alone (grey squares), or TWJ with clathrochelate **5.2** (20 eq.) (green crosses). The results show that the addition of clathrochelate **5.2** stabilizes the TWJ structure, since the melting temperature is increased from ≈40 °C to ≈60 °C (inflection point). It is worth noting that no significant stabilization was observed for the clathrochelates **5.3** and **5.4,** which lack the aromatic side chains. As a control to quantify the efficiency of this stabilization, we have used Tris-NP, a naphthalene trimer, one of the best known TWJ stabilizing synthetic agents.[127]

Secondly, a gel shift analysis was performed. Visualization was done under 302 nm after staining with a DNA dye SYBR blue (**Figure 5.6**). In this assay, three oligonucleotide strands are used to form an intermolecular TWJ. This assay thus tests the capability of the ligand to induce TWJ formation, rather than stabilization of a pre-formed TWJ. Unfortunately, this

analysis revealed that intermolecular TWJ were not formed in the presence of clathrochelate **5.2**, compared to Tris-NP, used as a TWJ formation positive control.

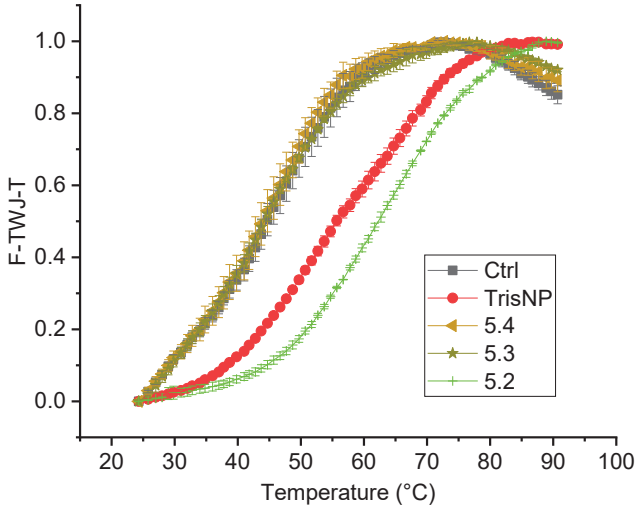

Figure 5.5 FRET-melting analysis. Normalized fluorescence (0 for intramolecular TWJ formation) function of temperature. Clathrochelates **5.2**-**5.4** used as synthetic agents. (20 eq. used in each experiment.) Tris-NP is a naphthalene trimer used as a positive control (20 eq.).

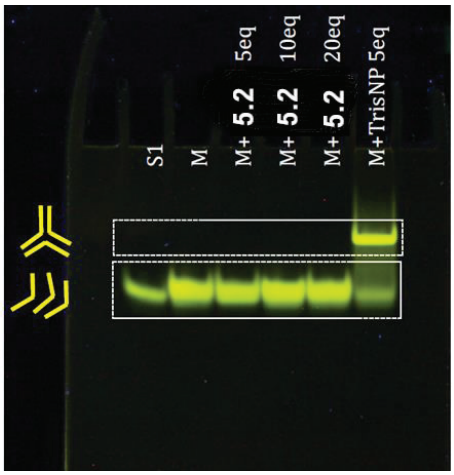

Figure 5.6 TWJ formation on a gel with controls: S1 as one DNA strand, M as mixed strands (S1+S2+S3). Clathrochelate **5.2** was used in 5, 10 or 20 equivalents. Visualization under 302 nm.

In summary, clathrochelate **5.2** was found to stabilize a pre-formed TWJ, but, unfortunately, they are ineffective in promoting the formation of TWJ-DNA. We hypothesized that an extension of the ligand π-system could be beneficial for the recognition process, and we have thus synthesized a pyrene-based clathrochelate. The results are described in the next section.

5.2.2 Pyrene-Based Iron Clathrochelates

Following the standard protocol, we have prepared clathrochelate complex **5.5** (**Scheme 5.3**) using pyrenequinone-dioxime. The latter was synthesized following a published procedure.[129]

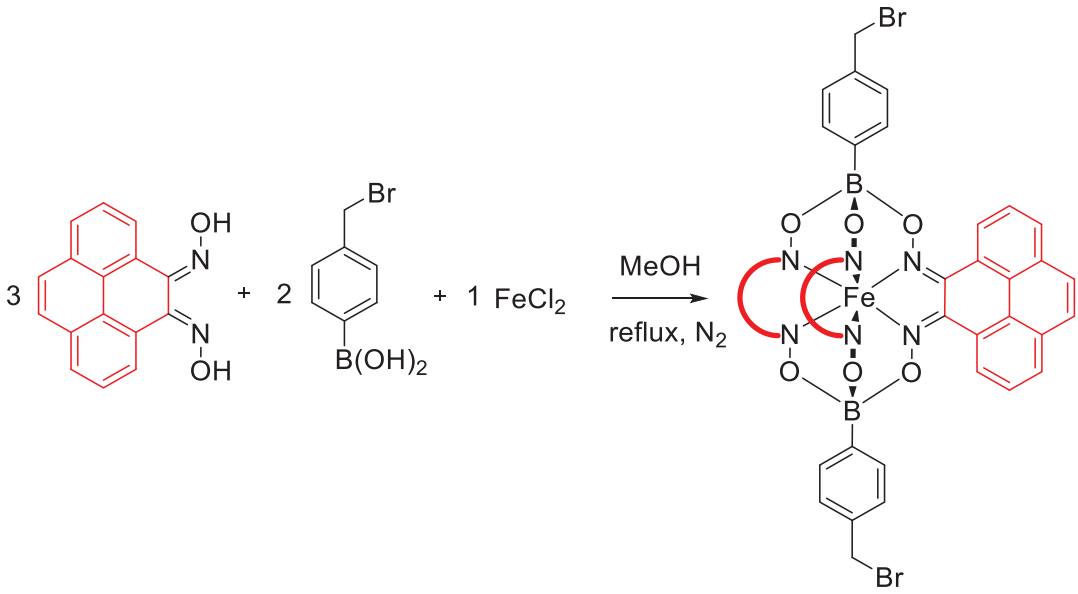

5.5

Scheme 5.3 Synthesis of clathrochelate complex **5.5**.

All attempts to purify clathrochelate **5.5** via column chromatography failed because of its low solubility. Attempts to prepare clathrochelate **5.6** from crude product **5.5** resulted in the formation of an insoluble precipitate. It is worth noting that a key pre-requesite for performing a DNA-TWJ stabilization analysis is the solubility of the respective synthetic agent in a DMSO/H_2O mixture. Therefore, further analyses were not performed.

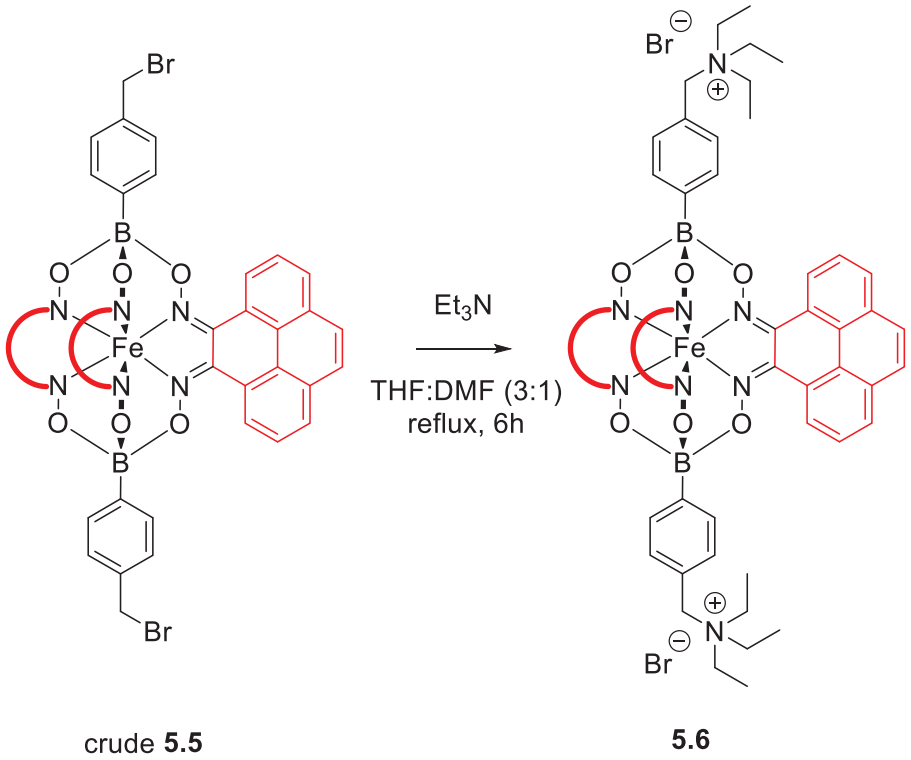

crude **5.5** **5.6**

Scheme 5.4 Attempted synthesis of clathrochelate complex **5.6**.

5.4 Outlook

In conclusion, we have found that phenanthrene-based clathrochelate **5.2** is able to stabilize TWJ-DNA in FRET-melting assays, but its presence was not sufficient to induce TWJ-DNA structure formation. Extended pyrene-based clathrochelate **5.6** is a promising candidate for efficient interaction with DNA, but, unfortunately, it was found to be insoluble. In view of the promising results obtained with **5.2**, further investigations with soluble versions of π-extended clathrochelates would be interesting to perform.

Chapter 6

Chiral Clathrochelates Based on Camphor-Dioximate Derivatives

O.M.P. synthesized and characterized the compounds, F.F.-T. and R.S. carried out the single crystal XRD analysis.

6.1 Introduction

Chiral coordination cages and chiral MOFs are interesting for enantioselective recognition, separation, and catalysis.[130,131] However, the synthesis of such systems can be challenging. One of the most feasible strategies to make chiral nanostructures is based on the direct use of building blocks with stereogenic centers. They can be either on the metal corner (vertice-directed) or on the ligand (edge- or face-directed) (**Figure 6.1**).

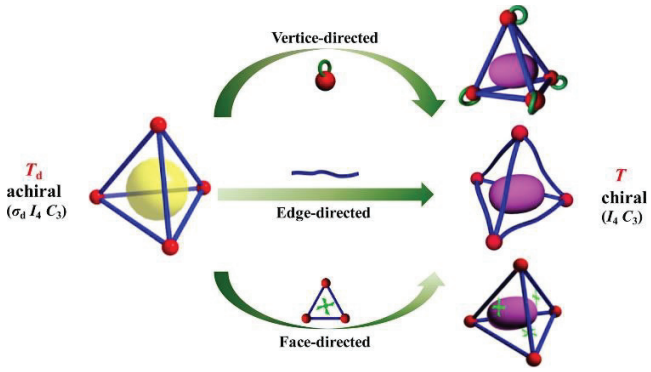

Figure 6.1 Representative spatial-direction strategies for constructing chiral coordination cages. Example illustrated with tetrahedral cages. Reproduced with permission from reference [130].

This strategy can be employed for the synthesis of coordination cages or polymeric networks. In order to perform enantioselective recognition of racemic mixtures of chiral guests, we have designed and synthesized chiral clathrochelate using chiral dioximate groups. They have been further investigated as chiral edge-directed building blocks in coordination cages and polymer networks.

6.1.1 Synthesis of the Camphor-Dioxime and Characterization

Following the synthetic strategy described in Chapter 5, we were able to prepare camphor-dioxime **6.1** (**Scheme 6.1**). It was synthesized from commercially available camphor-quinone in combination with hydroxylamine hydrochloride. We found that it is crucial to add a small amount of water in ethanol in order to promote the reaction. The camphor-dioxime was obtained in moderate yield after separation of side products.

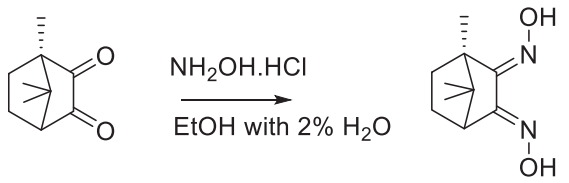

6.1 (47%)

Scheme 6.1 Synthesis of camphor-dioxime **6.1**.

^{1}H-NMR analysis of crude product **6.1** revealed a mixture of three products (**Figure 6.2)**. Two of these products were the two mono-oxime isomers **6.2** and **6.3** resulting from incomplete transformation of the camphor-quinone into camphor-dioxime. They were distinguishable by depicting a characteristic proton, highlighted in red in **Figure 6.2**. Each mono-oxime was separated by chromatography with CH_2Cl_2 using a gradient of 2% to 5% methanol. ^{1}H NMR spectra of each mono-oxime is presented in Chapter 8. The third product resulting from the synthesis was the desired camphor-dioxime **6.1**, which was distinguishable by analysis of the same characteristic NMR chemical shift of tertiary C-H proton. Interestingly, *syn* and *anti* isomers of dioxime **6.1** could be detected by NMR (**Figure 6.2**). Purification of the isomers was achieved by chromatographic separation with 10% methanol in CH_2Cl_2 (**Figure 6.3** for **6.1a**

and **Figure 6.4** for **6.1b**). For compound **6.1a**, ^{1}H NMR shows a remaining impurity (<5%) which is not attributed to **6.1b**, **6.2** or **6.3**.

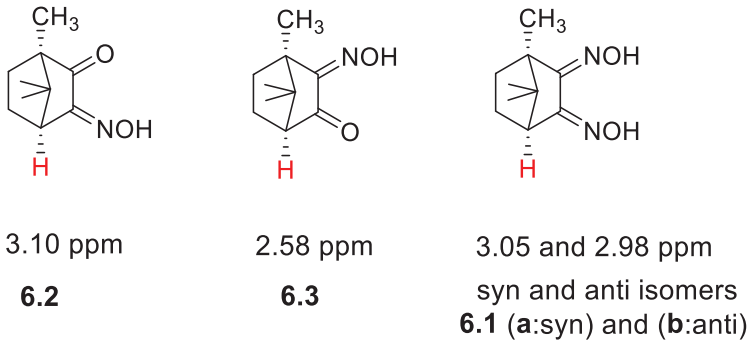

Figure 6.2 Mono-oximes **6.2** and **6.3** and dioxime **6.1** with syn and anti isomers.

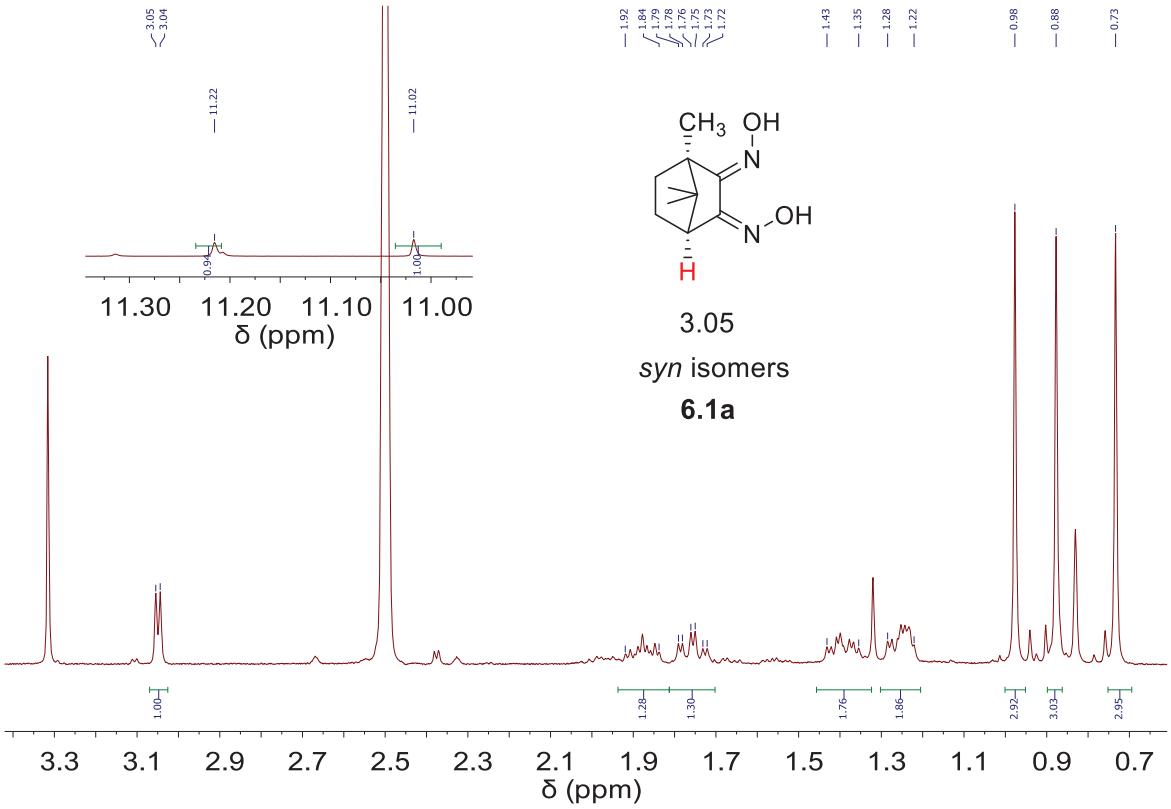

Figure 6.3 ^{1}H NMR spectra of dioxime **6.1a** (DMSO-d_6, 400 MHz)

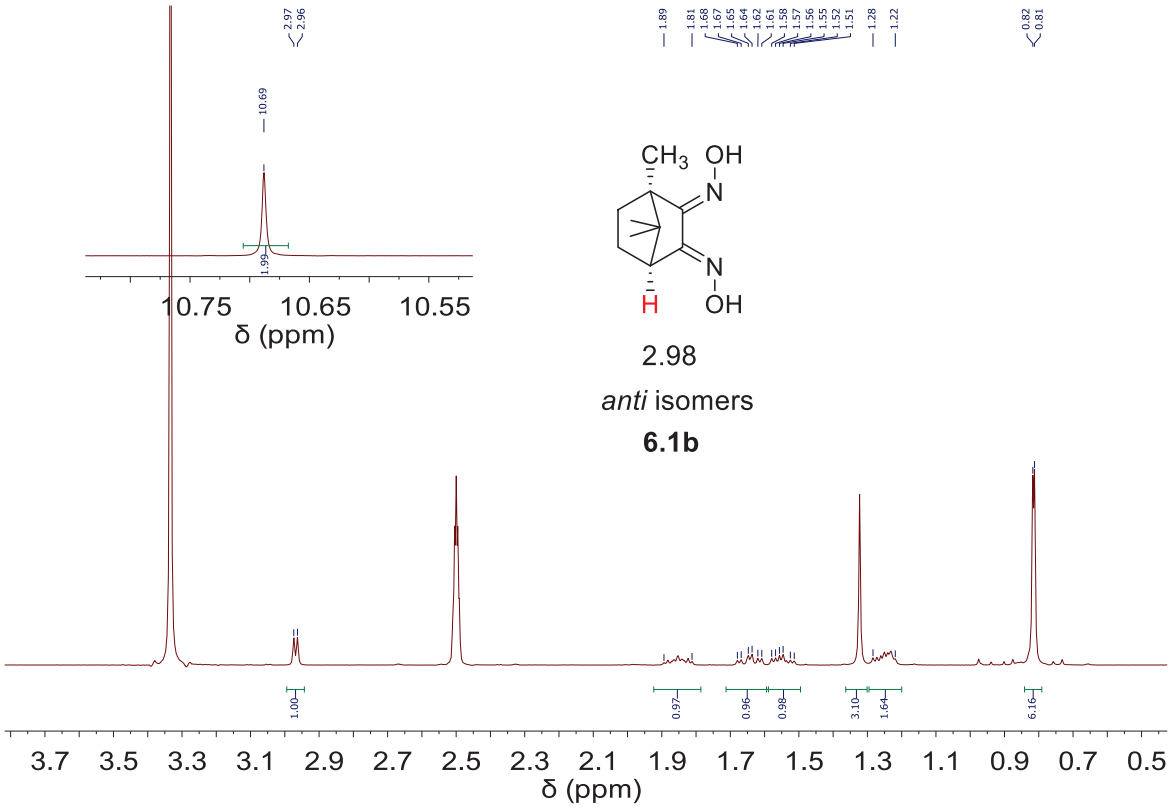

Figure 6.4 ^{1}H NMR spectra of dioxime **6.1b** (DMSO-d_6, 400 MHz)

Furthermore, we have characterized **6.1b** by single crystal X-ray diffraction. The crystals were obtained by slow evaporation of a DCM solution of purified **6.1b** (**Figure 6.5**).

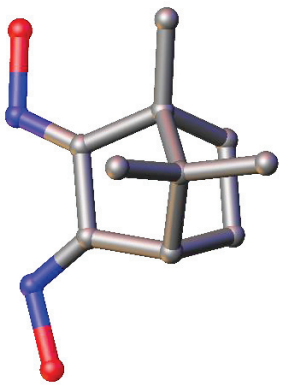

Figure 6.5 Molecular structure of **6.1b** in the crystal. H atoms and solvent are omitted for clarity. Color coding: C: grey, O: red, N: blue.

6.1.2 Synthesis and Characterization of Chiral Clathrochelates

Following the synthetic strategy described in previous chapters, we synthesized chiral clathrochelates **6.4-6.6** based on camphor-dioxime **6.1b** and commercially available 3,5-dibromophenyl boronic acid, 3-pyridylphenyl boronic acid or 4-carboxyphenyl boronic acid.

It has been previously reported, that in the case of nonsymmetrical α-dioximes, a mixture of *fac*- and *mer*-isomers of the corresponding clathrochelates are obtained in a statistical 1:3 ratio (*fac:mer*) (**Figure 6.6**).[2b] We obtained the corresponding clathrochelate in the similar statistical distribution, as we expected. Indeed, by a close analysis of the ^{1}H NMR spectra, we observed twelve peaks for –CH_3 protons, with 3 peaks for the *fac* isomer and 9 others for the *mer* isomer. The ratio of integrals showed a 1:3 statistical distribution.

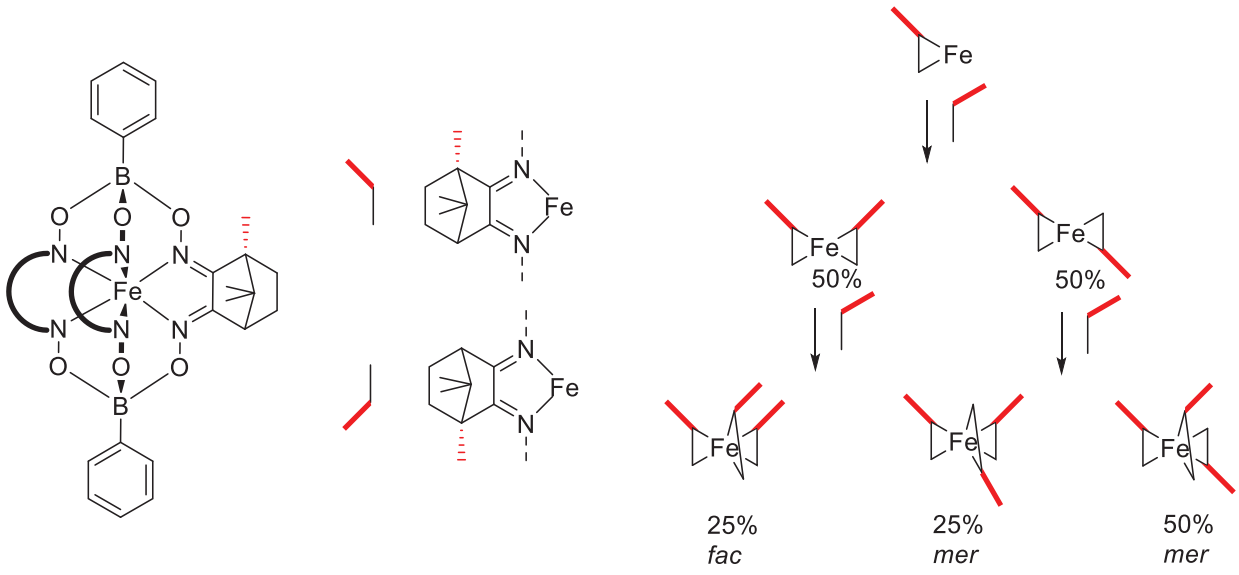

Figure 6.6 Statistical ratio (*fac:mer* obtained during synthesis of clathrochelates with non symmetrical α-dioxime.

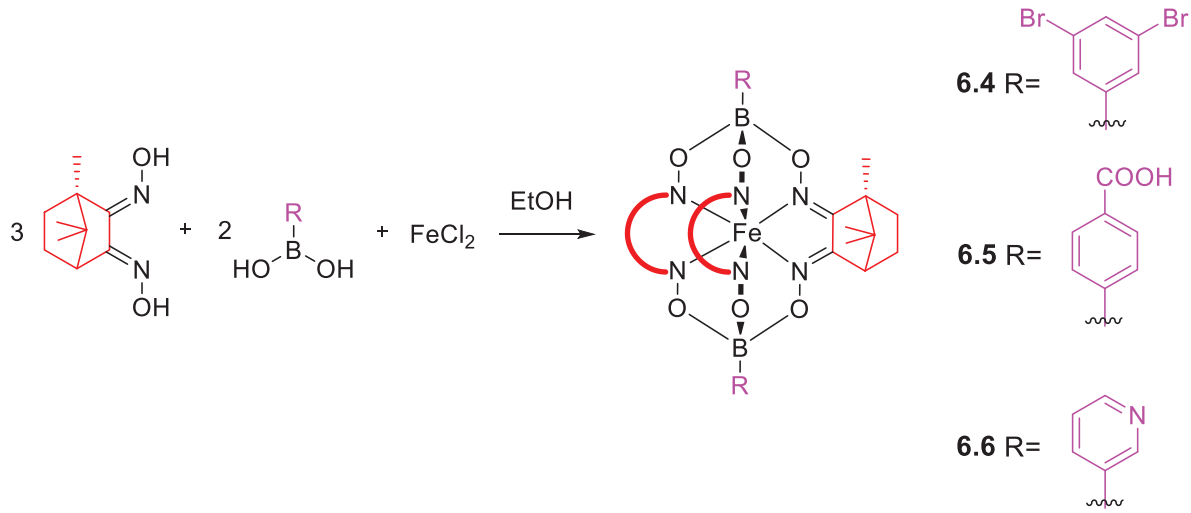

Scheme 6.2 Synthesis of camphor-dioximate clathrochelates **6.4-6.6**.

Despite several crystallization attempts , we were not able to isolate single-crystals for either **6.4**, **6.5** or **6.6**. The HRMS data were in line with the expected structures (experimental details in Chapter 8). The NMR data were unfortunately difficult to analyze due to numerous peak overlaps. Notwithstanding the poor analytical characterization, we are confident that clathrochelates **6.4-6.6** had formed, since the standard synthetic procedure seems to be quite versatile (Section1.1). Clathrochelates **6.4** and **6.6** showed good solubility in organic solvents such as DCM, but clathrochelate **6.5** was not soluble enough to be characterized by NMR. We failed to perform separation of the isomers by a column chromatography in CH_2Cl_2, due to their similar polarity.

6.2 Attempted Applications

In order to build chiral coordination cages, we have used clathrochelate **6.6** with terminal 3-pyridyl groups.

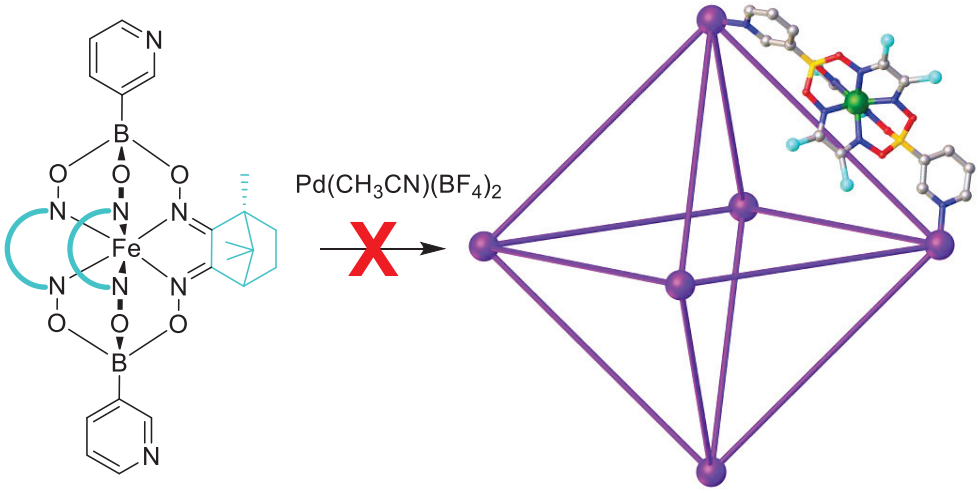

6.6

Scheme 6.3 Attempted synthesis of a coordination cage by reaction of clathrochelate **6.6** with $[Pd(CH_3CN)(BF_4)_2]$.

We performed the reaction of clathrochelate **6.6** with $[Pd(CH_3CN)(BF_4)_2]$ in CD_3CN for 24 h at 50°C, and reaction progress was monitored by ^1H NMR. However, no evidence of a cage formation was observed by ^1H NMR, DOSY NMR or HR-MS. We observed no proton shifts as expected for coordination with palladium. Moreover, after 24 h, the solution became colorless. We assume that a decomposition of the clathrochelate ligand had occurred.

We have also investigated the possibility to obtain polymer networks using chiral clathrochelate **6.4**. Recently, clathrochelate-based polymer networks have been described by Severin and coworkers.[33] The networks were formed by Pd-catalyzed polycross-coupling reactions of polybrominated clathrochelate complexes (for an example, see **Scheme 1.10** in Chapter 1). The same strategy was tested by a coworker, Dr. José Bila, with clathrochelate **6.4**.

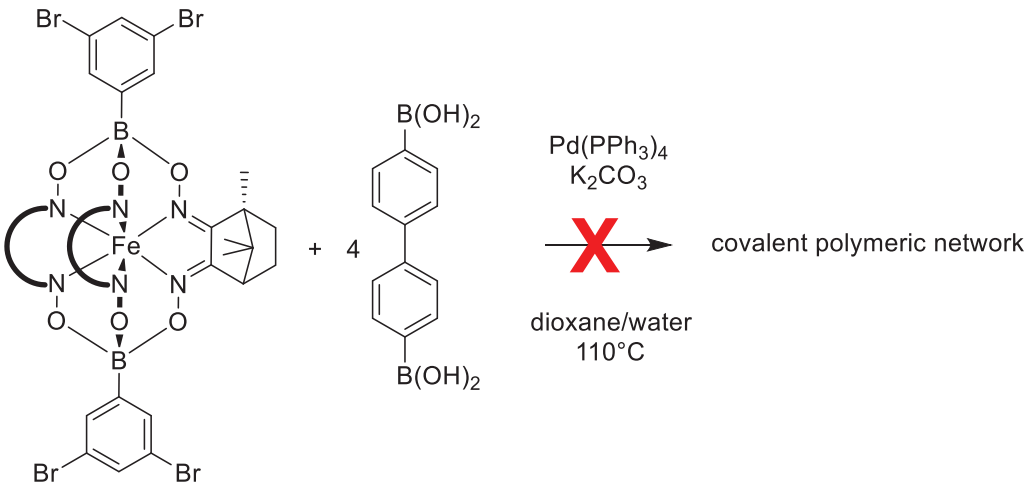

6.4

Scheme 6.4 Attempted synthesis of a polymeric network by a Pd-catalyzed poly-crosscoupling reaction. *The reaction was carried out by by Dr. José Bila*.

Unfortunately, decomposition of the clathrochelate was observed..

In conclusion, we have synthesized three chiral clathrochelates based on camphor-dioxime ligands. Unfortunately, due to an unusually poor stability in solution, we were unable to utilize them for the synthesis of a coordination cage or a polymeric network. Chiral clathrochelates remain promising candidates for generating chiral nanostructures. Further investigations are needed to increase their overall stability.

Chapter 7

Conclusion

In this thesis, we report the syntheses of novel boronate ester-capped clathrochelate complexes and their applications in supramolecular chemistry, materials science, and chemical biology. Clathrochelates are easy-to-access complexes. Their versatility arises either from the capping groups (boronate esters) or from the dioximato ligands. The solubility, the reactivity or the redox behavior can be tuned easily via modification of the surrounding functional groups.

Chapter 2 has evidenced the facile synthesis of long carboxylic acid-decorated Fe(II) dinuclear clathrochelate complexes, up to 3 nm. Furthermore, carboxylic acid-decorated bent, dinuclear clathrochelates were successfully incorporated into a Cu_4L_4-type coordination cage and into a 2-dimensional metal-organic framework (MOF).

In Chapter 3, we have shown the nearly quantitative incorporation of 4-pyridyl-decorated clathrochelate metalloligands into pillared paddle-wheel metal-organic frameworks by using the solvent-assisted ligand exchange technique. We concluded that the strong basicity of 4-pyridyl-decorated clathrochelates is the driving force for the exchange go to completion.

Chapter 4 was dedicated to novel low-valent cobalt clathrochelates. A first example of a Co(II) clathrochelate with a phenanthrenequinone dioximato groups is described. Chemical reductions of cobalt clathrochelates are reported, and ligand effects are investigated by crystallography.

Preliminary studies have shown that clathrochelates are able to stabilize three-way junctions (TWJ) in DNA. Chapter 5 describes the syntheses of clathrochelates with ligands containing pyrene-based, elongated π–systems. Unfortunately, these complexes were found to display poor solubility, hampering biological test.

In Chapter 6, the synthesis of chiral clathrochelate complexes from a camphor-derived dioxime ligand is described. Potential applications of these new clathrochelates in supramolecular chemistry and materials science were investigated. Unfortunately, facile decomposition of the

chiral clathrochelates was observed. Alternative synthetic strategies are needed to increase the stability of chiral clathrochelates.

To conclude, our results show that boronate ester-capped clathrochelate complexes are highly versatile. They are suitable building blocks for a wide range of applications, as demonstrated by the synthesis a large M_4L_4-type coordination cage, and by the preparation of clathrochelate-containing MOFs. Promising first results indicate that clathrochelates could find applications as stabilizers for TWJs.

Chapter 8

Experimental Details

8.1 General

All commercially available chemicals and solvents were used without further purification. Reactions were carried out under an atmosphere of N_2 using standard Schlenk techniques. Routine ^{1}H NMR and ^{13}C NMR spectra were obtained on a Bruker Avance III Spectrometer equipped with a 5 mm BBFO-Plus$_z$ probe and at 298 K. ^{1}H and ^{13}C shifts are reported in parts per million (ppm δ) referenced to the internal solvent.

Electrospray-ionisation MS data were acquired on a Q-Tof Ultima mass spectrometer.

Thermogravimetric analyses (TGA) were performed on a TGA 4000 from Perkin Elmer. Samples were placed in crucibles and heated from 30 °C to 700 °C at 10 °C/minute under N_2.

Powder X-ray diffraction (PXRD) patterns were recorded at room temperature with a Bruker D8 Discover diffractometer equipped with a LynxEye XE detector using non-monochromated Cu-radiation. Due to the sample nature, MOFs **3.3a, 3.3b, 3.3c**, **3.3d**, **3.5** and **3.7** were measured in transmission (Debye-Scherrer, 1.0 mm borosilicate capillary, spun at 30 rpm). Data are shown as measured. The samples were loaded without grinding (lack of mechanical stability of the crystal structure) into borosilicate glass capillaries of 1 mm diameter, together with the mother liquor, to prevent collapse during measurement. Capillaries were spun during measurement.

Dinitrogen (77K), carbon dioxide (273K) and hydrogen (77K) sorption measurements were performed on a Quantochrome Autosorb iQ analyzer.

Size exclusion chromatography was performed in CH_2Cl_2 (HPLC grade) with Bio-Beads SX-3 (200g).
Elemental analysis (C, H, N) were obtained with a Carlo Elba model 1106 microanalyzer.

Cyclic voltammetry (CV) experiments were performed using a SP150 potentiostat (BioLogic). All experiments were carried out under an atmosphere of dinitrogen in degassed and anhydrous dichloromethane solution containing $TBAPF_6$ (0.1 M) at a scan rate of 50 $mV \cdot s^{-1}$ up to 250 $mV \cdot s^{-1}$. The setup consisted of a platinum working electrode (surface area = 0.06 cm2), a platinum wire as the counter electrode, and a silver wire immersed in a 3 M NaCl solution. The recorded voltammograms have been referenced to the internal standard Fc/Fc+ (ferrocene/ferrocenium).

UV-Vis spectra were recorded on a Cary 60 Spectrometer (Agilent Technologies). Quartz Suprasil cuvettes from Helma Analytics (10 x 10 mm) were used for solution spectrophotometric measurements.

8.2 Experimental Procedures

8.2.1 Experimental Procedures from Chapter 2

Synthesis of 2.1-2.6:

Complex **2.1**: 1,4-diphenylboronic acid (100 mg, 0.60 mmol) and 4-ethoxycarbonylphenylboronic (469 mg, 2.42 mmol) were suspended in MeOH (75 mL) and heated under reflux for 30 min. A solution of nioxime (515 mg, 3.62 mmol) and anhydrous $FeCl_2$ (152 mg, 1.28 mmol) in MeOH (50 mL) was added, and the mixture was heated under reflux for 12 h, resulting in the formation of an orange suspension. After cooling to RT, the solid was isolated by centrifugation and washed with MeOH (50 mL) and Et_2O (25 mL). The product was purified by size-exclusion chromatography (CH_2Cl_2) to give ligand **2.1** as an orange powder. Yield: 115 mg, 14%. **^{1}H NMR** (600 MHz, CD_2Cl_2) δ 7.96 (d, J = 8.1 Hz, 4H), 7.73 (d, J = 8.1 Hz, 4H), 7.59 (s, 4H), 4.34 (q, J = 7.1 Hz, 4H), 2.92 (d, J = 13.9 Hz, 24H), 1.81 (s, 24H), 1.38 (t, J = 7.1 Hz, 6H). **^{13}C NMR** (151 MHz, CD_2Cl_2) δ 167.50, 152.65, 152.38, 132.16, 131.14, 130.33, 128.72, 61.21, 26.75, 22.15, 14.70 (C-B was not detected). **HRMS-ESI** *m/z* calculated for $C_{60}H_{71}B_4Fe_2N_{12}O_{16}$ $[M+H]^+$ 1371.4176, found 1371.4186.

Complex **2.2**: 1,3-diphenylboronic acid (100 mg, 0.60 mmol) and 4-ethoxycarbonylphenylboronic (469 mg, 2.42 mmol) were suspended in MeOH (60 mL) and heated under reflux for 20 min. A solution of nioxime (515 mg, 3.62 mmol) and anhydrous $FeCl_2$

(152 mg, 1.28 mmol) in MeOH (50 mL) was added, and the mixture was heated under reflux for 12 h, resulting in the formation of an orange suspension. After cooling to RT, the solid was isolated by centrifugation and washed with MeOH (50 mL) and Et_2O (20 mL). The product was purified by size-exclusion chromatography (CH_2Cl_2) to give ligand **2.2** as an orange powder. Yield: 156 mg, 19%. **^{1}H NMR** (400 MHz, CD_2Cl_2) δ 8.03-7.97 (m, 5H), 7.78 (d, J = 7.9 Hz, 4H), 7.63 (dd, J = 7.3, 1.4 Hz, 2H), 7.32 (t, J = 7.4 Hz, 1H), 4.39 (q, J = 7.2 Hz, 4H), 2.99-2.96 (m, 24H), 1.86 (s, 24H), 1.43 (t, J = 7.1 Hz, 6H). **^{13}C NMR** (151 MHz, CD_2Cl_2) δ 167.51, 152.60, 152.27, 135.65, 132.16, 131.69, 130.30, 128.71, 126.78, 61.23, 26.76, 26.72, 22.16, 22.13 (C-B was not detected). **HRMS-ESI** *m/z* calculated for $C_{60}H_{71}B_4Fe_2N_{12}O_{16}$ $[M+H]^+$ 1371.4176, found 1371.4244.

Complex **2.3**: 1,3-diphenylboronic acid (100 mg, 0.60 mmol) and 3-ethoxycarbonylphenylboronic (469 mg, 2.42 mmol) were suspended in MeOH (50 mL) and heated under reflux for 20 min. A solution of nioxime (515 mg, 3.62 mmol) and anhydrous $FeCl_2$ (152 mg, 1.28 mmol) in MeOH (50 mL) was added, and the mixture was heated under reflux for 12 h, resulting in the formation of an orange suspension. After cooling to RT, the solid was isolated by centrifugation and washed with MeOH (25 mL) and Et_2O (10 mL). The product was purified by size-exclusion chromatography (CH_2Cl_2) to give ligand **2.3** as an orange powder. Yield: 222 mg, 27%. **^{1}H NMR** (400 MHz, CD_2Cl_2) δ 8.30 (s, 2H), 7.97 (d, J = 8.4 Hz, 3H), 7.88 (d, J = 7.3 Hz, 2H), 7.60 (d, J = 7.3 Hz, 2H), 7.41 (t, J = 7.5 Hz, 2H), 7.28 (t, J = 7.3 Hz, 1H), 4.36 (q, J = 7.1 Hz, 4H), 2.94 (s, 24H), 1.82 (s, 24H), 1.39 (t, J = 7.1 Hz, 6H). **^{13}C NMR** (101 MHz, $CDCl_3$) δ 167.41, 151.72, 151.31, 141.28 (br, C-B), 138.89 (br, C-B), 136.28, 135.23, 132.94, 131.24, 129.20, 128.83, 127.19, 126.16, 60.49, 26.18, 26.12, 21.55, 21.52, 14.35. **HRMS-ESI**: *m/z* calculated for $C_{60}H_{71}B_4Fe_2N_{12}O_{16}$ $[M+H]^+$ 1371.4176, found 1371.4237.

Complex **2.4**: Complex **2.1** (20 mg, 14.6 µmol) and NaOH (1 M, 1.5 mL) were added to a 100 mL RBF, followed by THF (5.4 mL), CH_2Cl_2 (5.4 mL) and MeOH (10.8 mL). The resulting solution was stirred and heated at 60 °C for 12 h. After cooling to RT, HCl (1 M) was until a neutral pH was reached. The red-orange solid was isolated by centrifugation, washed with MeOH (25 mL) and Et_2O (10 mL), and dried under vacuum to give **2.4** in the form of an orange-red powder. Yield: 12.5 mg, 65%. **^{1}H NMR** (400 MHz, DMSO-d_6) δ 12.77 (broad s, 1H), 7.88 (d, J = 8.0 Hz, 4H), 7.68 (d, J = 8.0 Hz, 4H), 7.50 (s, 4H), 2.84 (s, 24H), 1.75 (s, 24H). **^{13}C NMR** (151 MHz, DMSO-d_6) δ 152.23, 151.89, 131.62, 130.39, 128.06, 25.87, 20.86, (C-CO_2H, C-CO_2H and C-B

were not detected). **HRMS-ESI** *m/z* calculated for $C_{56}H_{63}B_4Fe_2N_{12}O_{16}$ $[M+H]^+$ 1315.3550, found 1315.3611.

Complex **2.5**: Complex **2.2** (20 mg, 14.6 µmol) and NaOH (1 M, 1.5 mL) were added to a 100 mL RBF, followed by THF (8.1 mL), CH_2Cl_2 (2.7 mL) and MeOH (10.8 mL). The resulting solution was stirred and heated at 60 °C for 12 h. After cooling to RT, HCl (1 M) was until a neutral pH was reached. The red-orange solid was isolated by centrifugation, washed with MeOH (25 mL) and Et_2O (10 mL), and dried under vacuum to give **2.5** in the form of an orange-red powder. Yield: 11.9 mg, 62%. **^{1}H NMR** (600 MHz, DMSO-d_6) δ 7.94 (s, 1H), 7.88 (d, *J* = 8.1 Hz, 4H), 7.69 (d, *J* = 8.1 Hz, 4H), 7.49-7.43 (m, 2H), 7.20 (t, *J* = 7.3 Hz, 1H), 2.85 (broad s, 24H), 1.75 (s, 24H). **^{13}C NMR** (151 MHz, DMSO-d_6) *δ* 167.84, 152.26, 151.87, 135.42, 131.65, 130.92, 129.89, 128.09, 125.84, 25.94, 25.87, 20.91, 20.88 (C-B was not detected). **HRMS-ESI** *m/z* calculated for $C_{56}H_{63}B_4Fe_2N_{12}O_{16}$ $[M+H]^+$ 1315.3550, found 1315.3595

Complex **2.6**: Complex **2.3** (20 mg, 14.6 µmol) and NaOH (1 M, 1.5 mL) were added to a 100 mL RBF, followed by THF (5.4 mL), CH_2Cl_2 (5.4 mL) and MeOH (10.8 mL). The resulting solution was stirred and heated at 60 °C for 2 h. After cooling to RT, HCl (1 M) was until a neutral pH was reached. The red-orange solid was isolated by centrifugation, washed with MeOH (25 mL) and Et_2O (10 mL), and dried under vacuum to give **2.6** in the form of an orange-red powder. Yield: 16.3 mg, 85%. **^{1}H NMR** (400 MHz, DMSO-d_6) *δ* 12.72 (broad s, 1H), 8.18 (s, 2H), 7.94 (s, 1H), 7.87 (d, *J* = 7.6 Hz, 2H), 7.80 (d, *J* = 7.2 Hz, 2H), 7.47 (d, *J* = 7.3 Hz, 2H), 7.42 (t, *J* = 7.5 Hz, 2H), 7.19 (t, *J* = 7.3 Hz, 1H), 2.85 (s, 24H), 1.75 (s, 24H). **^{13}C NMR** (151 MHz, DMSO-d_6) *δ* 168.07, 152.17, 151.83, 136.04, 135.41, 132.55, 130.87, 129.57, 128.63, 127.34, 125.80, 25.92, 25.86, 20.90, 20.87 (C-B was not detected). **HRMS-ESI** *m/z* calculated for $C_{56}H_{61}B_4Fe_2N_{12}O_{16}$ $[M-H]^+$ 1313.3435, found 1313.3732.

Synthesis of cage 2.7: Complex **2.6** (7.30 mg, 5.55 µmol) and $Cu(NO_3)_2(H_2O)_3$ (1.33 mg, 5.55 µmol) were mixed in DMF (1.2 mL) in a 10mL vial. The resulting mixture was layered with acetone (1 mL) to give suitable crystals for diffraction analysis within 2 days. The product was isolated as red-orange plates. DMF was taken off from the vial and 2.5 mL of Et_2O was added to the crystals. Vigorous shaking was done to let solvent exchange then the vial was a left for 30 minutes with stirring at room temperature. Then the Et_2O layer was taken off and the

resulting crystalline material was drying 2h under vacuum with a diffusion pump and 11.55 mg of cage **2.7** was obtained.

X-ray diffraction analysis was performed with red-orange crystals taken from another batch following the same conditions before the drying step.

Synthesis of polymer 2.8: Complex **2.6** (18.1 mg, 13.7 μmol) and $Zn(NO_3)_2(H_2O)_6$ (4.1 mg, 13.7 μmol) were mixed in DMA (3 mL) in a 10mL vial. The resulting mixture was left for evaporation to give suitable crystals for diffraction analysis within 5 days. The product was isolated as red-orange plates suitable for X-ray diffraction analysis.

Selected NMR spectra

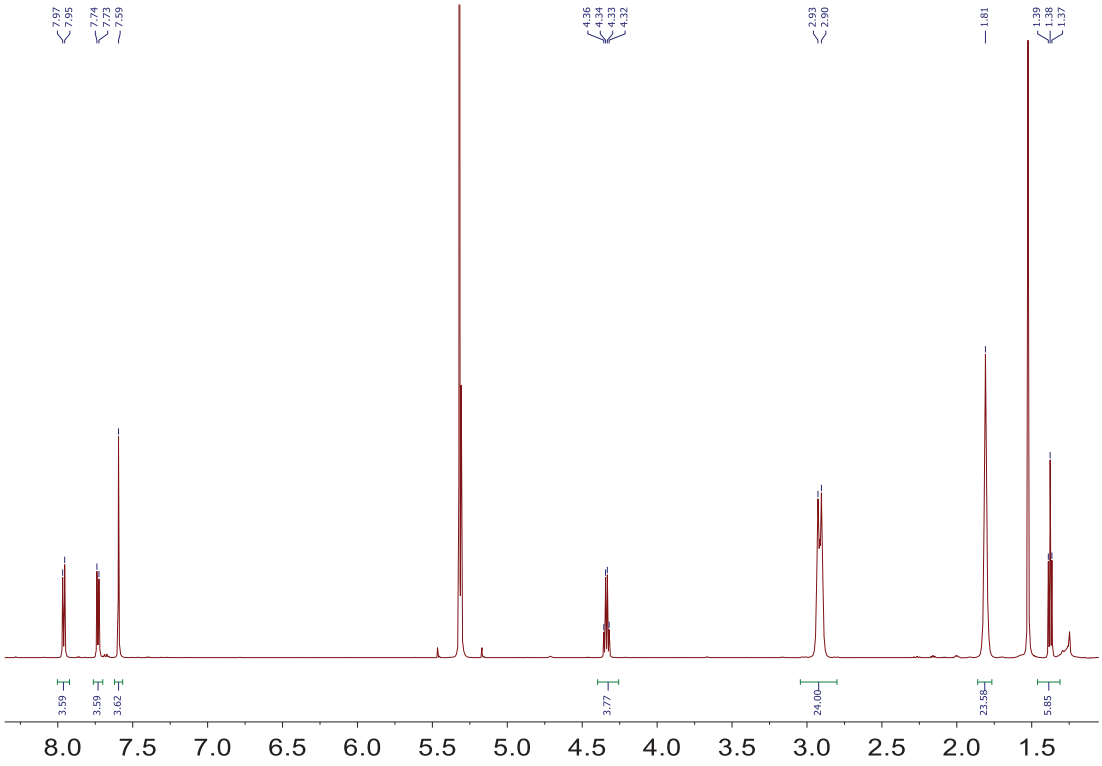

Figure 8.2.1 ^{1}H NMR spectrum of **2.1** in CD_2Cl_2.

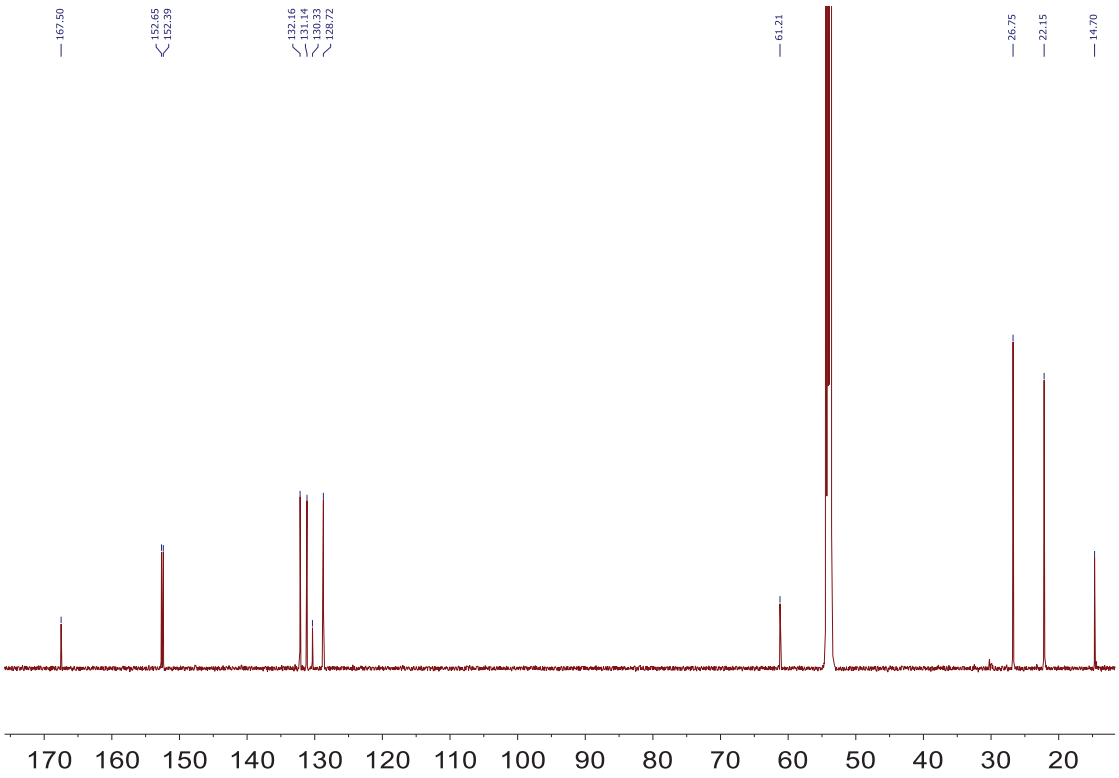

Figure 8.2.2 ^{13}C NMR spectrum of ligand **2.1** in CD_2Cl_2.

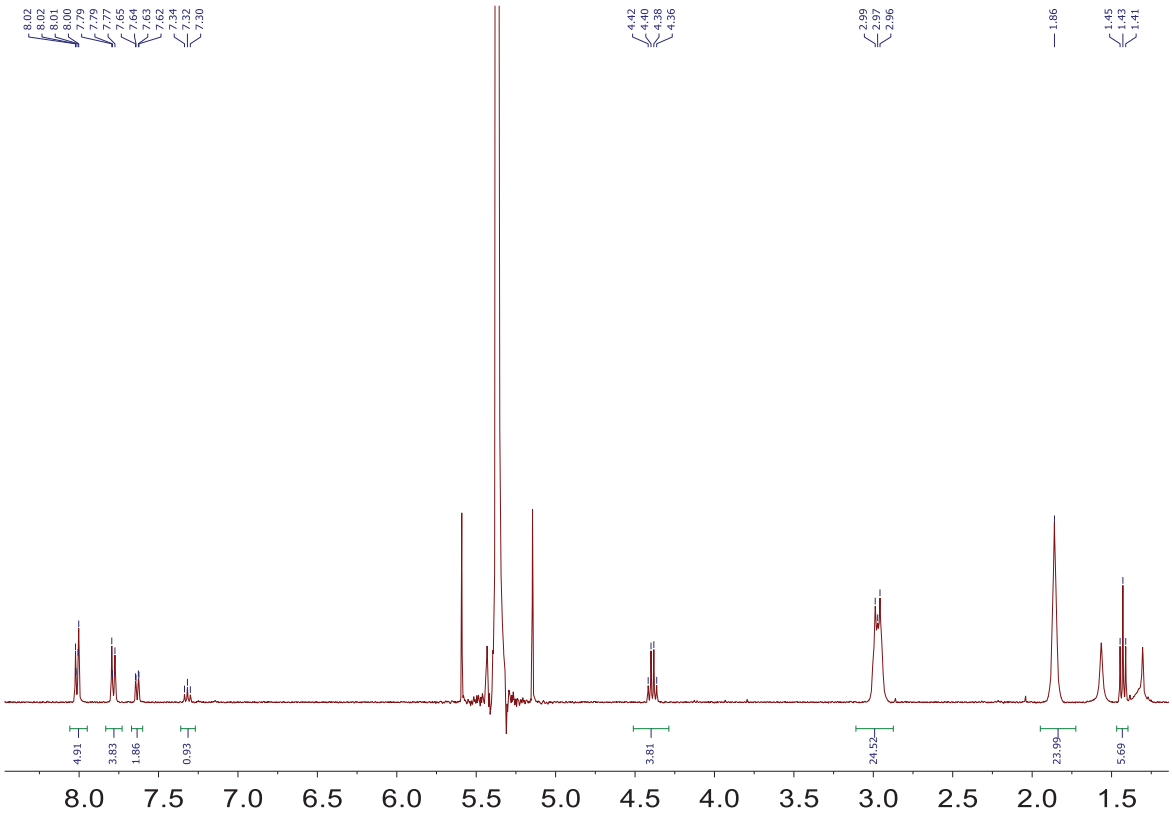

Figure 8.2.3 ^{1}H NMR spectrum of **2.2** in CD_2Cl_2.

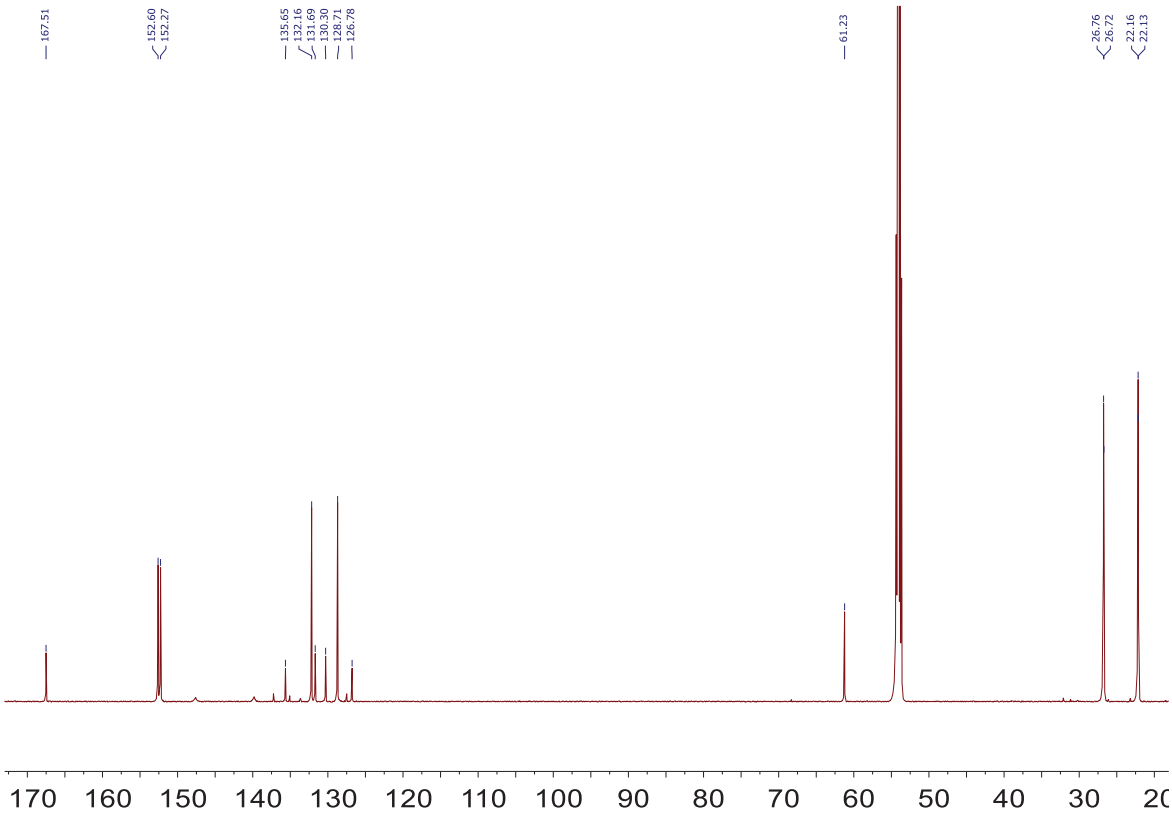

Figure 8.2.4 ^{13}C NMR spectrum of **2.2** in CD_2Cl_2.

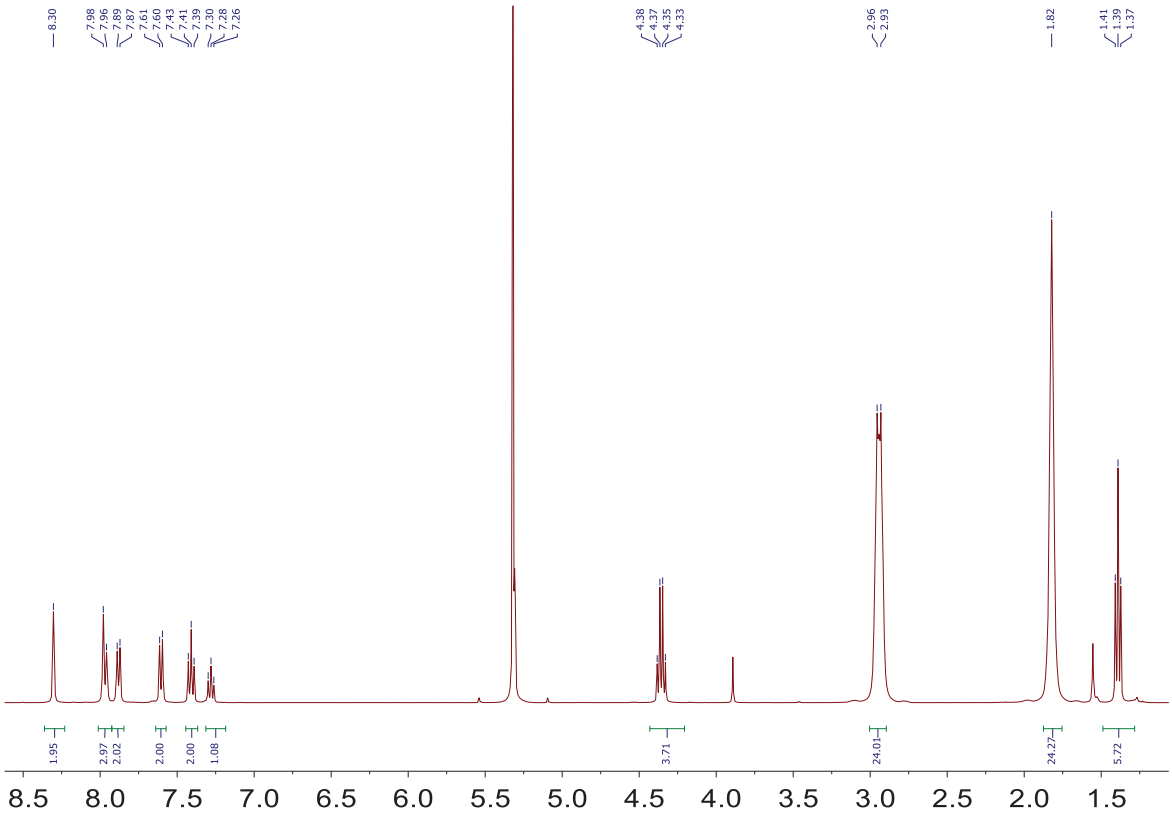

Figure 8.2.5 ^{1}H NMR spectrum of **2.3** in CD_2Cl_2.

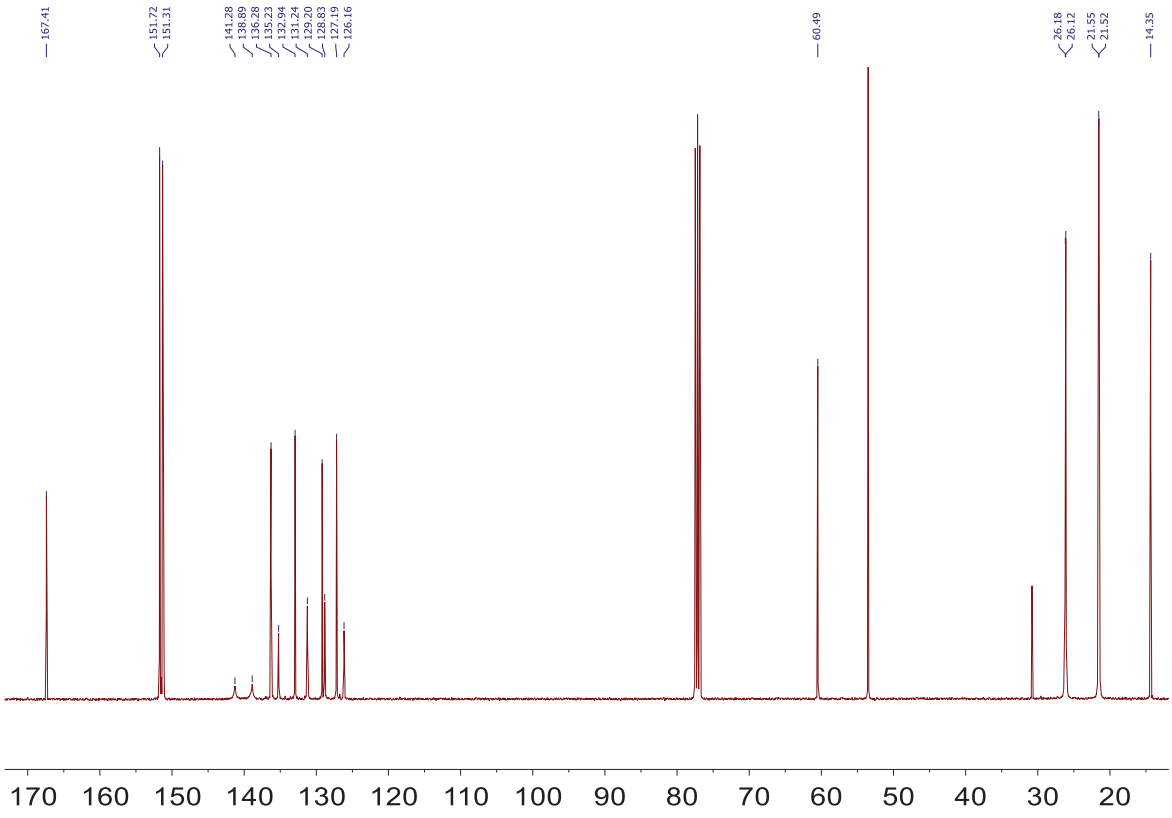

Figure 8.2.6 ^{13}C NMR spectrum of **2.3** in $CDCl_3$.

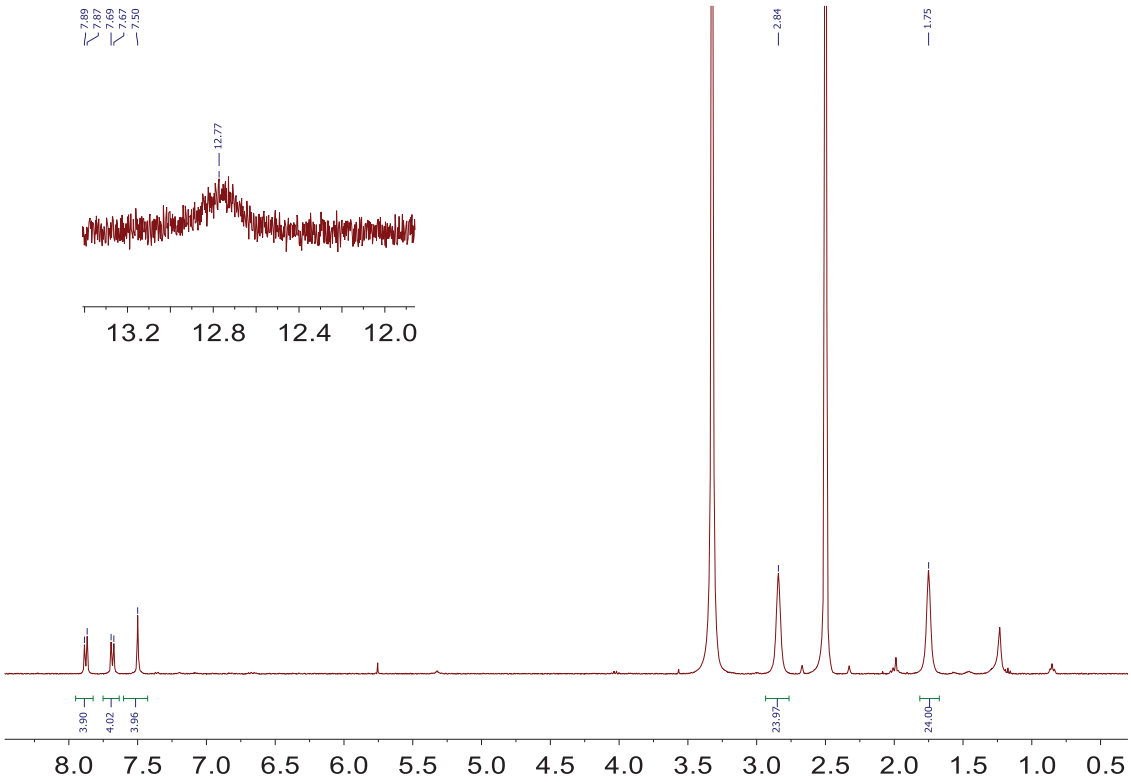

Figure 8.2.7 ^{1}H NMR spectrum of **2.4** in DMSO-d_6.

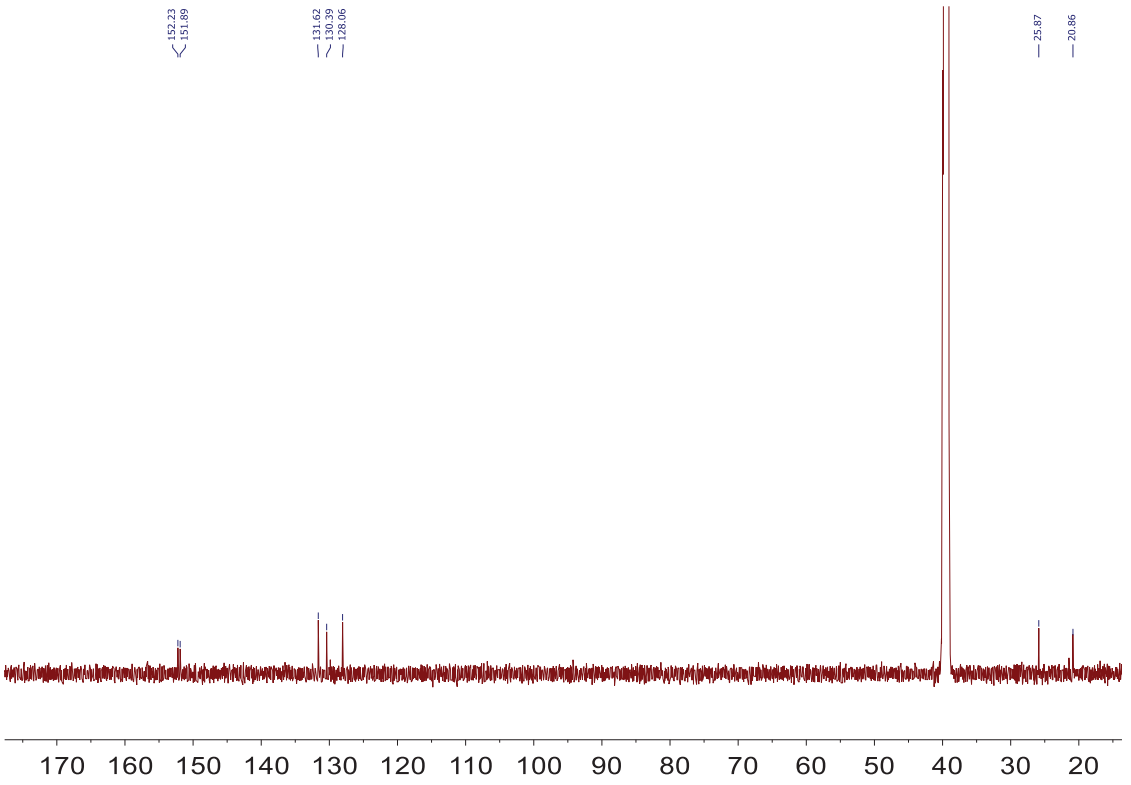

Figure 8.2.8 ^{13}C NMR spectrum of **2.4** in DMSO-d_6. The low quality of the spectrum is due to the poor solubility of **2.4.**

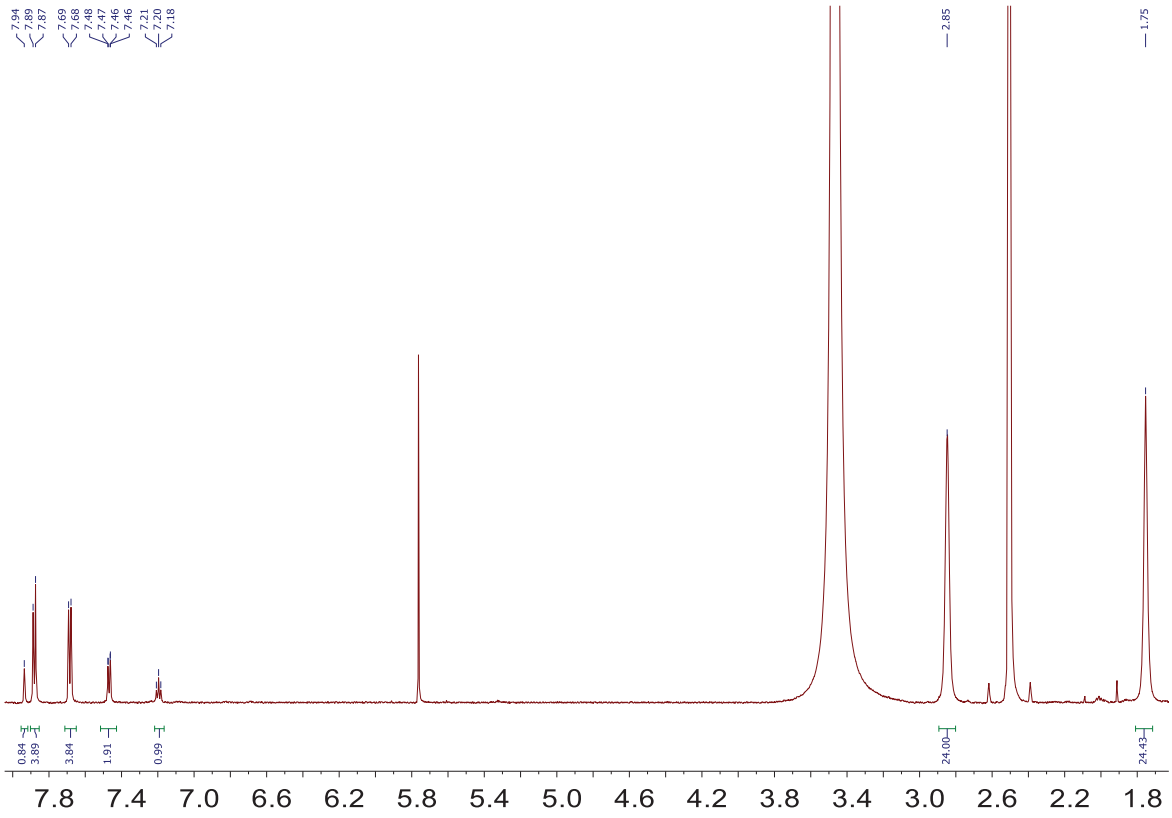

Figure 8.2.9 ^{1}H NMR spectrum of **2.5** in DMSO-d_6.

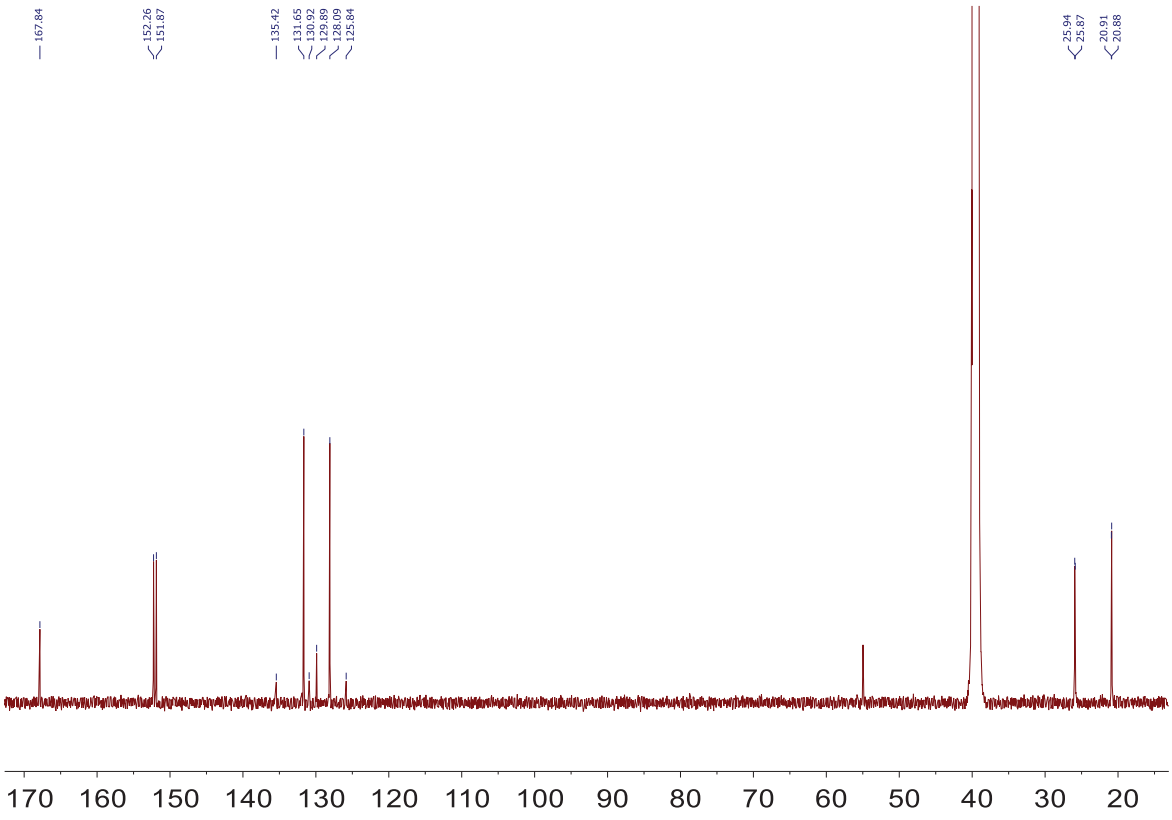

Figure 8.2.10 ^{13}C NMR spectrum of **2.5** in DMSO-d_6.

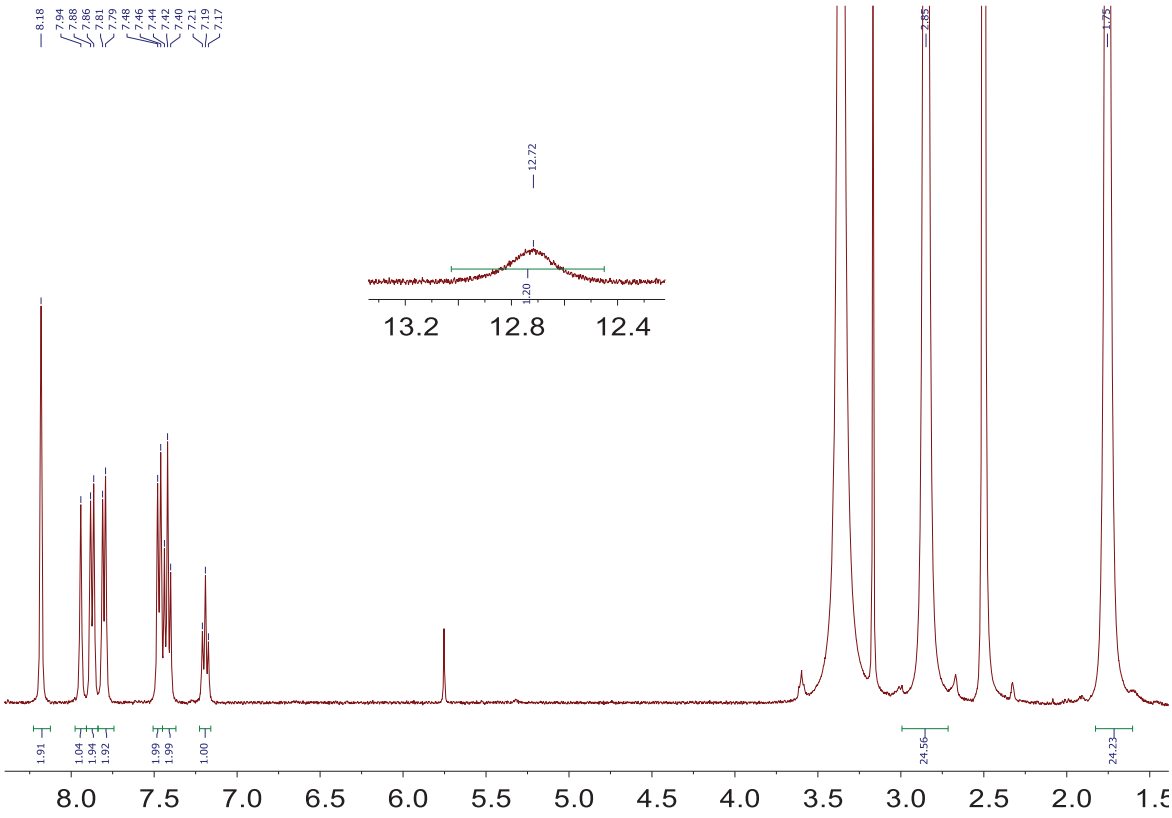

Figure 8.2.11 ^{1}H NMR spectrum of **2.6** in DMSO-d_6.

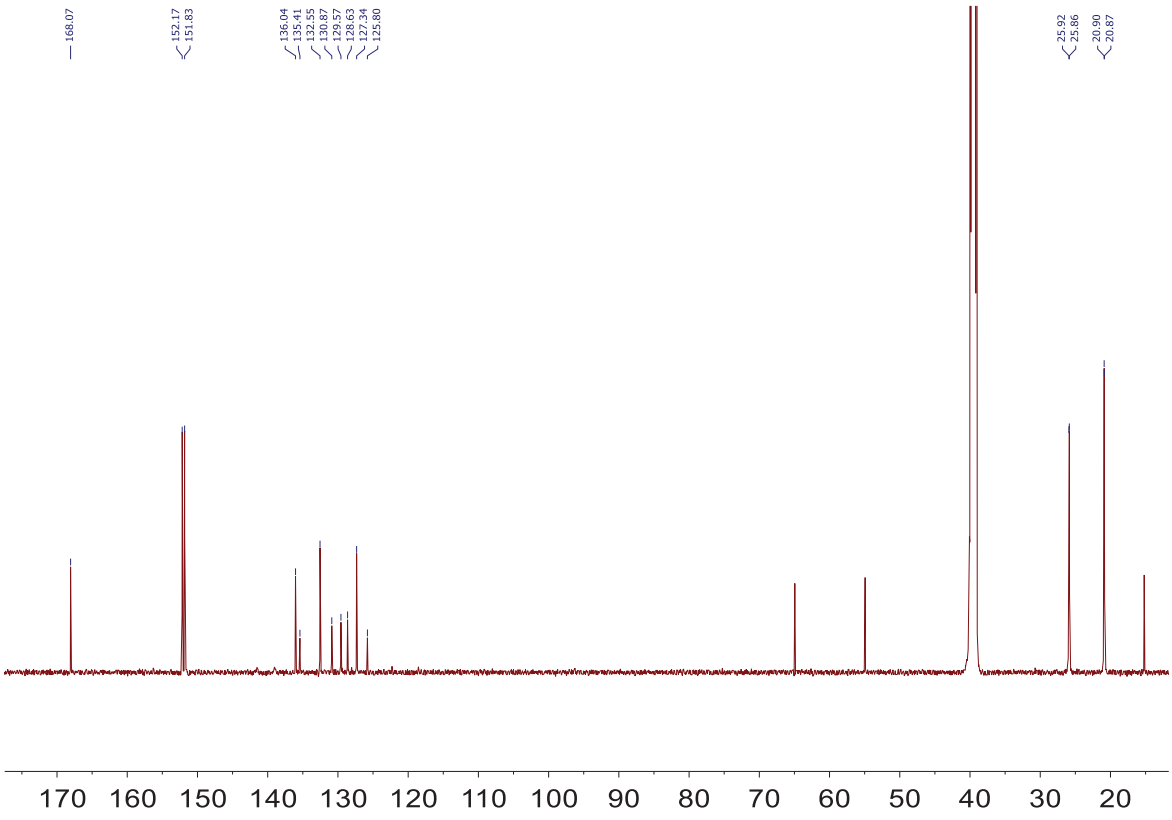

Figure 8.2.12 ^{13}C NMR spectrum of **2.6** in DMSO-d_6.

Selected HR-MS

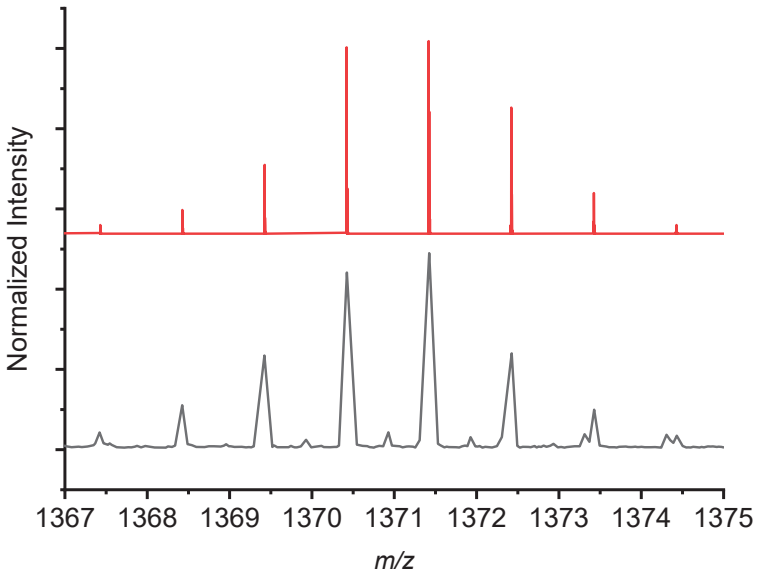

Figure 8.2.13 HR-MS spectrum of ligand **2.1** recorded in CH_2Cl_2:MeOH (1:1), ESI positive mode, red: theoretical spectrum, black: experimental spectrum.

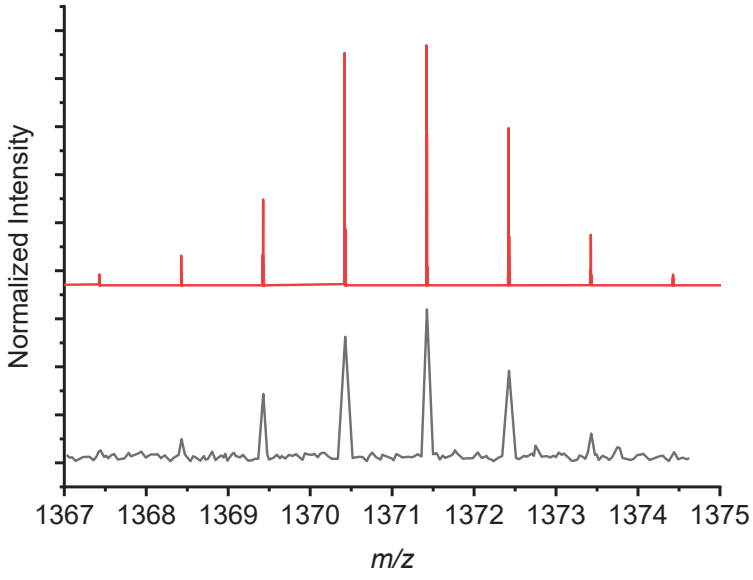

Figure 8.2.14 HR-MS spectrum of ligand **2.2** recorded in CH_2Cl_2:MeOH (1:1), ESI positive mode, red: theoretical spectrum, black: experimental spectrum.

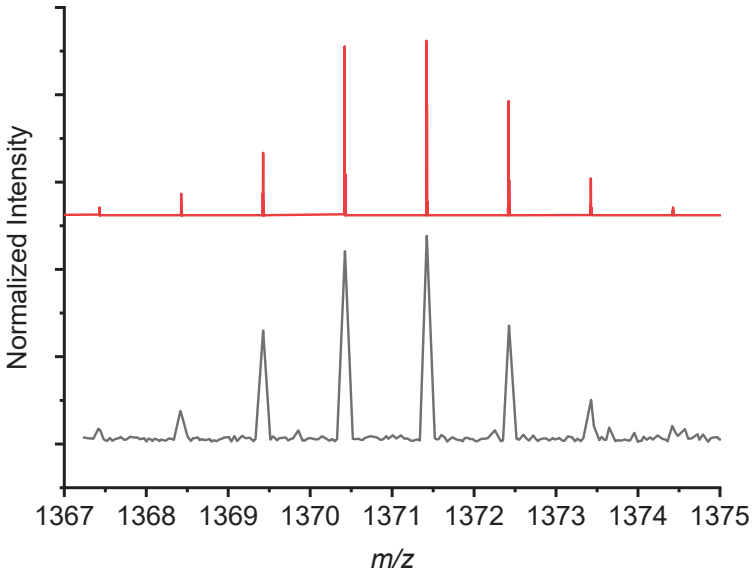

Figure 8.2.15 HR-MS spectrum of ligand **2.3** recorded in CH_2Cl_2:MeOH (1:1), ESI positive mode, red: theoretical spectrum, black: experimental spectrum.

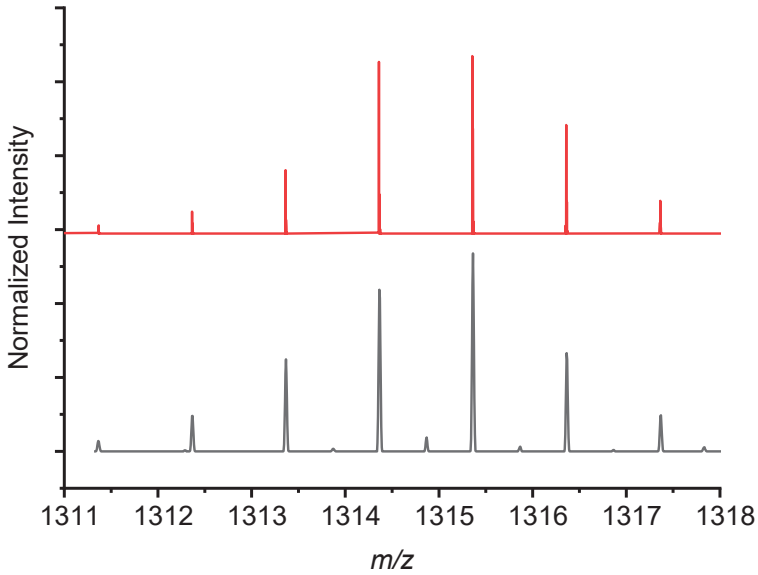

Figure 8.2.16 HR-MS spectrum of ligand **2.4** recorded in DMSO, ESI positive mode, red: theoretical spectrum, black: experimental spectrum.

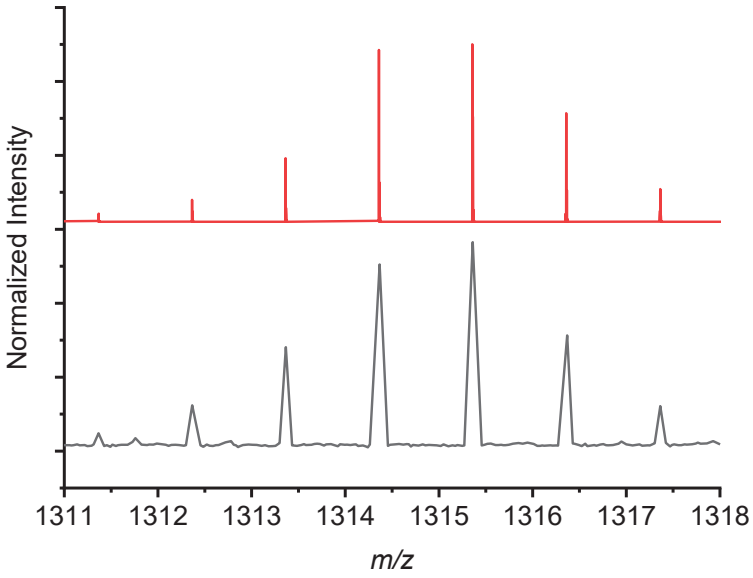

Figure 8.2.17 HR-MS spectrum of ligand **2.5** recorded in DMSO, ESI positive mode, red: theoretical spectrum, black: experimental spectrum.

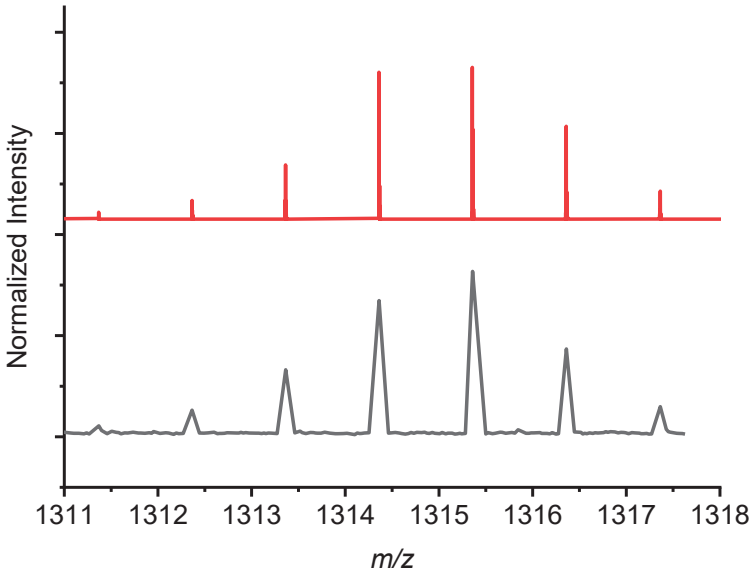

Figure 8.2.18 HR-MS spectrum of ligand **2.6** recorded in DMSO, ESI positive mode, red: theoretical spectrum, black: experimental spectrum.

Sorption experiments

In order to obtain a larger amount of cage **2.7**, the synthesis was performed with complex **2.6** (43.8 mg, 33.3 μmol) and metal salt $Cu(NO_3)_2(H_2O)_3$ (8 mg, 33.3 μmol) mixed in DMF (7.2 mL) resulting in the formation of a red-orange powder. Sorption experiments were performed after drying the solid for 8 h at 100 °C under vacuum.

N_2, H_2 and CO_2 sorption experiments are shown in **Figure 8.2.19**, **Figure 8.2.20** and **Figure 8.2.21**, respectively.

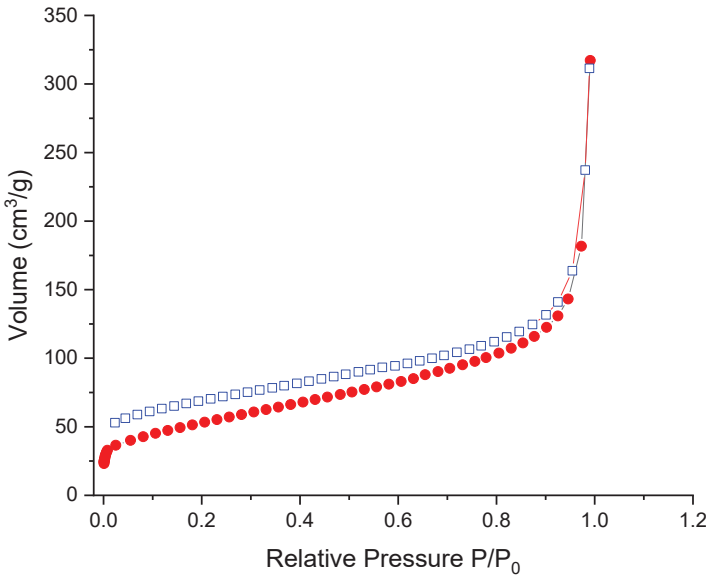

Figure 8.2.19 N_2 adsorption (red) and desorption (blue) isotherms at 77 K of cage **2.7**.

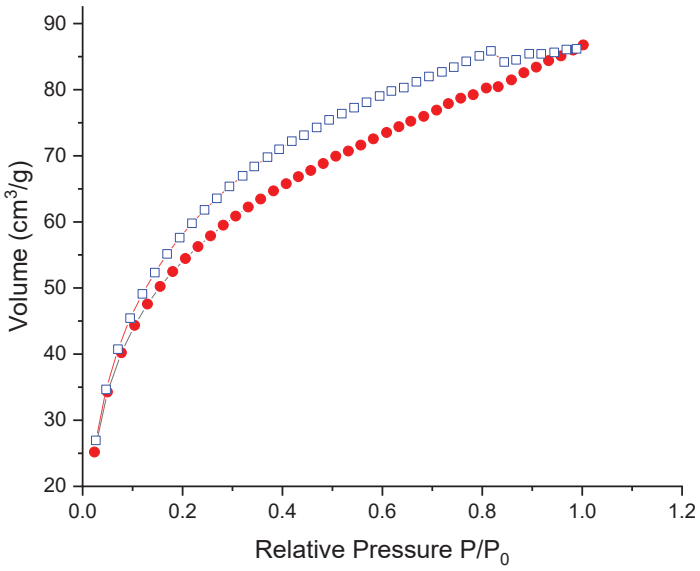

Figure 8.2.20 H_2 adsorption (red) and desorption (blue) isotherms at 77 K of cage **2.7**.

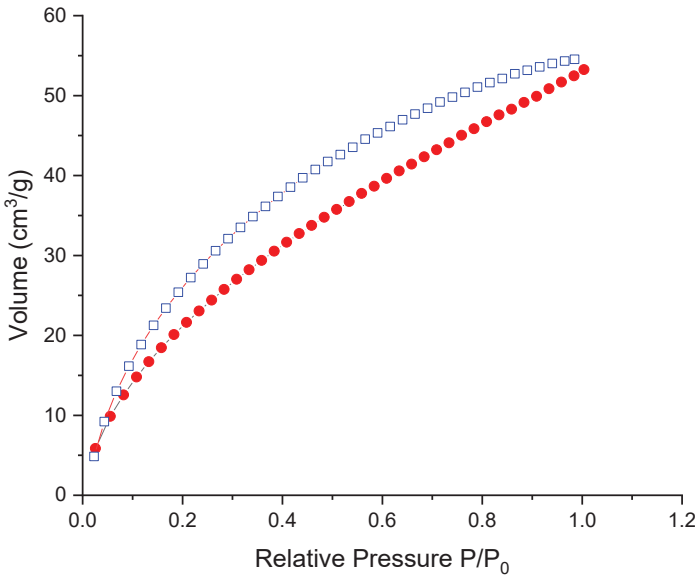

Figure 8.2.21 CO_2 adsorption (red) and desorption (blue) isotherms at 273 K of cage **2.7**.

8.2.2 Experimental Procedures from Chapter 3

Synthetic procedures

Ligands **3.2a** and **3.2c** were synthesized following published procedures.[104-105]

Ligand 3.2b: $FeCl_2$ (308 mg, 2.43 mmol), diethylglyoxime (1.05 g, 7.30 mmol) and pyridine-4-boronic acid (598 mg, 4.87 mmol) were dissolved in MeOH (135 mL). The mixture was heated to reflux during 3 h under N_2. Then, the red solution was cooled to RT, and the solvent was removed under reduced pressure. Subsequently, the resulting solid was dissolved in DCM (40 mL). The organic phase was washed with a saturated solution of $NaHCO_3$ (100 mL), dried ($MgSO_4$), and filtered. Removal of the solvent under vacuum gave **3.2b** in the form of a red powder (0.74 g, 46%).

^{1}H NMR (400 MHz, CD_2Cl_2) : 8.54 (s, 4H, C_{arom}), 7.59 (s, 4H, C_{arom}), 2.83 (q, J = 7.5 Hz, 12H, CH_2), 1.17 (t, J = 7.5 Hz, 18H, CH_3). **^{13}C{^{1}H} NMR** (101 MHz, CD_2Cl_2) δ : 158.91 (C_{arom}), 149.09 (C_{arom}), 127.39 (C=N), 21.43 (CH_3), 11.77 (CH_2) (C-B not detected). **HRMS (ESI TOF)** $[M+H]^+$ calcd for $[C_{28}H_{39}B_2FeN_8O_6]^+$ 661.2537, found 661.2552.

Ligand 3.2d: $FeCl_2$ (149 mg, 1.18 mmol), R-pulegone dioxime (551 mg, 3.53 mmol)[3] and pyridine-4-boronic acid (289 mg, 2.35 mmol) were dissolved in MeOH (140 mL). The mixture was heated to reflux during 3 h under N_2. Then, the red solution was cooled to RT, and the solvent was removed under reduced pressure. The resulting solid was dissolved in DCM (15 mL) and sonicated for 5 min. A filtration through silica gave an orange solution, which was evaporated under reduced pressure. Subsequently, the resulting red-orange solid was dissolved in DCM (40 mL). The organic phase was washed with a saturated solution of $NaHCO_3$ (100 mL), dried ($MgSO_4$), and filtered. Removal of the solvent and drying under vacuum for 14 h gave **3.2d** in the form of a red powder (793 mg). Yield was calculated accordingly to ^{1}H NMR for the dry product. The proportion of residual water in the ^{1}H NMR (Fig. S3) was integrated and two water molecules were found per clathrochelate complexes **3.2d**. They were removed from the total mass obtained to give the real mass and the yield of a dry **3.2d** product (92%).

Formation of a statistical ratio between *mer*- and *fac*- isomers (3 to 1 respectively) of **3.2d** is expected but not visible by NMR.

^{1}H NMR (400 MHz, CD_2Cl_2) δ : 8.52 (s, 4H, C_{arom}), 7.54 (s, 4H, C_{arom}), 3.17 (d, J = 19.9, 16.7, 5.6 Hz 6H, CH_2), 2.71 (ddd, J = 18.6, 11.6, 6.1 Hz, 3H, CH_2), 2.32 (dd, J = 18.7, 10.8 Hz, 3H, CH_2), 1.92 (s, 6H, CH_2), 1.46 – 1.43 (m, 3H, CH), 1.10 (d, J = 6.4 Hz, 9H, CH_3). **^{13}C{^{1}H} NMR** (101 MHz, CD_2Cl_2) δ : 153.15 (C_{arom}), 152.86 (C_{arom}), 149.08 (C=N), 127.33 (C=N), 34.58 (CH_3), 30.18 (CH), 29.15 (CH_2), 26.01(CH_2), 21.37 (CH_2) (C-B not detected). **HRMS (ESI TOF)** $[M+H]^+$ calcd for $[C_{31}H_{39}B_2FeN_8O_6]^+$ 697.2539, found 697.2538.

NMR spectra

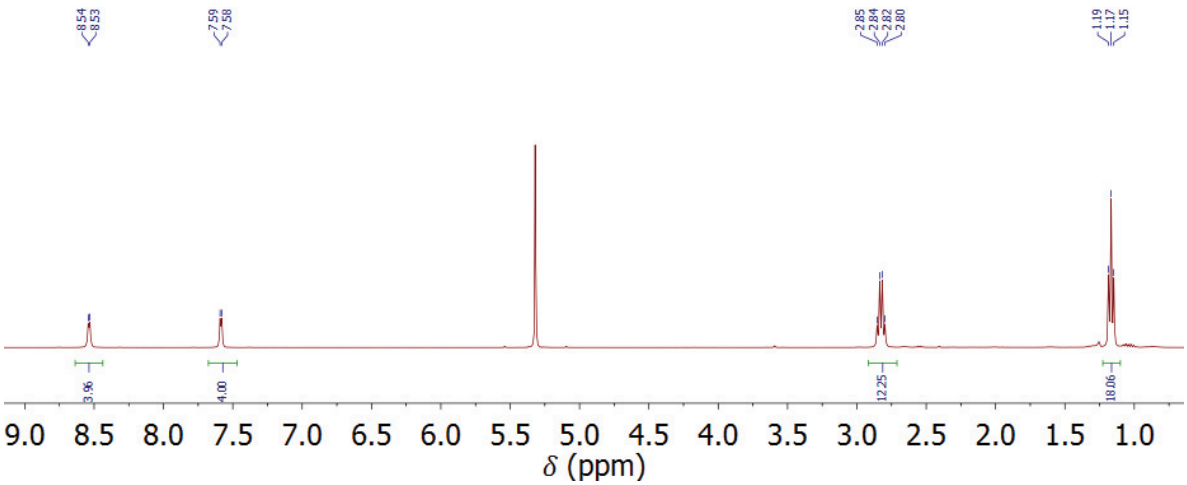

Figure 8.3.1 ^{1}H NMR of **3.2b** in CD_2Cl_2.

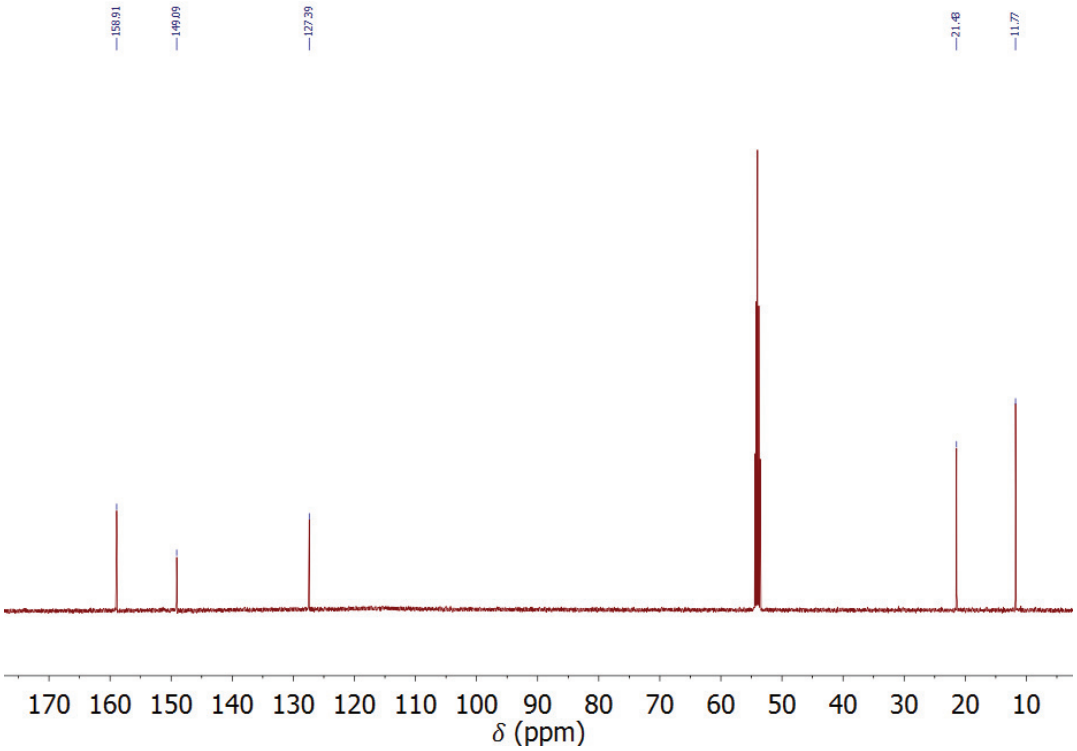

Figure 8.3.2 ^{13}C NMR of **3.2b** in CD_2Cl_2.

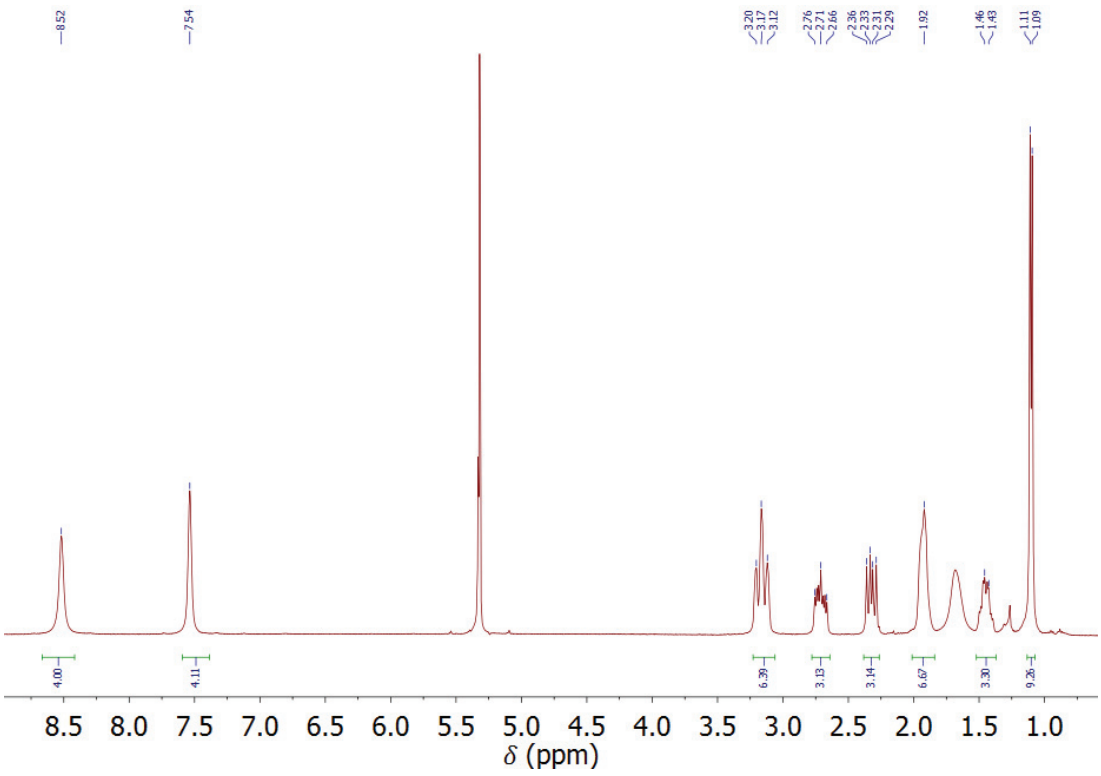

Figure 8.3.3 ^{1}H NMR of **3.2d** in CD_2Cl_2.

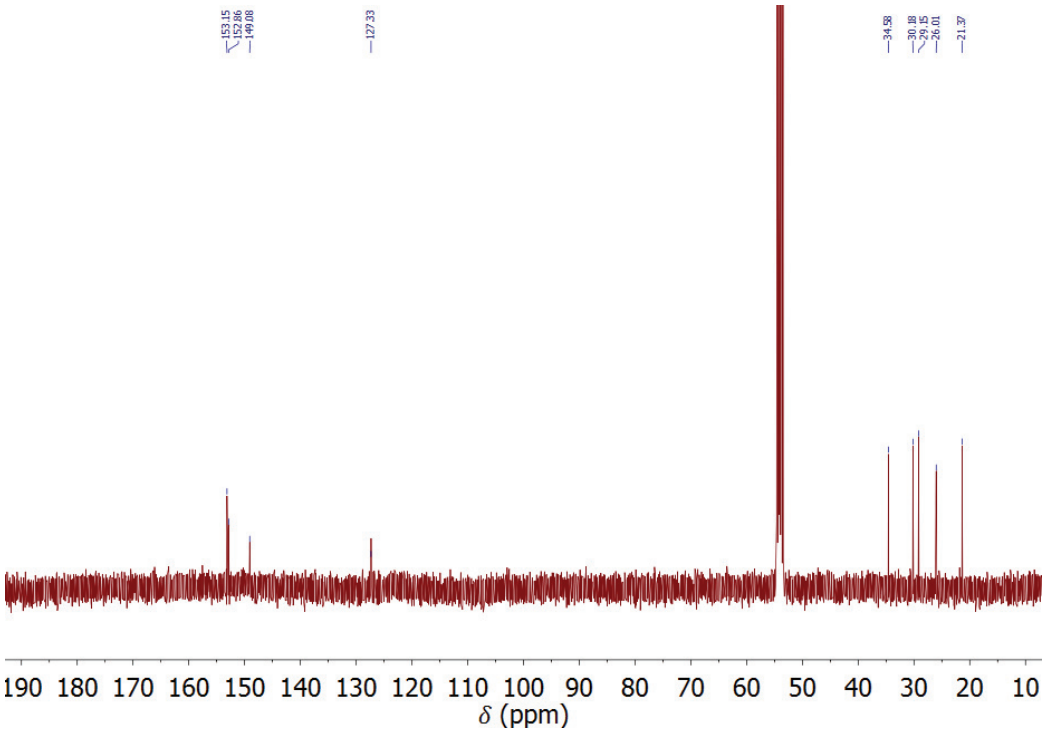

Figure 8.3.4 ^{13}C NMR of **3.2d** in CD_2Cl_2.

Solvent-Assisted Ligand Exchange:

Synthesis of the MOFs **3.3a, 3.3b, 3.3c,** and **3.3d**: Saturated DMF solutions of the clathrochelate complexes **3.2a**, **3.2b**, **3.2c** and **3.2d** were prepared by stirring a mixture of the respective complex (~ 75 – 96 mg) in DMF (4 mL) for 5 min at RT, followed by filtration. This procedure was repeated 7 times to obtain 28 mL of saturated solution of each clathrochelate complexes. Crystals of MOF **3.1** (30 mg) were immersed in a saturated solution of the respective metalloligand (7 mL), and the mixture was heated to 80 °C for 3 d. The progress of SALE was monitored by ^1H NMR and UV-Vis spectroscopy.

Synthesis of the MOFs **3.5** and **3.7**: Saturated DMF solutions of the clathrochelate complexe **3.2a** was prepared by stirring a mixture of the respective complex (~ 88 – 100 mg) in DMF (4 mL) for 5 min at RT, followed by filtration. This procedure was repeated 8 times to obtain 32 mL of saturated solution of each clathrochelate complexes. Crystals of MOF **3.4** or MOF **3.6** respectively (20 mg) were immersed in a saturated solution of the metalloligand **3.2a** (8 mL), and the mixture was heated to 80 °C for 3 d. The progress of SALE was monitored by ^1H NMR and UV-Vis spectroscopy.

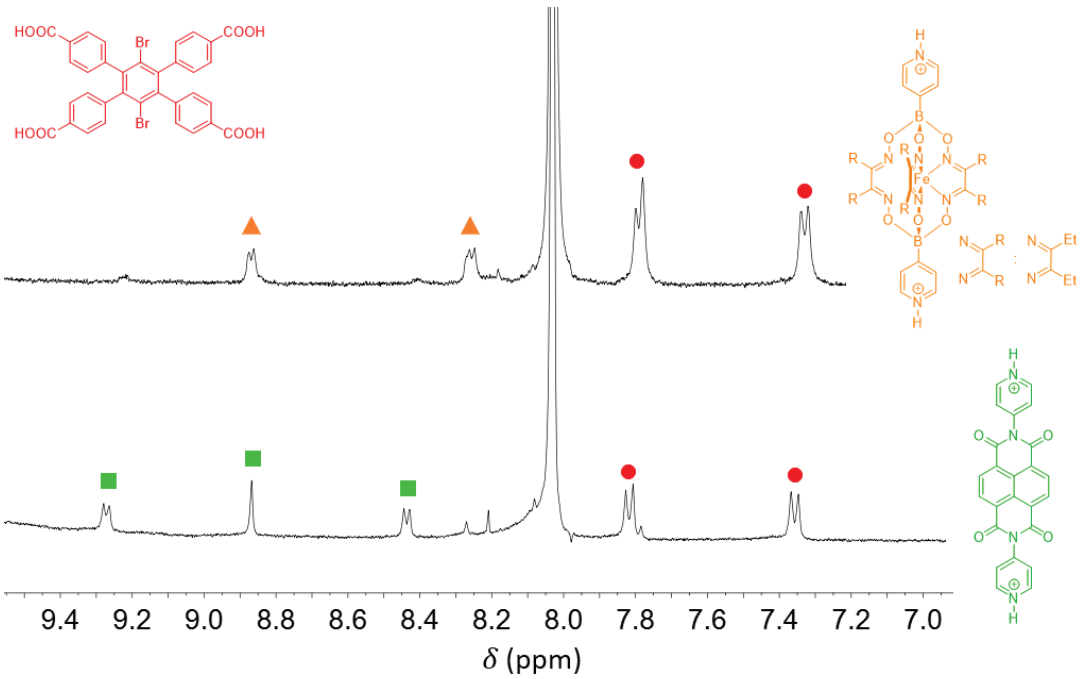

Figure 8.3.5 Progress of the conversion of **1** into **3.3b** as monitored by ^{1}H NMR spectroscopy (DMSO-d_6 + H_2SO_4, zoom on the aromatic region). Sample composition after 5 min (bottom), and after 3 days (top). Signals depicted in green correspond to the protonated **DPNI** linker, orange for the protonated clathrochelate **3.2b**, and red for the carboxylic acid ligand.

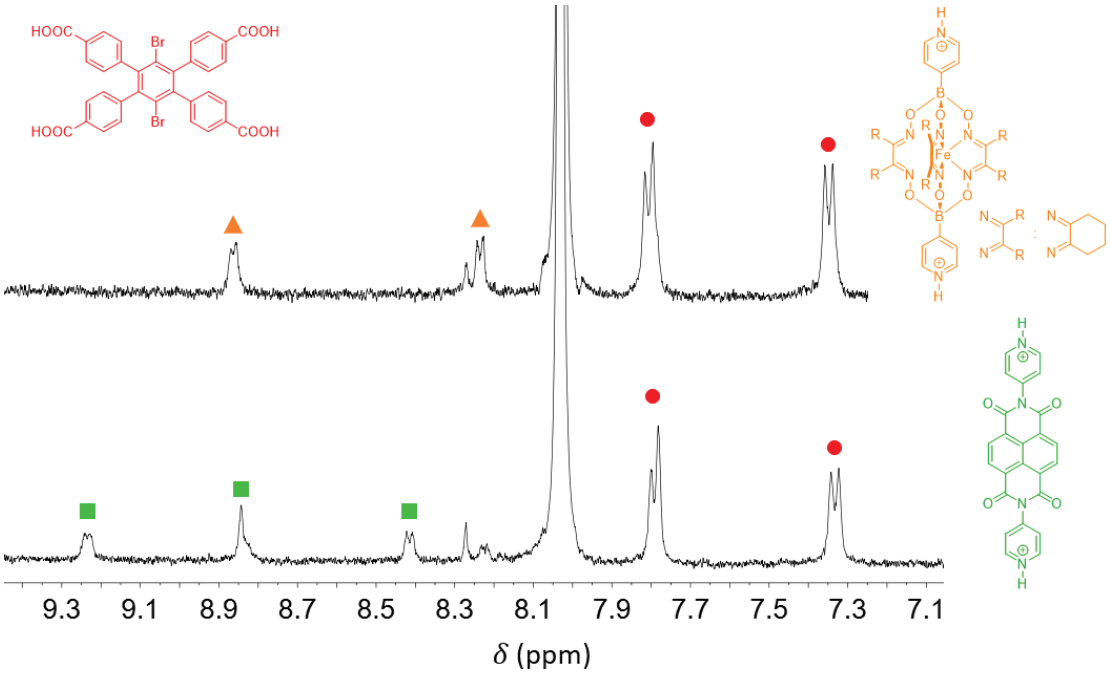

Figure 8.3.6 Progress of the conversion of **3.1** into **3.3c** as monitored by ^{1}H NMR spectroscopy (DMSO-d_6 + H_2SO_4, zoom on the aromatic region). Sample composition after 5 min (bottom), and after 3 days (top). Signals depicted in green correspond to the protonated **DPNI** linker, orange for the protonated clathrochelate **3.2c**, and red for the carboxylic acid ligand.

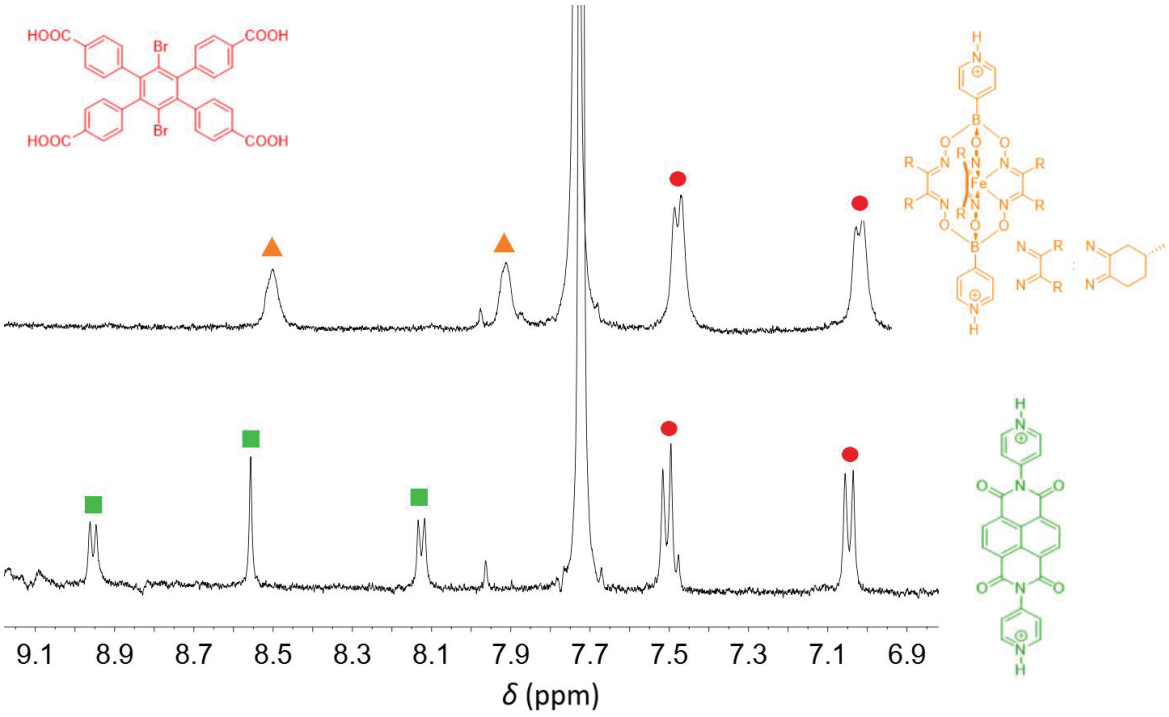

Figure 8.3.7 Progress of the conversion of **3.1** into **3.3d** as monitored by ^{1}H NMR spectroscopy (DMSO-d_6 + H_2SO_4, zoom on the aromatic region). Sample composition after 1 day (a), after 2 days (b), and after 3 days (c). Signals depicted in green correspond to the protonated **DPNI** linker, orange for the protonated clathrochelate **3.2d**, and red for the carboxylic acid ligand.

PXRD spectra

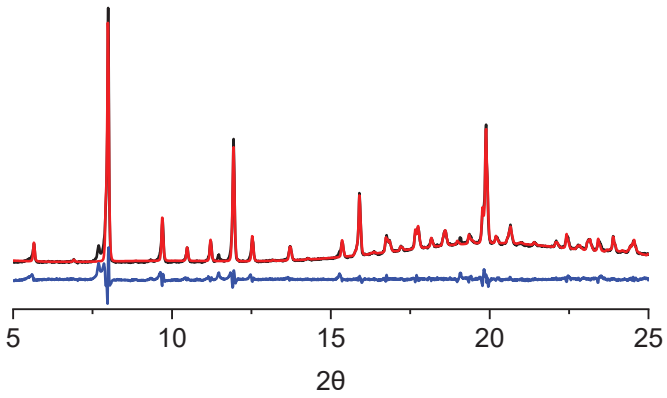

Figure 8.3.8 Comparison of PXRD patterns: **3.1** calculated (red), **3.1** observed (black) and the difference (blue).

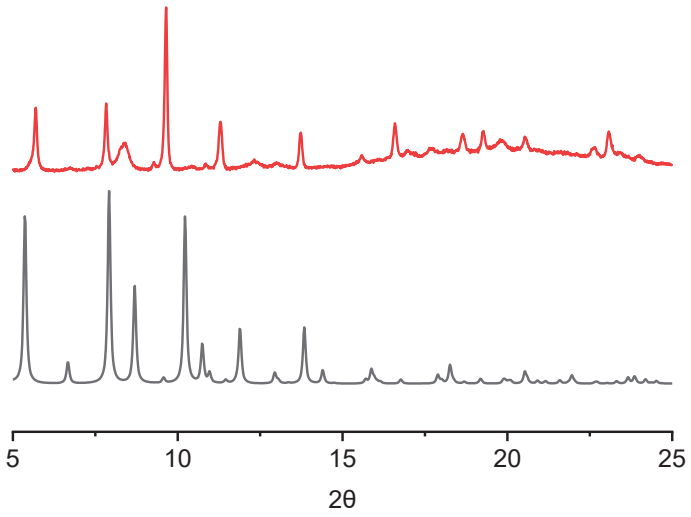

Figure 8.3.9 Comparison between **3.1** (black) as published and **3.3b** (red).

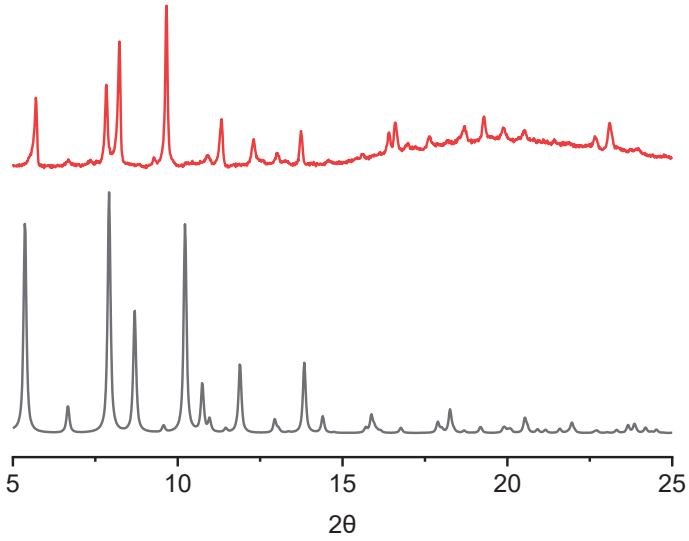

Figure 8.3.10 Comparison between **3.1** (black) as published and **3.3c** (red).

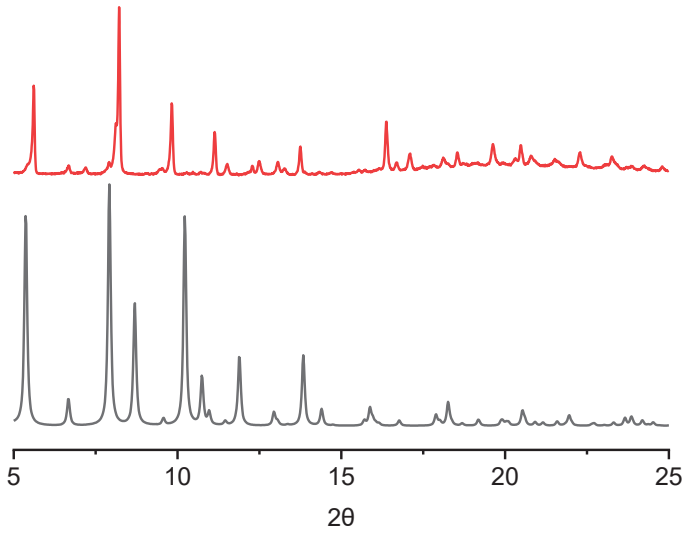

Figure 8.3.11 Comparison between **3.1** (black) as published and **3.3d** (red).

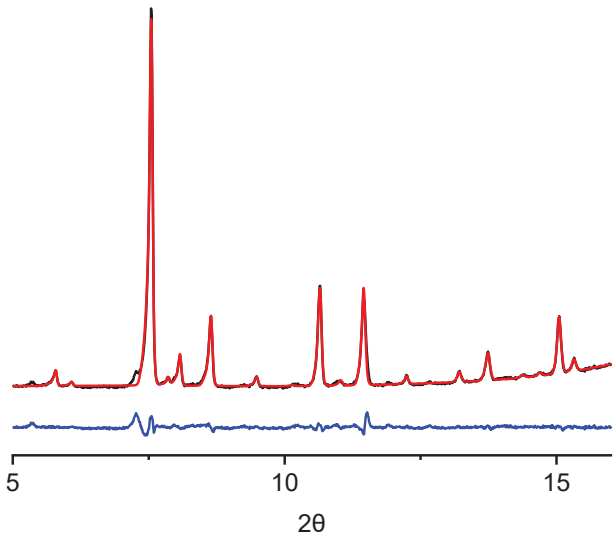

Figure 8.3.12 Comparison of PXRD patterns: **3.4** calculated (red), **3.4** observed (black) and the difference (blue).

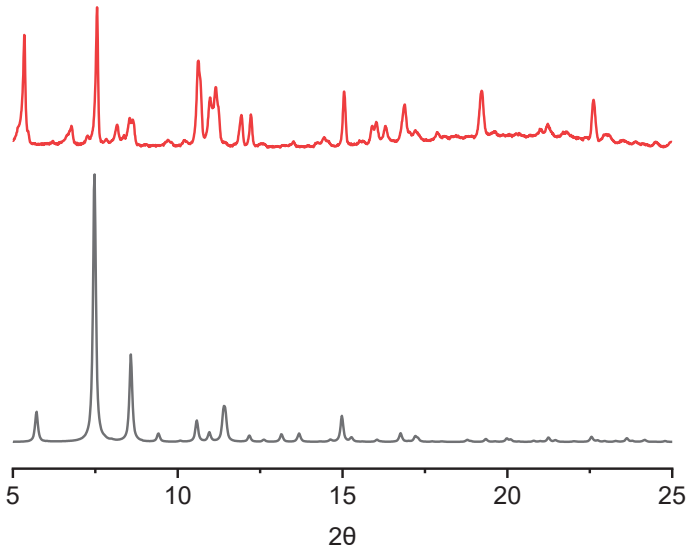

Figure 8.3.13 Comparison between **3.4** (black) as published and **3.5** (red).

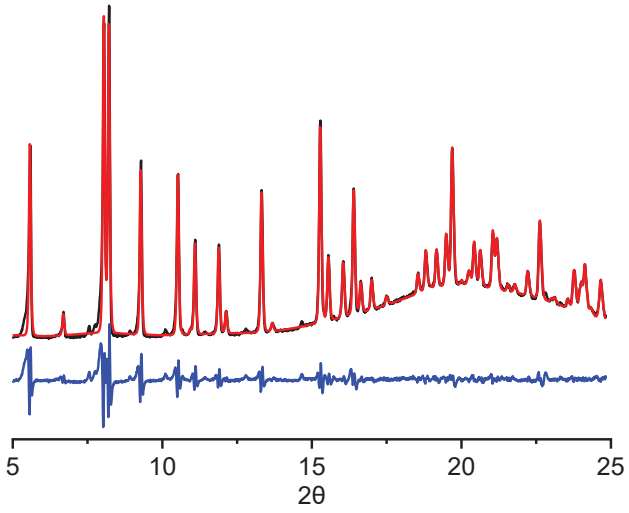

Figure 8.3.14 Comparison of PXRD patterns: **3.6** calculated (red), **3.6** observed (black) and the difference (blue).

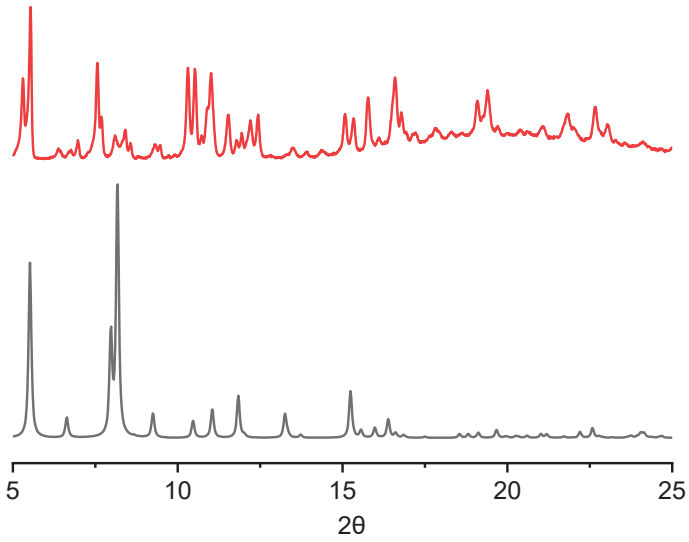

Figure 8.3.15 Comparison between **3.6** (black) as published and **3.7** (red).

UV/Vis spectra

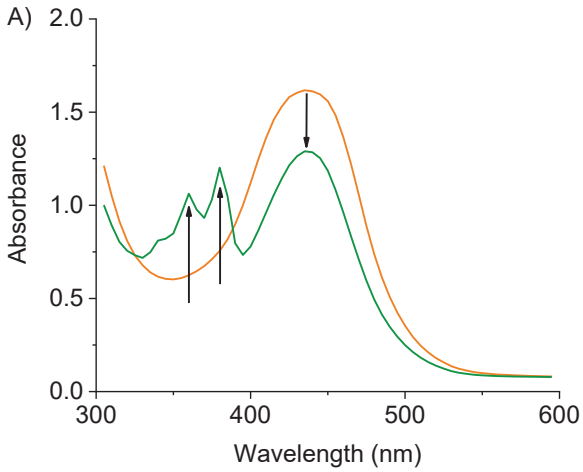

Figure 8.3.16 Stacking of UV-Vis spectra obtained from solutions of SALE with MOF **3.5** in DMF, after 5 min (orange) and after 3 days (green).

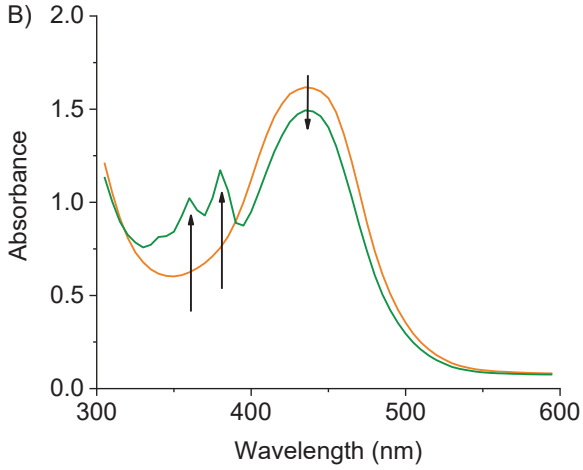

Figure 8.3.17 Stacking of UV-Vis spectra obtained from solutions of SALE with MOF **3.7** in DMF, after 5 min (orange) and after 3 days (green).

8.2.3 Experimental Procedures from Chapter 4

Synthesis of the Co(II) complexes:

Complex 4.1: Phenylboronic acid (142.9 mg, 1.17 mmol), nioxime (250.1 mg, 1.76 mmol) and $CoCl_2$ (76.2 mg, 0.586 mmol) were suspended in MeOH (55 mL) and heated under reflux for 12 h under inert atmosphere. After cooling to RT, the resulting solid was isolated by filtration, and washed with MeOH (30 mL) and Et_2O (15 mL) to give complex **4.1** as a brown-yellow powder. Yield: 246 mg, 64%. **HRMS-ESI** *m/z* calculated for $C_{30}H_{34}B_2CoN_6O_6$ $[M]^+$ 655.2052, found 655.2070. **EA** Anal. Calcd for $C_{30}H_{34}B_2CoN_6O_6$ C, 55.00; H, 5.23; N, 12.83. Found C, 54.93; H, 5.12; N, 12.77.

Complex 4.2: Pentafluorophenylboronic acid (348.5 mg, 1.64 mmol), nioxime (350.8 mg, 2.46 mmol) and $CoCl_2$ (106.8 mg, 0.822 mmol) were suspended in MeOH (75 mL) and heated under reflux for 12 h under inert atmosphere. After cooling to RT, the resulting solid was isolated by filtration, and washed with MeOH (50 mL) and Et_2O (25 mL) to give complex **4.2** as a brown-yellow powder. Yield: 363 mg, 53%. **HRMS-ESI** *m/z* calculated for $C_{30}H_{24}B_2CoF_{10}N_6O_6$ $[M]^+$ 835.1110, found 835.1124. **EA** Anal. Calcd for $C_{30}H_{24}B_2CoF_{10}N_6O_6$ C, 43.15; H, 2.90; N, 10.06. Found C, 43.27; H, 2.90; N, 9.96.

Complex 4.5: Phenylboronic acid (160.5 mg, 1.32 mmol), phenanthrenequinone dioxime (470.5 mg, 1.98 mmol) and $CoCl_2$ (85.4 mg, 0.658 mmol) were suspended in MeOH (75 mL) and heated under reflux for 12 h under inert atmosphere. After cooling to RT, the resulting solid was isolated by filtration, and washed with MeOH (50 mL) and Et_2O (25 mL) to give complex **4.5** as a brown-yellow powder. Yield: 228 mg, 37%. **HRMS-ESI** *m/z* calculated for $C_{54}H_{34}B_2CoN_6O_6$ $[M]^+$ 943.2052, found 943.2057. **EA** Anal. Calcd for $C_{54}H_{34}B_2CoN_6O_6$ C, 68.75; H, 3.63; N, 8.91. Found C, 68.81; H, 3.64; N, 8.81.

Synthesis of the Co(I) complexes:

Complex 4.3: Complex **4.1** (40.3 mg, 0.062 mmol) was dissolved in THF (80 mL) in a glovebox. C_8K (10.0 mg, 0.074 mmol) and 18-crown-6 (19.6 mg, 0.074 mmol) were added as solids. The reaction mixture was stirred at RT for 30 min under inert atmosphere. The resulting blue solution was filtered and Et_2O was added (25 mL) to obtain a blue precipitate. A filtration under N_2 gave complex **4.3** as a dark blue powder. Yield: 32.1 mg, 47%. **HRMS-ESI** *m/z* calculated for $C_{30}H_{34}B_2CoN_6O_6$ $[M]^+$ 655.2058, found 655.2068. An elemental analysis was not performed due to the very high sensitivity of the compounds. Crystals of **4.3** were obtained in the glovebox by slow diffusion of pentane into a solution of **4.3** in THF.

Complex 4.4: Complex **4.2** (51.4 mg, 0.062 mmol) was dissolved in THF (80 mL) in a glovebox. C_8K (10.0 mg, 0.074 mmol) and 18-crown-6 (19.6 mg, 0.074 mmol) were added as solids. The reaction mixture was stirred at RT for 30 min under inert atmosphere. The resulting blue solution was filtered and Et_2O was added (25 mL) to obtain a blue precipitate. A filtration under N_2 gave complex **4.4** as a dark blue powder. Yield: 40.6 mg, 51%. **HRMS-ESI** *m/z* calculated for $C_{30}H_{24}B_2CoN_6O_6$ $[M]^+$ 835.1116, found 835.1128. An elemental analysis was not performed due to the very high sensitivity of the compounds. Crystals of **4.4** were obtained in the glovebox by slow diffusion of pentane into a solution of **4.4** in THF.

Complex 4.6: Complex **4.5** (58.1 mg, 0.062 mmol) was dissolved in THF (100 mL) in the glovebox. C_8K (10.0 mg, 0.074 mmol) and 18-crown-6 (19.6 mg, 0.074 mmol) were added as solids. The reaction mixture was stirred at RT for 2 h under inert atmosphere. The resulting green solution was filtered and Et_2O was added (25 mL) to obtain a green precipitate. A filtration under N_2 gave complex **4.6** as a green powder. Yield: 34.3 mg, 42%. **HRMS-ESI** *m/z* calculated for $C_{66}H_{58}B_2CoN_6O_{12}K$ $[M]^+$ 1246.3268, found 1248.3308. An elemental analysis was not performed due to the very high sensitivity of the compounds. Crystals of **4.6** were obtained in the glovebox by slow evaporation of a THF solution.

Cyclic voltammetry

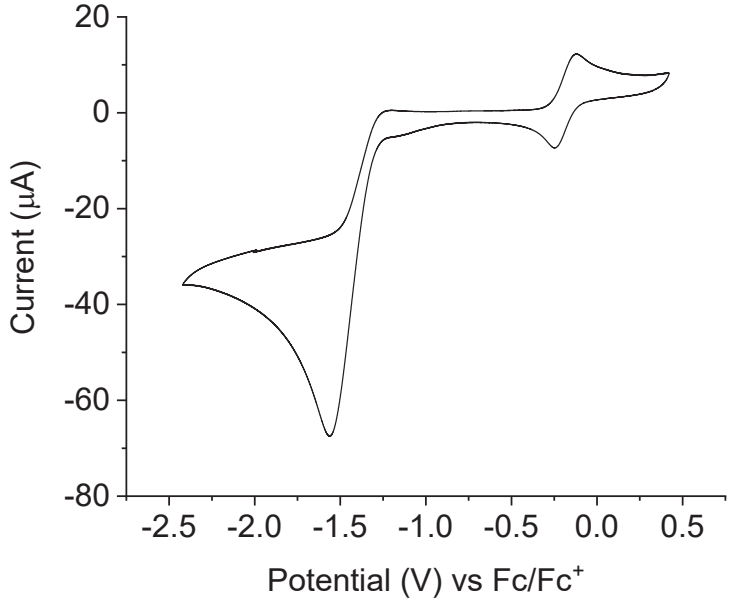

Figure 8.4.1 Cyclic voltammogram of complex **4.1** in DCM with $TBAPF_6$ (0.1 M) as electrolyte. (CE and WE: Pt, RE: 3M NaCl). Scan rate= 100 $mV \cdot s^{-1}$. Redox transition are observed at $E_{1/2}$ = –0.19 V (Co(II)/Co(III)) and $E_{1/2}$ = –1.40 V (Co(I)/Co(II)).

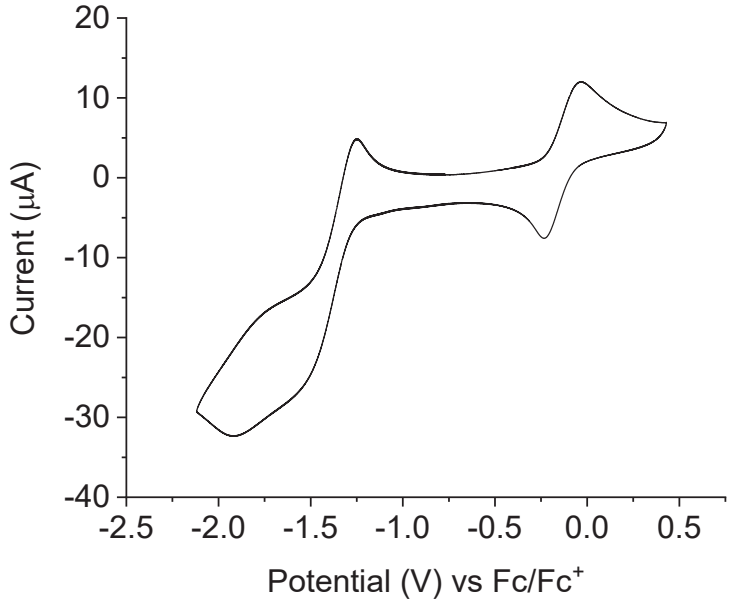

Figure 8.4.2 Cyclic voltammogram of complex **4.2** in DCM with $TBAPF_6$ (0.1 M) as electrolyte. (CE and WE: Pt, RE: 3M NaCl). Scan rate= 100$mV \cdot s^{-1}$. Redox transition are observed at $E_{1/2}$ = –0.13 V (Co(II)/Co(III)) and $E_{1/2}$ = –1.42 V (Co(I)/Co(II)).

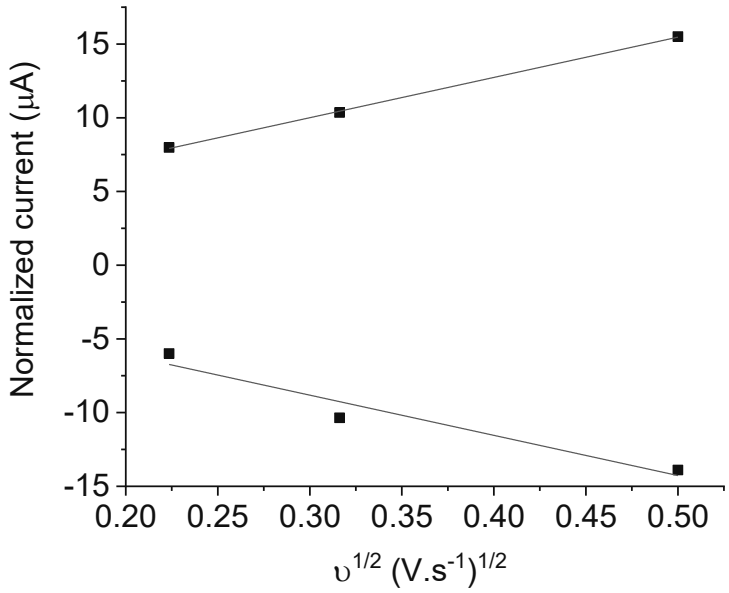

Figure 8.4.3 Linear dependence of I_{pc} and I_{pa} versus the square root of the can rate of the oxidation wave of complex **4.1** (DCM, $TBAPF_6$ 0.1M) at 50, 100 and 250 $mV \cdot s^{-1}$.

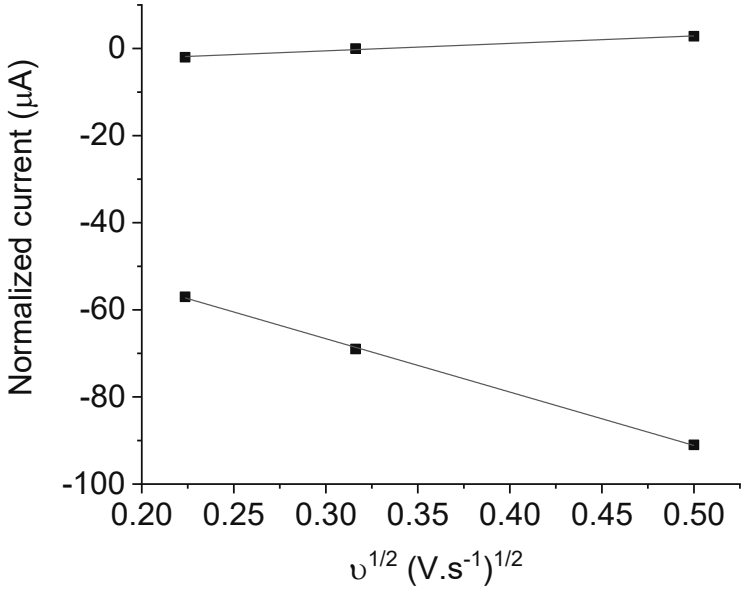

Figure 8.4.4 Linear dependence of I_{pc} and I_{pa} versus the square root of the can rate of the reduction wave of complex **4.1** (DCM, $TBAPF_6$ 0.1M) at 50, 100 and 250 $mV \cdot s^{-1}$.

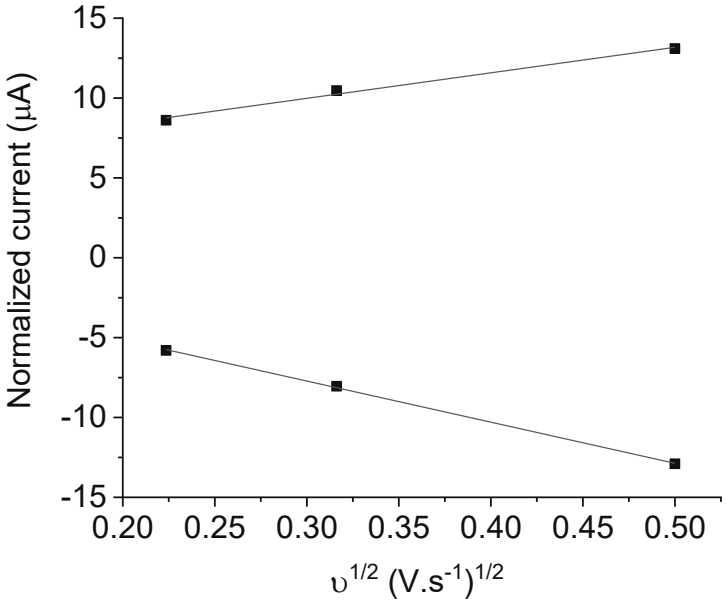

Figure 8.4.5 Linear dependence of I_{pc} and I_{pa} versus the square root of the can rate of the oxidation wave of complex **4.2** (DCM, $TBAPF_6$ 0.1M) at 50, 100 and 250 $mV \cdot s^{-1}$.

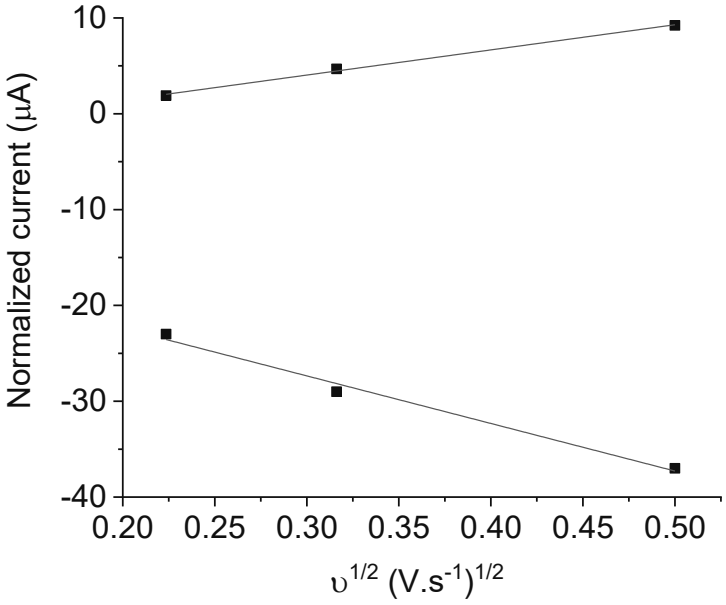

Figure 8.4.6 Linear dependence of I_{pc} and I_{pa} versus the square root of the can rate of the reduction wave of complex **4.2** (DCM, $TBAPF_6$ 0.1M) at 50, 100 and 250 $mV \cdot s^{-1}$.

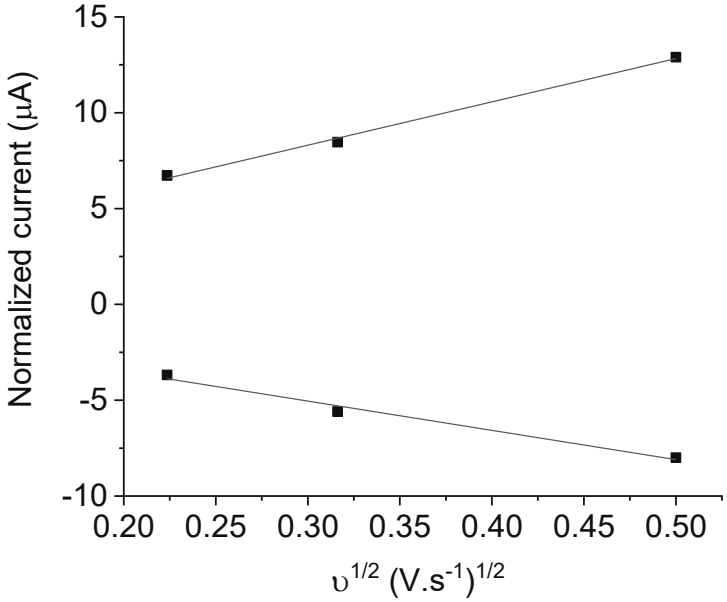

Figure 8.4.7 Linear dependence of I_{pc} and I_{pa} versus the square root of the can rate of the oxidation wave of complex **4.5** (DCM, $TBAPF_6$ 0.1M) at 50, 100 and 250 $mV{\cdot}s^{-1}$.

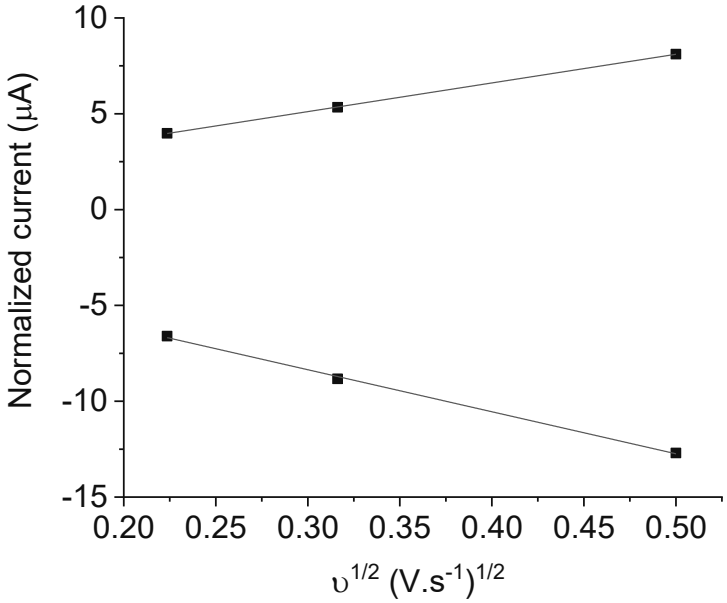

Figure 8.4.8 Linear dependence of I_{pc} and I_{pa} versus the square root of the can rate of the reduction wave of complex **4.5** (DCM, $TBAPF_6$ 0.1M) at 50, 100 and 250 $mV.s^{-1}$.

UV/vis spectroscopy

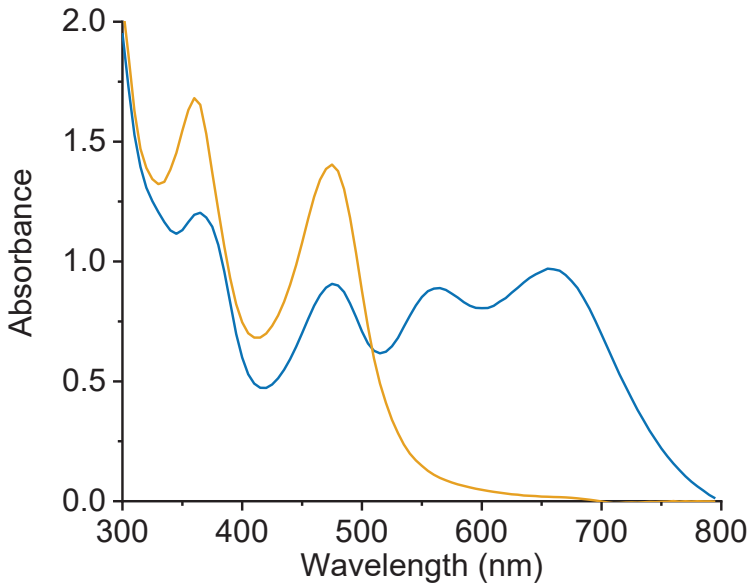

Figure 8.4.9 UV/vis spectra of complex **4.1** (yellow) and complex **4.3** (blue) in THF under N_2.

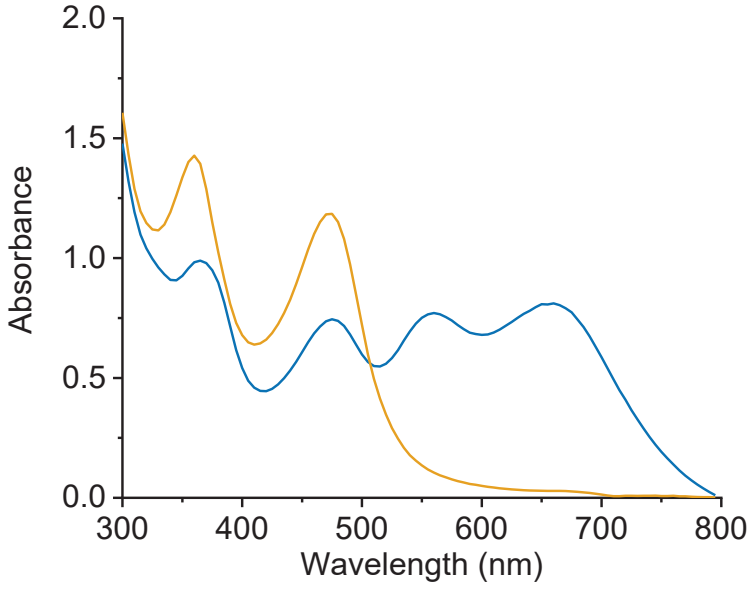

Figure 8.4.10 UV/vis spectra of complex **4.2** (yellow) and complex **4.4** (blue) in THF under N_2.

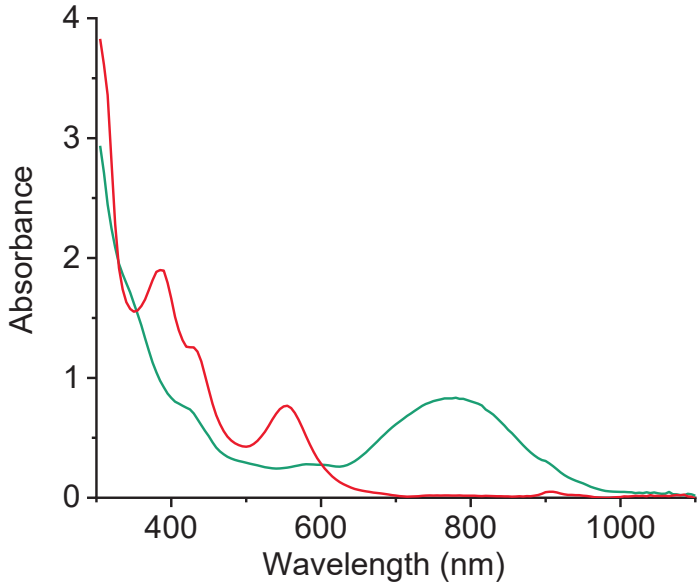

Figure 8.4.11 UV/vis spectra of complex **4.5** (red) and complex **4.6** (green) in THF under N_2.

8.2.4 Experimental Procedures from Chapter 5

Synthesis of compounds 5.1-5.2 and 5.5-5.6:

Complex 5.1: Phenanthrenequinone dioxime (829.1mg, 3.48 mmol), 4-bromomethylphenylboronic acid (500 mg, 2.32 mmol) and anhydrous $FeCl_2$ (147 mg, 1.16 mmol) were dissolved in MeOH (150 mL) and heated under reflux and inert atmosphere overnight. The purple solution obtained was allowed to cool to RT and the solvent was removed under vacuum. The product **5.1** was purified by silica gel column chromatography (DCM) to yield a purple powder (628 mg, 48%). **^{1}H NMR** (400 MHz, CD_2Cl_2): δ (ppm) 9.70 (dd, 6H, Ar-*CH*), 8.28 (d, 6H, Ar-*CH*), 8.15 (m, 4H, Ar-*CH*), 7.65 (d, 4H, Ar-*CH*), 7.59 (td, 4H, Ar-*CH*), 7.52 (td, 4H, Ar-*CH*), 4.80 (s, 1H, *CH_2*-Br), 4.72 (s, 1H, *CH_2*-Br). **^{13}C NMR** (101 MHz, CD_2Cl_2): δ (ppm) 35.07 (*CH_2*-Br), 124.20, 124.88, 128.88, 129.32, 131.03, 131.53, 132.77, 132.92, 132.97, 138.17 (Ar-*C*), 148.18 (N-*C*), (C-B not detected). **HRMS (ESI TOF)** *m/z* c calculated for $C_{56}H_{36}B_2Br_2FeN_6O_6$ $[M-H]^+$ 1126.0598; found: 1126.0597.

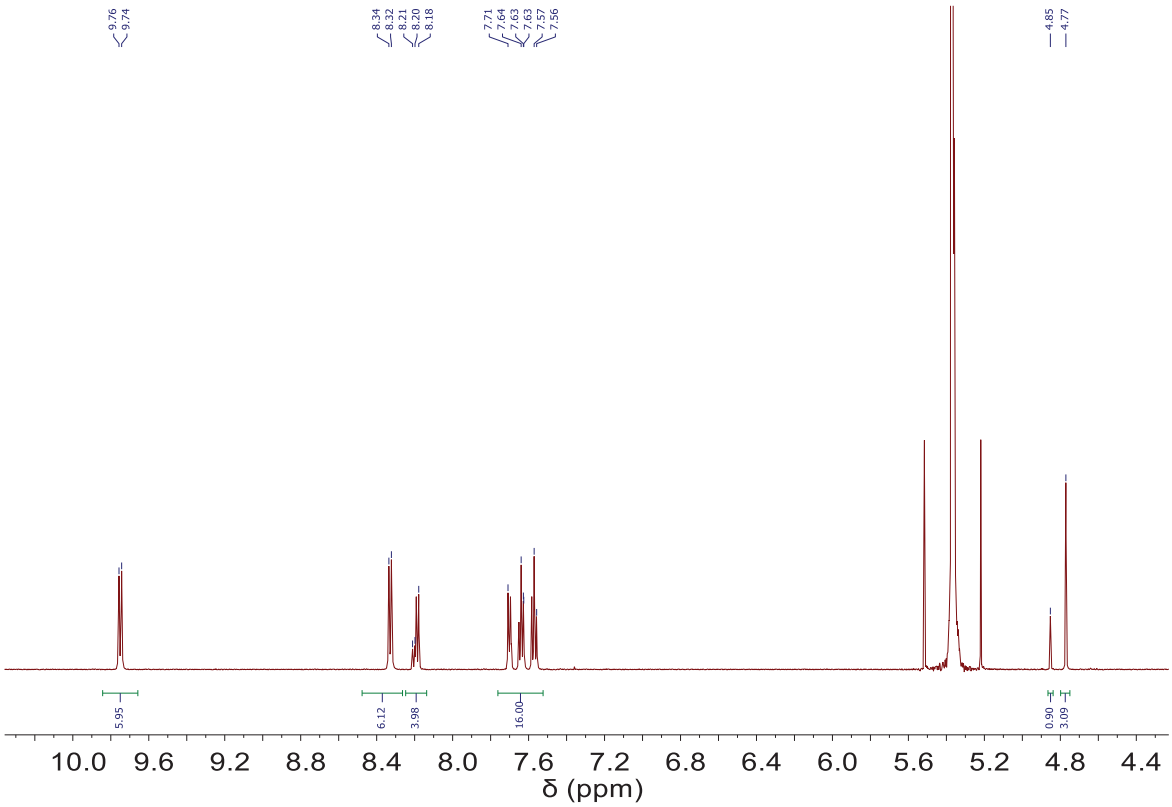

Figure 8.4.12 ^{1}H NMR spectra of complex **5.1** (CD_2Cl_2).

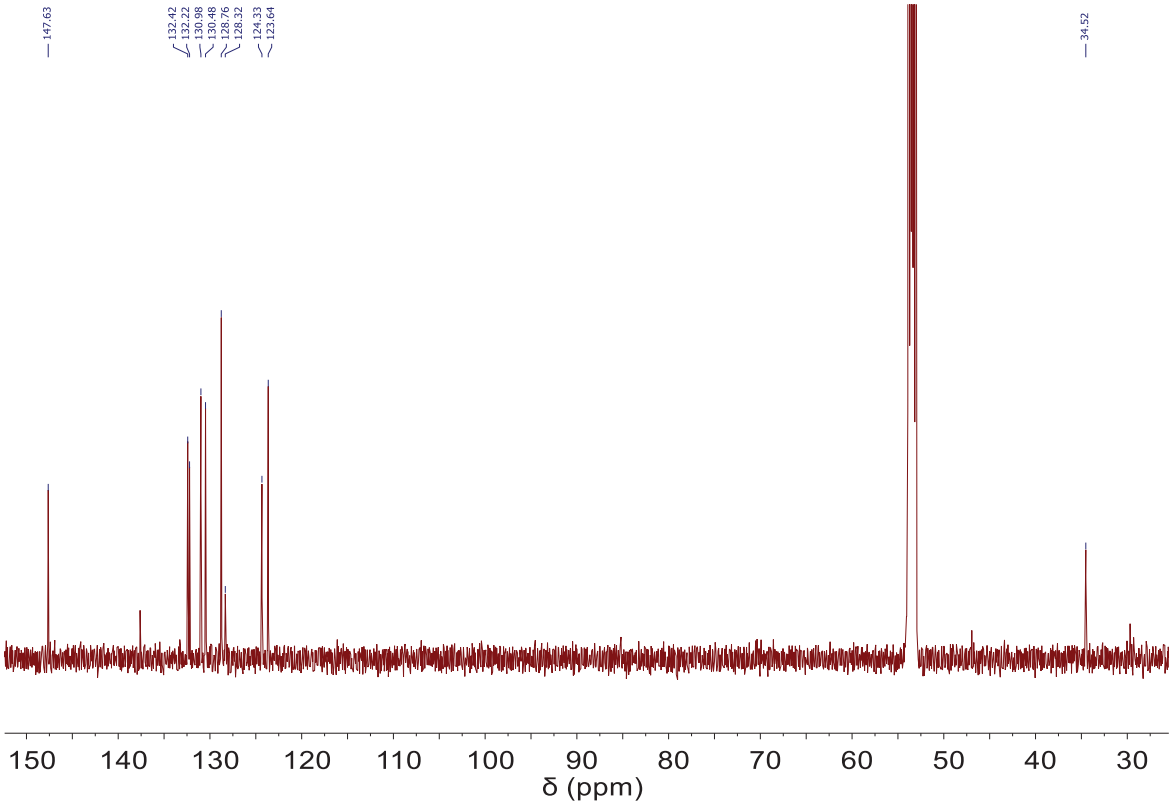

Figure 8.4.13 ^{13}C NMR spectra of complex **5.1** (CD_2Cl_2).

Complex 5.2: (*The synthesis was done by Dr. José Bila*) Triethylamine (5 mL) was added dropwise to a solution of compound **5.1** (30 mg, 0.12 mmol) in THF (20 mL) and the reaction mixture stirred overnight at 70 °C. The resulting precipitates were isolated by filtration, washed with THF ((15 mL) and diethyl ether (15 mL) and dried under vacuum to yield a purple powder **5.2** (31 mg, 87%). δ **^{1}H NMR** (CD_3CN, 400 MHz, TMS) δ (ppm) 1.38 (t, 18H, *CH_3*), 3.24 (q, 12H, *CH_2*), 4.43 (s, 4H, *CH_2*), 7.56 (m, 8H, Ar-CH), 8.17 (d, 4H, Ar-CH), 8.32 (d, 6H, Ar-CH), 9.57 (dd, 6H, Ar-CH), **^{13}C NMR** (101 MHz, DMSO): δ (ppm) 8.13 (*CH_3*), 52.7 (*CH_2*), 60.4 (*CH_2*), 124, 125.1, 129.5, 130.2, 132.4, 132.8, (Ar-*C*), 147.9 (N-*C*), (C-B not detected). **HRMS-ESI** (positive mode): *m/z* calculated for $C_{68}H_{66}B_2FeN_8O_6$ $[M]^{2+}$ 584.23149; found: 584.23500.

Complex 5.5: Phenanthrenequinone dioxime (207.1mg, 0.789 mmol), 4-bromomethylphenylboronic acid (113.1 mg, 0.526 mmol) and anhydrous $FeCl_2$ (33.4 mg, 0.261 mmol) were dissolved in MeOH (50 mL) and heated under reflux and inert atmosphere overnight. The dark violet solution obtained was allowed to cool to RT and the solvent was removed under vacuum. The product **5.5** could not be purified by silica gel column chromatography because of its low solubility. NMRs and HR-MS characterizations were not successful for the same reason.

Complex 5.6: Triethylamine (11.5 mL) was added dropwise to a solution of crude compound **5.5** (47.7 mg) in THF (20 mL) and the reaction mixture stirred for 3 days at 70 °C. The resulting precipitate was isolated by filtration, washed with THF (15 mL) and diethyl ether (15 mL) and dried under vacuum to yield a dark violet powder **5.6**. The product **5.6** could not be purified because of its low solubility in all organic solvents tested. ^{1}H and ^{13}C NMRs and HR-MS characterizations were not recorded for the same reason.

8.2.5 Experimental Procedures from Chapter 6

Complex 6.1: A precipitate of 1R-camphorquinone (1.00 g, 6.016 mmol) was prepared in water. A saturated solution of hydroxylamine hydrochloride (20.90 g, 300.8 mmol, 50 eq) and sodium carbonate (31.88 g, 300.8 mmol, 50 eq) was added. The reaction was heated to reflux for two days, cooled at RT for precipitate the product and filtered to obtain a white powder which was extracted with ethyl acetate, dried over $MgSO_4$ and concentrated. The product was

purified by column chromatography (1:1 EA/hexane). **^{1}H NMR** (400 MHz, CD_2Cl_2): δ (ppm) 10.69 (s, 2H), 2.97 (d, 1H), 1.85 (m, 1H), 1.65 (m, 6H), 1.76 (m, 1H), 1.54 (m, 1H), 1.28 (s, 3H), 1.25 (m, 2H), 0.82 (d, 6H). **HRMS (ESI)** *m/z* calcd for $C_{10}H_{16}N_2O_2$ $[M+H]^+$ 197.13, found 197.17.

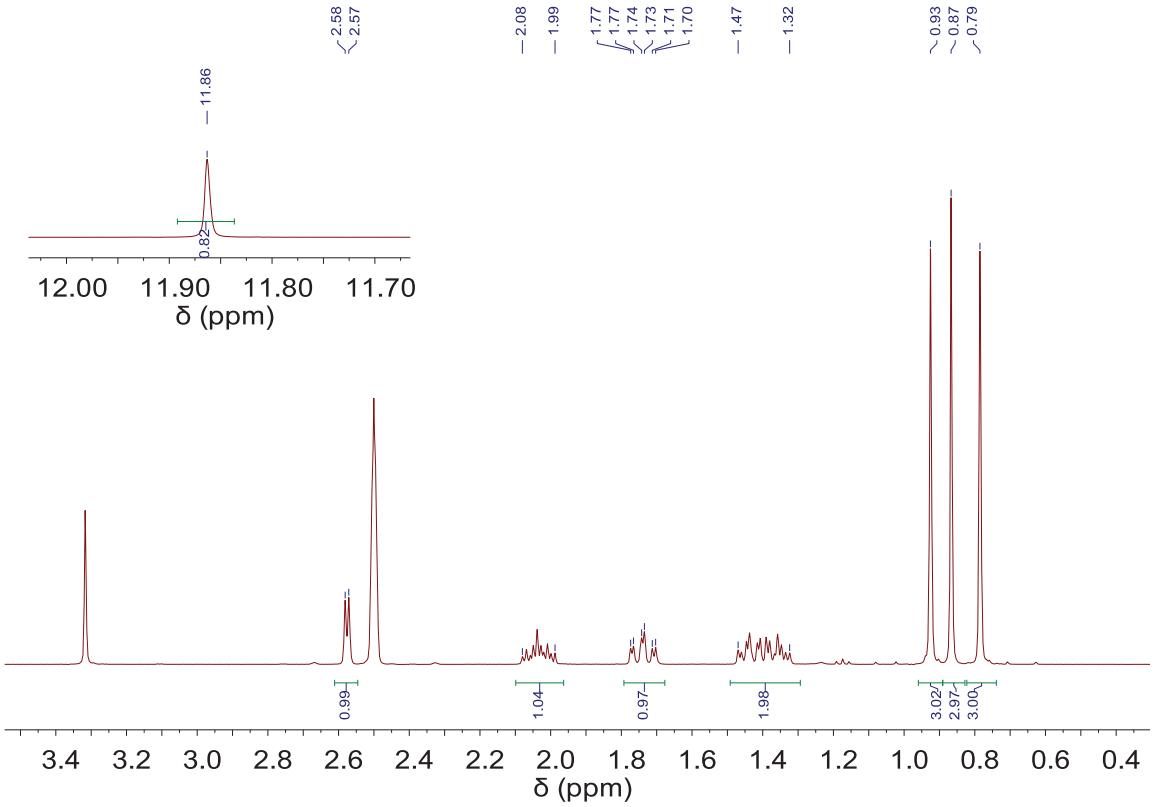

Figure 8.6.1 ^{1}H NMR spectra of mono-oxime **6.2** (DMSO-d_6, 400 MHz)

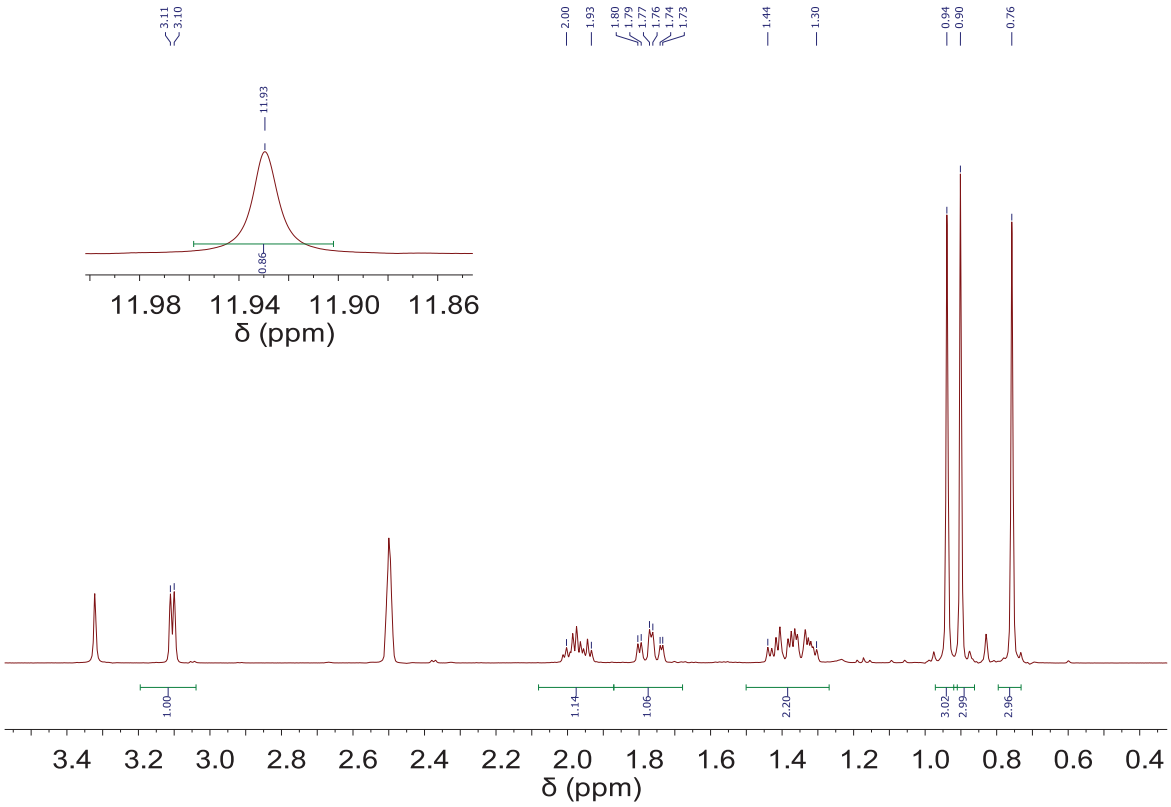

Figure 8.6.2 ^{1}H NMR spectra of mono-oxime **6.3** (DMSO-d_6, 400 MHz)

Synthesis of compounds 6.4-6.6:

Complex 6.4: Camphor-dioxime (120 mg, 0.611 mmol), 3,5-bromophenylboronic acid (114 mg, 0.408 mmol) and anhydrous $FeCl_2$ (25.8 mg, 0.204 mmol) were dissolved in MeOH (150 mL) and heated under reflux and inert atmosphere overnight. The red solution obtained was allowed to cool to RT and the solvent was removed under vacuum. Water was added (120 mL) to the resulting powder.Then, the product was extracted with DCM (140 mL) to yield an orange-red powder. **^{1}H NMR** (400 MHz, CD_2Cl_2): δ (ppm) 7.55 (s, 6H), 3.15 (m, 3H), 2.14 (m, 3H), 1.90 (m, 6H), 1.76 (m, 3H), 1.53 (m, 6H), 1.44 (m, 9H), 0.98 (m, 9H), 0.92 (m, 9H). **^{13}C NMR** (101 MHz, CD_2Cl_2): δ (ppm) 11.77, 11.87, 14.47, 18.03, 18.13, 21.15, 21.39, 23.28, 25.06, 25.12, 27.64, 29.95, 30.24, 32.52, 33.34, 33.45, 49.95, 54.40, 56.15, 56.34, 56.48, 56.61, 122.88, 133.20, 133.28, 133.72, 133.74, 160.20, 160.30, 160.46, 160.55, 161.78, 161.95, 162.14, 162.19 (C-B not detected).

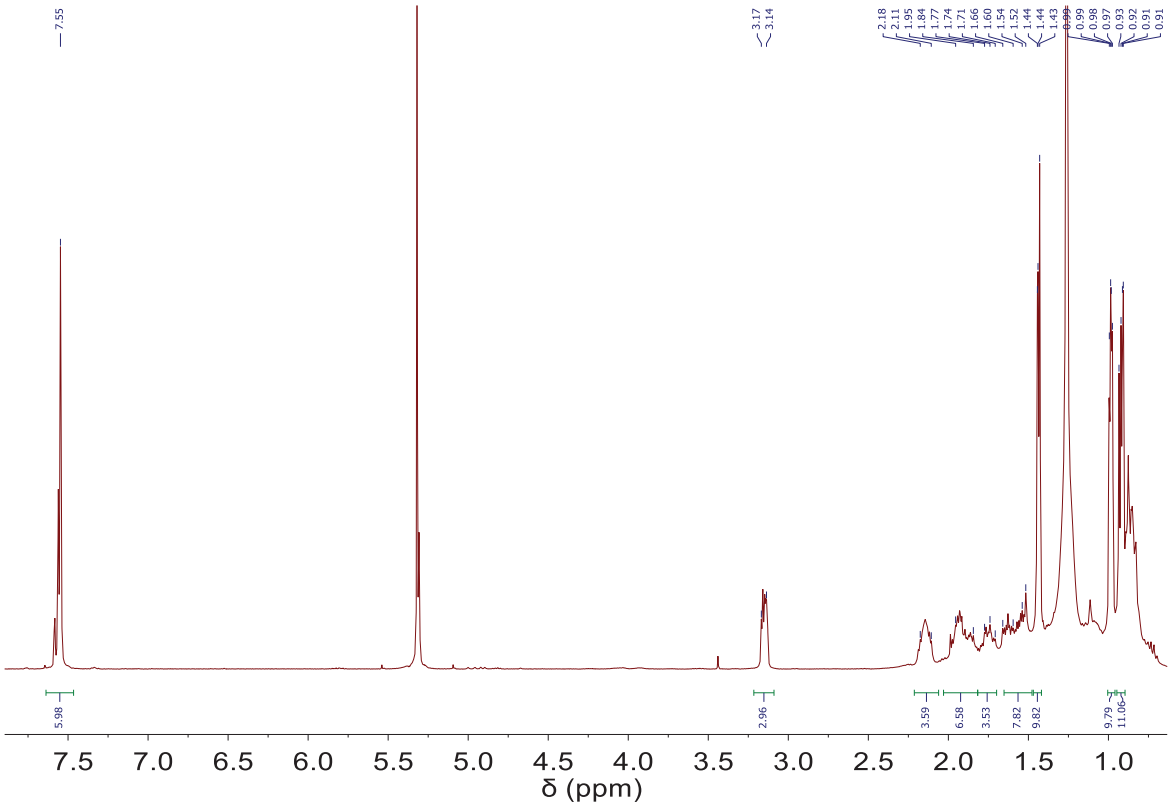

Figure 8.4.14 ^{1}H NMR spectra of complex **6.4** (CD_2Cl_2).

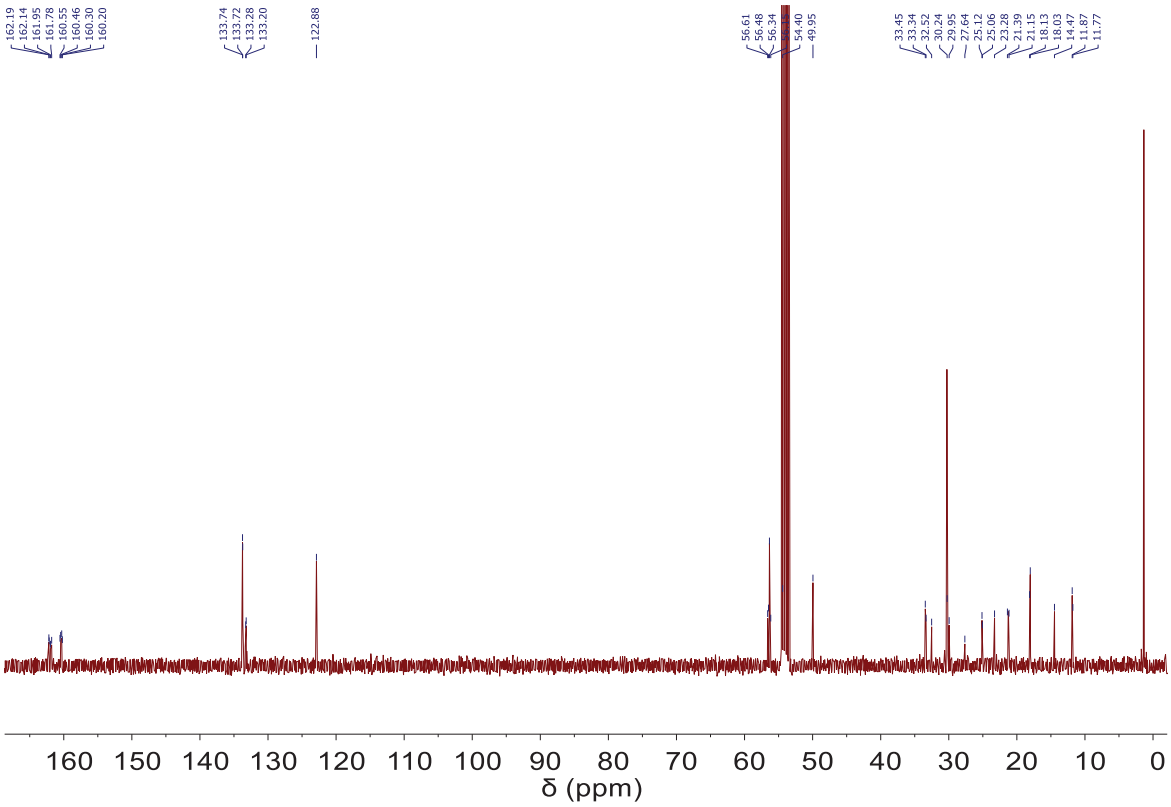

Figure 8.4.15 ^{13}C NMR spectra of complex **6.4** (CD_2Cl_2).

Complex 6.5: Camphor-dioxime (82.4 mg, 0.420 mmol), 4-carboxyphenylboronic acid (46.4 mg, 0.280 mmol) and anhydrous $FeCl_2$ (17.7 mg, 0.140 mmol) were dissolved in MeOH (150 mL) and heated under reflux and inert atmosphere overnight. The red solution obtained was allowed to cool to RT and the solvent was removed under vacuum. Water was added (120 mL) to the resulting powder.Then, the product was extracted with DCM (140 mL) to yield an orange-red powder. ^{1}H NMR and ^{13}C NMR were not recorded. **HRMS (ESI TOF)** *m/z* calculated for $C_{44}H_{52}B_2FeN_6O_{10}$ $[M+H]^+$ 902.3296; found: 902.3300.

Complex 6.6: Camphor-dioxime (51.0 mg, 0.260 mmol), 3-pyridylphenylboronic acid (21.2 mg, 0.173 mmol) and anhydrous $FeCl_2$ (10.9 mg, 0.087 mmol) were dissolved in MeOH (50 mL) and heated under reflux and inert atmosphere overnight. The red solution obtained was allowed to cool to RT and the solvent was removed under vacuum. Water was added (100 mL) to the resulting powder.Then, the product was extracted with DCM (120 mL) to yield an orange-red powder. **^{1}H NMR** (400 MHz, CD_2Cl_2): δ (ppm) 7.49 (m, 3H), 7.24 (m, 5H), 3.13 (dd, 3H), 2.13 (m, 3H), 1.85 (m, 6H), 1.62 (m, 3H), 1.52-1.43 (m, 13H), 0.98-0.91 (m, 23H). **HRMS (ESI TOF)** *m/z* calculated for $C_{40}H_{50}B_2FeN_8O_6$ $[M+H]^+$ 817.3388; found: 817.5800.

Attempted synthesis of a coordination cags with clathrochelate 6.6:

A solution of tetrakis(acetonitrile)palladium(II) tetrafluoroborate (18.0 mg, 16.5 µmol) in MeCN-*deuterated* (1.2 mL) was prepared. A second solution of the clathrochelate **6.6** (3.2 mg, 4.60 µmol, 2 eq) in MeCN-*deuterated* (V_{total} = 8 mL) was added. The reaction was heated to 50°C overnight. Discoloration was observed, indicating decomposition of **6.6**.

8.3 Crystallographic Data

Crystallographic data for the compounds from Chapter 2

Data were collected using a SuperNova, Dual, Cu at zero, AtlasS2 diffractometer operating at *T* = 140.00(10) K for **2.1, 2.2** and **2.3** and at 100.00(10) K for cage **2.7**. Data were measured using ω scans using Cu K_α radiation. The diffraction pattern was indexed and the total number of runs and images was based on the strategy calculation from the program CrysAlis^{Pro}.[133]

Data reduction, scaling and absorption corrections were performed using CrysAlis^{Pro}.[133]

The structure was solved with the ShelXT solution program[2] using dual methods and by using Olex2 as the graphical interface[134]. The model was refined with ShelXL 2018/3 using full matrix least squares minimisation on *F*[135-136]. All non-hydrogen atoms were refined anisotropically. Hydrogen atom positions were calculated geometrically and refined using the riding model. Disordered solvent molecules in **2.1** and **2.2** were removed by SQUEEZE.[136]

Additional electron density in **2.3** and **2.7**, too disordered to be modelled, was taken into account by using the solvent-masking program in Olex2.[136]

Crystallographic data have been deposited with the Cambridge Crystallographic Data Centre and correspond to the following codes: **2.1** (2018324), **2.2** (2018325), **2.3** (2018313), **2.7** (2018314).

Compound	**2.1**	**2.2**	**2.3**
Formula	$C_{62}H_{74}B_4Cl_4Fe_2N_{12}O_{16}$	$C_{60}H_{70}B_4Fe_2N_{12}O_{16}$	$C_{60}H_{70}B_4Fe_2N_{12}O_{16}$
$D_{calc.}$/ g cm^{-3}	1.262	1.040	1.329
μ/mm^{-1}	4.624	3.134	4.005
Formula Weight	1540.07	1370.22	1370.22
Colour	clear dark red	clear intense orange	clear intense orange
Shape	prism	plate	plate
Size/mm^3	0.23×0.10×0.07	0.50×0.28×0.15	0.26×0.20×0.03
T/K	140.00(10)	140.00(10)	140.00(10)
Crystal System	triclinic	monoclinic	triclinic
Space Group	$P\bar{1}$	*C*2/*c*	$P\bar{1}$
a/Å	14.3805(12)	30.531(3)	9.3332(17)
b/Å	15.0135(9)	15.7057(7)	16.089(2)
c/Å	20.5688(16)	37.830(3)	24.3598(19)
α/°	75.919(6)	90	97.384(9)
β/°	79.102(7)	105.320(8)	99.238(10)
γ/°	71.401(7)	90	105.469(14)
V/Å^3	4052.3(6)	17496(2)	3422.8(9)
Z	2	8	2
Z'	1	1	1
Wavelength/Å	1.54184	1.54184	1.54184
Radiation type	Cu$K\alpha$	Cu$K\alpha$	Cu$K\alpha$
Θ_{min}/°	3.168	3.001	3.720
Θ_{max}/°	72.966	50.435	73.416
Measured Refl's.	33053	38965	23790
Ind't Refl's	15611	9144	13079
Refl's with I > 2σ(I)	10472	4902	6113
R_{int}	0.0571	0.1186	0.0855
Parameters	960	897	833
Restraints	228	1913	1529
Largest Peak/e Å^{-3}	1.950	1.035	1.235
Deepest Hole/e Å^{-3}	-0.618	-0.550	-0.712
GooF	1.044	1.451	1.147
wR_2 (all data)	0.2916	0.4444	0.4078
wR_2	0.2671	0.4080	0.3465
R_1 (all data)	0.1273	0.2027	0.2102
R_1	0.0993	0.1467	0.1333

Compound	**2.7**	**2.8**
Formula	$C_{236}H_{268}B_{16}Cu_4Fe_8N_{52}O_{68}$	$C_{60}H_{69}B_4Fe_2N_{13}O_{17}Zn$
$D_{calc.}$/ g cm^{-3}	0.844	1.182
μ/mm^{-1}	2.612	3.661
Formula Weight	5794.93	1464.59
Colour	clear dark orange	clear intense orange
Shape	plate	plate
Size/mm^3	0.21×0.05×0.03	0.14×0.08×0.07
T/K	100.00(10)	100.01(10)
Crystal System	triclinic	monoclinic
Space Group	$P\bar{1}$	*C*2/*c*
a/Å	23.4228(10)	30.411(3)
b/Å	24.0133(10)	15.0758(8)
c/Å	25.6304(10)	36.831(3)
α/°	116.951(4)	90
β/°	92.159(3)	102.957(11)
γ/°	113.175(4)	90
V/Å^3	11395.5(9)	16456(3)
Z	1	8
Z'	0.5	1
Wavelength/Å	1.54184	1.54184
Radiation type	Cu $K\alpha$	Cu $K\alpha$
Θ_{min}/°	2.625	3.393
Θ_{max}/°	76.311	51.161
Measured Refl's.	85267	36264
Ind't Refl's	45920	8833
Refl's with I > 2σ(I)	19215	5418
R_{int}	0.0958	0.0880
Parameters	1872	971
Restraints	1397	314
Largest Peak/e Å^{-3}	0.745	0.664
Deepest Hole/e Å^{-3}	-0.745	-0.642
GooF	0.854	1.021
wR_2 (all data)	0.2374	0.2165
wR_2	0.2064	0.1902
R_1 (all data)	0.1460	0.1259
R_1	0.0826	0.0805

Crystallographic data for the compounds from Chapter 3

Bragg-intensities of **3.3a**, **3.3d**, **3.5** and **3.7** were collected at different temperatures using Cu *Kα* radiation. A Rigaku SuperNova dual system diffractometer with an Atlas CCD detector was used for compounds **3.3a** and **3.7**, and one equipped with an Atlas S2 CCD detector for compounds **3.3d** and **3.5**. The datasets were reduced and corrected for absorption, with the help of a set of faces enclosing the crystals as snugly as possible, with *CrysAlis*^{Pro}.[133-134]

The solutions and refinements of the structures were performed by the latest available version of *ShelXT* and *ShelXL*.[135] All non-hydrogen atoms were refined anisotropically using full-matrix least-squares based on $|F|^2$. The hydrogen atoms were placed at calculated positions by means of the "riding" model in which each H-atom was assigned a fixed isotropic displacement parameter with a value equal to 1.2 U_{eq} of its parent C-atom (1.5 U_{eq} for the methyl groups). This model failed, however, in **3.5** for all hydrogens and in **3.7** for those on the clathrochelate. This failure is due to the existence of orientational disorder compounded by the presence of reflection-symmetries (no reasonably complex molecule will crystallise in a space group such as *I*4/*mmm* without need). The appropriate treatment of this kind of disorder much exceeds the capacities of today's programs.

Crystallographic data have been deposited with the Cambridge Crystallographic Data Centre and correspond to the following codes: **3.3a** (1972501), **3.3d** (1972502), **3.5** (1972503) and **3.7** (1972505). These data can be obtained free of charge via www.ccdc.cam.ac.uk/data_request/cif, or by emailing data_request@ccdc.cam.ac.uk, or by contacting The Cambridge Crystallographic Data Centre.

The structure of most MOFs are highly disordered in general. This disorder, due to orientational or dynamical disorder, voids and guest molecules, often generates reflection-symmetries further compounding the situation. Therefore, we are often facing broad and weak reflections, especially at high angles, resulting in a too low number of reflections and unsatisfactory confidence factors.

Additional electron density found in the difference Fourier map (due to highly disordered solvent and counter-ion molecules) was removed in all structures by help of the solvent-masking program in *OLEX2.*[136]

Compound	**3.3a**	**3.3d**	**3.5**	**3.7**
Formula	$C_{50}H_{30}B_2Br_2FeN_8O_{14}Zn_2$	$C_{63}H_{46}B_2Br_2FeN_8O_{14}Zn_2$	$B_6C_{158}Fe_3N_{32}O_{34}Zn_6$	$C_{64}H_{32}B_2FeN_{12}O_{14}Zn_3$
$D_{calc.}$/ g cm^{-3}	0.556	0.654	0.489	0.403
μ/mm^{-1}	1.865	1.975	1.275	0.977
Formula Weight	1334.85	1507.11	3514.53	1466.59
Colour	clear intense orange	clear intense orange	clear dark purple	clear intense purple
Shape	prism	plate	plate	prism
Size/mm^3	0.52×0.20×0.08	0.55×0.18×0.07	0.49×0.34×0.05	0.55×0.18×0.13
T/K	210.00(10)	293(2)	200.00(10)	140.00(10)
Crystal System	orthorhombic	orthorhombic	tetragonal	orthorhombic
Space Group	*Pmmm*	*Pmmm*	*I*4/*mmm*	*Pmmm*
a/Å	11.6785(5)	10.9173(7)	16.71400(10)	16.2432(10)
b/Å	15.6070(4)	16.0826(7)	16.71400(10)	17.1019(17)
c/Å	21.8880(11)	21.8056(17)	85.4144(11)	21.7542(17)
α/°	90	90	90	90
β/°	90	90	90	90
γ/°	90	90	90	90
V/Å^3	3989.4(3)	3828.6(4)	23861.2(4)	6043.1(8)
Z	1	1	2	1
Z'	0.125	0.125	0.0625	0.125
Wavelength/Å	1.54184	1.54184	1.54184	1.54184
Radiation type	Cu $K\alpha$	Cu $K\alpha$	Cu $K\alpha$	Cu $K\alpha$
Θ_{min}/°	3.478	2.748	4.276	3.753
Θ_{max}/°	75.469	66.595	50.430	50.421
Measured Refl's.	25183	14886	51832	14293
Ind't Refl's	4416	3806	3632	3552
Refl's with I > 2(I)	3156	2840	3338	2744
R_{int}	0.0815	0.0498	0.0528	0.0731
Parameters	136	173	276	200
Restraints	260	323	704	421
Largest Peak/e Å^{-3}	1.957	3.223	2.220	4.430
Deepest Hole/e Å^{-3}	-1.521	-1.163	-1.101	-1.160
GooF	1.282	1.556	1.985	1.517
wR_2 (all data)	0.3362	0.3848	0.4001	0.3785
wR_2	0.3184	0.3671	0.3891	0.3593
R_1 (all data)	0.1201	0.1484	0.1136	0.1502
R_1	0.1063	0.1339	0.1096	0.1339
Total accessible volume/Å^3	2974.9	2332.5	17878.2	4794.2

Crystallographic data for the compounds from Chapter 4

Data were measured using ω scans using Cu K_α radiation for complexes **4.1**, **4.3**, **4.4**, **4.6** and for Mo K_α radiation complexes **4.2** and **4.5**. The diffraction pattern was indexed and the total number of runs and images was based on the strategy calculation from the program CrysAlis^{Pro}.[133-134]

Compound	**4.1**	**4.2**	**4.3**
Formula	$C_{30}H_{34}B_2CoN_6O_6$	$C_{32}H_{27}B_2CoF_{10}N_7O_6$	$C_{50}H_{74}B_2CoKN_6O_{14}$
$D_{calc.}$/ g cm^{-3}	1.397	1.720	1.007
μ/mm^{-1}	4.758	0.621	2.788
Formula Weight	655.18	876.15	1102.80
Colour	clear dark red	clear dark red	clear dark blue
Shape	needle	prism	needle
Size/mm^3	0.69×0.04×0.02	0.35×0.26×0.19	0.77×0.05×0.04
T/K	140.00(10)	140.00(10)	140.00(10)
Crystal System	triclinic	triclinic	trigonal
Space Group	$P\bar{1}$	P-1	R-3
a/Å	10.9358(3)	9.4558(3)	49.7043(14)
b/Å	11.9819(4)	13.1751(4)	49.7043(14)
c/Å	13.2216(3)	14.2464(4)	15.3050(5)
α/°	105.448(2)	96.039(2)	90
β/°	94.284(2)	95.933(2)	90
γ/°	108.634(3)	104.624(3)	120
V/Å^3	1557.91(8)	1692.17(8)	32746(2)
Z	2	2	18
Z'	1	1	1
Wavelength/Å	1.54184	0.71073	1.54184
Radiation type	Cu K_α	Mo K_α	Cu K_α
Θ_{min}/°	3.523	2.754	3.064
Θ_{max}/°	75.928	37.602	73.048
Measured Refl's.	15931	36159	53661
Ind't Refl's	6399	16953	14044
Refl's with I > 2σ(I)	5985	14030	9245
R_{int}	0.0254	0.0214	0.0618
Parameters	506	524	732
Restraints	334	0	158
Largest Peak/e Å^{-3}	0.343	0.565	0.299
Deepest Hole/e Å^{-3}	-0.264	-0.600	-0.272
GooF	1.043	1.039	0.964
wR_2 (all data)	0.0867	0.0923	0.1094
wR_2	0.0851	0.0853	0.0989
R_1 (all data)	0.0371	0.0487	0.0792
R_1	0.0341	0.0365	0.0467

Compound	**4.4**	**4.5**	**4.6**
Formula	$C_{92}H_{112}B_4Co_2F_{20}K_2N_{12}O_{26}$	$C_{56}H_{38}B_2Cl_4CoN_6O_6$	$C_{86}H_{98}B_2CoKN_6O_{17}$
$D_{calc.}$/ g cm^{-3}	1.394	1.568	1.359
μ/mm^{-1}	3.814	0.655	2.796
Formula Weight	2421.23	1113.27	1607.35
Colour	black	red	dark green
Shape	plate	prism	plate
Size/mm^3	0.60×0.41×0.04	0.36×0.08×0.05	0.92×0.29×0.09
T/K	139.99(10)	140.00(10)	140.00(10)
Crystal System	orthorhombic	orthorhombic	triclinic
Space Group	*Pbcn*	*Pca*2$_1$	*P*-1
a/Å	51.542(3)	19.1336(4)	12.5787(4)
b/Å	22.7187(10)	10.5861(3)	13.2453(5)
c/Å	19.7112(9)	46.5572(12)	27.0193(7)
α/°	90	90	84.868(2)
β/°	90	90	77.958(2)
γ/°	90	90	63.112(3)
V/Å^3	23081(2)	9430.2(4)	3926.6(2)
Z	8	8	2
Z'	1	2	1
Wavelength/Å	1.54184	0.71073	1.54184
Radiation type	Cu K$_\alpha$	Mo K$_\alpha$	Cu K$_\alpha$
Θ_{min}/°	3.090	2.903	3.345
Θ_{max}/°	66.600	29.490	80.805
Measured Refl's.	111775	104007	42864
Ind't Refl's	20373	23042	16040
Refl's with I > 2σ(I)	12314	17309	13789
R_{int}	0.1525	0.0624	0.0498
Parameters	1518	1352	1074
Restraints	469	1379	210
Largest Peak/e Å^{-3}	1.709	0.530	1.211
Deepest Hole/e Å^{-3}	-1.229	-0.654	-0.781
GooF	1.049	1.057	1.068
wR_2 (all data)	0.3998	0.1336	0.1925
wR_2	0.3666	0.1189	0.1850
R_1 (all data)	0.1743	0.0895	0.0774
R_1	0.1376	0.0593	0.0681

Crystallographic data for the compounds from Chapter 6

A final ata refinement was not performed for **6.1b**, because of the poor quality quality of the diffraction data.

Chapter 9

References

1) J. D. Curry, D. H. Busch*, J. Am. Chem. Soc*. **1964**, 86, 592-594.

2) a) Y.Z. Voloshin, N.A. Kostromina, Clathrochelates: Synthesis, Structure and Properties, Elsevier, **2002**. b) R. Voloshin, Y. Belaya, I. Krämer, Cage Metal Complexes: Clathrochelates Revisited, Springer, **2017**.

3) D. R. Boston, N. J. Rose, *J. Am. Chem. Soc*. **1968**, 90, 6859-6860.

4) M. D. Wise, K. Severin, "Functionalised Clathrochelate Complexes as Supramolecular Building Blocks." EPFL, **2015**.

5) Y. Z. Voloshin, S. V. Korobko, A. V. Dolganov, V. V. Novikov, A. V. Vologzhanina, Y. N. Bubnov, *Inorg. Chem. Commun*. **2011**, 14, 1043-1047.

6) Y. Z. Voloshin, O. A. Varzatskii, S. V. Kobko, M. Y. Antipin, I. I. Vorontsov, K. A. Lyssenko, D. I. Kochubey, S. G. Nikitenko, N. G. Strizhakova, *Inorg. Chim. Acta* **2004**, 357, 3187-3204.

7) Y. Z. Voloshin, E. V. Polshin, *Polyhedron* **1992**, 11, 457-461.

8) Y. Z. Voloshin, O. A. Varzatskii, A. S. Belov, Z. A. Starikova, N. G. Strizhakova, A. V. Dolganov, D. I. Kochubey, Y. N. Bubnov, *Inorg. Chim. Acta* **2010**, 363, 134-146.

9) R. S. Drago, J. H. Elias, *J. Am. Chem. Soc.* **1977**, 99, 6570-6577.

10) Y. Z. Voloshin, A. V. Dolganov, O. A. Varzatskii, Y. N. Bubnov, *Chem Commun.* **2011**, 47, 7737-7739.

11) P. Zhang, M. Wang, J. Dong, X. Li, F. Wang, L. Wu, L. Sun, *J. Phys. Chem. C*. **2010**, 114, 15868-15874.

12) Y. Z. Voloshin, O. A. Varzatskii, A. S. Belov, A. Y. Lebedev, I. S. Makarov, M. E. Gurskii, M. Y. Antipin, Z. A. Starikova, Y. N. Bubnov, *Inorg. Chim. Acta* **2007**, 360, 1543-1554.

13) Y. Z. Voloshin, O. A. Varzatskii, A. I. Stash, V. K. Belsky, Y. N. Bubnov, I. I. Vorontsov, K. A. Potekhin, M. Y. Antipin, E. V. Polshin, *Polyhedron* **2001**, 20, 2721-2733.

14) S. A. Kubow, K. J. Takeuchi, J. J. Grzybowski, A. J. Jircitano, V. L. Goedken, *Inorg. Chim. Acta* **1996**, 241, 21-30.

15) S. M. Jansze, K. Severin, *Acc. Chem. Res*. **2018**, 51, 2139-2147.

16) a) J. G. Muller, J. J. Grzybowski, K. J. Takeuchi, *Inorg. Chem*. **1986**, 25, 2665-2667. b) Y. Z. Voloshin, V. V. Novikov, Y. V. Nelyubina, A. S. Belov, D. M. Roitershtein, A. Savitsky, A. Mokhir, J. Sutter, M. E. Miehlich, K. Meyer, *Chem. Commun*. **2018**, 54, 3436-3439. c) Y. Z.

Voloshin, O. A. Varzatskii, A. V. Palchik, N. G. Strizhakova, I. I. Vorontsov, M. Y. Antipin, D. I.Kochubey, B. N. Novgorodov, *New J. Chem.* **2003**, 27, 1148-1155. d) Y. Z. Voloshin, O. A. Varzatskii, V. V. Novikov, N. G. Strizhakova, I. I. Vorontsov, A. V. Vologzhanina, K. A. Lyssenko, G. V. Romanenko, M. V. Fedin, V. I. Ovcharenko, Y. N. Bubnov, *Eur. J. Inorg. Chem*. **2010**, 5401-5415.

17) G. E. Zelinskii, A. S. Belov, I. G. Belaya, A. V. Vologzhanina, V. V. Novikov, O. A. Varzatskii, Y. Z. Voloshin, *New J. Chem.* **2017**, 41, 3251-3259.

18) I. N. Denisenko, O. A. Varzatskii, R. A. Selin, A. S. Belov, E. G. Lebed, A. V. Vologzhanina, Y. V. Zubavichus, Y. Z. Voloshin, *RSC Adv*. **2018**, 13578-13587.

19) C. Engtrakul, W. J. Shoemaker, J. J. Grzybowski, I. Guzei, A. Rheingold*, Inorg. Chem*. **2000,** 39, 5161-5163.

20) O. Pantani, S. Naskar, R. Guillot, P. Millet, E. Anxolabèhére-Mallart, A. Aukauloo*, Angew. Chem. Int. Ed*. **2008**, 47, 9948-9950.

21) M. Robbins, D. Naser, J. Heiland, J. Grzybowski*, Inorg. Chem*. **1985**, 24, 3381-3387.

22) J. W. Steed, J. L. Atwood, Supramolecular Chemistry, Wiley, Chichester, UK, **2009**.

23) M. D. Wise, A. Ruggi, M. Pascu, R. Scopelliti, K. Severin, *Chem. Sci*. **2013**, 4, 1658-1662.

24) Y. Y. Zhang, Y. J. Lin, G. X. Jin, *Chem. Commun.* **2014**, 50, 2327-2329.

25) M. D. Wise, J. J. Holstein, P. Pattison, C. Besnard, E. Solari, R. Scopelliti, G. Bricogne, K. Severin, *Chem. Sci.* **2015**, 6, 1004-1010.

26) S. M. Jansze, G. Cecot, M. D. Wise, K. O. Zhurov, T. K. Ronson, A. M. Castilla, A. Finelli, P. Pattison, E. Solari, R. Scopelliti, et al., *J. Am. Chem. Soc*. **2016**, 138, 2046-2054.

27) G. Cecot, B. Alameddine, S. Prior, R. De Zorzi, S. Geremia, R. Scopelliti, F. T. Fadaei, E. Solari, K. Severin, *Chem. Commun*. **2016**, 52, 11243-11246.

28) G. Cecot, M. Marmier, S. Geremia, R. De Zorzi, A. V. Vologzhanina, P. Pattison, E. Solari, F. Fadaei Tirani, R. Scopelliti, K. Severin*, J. Am. Chem. Soc*. **2017**, 139, 8371-8381.

29) G. Cecot, M. T. Doll, O. M. Planes, A. Ramorini, R. Scopelliti, F. Fadaei-Tirani, K. Severin, *Eur. J. Inorg. Chem*. **2019**, 2972-2976.

30) S. M. Jansze, D. Ortiz, F. Fadaei Tirani, R. Scopelliti, L. Menin, K. Severin, *Chem. Commun.* **2018**, 54, 9529-9532.

31) M. Marmier, M. D. Wise, J. J. Holstein, P. Pattison, K. Schenk, E. Solari, R. Scopelliti, K. Severin, *Inorg. Chem.* **2016**, 55, 4006-4015.

32) W. Liu, W. Huang, M. Pink, D. Lee*, J. Am. Chem. Soc*. **2010**, 132, 11844-11846.

33) J. L. Bila, J. Pijeat, A. Ramorini, F. Fadaei-Tirani, R. Scopelliti, E. Baudat, K. Severin *Dalton Trans*. **2019**, 48, 4582-4588.

34) Y. Z. Voloshin, V. V. Novikov, Y. V. Nelyubina, *RSC Adv*. **2015**, 5, 72621-72637.

35) O. A. Varzatskii, V. V. Novikov, S. V. Shulga, A. S. Belov, A. V. Vologzhanina, V. V. Negrutska, I. Y. Dubey, Y. N. Bubnov, Y. Z. Voloshin, *Chem. Commun*. **2014**, 50, 3166-3168.

36) V. V Novikov, O. A. Varzatskii, V. V. Negrutska, Y. N. Bubnov, L. G. Palchykovska, I. Y. Dubey, Y. Z. Voloshin, *J. Inorg. Biochem*. **2013**, 124, 42-45.

37) A. S. Belov, A. V. Vologzhanina, V. V. Novikov, V. V. Negrutska, I. Y. Dubey, Z. A. Mikhailova, E. G. Lebed, Y. Z. Voloshin*, Inorg. Chim. Acta* **2014**, 421, 300-306.

38) P. Connolly, J. H. Espenson, *Inorg. Chem.* **1986**, 25, 2684-2688.

39) O. Pantani, S. Naskar, R. Guillot, P. Millet, E. Anxolabéhère-Mallart, A. Aukauloo, *Angew. Chem. Int. Ed.* **2008**, 47, 9948-9950.

40) M. Antuch, A. Ranjbari, S. A. Grigoriev, J. Al-Cheikh, A. Villagrá, L. Assaud, Y. Z. Voloshin, P. Millet, *Electrochim. Acta* **2017**, 245, 1065-1074.

41) A. V. Dolganov, A. S. Belov, V. V. Novikov, A. V. Vologzhanina, A. Mokhir, Y. N. Bubnov, Y. Z. Voloshin, *Dalton Trans*. **2013**, 42, 4373-4376.

42) Y. Z. Voloshin, A. V. Dolganov, O. A. Varzatskii, Y. N. Bubnov, *Chem. Commun*. **2011**, 47, 7737-7739.

43) M. Antuch, P. Millet, A. Iwase, A.Kudo, S. A. Grigoriev, Y. Z. Voloshin, *Electrochim. Acta* **2017**, 258, 255-265.

44) A. S. Pushkarev, M. A. Solovyev, S. A. Grigoriev, I. V. Pushkareva, Y. Z. Voloshin, N. V. Chornenka, A. S. Belov, P. Millet, V. N. Kalinichenko, A. G. Dedov*, Int. J. Hydrog. Energy* **2020**, 45, 26206-26216.

45) J. Al Cheikh, A. Villagra, A. Ranjbari, A. Pradon, M. Antuch, D. Dragoe, P. Millet, L. Assaud, *Appl. Catal. B-Environ*. **2019**, 250, 292-300.

46) S. A. Grigoriev, A. S. Pushkarev, I. V. Pushkareva, P. Millet, A. S. Belov, V. V. Novikov, I. G. Belaya, Y. Z. Voloshin, *Int. J. Hydrog. Energy* **2017**, 42, 27845-27850.

47) A. G. Dedov, Y. Z. Voloshin, A. S. Belov, A. S. Loktev, A. S. Bespalov, V. M. Buznik, *Mendeleev Communications* **2019**, 29, 669-671.

48) Y. A. Kabachii, S. Y. Kochev, S. S. Abramchuk, A. S. Golub, P. M. Valetskii, O. Y. Antonova, Y. N. Bubnov, V. A. Nadtochenko, *Russ. Chem. Bull*. **2017**, 66, 2048-2056.

49) A. V. Dolganov, O. V. Tarasova, D. N. Moiseeva, E. E. Muryumin, *Int. J. Hydrog. Energy* **2016**, 41, 9312-9319.

50) Y. Z. Voloshin, A. S. Belov, A. V. Vologzhanina, G. G. Aleksandrov, A. V. Dolganov, V. V. Novikov, O. A. Varzatskii, Y. N. Bubnov, *Dalton Trans*. **2012**, 41, 6078-6093.

51) S. El Ghachtouli, M. Fournier, S. Cherdo, R. Guillot, M. F. Charlot, E. Anxolabéhère-Mallart, M. Robert, A. Aukauloo, *J. Phys. Chem. C* **2013**, 117, 17073-17077.

52) For review articles, see: (a) H. Ghasempour, K. Y. Wang, J. A. Powell, F. ZareKarizi, X. L. Lv, A. Morsali, H. C. Zhou, *Coord. Chem. Rev.* **2021**, 426. (b) X. X. Xie, Y. C. Yang, B. H. Dou, Z. F. Li, G. Li, *Coord. Chem. Rev*. **2020**, 403. (c) S. Ali Akbar Razavi, A. Morsali, *Coord. Chem. Rev.* **2019**, 399. (d) S. Yuan, L. Feng, K. Wang, J. Pang, M. Bosch, C. Lollar, Y. Sun, J. Qin, X. Yang, P. Zhang, Q. Wang, L. Zou, Y. Zhang, L. Zhang, Y. Fang, J. Li, H. C. Zhou, *Adv. Mater.* **2018**, 30-. (e) M. Bosch, S. Yuan, W. Rutledge, H. C. Zhou, *Acc. Chem. Res*. **2017**, 50, 857-865.

53) For selected examples, see:

(a) Y. Ye, T. R. Cook, S. P. Wang, J. Wu, S. Li, P. J. Stang, *J. Am. Chem. Soc*. **2015**, 137, 11896-11899. (b) B. Kilbas, S. Mirtschin, R. Scopelliti, K. Severin, *Chem. Sci*. **2012**, 3, 701-704. (c) S. Mirtschin, A. Slabon-Turski, R. Scopelliti, A. H. Velders, K. Severin, *J. Am. Chem. Soc*. **2010**, 132, 14004-14005. (d) F. A. Cotton, C. A. Murillo, R. Yu, *Dalton Trans*. **2006**, 3900-3905. (e) F. A. Cotton, C. A. Murillo, S. E. Stiriba, X. Wang, R. Yu, *Inorg. Chem.* **2005**, 44, 8223-8233. (f) P. S. Mukherjee, N. Das, Y. K. Kryschenko, A. M. Arif, P. J. Stang, *J. Am. Chem. Soc.* **2004**, 126, 2464-2473. (g) N. Das, P. S. Mukherjee, A. M. Arif, P. J. Stang, *J. Am. Chem. Soc*. **2003**, 125, 13950-13951.

(h) J. K. Bera, P. Angaridis, F. A. Cotton, M. A. Petrukhina, P. E. Fanwick, R. A. Walton, R. *J. Am. Chem. Soc.* **2001**, 123, 1515-1516.

54) For review articles, see:

(a) E. J. Gosselin, C. A. Rowland, E. D. Bloch, *Chem. Rev*. **2020**, 120, 8987-9014. (b) E. S. M. El-Sayed, D. Yuan, *Chem. Lett.* **2020**, 49, 28-53. (c) G. E. Decker, G. R. Lorzing, M. M. Deegan, E. D. Bloch, *J. Mater. Chem.* **2020**, 8, 4217-4229. (d) S. Mollick, S. Fajal, S. Mukherjee, S. K. Ghosh, *Chem. - Asian J.* **2019**, 14, 3096-3108. (e) N. Hosono, S. Kitagawa, *Acc. Chem. Res*. **2018**, 51, 2437-2446. (f) N. Ahmad, A. H. Chughtai, H. A. Younus, F. Verpoort, *Coord. Chem. Rev*. **2014**, 280, 1-27. (g) M. Köberl, W. A. Cokoja, W. A. Herrmann, F. E. Kühn, *Dalton Trans*. **2011**, 40, 6834-6859.

55) For review articles on metalloligands, see:

(a) M. Hardy, A. Lützen, *Chem. - Eur. J*. **2020** (b) F. Li, L. F. Lindoy, *Aust. J. Chem*. **2019**, 72, 731-741. (c) J. Gil-Rubio, J. Vicente, *Chem. - Eur. J*. **2018**, 24, 32-46. (d) S. Srivastava, R. Gupta, *CrystEngComm* **2016**, 18, 9185-9208. (e) L. Li, D. J. Fanna, N. D. Shepherd, L. F. Lindoy, F. Li, *J. Inclusion Phenom. Macrocyclic Chem*. **2015**, 82, 3-12. (f) G. Kumar, R. Gupta, *Chem. Soc. Rev.* **2013**, 42, 9403-9453. (g) E. C. Constable, *Coord. Chem. Rev*. **2008**, 252, 842-855.

56) (a) S. M. Jansze, M. D. Wise, A. V. Vologzhanina, R. Scopelliti, K. Severin, *Chem. Sci*. **2017**, 8, 1901-1908. (b) A. Ardavan, A. M. Bowen, A. Fernandez, A. J. Fielding, D. Kaminski, F. Moro, C. A. Muryn, M. D. Wise, A. Ruggi, E. J. L. McInnes, K. Severin, G. A. Timco, F. Tuna, G. F. S. Whitehead, R. E. P. Winpenny, *npj Quantum Inf*. **2015**, 1, 15012.

57) (a) S. A. Boer, W. Cao, B. K. Glascott, D. R. Turner, *Chemistry* **2020**, 2, 613-625. (b) G. A. Taggart, G. R. Lorzing, M. R. Dworzak, G. P. A. Yap, E. D. Bloch, *Chem. Commun*. **2020**, 56, 8924-8927. (c) W. M. Bloch, R. Babarao, M. L. Schneider, *Chem. Sci*. **2020**, 11, 3664-3671. (d) G. A. Craig, P. Larpent, H. Urabe, A. Legrand, M. Bonneau, S. Kusaka, S. Furukawa, *Chem. Commun.* **2020**, 56, 3689-3692. (e) G. A. Craig, P. Larpent, S. Kusaka, R. Matsuda, S. Kitagawa, S. Furukawa, *Chem. Sci*. **2018**, 9, 6463-6469. (f) J. Kang, L. Chen, H. Cui, L. Zhang, C. Y. Su, *Chin. J. Chem*. **2017**, 35, 964-968. (g) L. Chen, J. Kang,H. Cui, Y. Wang, L. Liu, L. Zhang, C. Y. Su, *Dalton Trans*. **2015**, 44, 12180-12188. (h) L. Chen, T. Yang, H. Cui, T. Cai, L. Zhang, C. Y. Su, *J. Mater. Chem. A* **2015**, 3, 20201-20209. (i) S. A. Boer, D. R. Turner, *Chem. Commun*. **2015**, 51, 17375-17378. (j) V. Brega, M. Zeller, Y. He, H. Peter Lu, J. K. Klosterman, *Chem. Commun.* **2015**, 51, 5077-5080. (k) J. R. Li, J. Yu, W. Lu, L. B. Sun, J. Sculley, P. B. Balbuena, H. C. Zhou, *Nat. Commun*. **2013**, 4, 1538-1546. (l) W. Lu, D. Yuan, A. Yakovenko, H. C. Zhou, *Chem. Commun*. **2011**, 47, 4968-4970. (m) J. R. Li, H. C. Zhou, *Nat. Chem*. **2010**, 2, 893-898. (n) M. Jaya Prakash, M. Oh, X. Liu, K. N. Han, G. H. Seong, M. S. Lah, *Chem. Commun*. **2010**,

46, 2049-2051. (o) J. R. Li, A. A. Yakovenko, W. Lu, D. J. Timmons, W. Zhuang, D. Yuan, H. C. Zhou, *J. Am. Chem. Soc*. **2010**, 132, 17599-17610.

58) R. J. Doedens, *Prog. Inorg. Chem*. **2007**, 21, 209-230.

59) G. M. Brown, R. Chidambaram, *R. Acta Crystallogr. Sect. B: Struct. Crystallogr. Cryst. Chem.* **1973**, B29, 2393-2403.

60) Z. Yin, S. Wan, J. Yang, M. Kurmoo, M. H. Zeng, *Coord. Chem. Rev*. **2019**, 378, 500-512.

61) S. M. Cohen, *J. Am. Chem. Soc*. **2017**, 139, 2855-2863.

62) S. M. Cohen, *Chem. Rev*. **2012**, 112, 970-1000.

63) K. K. Tanabe, S. M. Cohen, *Chem. Soc. Rev*. **2011**, 40, 498-519.

64) Z. Wang, S. M. Cohen, *Chem. Soc. Rev.* **2009**, 38, 1315-1329.

65) O. Cui, O. Wang, Y. Zhao, W. Y. Sun, *Cryst. Growth Des*. **2019**, 19, 1454-1470.

66) O. Karagiaridi, W. Bury, J. E. Mondloch, J. T. Hupp, O. K. Farha, *Angew. Chem. Int. Ed*. **2014**, 53, 4530-4540.

67) P. Deria, J. E. Mondloch, O. Karagiaridi, W. Bury, J. T. Hupp, O. K. Farha, *Chem. Soc. Rev.* **2014**, 43, 5896-5912.

68) Y. Han, J. R. Li, Y. Xie, G. Guo, *Chem. Soc. Rev*. **2014**, 43, 5952-5981.

69) Instead of linker replacement, it is also possible to install additional linkers in MOFs. For a review, see: Q. Pang, B. Tu, Q. Li, *Dalton Trans*. **2019**, 48, 12000-12008.

70) B. J. Burnett, P. M. Barron, C. Hu, W. Choe, W. *J. Am. Chem. Soc*. **2011**, 133, 9984-9987.

71) W. Danowski, T. Van Leeuwen, S. Abdolahzadeh, D. Roke, W. R. Browne, S. J. Wezenberg, B. L. Feringa, *Nat. Nanotechnol*. **2019**, 14, 480-494.

72) L. H. Cao, X. Liu, X. H. Tang, J. Liu, X. Q. Xu, S. Q. Zang, Y. M. Ma, *Chem. Commun.* **2019**, 55, 12671-12674.

73) M. Gharib, L. Esrafili, A. Morsali, P. Retailleau, *Dalton Trans*. **2019**, 48, 8803-8814.

74) S. A. A. Razavi, A. Morsali, *Chem. - Eur. J.* **2019**, 25, 10876-10885.

75) Z. Shao, C. Huang, J. Dang, Q. Wu, Y. Liu, J. Ding, H. Hou, *Chem. Mater*. **2018**, 30, 7979-7987.

76) G. W. Xiao, T. F. Chen, X. Z. Sun, H. Guo, Z. F. Li, Y. H. Deng, C. Q. Wan, *Dalton Trans*. **2017**, 46, 12036-12040.

77) S. Shin, S. Jeong, D. Kim, M. S. Lah, *Cryst. Growth Des.* **2017**, 17, 2228-2237.

78) Y. Xu, N. A. Vermeulen, Y. Liu, J. T. Hupp, O. K. Farha, *Eur. J. Inorg. Chem*. **2016**, 4345-4348.

79) M. C. So, M. H. Beyzavi, R. Sawhney, O. Shekhah, M. Eddaoudi, S. S. Al-Juaid, J. T. Hupp, O. K. Farha, *Chem. Commun*. **2015**, 51, 85-88.

80) S. Jeong, D. Kim, X. Song, M. Choi, N. Park, M. S. Lah, *Chem. Mater*. **2013**, 25, 1047-1054.

81) O. Karagiaridi, W. Bury, E. Tylianakis, A. A. Sarjeant, J. T. Hupp, O. K. Farha, *Chem. Mater.* **2013**, 25, 3499-3503.

82) W. Bury, D. Fairen-Jimenez, M. B. Lalonde, R. Q. Snurr, O. K. Farha, J. T. Hupp, *Chem. Mater.* **2013**, 25, 739-744.

83) N. A. Vermeulen, O. Karagiaridi, A. A. Sarjeant, C. L. Stern, J. T. Hupp, O. K. Farha, J. F. Stoddart, *J. Am. Chem. Soc*. **2013**, 135, 14916-14919.

84) W. Xi, Y. Liu, Q. Xia, Z. Li, Y. Cui, *Chem. - Eur. J.* **2015**, 21, 12581-12585.

85) S. T. Madrahimov, T. A. Atesin, O. Karagiaridi, A. A. Sarjeant, O. K. Farha, J. T. Hupp, S. T. Nguyen, *Cryst. Growth Des*. **2014**, 14, 6320-6324.

86) S. Takaishi, E. J. DeMarco, M. J. Pellin, O. K. Farha, J. T. Hupp, *Chem. Sci*. **2013**, 4, 1509-1513.

87) X. Zhang, J. Sun, G. Wei, Z. Liu, H. Yang, K. Wang, H. Fei, *Angew. Chem. Int. Ed*. **2019**, 58, 2844-2849.

88) C. Tan, X. Han, Z. Li, Y. Liu, Y. Cui, *J. Am. Chem. Soc.* **2018**, 140, 16229-16236.

89) S. S. Zhao, H. Zhang, L. Wang, L. Chen, Z. J. Xie, *Mater. Chem. C* **2018**, 6, 11701-11706.

90) S. Y. Han, D. L. Pan, H. Chen, X. B. Bu, Y. X. Gao, H. Gao, Y. Tian, G. S. Li, G. Wang, S. L. Cao, C. Q. Wan, G. C. Guo, *Angew. Chem. Int. Ed*. **2018**, 57, 9864-9869,

91) G. G. Miera, A. B. Gómez, P. J. Chupas, B. Martín-Matute, K. W. Chapman, A. E. Platero-Prats, *Inorg. Chem*. **2017**, 56, 4576-4583.

92) C. Liu, C. Zeng, T. Y. Luo, A. D. Merg, R. Jin, N. L. Rosi, *J. Am. Chem. Soc*. **2016**, 138, 12045-12048.

93) W. Wang, L. Wang, Z. Li, Z. Xie, *Chem. Commun*. **2016**, 52, 5402-5405.

94) T. Li, M. T. Kozlowski, E. A. Doud, M. N. Blakely, N. L. Rosi, *J. Am. Chem. Soc*. **2013**, 135, 11688-11691.

95) M. Kim, J. F. Cahill, H. Fei, K. A. Prather, S. M. Cohen, *J. Am. Chem. Soc*. **2012**, 134, 18082-18088.

96) C. W. Tsai, J. W. Niemantsverdriet, E. H. G. Langner, *Microporous Mesoporous Mater*. **2018**, 262, 98-105.

97) M. B. Lalonde, J. E. Mondloch, P. Deria, A. A. Sarjeant, S. S. Al-Juaid, O. I. Osman, O. K. Farha, J. T. Hupp, *Inorg. Chem*. **2015**, 54, 7142-7144.

98) M. E. Schweinefuß, S. Springer, I. A. Baburin, T. Hikov, K. Huber, S. Leoni, M. Wiebcke, *Dalton Trans*. **2014**, 43, 3528-3536.

99) H. Fei, J. F. Cahill, K. A. Prather, S. M. Cohen, *Inorg. Chem.* **2013**, 52, 4011-4016.

100) O. Karagiaridi, M. B. Lalonde, W. Bury, A. A. Sarjeant, O. K. Farha, J. T. Hupp, J*. Am. Chem. Soc.* **2012**, 134, 18790-18796.

101) M. Erkartal, U. Erkilic, B. Tam, H. Usta, O. Yazaydin, J. T. Hupp, O. K. Farha, U. Sen, *Chem. Commun.* **2017**, 53, 2028-2031.

102) J. Q. Jiang, C. X. Yang, X. P. Yan, *Chem. Commun*. **2015**, 51, 6540-6543.

103) S. M. Jansze, K. Severin, *J. Am. Chem. Soc*. **2019**, 141, 815-819.

104) O. K. Farha, C. D. Malliakas, M. G. Kanatzidis, J. T. Hupp, *J. Am. Chem. Soc*. **2010**, 132, 950-952.

105) H. Chung, P. M. Barron, R. W. Novotny, H. T. Son, C. Hu, W. Choe, *Cryst. Growth Des.* **2009**, 9, 3327-3332.

106) B. J. Burnett, W. Choe, *CrystEngComm* **2012**, 14, 6129-6131.

107) M. Y. Masoomi, A. Morsali, A. Dhakshinamoorthy, H. Garcia, *Angew. Chem. Int. Ed.* **2019**, 58, 15188-15205.

108) J. Calbo, M. J. Golomb, A. Walsh, *J. Mater. Chem. A* **2019**, 7, 16571-16579.

109) a) E. G. Lebed, A. S. Belov, A. V. Dolganov, A. V. Vologzhanina, A. Szebesczyk, E. Gumienna-Kontecka, H. Kozlowski, Y. N. Bubnov, I. Y. Dubey, Y. Z. Voloshin, *Inorg. Chem. Commun.* **2013**, *30*, 53-57. b) Y. Z. Voloshin, A. Y. Lebedev, V. V. Novikov, A. V. Dolganov, A. V. Vologzhanina, E. G. Lebed, A. A. Pavlov, Z. A. Starikova, M. I. Buzin, Y. N. Bubnov, *Inorg. Chim. Acta* **2013**, *399*, 67-78. c) Y. Z. Voloshin, I. G. Belaya, A. S. Belov, V. E. Platonov, A. M. Maksimov, A. V. Vologzhanina, Z. A. Starikova, A. V. Dolganov, V. V. Novikov, Y. N. Bubnov, *Dalton Trans.* **2012**, *41*, 737-746.

110) For selected examples, see: a) A. S. Belov, I. G. Belaya, V. V. Novikov, Z. A. Starikova, E. V. Polshin, A. V. Dolganov, E. G. Lebed, *Inorg. Chim. Acta* **2013**, *394*, 269-281. b) Y. Z. Voloshin, O. A. Varzatskii, A. S. Belov, Z. A. Starikova, A. V. Dolganov, V. V. Novikov, Y. N. Bubnov, *Inorg. Chim. Acta* **2011**, *370*, 322-332. c) Y. Z. Voloshin, O. A. Varzatskii, A. S. Belov, A. V. Vologzhanina, Z. A. Starikova, A. V. Dolganov, V. V. Novikov, *Inorg. Chim. Acta* **2009**, *362*, 5144-5150. d) Y. Z. Voloshin, O. A. Varzatskii, A. V. Palchik, N. G. Strizhakova, I. I. Vorontsov, M. Y. Antipin, D. I. Kochubey, B. N. Novgorodov, *New J. Chem.* **2003**, *27*, 1148-1155.

111) Y. Z. Voloshin, O. A. Varzatskii, I. I. Vorontsov, M. Y. Antipin, *Angew. Chem. Int. Ed.* **2005**, *44*, 3400-3402.

112) Y. Z. Voloshin, O. A. Varzatskii, V. V. Novikov, N. G. Strizhakova, I. I. Vorontsov, A. V. Vologzhanina, K. A. Lyssenko, G. V. Romanenko, M. V. Fedin, V. I. Ovcharenko, Y. N. Bubnov, *Eur. J. Inorg. Chem.* **2010**, *2010*, 5401-5415.

113) W. Liu, W. Huang, C. H. Chen, M. Pink, D. Lee, *Chem. Mater.* **2012**, *24*, 3650-3658.

114) M. T. Dinh Nguyen, M. F. Charlot, A. Aukauloo, *J. Phys. Chem. A* **2011**, *115*, 911-922.

115) M. Antuch, P. Millet, *ChemPhysChem* **2018**, 19, 2549-2558.

116) a) G. G. Kazakov, N. O. Druzhkov, V. K. Cherkasov, *Russ. J. Coord. Chem.* **2020**, *46*, 178-192. b) Y. Bai, W. Chen, J. Li, C. Cui, *Coord. Chem. Rev.* **2019**, *383*, 132-154.

117) G. E. Zelinskii, A. A. Pavlov, A. S. Belov, I. G. Belaya, A. V. Vologzhanina, Y. V. Nelyubina, N. N. Efimov, Y. V. Zubavichus, Y. N. Bubnov, V. V. Novikov, Y. Z. Voloshin, *ACS Omega* **2017**, *2*, 6852-6862.

118) D. M. J. Lilley, *Quat. Rev. Bioph*. **2000**, 33, 109-159.

119) a) T. Ihara, T. Ishii, N. Araki, A. W. Wilson, A. Jyo, *J. Am. Chem. Soc.* **2009**, 131, 3826-3827. b) K. Tanaka, Y. Yamada, M. Shionoya, *J. Am. Chem. Soc.* **2002**, 124, 8802-8803.

120) J. Novotna, A. Laguerre, A. Granzhan, M. Pirrotta, M. P. Teulade-Fichou, D. Monchaud, *Org. Biomol. Chem.* **2015**, 13, 215-222.

121) J. Zell, F. R. Sperti, S. Britton, D. Monchaud*, RSC Chem. Biol.* **2021**, online.

122) Y. Takezawa, J. Müller, M. Shionoya, *Chem. Lett.* **2017**, 46, 622-633.

123) M. J. O'Connor, *Moll. Cell*, **2015**, 60, 4, 547-560.

124) a) E. Meggers, P. L. Holland, W. B. Tolman, F. E. Romesberg, P. G. Schultz, *J. Am. Chem. Soc.* **2000**, 122, 10714-10715. b) K. Tanaka, A. Tengeiji, T. Kato, N. Toyama, M. Shiro, M. Shionoya, *J. Am. Chem. Soc.* **2002**, 124, 12494-12498.

125) A. Oleksi, A. G. Blanco, R. Boer, I. Usón, J. Aymamí, A. Rodger, M. J. Hannon, M. Coll, *Angew. Chem. Int. Ed.* **2006**.

126) S. A. Barros, D. M. Chenoweth, *Angew. Chem. Int. Ed.* **2014**, 53, 13746-13750.

127) J. H. Chong, M. J. MacLachlan, *Chem. Soc. Rev.* **2009**, 38, 3301-3315.

128) a) 45, 1227-1231. b) J. Novotna, A. Laguerre, A. Granzhan, M. Pirrotta, M. P. Teulade-Fichou, D. Monchaud, *Org. Biomol. Chem.* **2015**, 13, 215-222.

129) S. Sasaki, S. Suzuki, K. Igawa, K. Morokuma, G. Konishi, *J. Org. Chem.* **2017**, 82, 6865-6873.

130) M. Pan, K. Wu, J. H. Zhang, C. Y. Su, *Coord. Chem. Rev.* **2019**, 378, 333-349.

131) L. J. Chen, H. B. Yang, M. Shionoya, *Chem. Soc. Rev.* **2017**, 46, 2555-2576.

132) J. L. Bolliger, A. M. Belenguer, J. R. Nitschke, *Angew. Chem. Int. Ed.* **2013**, 52, 7958-7962.

133) CrysAlis^{Pro} Software System, Rigaku Oxford Diffraction, **2018.**

134) G. M. Sheldrick, *Acta Cryst.* **2015**, A71, 3.

135) G. M. Sheldrick, *Acta Cryst.* **2015**, C71, 3.

136) O. V. Dolomanov, L. J. Bourhis, R. J. Gildea, J. A. K. Howard, H. Puschmann, H. *J. Appl. Cryst.* **2009**, *42*, 339-341.

French

07.09.1993

Chemin des vergers 5
1162 Saint-Prex
Suisse

+41 79 293 09 86

ophelie.planes@epfl.ch

Industrial Skills

GMP-BPF

Six Sigma (Yellow Belt)

Instruments

NMR, HPLC, GC-MS,

Electrochemistry: Cyclic

Voltammetry, TGA, UV-vis, FT-

IR, Chromatography: SEC, TLC

Ophélie Marie Planes

PROFESSIONAL EXPERIENCE

Sept 2016 – Present **Ecole Polytechnique Fédérale de Lausanne – Switzerland**
Doctoral Assistant

- Developed redox-active molecules and successfully employed them in coordination cages for potential use as electron reservoirs in industrial batteries
- Improvement of a MOF synthesis process via an innovative method (Solvent Assisted Linker Exchange) as a more efficient and faster new route for potential chiral guests enantiodifferenciation
- Oversaw 2 students and performed as teaching assistant (750+ hours)

Sept 2016 – Janv 2016 **Ecole Polytechnique Fédérale de Lausanne – Switzerland**
Research Internship

- Designed and synthesized large carboxylate molecules to create neutral metal-organic polyhedra as a future host-guest receptor

April 2015 – Aug 2015 **Cambridge University – United Kingdom**
Research Internship

- Yield improvement of a seven-step synthesis of an organic molecule to be used as a cargo-molecule for guests transportation

June 2013 – July 2013 **CNRS – France**
Research Internship

- Synthesized a thioether functionalized as a tripodal ligand to be used into a molecular machine as a molecular rotor

EDUCATION

Sept 2016 – Present **Ecole Polytechnique Fédérale de Lausanne – Switzerland**
PhD in Chemistry at the interface of Organic and Inorganic Chemistry

Sept 2016 – Sept 2014 **Université Paul Sabatier – Toulouse III - France**
Msc in Applied and Fundamental Organic Chemistry June 2014

Université Paul Sabatier – Toulouse III - France
Sept 2012 *Bachelor in Chemistry, 2nd and 3rd year*

June 2012 **Ecole Superieure de Chimie Organique et Minérale –France**

Languages

English – *C1*

German - *A2/B1*

French - *Native*

EXTRACURRICULAR ACTIVITIES

Mars-Oct 2019 **Vice-President at TEDxEcublens, Switzerland**

- Managing and coordinating a team of 20+ persons to organize a conference with different speakers about "power of connections"
- Connecting academic institutions and the team to ensure public relations and efficiency of processes

CONFERENCES

- **2019** International Symposium on Macrocyclic and Supramolecular Chemistry – Lecce (Italy)
  Poster « Insertion of Functionalized Metalloligands into Pillared-Paddlewheel MOFs by Solvent-Assisted Linker Exchange»
- **2018** Swiss Snow Symposium – Saas Fee (Switzerland)
  Poster « Clathrochelates as redox-active building blocks »
- **2018** SupraLyon – Lyon (France)
  Poster « Coordination Cages Based on Novel Metalloligands »

AWARDS and EXTRA-CERTIFICATIONS

2019 Lean Management Basics with **Six Sigma** Worshop (certification from ARIAQ institute)

2019 **GMP-BPF in Industry** (Certification with 80-90% Grade from ARIAQ

2018 Excellence Teaching Award at EPFL

2015 "Prix Excellence" for An Internship Abroad (Cambridge)

PUBLICATIONS

- T. N. Nguyen, S. Kampouri, B. Valizadeh, W. Luo, D. Ongari, **O. M. Planes**, *et al*. ACS *Appl. Mater. Interfaces,* **2018**, 10, 30035-30039.
- G. Cecot, M. T. Doll, **O. M. Planes** *et al. Eur. J. Inorg. Chem.,* **2019**, 25, 2972-2976.
- Y. Liu, P. Varava, A. Fabrizio, L.Y.M. Eymann, A. G. Tskhovrebov, **O. M. Planes** *et al*., *Chem. Sci.* **2019**, 10, 5719-5724.
- A. A. Suleymanov, A. Ruggi, **O. M. Planes**, A. S. Chauvin et al., *Chem. Eur. J*., **2019**, 25, 6718-6721.
- L. Y. M. Eymann, A. Shved, B. F.Curchod, Y. Liu, **O. M. Planes** *et al*., *J. Am. Chem. Soc*. **2019**, 141, 43, 17112-17116.
- **O. M. Planes,** P. Schouwink, J. L. Bila, , F. Fadaei-Tirani, R. Scopelliti and K. Severin, *Cryst. Growth Des*. **2020**, 20, 3, 1394-1399.
- **O. M. Planes**, S. M. Jansze, R. Scopelliti, F. Fadaei-Tirani, K. Severin, *Inorg. Chem*. **2020**, 59, 19, 14544-14548.

Ce document a été imprimé au Centre d’impression EPFL,
imprimerie climatiquement neutre, certifiée myClimate.